

UNIVERSITÉ DE HAUTE-ALSACE
UNIVERSITÉ DE STRASBOURG

Thèse

Pour l'obtention du grade de
Docteur de l'Université de Haute-Alsace

École Doctorale: Mathématiques, Sciences de l'Information et de l'Ingénieur
(ED 269) Discipline : Informatique

Présentée et soutenue publiquement

par

Ali El Hadi ISMAIL FAWAZ

The 8th of January 2024

**Deep Learning For Time Series
Analysis With Application On Human
Motion**

Jury

Rapporteur	Prof. Pierre-François MARTEAU, Université de Bretagne Sud
Rapporteur	Prof. Laurent OUDRE, Ecole Normale Supérieure Paris-Saclay
Examinatrice	Dr. HDR Latifa OUKHELLOU, Université Gustave Eiffel
Examinatrice	Dr. Georgiana IFRIM, University College Dublin
Directeur de thèse	Prof. Germain FORESTIER, Université de Haute-Alsace
co-Directeur de thèse	Prof. Jonathan WEBER, Université de Haute-Alsace
co-Directeur de thèse	Dr. Maxime DEVANNE, Université de Haute-Alsace
Co-Encadrant de thèse	Dr. HDR Stefano BERRETTI, University of Florence

UNIVERSITÉ DE HAUTE-ALSACE

Résumé

Deep Learning For Time Series Analysis With Application On Human Motion

Les séries temporelles, définies par des points de données espacés régulièrement dans le temps, sont essentielles dans divers domaines, notamment la médecine, les télécommunications et l'énergie. L'analyse des séries temporelles consiste à extraire des informations, des modèles et des tendances pour répondre à diverses tâches. La classification peut identifier des individus ayant des mouvements normaux ou anormaux en fonction de leurs séquences de mouvements basées sur le squelette. Les tâches de régression incluent la prédiction de la progression de la récupération d'un patient en fonction de ses mouvements. Le clustering peut analyser des données boursières pour détecter des comportements similaires entre actions. Le prototypage, utilisé dans les exercices de rééducation, augmente la quantité de données pour les chercheurs.

Étant donné les dépendances temporelles, développer des algorithmes efficaces pour l'analyse de séries temporelles nécessite de considérer ces relations. Ces dernières années, de nombreuses approches ont émergé pour résoudre diverses tâches d'analyse de séries temporelles. Elles incluent des méthodes basées sur la distance pour la classification, l'extraction de caractéristiques temporelles pour la régression et l'analyse de formes pour le clustering. Récemment, l'apprentissage profond, grâce à son succès dans des domaines comme le traitement du langage naturel et la classification d'images, s'est montré efficace pour l'analyse de séries temporelles.

Cette thèse aborde plusieurs tâches d'analyse de séries temporelles en utilisant des techniques d'apprentissage profond. Nous contribuons à la classification en améliorant les modèles profonds avec une ingénierie avancée des caractéristiques, en proposant des modèles de base comme points de départ et en développant une architecture novatrice, le plus petit réseau atteignant des performances de pointe. Nous traitons également le manque de données annotées avec des approches d'apprentissage auto-supervisé.

Nos contributions sont mises en valeur à travers des applications réelles, notamment dans l'analyse de séquences de mouvements humains pour la reconnaissance d'actions et la rééducation. Nous avons développé un modèle génératif pour les données de mouvements humains, utile pour des applications telles que la production cinématographique et le développement de jeux. De plus, dans le domaine du prototypage de séries temporelles, nous proposons une méthode pour générer des échantillons synthétiques via une analyse basée sur les formes, augmentant ainsi les données disponibles pour entraîner les modèles d'apprentissage profond pour les tâches de régression lorsque la collecte de données est coûteuse.

Enfin, nous entreprenons une évaluation approfondie des modèles discriminatifs et génératifs, en discutant les limitations des méthodologies d'évaluation actuelles. Nous plaidons pour l'établissement d'un processus d'évaluation unifié et équitable, robuste et résistant à la manipulation. À travers des expériences approfondies sur des données publiques, nous visons à faire progresser le domaine de l'analyse de séries temporelles en apportant de nouvelles méthodologies, démontrant leur impact significatif sur des applications pratiques.

UNIVERSITY OF HAUTE-ALSACE

*Abstract***Deep Learning For Time Series Analysis With Application On Human Motion Sequences**

Time series data, defined by equally spaced data points over time, is fundamental across various domains, notably in medical, telecommunication and energy etc. The analysis and mining of time series data involve extracting meaningful information, patterns, and trends to address various tasks. Classification can include identifying individuals with normal or abnormal movement based on their skeleton-based motion sequences. Clustering applications might involve analyzing stock market data to find similar behavior patterns among stocks. Prototyping is used in physical therapy exercises to expand the available data for researchers. Regression tasks include predicting the progress of a patient's recovery based on their movement data. Each of these applications highlights the diverse and critical uses of time series analysis.

Given the inherent temporal dependencies, developing effective time series analysis algorithms requires careful consideration of these temporal relationships. Over the past decade, numerous approaches have emerged to tackle different time series analysis tasks. These include for example distance-based methods for classification, temporal feature extraction for regression and shape analysis for clustering. Recently, deep learning has gained significant attention due to its success in other fields like natural language processing and image classification, and proved to be effective for time series analysis.

This thesis aims to address multiple time series analysis tasks using deep learning techniques. We contribute to the field of classification by enhancing deep models with advanced feature engineering, proposing foundation models to be used as starting points, and developing a novel architecture that remains the smallest network achieving state-of-the-art performance. Additionally, we tackle the issue of limited labeled data with self-supervised learning approaches.

Our contributions are showcased through real-world applications, particularly in analyzing human motion sequences for action recognition and physical rehabilitation. We developed a generative model for human motion data, valuable for applications such as cinematic production and game development. Additionally, in time series prototyping, we propose a method to generate synthetic samples via shape-based analysis, expanding the data available for training deep learning models for regression tasks when data collection is costly.

Finally, we undertake a thorough evaluation of both discriminative and generative models, shedding light on the limitations of current evaluation methodologies. We advocate for the establishment of a unified and fair evaluation process that is robust and resistant to manipulation. Through extensive experiments on public data, we aim to advance the field of time series analysis by providing novel insights and methodologies, demonstrating their significant impact on practical applications.

Acknowledgements

This work would not have been possible without the invaluable contributions and support of many individuals, whom I would like to sincerely thank here.

First and foremost, I would like to express my deepest gratitude to my supervisors, Dr. Maxime Devanne, Dr. Stefano Berretti, Prof. Jonathan Weber, and Prof. Germain Forestier. Their supervision, guidance, and encouragement over the past three years have shaped not only this thesis but also my growth as a researcher. The experience and knowledge I have gained through their mentorship have been truly enriching.

I would like to express my gratitude to Prof. Pierre-François Marteau and Prof. Laurent Oudre for accepting to review my manuscript, and to Dr. Latifa Oukhellou and Dr. Georgiana Ifrim for serving as members of the jury. Your time and expertise in evaluating this work are greatly appreciated.

I would like to thank Dr. Stefano Berretti for hosting me at the MICC Institute at the University of Florence for an academic research visit. This collaboration was an invaluable opportunity, and I deeply appreciate the hospitality and support.

I would like to thank Prof. Geoffrey I. Webb for hosting me at Monash University for a two-week academic research visit. The discussions and collaboration we shared were instrumental to my growth, and I am grateful for the opportunity to gain new perspectives and insights.

I would like to thank Dr. Patrick Schäfer for hosting me at Humboldt-University in Berlin and for inviting me to give a seminar on my PhD work.

I would like to thank Dr. François Petitjean and Dr. Hassan Ismail Fawaz for the many discussions we had on time series analysis.

I would like to thank Prof. Anthony Bagnall for nominating me as a core developer in the *aeon* toolkit, which allowed me to advance my research and promote my work.

I would also like to express my gratitude to the Mésocentre of Strasbourg for providing essential computational resources, including access to the GPU cluster, which was crucial for conducting my experiments.

I am thankful to the Agence Nationale de la Recherche for funding my PhD through the DELEGATION ANR project (grant NR-21-CE23-0014), without which this research would not have been possible.

Last but certainly not least, I would like to thank all of my colleagues at the Université de Haute-Alsace. Your contributions, both professionally and personally, have been invaluable throughout this journey.

Finally, I want to express my deepest gratitude to my parents, brothers, and friends for their unwavering support over the past three years and in all the years leading up to this point. Your encouragement and belief in me have been my constant source of strength.

Contents

Résumé	iii
Abstract	v
Acknowledgements	vii
Résumé des chapitres	1
Chapitre 1 : État de l’art pour l’analyse des séries temporelles : Apprentissage supervisé et non supervisé	1
Chapitre 2 : Évaluation comparative des modèles d’apprentissage automatique sur les données de séries temporelles	4
Chapitre 3 : Vers la recherche de modèles de fondation pour la classification des séries temporelles	5
Chapitre 4 : Réduire la complexité des modèles d’apprentissage profond pour la classification des séries temporelles	8
Chapitre 5 : Apprentissage semi-supervisé et auto-supervisé pour les données de séries temporelles avec un manque de labels	10
Chapitre 6 : Analyse de séries temporelles pour les données de mouvement humain	11
Chapitre 7 : Métriques d’évaluation pour la génération de mouvement humain	14
Chapitre 8 : Recherche reproductible	16
Introduction	19
1 State Of The Art For Time Series Analysis: Supervised and Unsupervised Learning	27
1.1 Introduction	27
1.2 Supervised Learning: Time Series Classification and Extrinsic Regression	27
1.2.1 Time Series Classification	27
1.2.2 Time Series Extrinsic Regression	56
1.3 Unsupervised Learning: Prototyping, Clustering and Self-Supervised .	58
1.3.1 Time Series Prototyping (TSP)	58
1.3.2 Time Series CLustering (TSCL)	63
1.3.3 Self-Supervised Learning for Time Series Analysis	70
1.4 Conclusion	75
2 Benchmarking Machine Learning Models on Time Series Data	77
2.1 Introduction	77
2.2 Background and Current Benchmarking Methods	77
2.2.1 Ranking Comparates	78
2.2.2 Pairwise Comparisons with the CDD	78
2.3 Limitations of the CDD	82
2.3.1 Instability of the Average Rank	82

2.3.2	Insufficient Attention to the Magnitude of Wins and Losses . . .	84
2.3.3	Null Hypothesis Significance Testing	84
2.3.4	The Use of Multiple Test Corrections	85
2.4	An Alternative Approach	87
2.5	The Multi-Comparison Matrix	89
2.5.1	MCM Examples	90
2.6	Conclusion	91
3	Towards Finding Foundation Models for Time Series Classification	93
3.1	Introduction	93
3.2	Hand-Crafted Convolution Filters	94
3.2.1	Are There Any Common Learned Convolution Filters Between Datasets?	94
3.2.2	Construction of Hand-Crafted Filters	95
3.2.3	Integration Into Deep Learning Architectures	97
3.2.4	Experimental Setup	99
3.2.5	Experimental Results	100
3.2.6	Analysis	102
3.3	Finding Foundation Models for Time Series Classification Using A Pre- text Task	105
3.3.1	Foundation Model Architecture Construction	107
3.3.2	Backbone Selection	108
3.3.3	Does It Make Sense To Use Batch Normalization On Different Datasets?	108
3.3.4	Experimental Setup	109
3.3.5	Experimental Results	112
3.3.6	Analysis	114
3.4	Conclusion	117
4	Reducing Complexity in Deep Learning Models for Time Series Classification	119
4.1	Introduction	119
4.2	The LITE Architecture	120
4.2.1	LITETime: An Ensemble Approach	122
4.2.2	Experimental Setup	122
4.2.3	Experimental Results	122
4.2.4	Ablation Studies	125
4.3	LITEMV: Addressing Multivariate Time Series Classification	128
4.3.1	Model Adaptation For Multivariate Time Series	129
4.3.2	Experimental Setup	130
4.3.3	Experimental Results	130
4.3.4	Analysis On Dataset Characteristics When Comparing LITEMVTime and ConvTran	132
4.4	Discussion Over Limitations of LITE and LITEMV	133
4.5	Conclusion	134
5	Semi-Supervised and Self-Supervised Learning for Time Series Data with a Lack of Labels	137
5.1	Introduction	137
5.2	TRILITE: TRIPlet Loss In Time	138
5.2.1	Model Construction	138

5.2.2	Triplet Loss	138
5.2.3	Triplet Generation	140
5.3	Experimental Setup	141
5.4	Experimental Results	143
5.4.1	Comparing To State-Of-The-Art	143
5.4.2	Use Case 1: Small Annotated Time Series Datasets	144
5.4.3	Use Case 2: Partially Annotated Time Series Datasets	145
5.5	Conclusion	146
6	Time Series Analysis For Human Motion Data	149
6.1	Introduction	149
6.2	Advancing Human Motion Rehabilitation Assessment with LITEMV-Time	152
6.2.1	Experimental Setup & Dataset Preprocessing	152
6.2.2	Competitor Models	154
6.2.3	Experimental Results	154
6.2.4	Enhancing Trust and Transparency in Human Rehabilitation Assessment With LITEMV	155
6.3	Extending Human Motion Rehabilitation Data With Time Series Prototyping	156
6.3.1	Generating Effective Time Series Prototypes With ShapeDBA	157
6.3.2	Weighted Average of Human Motion Sequences for Improving Rehabilitation Assessment	164
6.4	Exploring Deep Generative Models for Human Motion Generation	172
6.4.1	Background Work	173
6.4.2	Proposed Model	175
6.4.3	Experimental Setup	177
6.4.4	Experimental Results	178
6.5	Conclusion	183
7	Evaluation Metrics For Human Motion Generation	185
7.1	Introduction	185
7.2	Generative Models Metrics	186
7.2.1	Definitions	186
7.2.2	Fidelity Metrics	187
7.2.3	Diversity Metrics	192
7.3	Proposed Metric: Warping Path Diversity (WPD)	197
7.4	Experimental Setup	199
7.4.1	Backbone Architectures	201
7.4.2	Implementation Details	201
7.4.3	Training on Different Loss Parameters	201
7.4.4	Class Imbalanced Generation Setup	202
7.5	Results and Analysis	202
7.6	Conclusion	204
8	Reproducible Research	207
8.1	Introduction	207
8.2	Time Series Analysis With <i>aeon</i>	208
8.2.1	Deep Learning For Time Series With <i>Aeon</i>	208
8.2.2	Other Tasks With <i>Aeon</i>	209
8.3	What Makes A Work Reproducible ?	209

8.3.1	Code Documentation	209
8.3.2	Extendibility	210
8.3.3	Code Architecture	210
8.3.4	How To Check For All These Requirements	211
8.4	Hardware Utilization and Accessible Code Repositories	211
8.5	Published Work Serving For Analysis And Reproducibility	211
8.5.1	Elastic Warping Visualization	212
8.5.2	Convolutional Filter Space Visualization	212
8.5.3	Augmenting Time Series Classification Datasets With Elastic Averaging	213
8.5.4	KAN It Work For Time Series Classification ?	213
8.5.5	Published Webpages With Associated Papers	213
8.5.6	Deep Learning For Time Series Classification: A Webpage	213
8.6	Conclusion	214
	Conclusion and future works	215
	Financing	219
	Bibliography	221

List of Figures

1	Time Series Extrinsic Regression (TSER) is the task of predicting continuous labels of the time series samples.	20
2	Time Series CLustering (TSCL) is the task of discovering common information between samples of time series in order to group them into clusters.	20
3	Time Series Prototyping (TSP) is the task of finding a representative of a collection of time series of a similar group.	21
4	Time Series Classification (TSC) is the task of predicting a discrete label of the time series samples.	21
5	The number of research papers mentioning “deep learning” and “time series classification” increased rapidly in the last years.	22
1.1	Eight sections of Time Series Classification models from the literature: shapelet based, convolution based, distance based, feature based, interval based, dictionary based, hybrid based and deep learning based.	29
1.2	Example of DTW alignment path computation between two series (in red and in blue) from the ItalyPowerDemand dataset of the UCR archive. The DTW optimal alignment path between both series is presented in gray.	31
1.3	DTW optimal alignment vs the ED’s assumption of a perfect alignment on two time series of the ItalyPowerDemand dataset of the UCR archive.	32
1.4	Standard Convolution applied on a multivariate input time series of dimensions 3, convoluted with two times with three different convolutional filters, producing a convolutional output per filter, that are then summed together to produce two final outputs. The convolution operation starts with an element wise multiplication followed by a summation operation.	43
1.5	DepthWise Separable convolution multivariate input time series of dimensions 3, convoluted one time with three different convolutional filters, producing a convolutional output per filter, that go through a weighted summed to produce two final outputs. The convolution operation starts with an element wise multiplication followed by a summation operation.	44
1.6	The MultiLayer Perceptron (MLP) architecture (Wang, Yan, and Oates, 2017) for Time Series Classification.	50
1.7	Time-CNN (Zhao et al., 2017) architecture for Time Series Classification.	51
1.8	The Fully Convolutional Network (FCN) (Wang, Yan, and Oates, 2017) architecture for Time Series Classification.	52

1.9	The Residual Network (ResNet) architecture (Wang, Yan, and Oates, 2017) for Time Series Classification.	52
1.10	The Encoder architecture (Serra, Pascual, and Karatzoglou, 2018) for Time Series Classification.	53
1.11	The Inception architecture (Ismail Fawaz et al., 2020) for Time Series Classification.	54
1.12	The Disjoint-CNN architecture (Foumani, Tan, and Salehi, 2021) for Time Series Classification.	55
1.13	The ConvTran architecture (Foumani et al., 2024a) for Time Series Classification.	56
1.14	Time Series Prototyping comes down to finding a good representative of the input set of time series . This example uses the ECG5000 dataset of the UCR archive (Dau et al., 2019).	59
1.15	AE based architecture with a reconstruction loss for Time Series CLustering. The first step is to train the AE architecture to reconstruction the input time series . The second step is to generate the latent features and apply a clustering algorithm on top of these feature.	67
1.16	AE based architecture with a multi-reconstruction loss (Ghasedi Dizaji et al., 2017) for Time Series CLustering. The first step is to train the AE architecture to reconstruction the input time series as well as each layer of the AE network . The second step is the same as in Figure 1.15	69
1.17	The difference between using deep learning for Time Series Classification, Extrinsic Regression and Representation Learning (Self-Supervised Learning, SSL).	71
2.1	Critical Difference Diagram between five state-of-the-art models of TSC evaluated on 128 datasets of the UCR archive highlighting the average rank of each model over all datasets. If a clique is formed between two models it means that no conclusion can be made on the statistical significance in difference of performance between this pair of models.	78
2.2	Manipulation of the ranks of DrCIF and InceptionTime and the statistical significance of their pairwise differences by inclusion of similar comparates. When ResNet is replaced by STSF , DrCIF moves from a “ worse ” to a “ better ” rank, and the pairwise differences between DrCIF and InceptionTime change from being not statistically significant to statistically significant.	83
2.3	Manipulation of the ranks of DrCIF and TS-CHIEF and the statistical significance of their pairwise differences by inclusion of weakened comparates. When a weakened variant of TS-CHIEF (TS-CHIEF*) is replaced by a weakened variant of DrCIF (DrCIF*), DrCIF moves from a “ worse ” to a “ better ” rank and the pairwise differences between DrCIF and TS-CHIEF change from being not statistically significant to statistically significant.	83

2.4	Two examples demonstrate the instability of pairwise significance under the Holm correction: (a) for the comparates BOSS, Catch22, TSF, and WEASEL; and (b) for the comparates DrCIF, HC2, Hydra, and MultiRocket. The statistical significance of pairwise differences between comparates is influenced by the additional comparates included in the comparison. In each case, four different patterns of statistically significant pairwise differences, (i), (ii), (iii), and (iv), are shown in the left column (pairs with non-significant differences according to the Wilcoxon signed-rank test with Holm correction are connected by a black line). Randomly chosen examples of additional comparates that result in the given pattern of statistically significant pairwise differences are shown in the right column.	86
2.5	A visualization of the Bayesian Signed Rank Test proposed in (Benavoli et al., 2017) as a replacement for the Wilcoxon Signed Rank Test is provided. As illustrated, the Bayesian test offers information on the probability that the null hypothesis is true, given the performance metrics of both InceptionTime and ROCKET on the 108 tasks from the UCR archive.	88
2.6	MCM showing all pairwise comparisons between MultiROCKET, ROCKET, InceptionTime, ResNet, and FCN on the 128 datasets of the UCR archive. In this setup, the full pairwise comparison is presented.	90
2.7	MCM showing pairwise comparisons between InceptionTime and each of ROCKET, MultiROCKET, FCN and ResNet on the 128 datasets of the UCR archive.	91
3.1	t-SNE two-dimensional projection of the first-layer convolution filters learned by CNN models on four ECG datasets (ECG200 , ECG5000 , ECGFiveDays , TwoLeadECG). The clustering of filters in the t-SNE space suggests that deep CNN models can identify common, generic filters across different datasets.	95
3.2	Three hand-crafted filters detecting: (1) increasing trends, (2) decreasing trends and (3) peaks in a time series. The orange points indicates on which time stamps the filters are activated after being convolved with an input time series from the Meat dataset of the UCR Archive.	97
3.3	The CO-FCN architecture, applied non trainable hand-crafted convolution filters on the input data, followed by the rest of the FCN architecture (Wang, Yan, and Oates, 2017).	98
3.4	The H-FCN architecture using non trainable hand-crafted filters in parallel to trainable convolution filters.	99
3.5	The H-Inception architecture using non trainable hand-crafted filters in parallel to trainable convolution filters of Inception (Ismail Fawaz et al., 2020).	99
3.6	Results over 128 datasets of the UCR archive (Dau et al., 2019) presented in a 1v1 scatter plot format between FCN, InceptionTime (IT) and their variants CO-FCN, H-FCN and H-InceptionTime (H-IT) using the hand-crafted convolution filters.	100
3.7	Critical Difference Diagram (Benavoli, Corani, and Mangili, 2016) presenting a comparison between three proposed networks and three state-of-the-art deep learning models for TSC, aggregated over the 128 datasets of the UCR archive.	101

- 3.8 Multi-Comparison Matrix (Chapter 2) presenting a comparison between three proposed networks and three state-of-the-art deep learning models for TSC, aggregated over the 128 datasets of the UCR archive. 102
- 3.9 Multi-Comparison Matrix (Chapter 2) presenting a comparison between H-InceptionTime, InceptionTime, and two state-of-the-art non-deep learning models for TSC, ROCKET and MultiROCKET, aggregated over the 128 datasets of the UCR archive. 102
- 3.10 Hand-crafted increasing trend detection filter of size $K = 8$ and its closest learned filter on the CinCECGTorso dataset. The learned filter is from the first layer of the original FCN. 103
- 3.11 T-SNE two-dimensional projection of the 128 filters learned by the first layer of the original FCN and the 64 filters learned by the first layer of the H-FCN on the CricketY dataset of the UCR Archive. The two hand-crafted increasing and decreasing trend detection filters are also projected in the two-dimensional space. 104
- 3.12 Training phase of the FCN and H-FCN architectures on the FiftyWords dataset while monitoring the validation loss on the test set. The training loss of H-FCN converges faster than the training loss of FCN. Also, the validation loss of H-FCN is always below the validation loss of FCN. This shows that H-FCN generalizes better than FCN on this dataset. 105
- 3.13 Summary of the proposed pretext task approach. Given an archive of N datasets, the first step is to train a pre-trained model on all of the datasets, where the classification task is to predict the dataset each time series belongs to. The second step is to copy the pre-trained model and follow it with an add-on model randomly initialized. The second step is done for each of the N datasets of the archive independently. After constructing the N new models, they are fine-tuned on each dataset depending on the task of each one. 106
- 3.14 The architecture of H-Inception divided into two sub-models. The first model is the pre-trained model, trained on the pretext task, while the second model is the randomly initialized add-on model. The H-Inception model is made of six Inception modules, where each module contains three convolution layers and a Max Pooling layer followed by a concatenation, a batch normalization layer and an activation function. Each Inception module, except the first one, is preceded by a bottleneck layer to reduce the dimensionality and hence the number of parameters. The first Inception module contains the hybrid addition, which is the hand-crafted convolution filter. Residual connections exist between the input and the third module, as well as between the third module and the output. 109

3.15	An example using the proposed Batch Normalizing Multiplexer (BNM) that solves the problem of learning a batch normalization layer on multiple samples of different distributions (datasets). The BNM is made of multiple batch normalization layers (with blue and red contours) proceeded by a multiplexer. This multiplexer has three different nodes: (a) input node, where the input time series goes through, (b) the control node, where the information about the dataset this input time series belong to goes through, and (c) the output node. The path selected for the output node is controlled by the node (b). It is important to note that the BNM, such as the traditional batch normalization layer, learns on the whole batch. The only difference is that more than one batch normalization layer will be fed by parts of this batch, which intuitively means the flow of information is slower when using the BNM.	110
3.16	A 1v1 scatter plot that compares the performance of H-InceptionTime (baseline) and PHIT following the accuracy metric.	113
3.17	A Multi-Comparison Matrix (MCM) representing the comparison between the proposed approach PHIT with the state-of-the-art approaches. The winning approach following the average performance is MultiROCKET and in second comes our approach. No conclusion can be found on the difference of performance between MultiROCKET and PHIT given the high p-value.	113
3.18	Comparing the performance of the proposed approach and its change with respect to the training set size. The curve represents the difference in performance between the proposed approach and the baseline . A positive value (above the tie line) represents a win for the pre-training approach. For each plot, we show this comparison on the datasets of the same type in the UCR archive. The x -axis represents the number of training examples (in \log_{10} scale). The y -axis represents the difference of accuracy between the usage of our pre-training approach and the baseline.	115
3.19	A two dimensional representation of the filters coming from the first Inception module of the baseline , pre-trained and fine tuned models. The used datasets in this study are ECG200 (left) and NonInvasiveFetalECGThorax1 (right). The two dimensional representation is done using t -SNE coupled with DTW to as a distance measure. Some areas can be seen to be in common between the three models in the case of large datasets (right) however it is not the case for small datasets (left).	116
4.1	Difficulties in deploying a high-parameter deep learning model, such as FCN, on a Sony robot for ground type classification. The extensive computational resources and memory required by FCN present significant challenges for resource-constrained devices.	120
4.2	The proposed LITE architecture for Time Series Classification.	121
4.3	MCM (Chapter 2) showing the comparison between (LITE, LITE-Time) and the rest of the state-of-the-art deep learning models for time series classification.	123

4.4	For each model, the y-axis shows accuracy on the FreezerSmallTrain dataset, and the x-axis shows FLOPS in a \log_{10} scale. Circle diameter represents the number of trainable parameters. The smallest model, LITE (ours), has $10k$ parameters and the lowest FLOPS (4 in \log_{10} scale), while achieving the highest test accuracy.	124
4.5	The Heat Map shows the one-vs-one comparison between the Striped-LITE and the three variants: (1) Add-Custom-Filters, (2) Add-Multiplexing- Convolution and (3) Add-Dilated-Convolution. The colors of the Heat Map follow the value of the first line in each cell. This value is the difference between the value of the first line (average accuracy when winning/losing). The second line represents the Win/Tie/Loss count between the models in question (wins for the column model). The last line is the statistical P-Value between the two classifier using the Wilcoxon Signed Rank Test	125
4.6	The stripped version of the LITE architecture for Time Series Classification.	126
4.7	One-vs-one comparison between LITETime and LITETime with Standard convolutions over the 128 datasets of the UCR archive (Dau et al., 2019).	127
4.8	A Critical Difference diagram showcasing the comparison of performance of LITETime when more or less LITE models are used in the ensemble.	127
4.9	A Multi-Comparison Matrix (Chapter 2) showcasing the comparison of performance of LITETime-10,9 and 8 with other LITETime models with varying number of LITE heads.	128
4.10	A Comparison on the Beef dataset of the UCR archive (Dau et al., 2019) between the ensemble of LITE and Inception models. The x -axis represents the number of models used in each ensemble and the y -axis the performance of the ensemble on the test set of the Beef dataset.	129
4.11	A Multi-Comparison Matrix (MCM) showcasing the performance of LITEMVTime, LITETime, InceptionTime, Disjoint-CNN and ConvTran on the 30 datasets of the UEA archive.	130
4.12	Difference of performance between LITEMVTime and ConvTran with respect to the number of training samples in log scale.	132
4.13	Difference of performance between LITEMVTime and ConvTran with respect to the number of channels in log scale.	133
4.14	Number of parameters of Standard Convolutions and DWSCs in function of number of convolution filters to learn and their kernel size.	134
5.1	Overview of our TRILITE model with a triplet input example taken form the Beef dataset of the UCR archive (Dau et al., 2019).	139
5.2	Schema of the relaxed spaced controlled by the margin α with an input example taken form the Beef dataset of the UCR archive (Dau et al., 2019).	139
5.3	A mixed up pos is built from three time series including the ref . The resulting time series is close to the <i>ref</i> except some areas as highlighted in the red circle . A mask is then applied on the mixed up pos to generate the final sample , where the unmasked parts are replaced by a Gaussian noise.	142

5.4	A mixed up neg is built from three time series excluding the ref used to generate the <i>pos</i> sample. The resulting time series is close to the <i>not ref</i> except some areas as highlighted in the red circle . A mask is then applied on the mixed up neg to generate the final sample , where the unmasked parts are replaced by a Gaussian noise.	142
5.5	Comparing the proposed TRILITE approach to two state-of-the-art SSL models: DCNN (Franceschi, Dieuleveut, and Jaggi, 2019) and MCL (Wickstrøm et al., 2022). We compare the classification of TRILITE latent spaces to MCL’s latent space using a 1NN and to DCNN’s latent space using both 1NN and a Support Vector Machine classifier (Vapnik, 2013) following the original work of both comparates.	143
5.6	Scatter plots comparing the proposed TRILITE model to FCN.	144
5.7	The MCM (Chapter 2) comparing concat(TRILITE,FCN)+1LP to FCN and TRILITE+1LP over the 85 datasets of the UCR archive.	145
5.8	Comparison of experiment 1 and experiment 2. In experiment 1, the TRILITE model is trained only on the labeled subset (30% of the data). On the contrary, in experiment 2, the TRILITE model is trained on the whole train set. The evaluation is done on the whole test set.	145
6.1	Example of one sample per action (12 total) taken from the HumanAct12 action recognition skeleton based dataset (Guo et al., 2020). Each skeleton is made of five body parts, right arm , left arm , spine & neck , right leg and left leg	150
6.2	Example of one sample taken from the HumanAct12 action recognition skeleton based dataset (Guo et al., 2020) represented as a Multivariate Time Series. For the sake of visualization we consider only five joints: head , left wrist , right wrist , left ankle , and right ankle , each in a 3D space, resulting in an MTS of 15 dimensions.	151
6.3	Visualization of one sample from the Kimore skeleton based human rehabilitation dataset (Capecchi et al., 2019), per exercise.	153
6.4	The distribution of the scores given by experts to healthy and unhealthy patients when performing each of the five different exercises. The threshold set to discretize these scores is chosen to be the middle point posed at 50.	154
6.5	Explainability of the LITEMV model using the Class Activation Map (CAM) on the feature of the last DWSC layer. The colorbar values represent the normalized (between 0 and 1) scores of the CAM. Five samples each from one of the five exercises are presented with the CAM scores on different time stamps. A higher CAM score indicates the importance of a time stamp for the decision making of LITEMV.	156
6.6	Explainability of the LITEMV model using the Class Activation Map (CAM) on the feature of the last DWSC layer. Two samples from the test split of the same exercise are presented, the first (top) having a ground truth of class 1, and the second (bottom) having a ground truth of class 0. LITEMV correctly classifies the first sample but incorrectly the second. It can be seen that the important time stamp in the case of the correctly classified sample has higher color intensity, so higher CAM score, compared to the same time stamp from the incorrectly classified sample.	157

6.7	A qualitative evaluation of the proposed average technique compared to other approaches on a GunPoint dataset. The ShapeDBA algorithm is the only approach to not generate out-of-distribution artifacts. . . .	159
6.8	Calculation of the ShapeDTW measure between two time series. The overlapping area between the two sliding windows is recomputed. . . .	161
6.9	A more efficient implementation of the ShapeDTW measure with the identity descriptor involves sliding a window over the time stamp pairwise Euclidean matrix between the two time series, instead of applying DTW directly on their multivariate transformation. The data from each window position is collected into a zero-initialized matrix, which is then processed using the DTW algorithm, significantly reducing computational overhead. . . .	162
6.10	An MCM comparing ShapeDBA to other averaging approaches, coupled with k -means and their associated similarity measure, and k -shape, on the ARI metric. . . .	162
6.11	1v1 Comparison between using k -means with ShapeDBA-ShapeDTW and other approaches from the literature using the Adjusted Rand Index clustering metric. . . .	163
6.12	The ECGFiveDays dataset from the UCR archive provides two examples from each class. In this dataset, the majority of the time stamps are noisy, with the critical information localized in the central section of the time series. ShapeDBA does not perform well on this dataset, with an ARI score of almost 0.042. . . .	163
6.13	An MCM (Chapter 2) showing ShapeDBA's (ours) duration (in seconds) compared to other approaches to finalize the clustering task on 123 datasets of the UCR archive (Dau et al., 2019). . . .	164
6.14	We determine the N nearest neighbors for each reference in the dataset using Dynamic Time Warping (DTW). Each neighbor is assigned a weight according to its DTW distance from the reference. These weights are then utilized to compute a weighted average sequence through ShapeDBA. Subsequently, a weighted score is calculated, allowing us to expand the regression training dataset with this new synthetic sample. . . .	166
6.15	Averaging six human motion sequences (Examples 0 to 5 shown on the top left/right) with uniformly distributed weights results in an unrealistic example (bottom right skeleton sequence). The 2D t-SNE (Maaten and Hinton, 2008) projection of these sequences (bottom left) illustrates that the averaged sequence falls outside the manifold of the original sequences. . . .	166
6.16	Visualization of three examples: the top row shows a real sample, the middle row displays a noisy sample, and the bottom row features a sample generated using the weighted ShapeDBA method. Each sequence is represented by 10 frames, arranged sequentially from left to right. . . .	168

- 6.17 Visualization of two real sequences (top and bottom) and their corresponding weighted ShapeDBA sequence (middle). The generated average sequence preserves the temporal alignment of the top sequence, which has a higher weight, while also incorporating features like the patient’s height from the bottom sequence. 168
- 6.18 Summary of our proposed Supervised VAE (SVAE) architecture: The input skeleton sequences are processed by the encoder to learn a Gaussian distribution in the latent space. From this distribution, a random sample is drawn and utilized in two ways: it is fed into a classifier for the action recognition task and also into the decoder to reconstruct the original sequence. This dual functionality enhances both the generative and discriminative capabilities of the model. . . . 173
- 6.19 The Variational Auto-Encoder (VAE) model for human motion generation leverages an FCN backbone in both the Encoder and Decoder. In the Decoder, standard one-dimensional convolutions are replaced with transposed convolutions. Each convolution layer is followed by batch normalization and a ReLU activation function. The SVAE model further includes Fully Connected layers to enhance its functionality. 176
- 6.20 The 2D projection of the latent space (using PCA) for the VAE, CVAE and SVAE models on the training samples shows distinct separation of latent points corresponding to each action label in the case of SVAE compared to no separation in the cases of VAE and CVAE. 180
- 6.21 Generated samples from the proposed SVAE models are conditioned on four different actions: Warm Up, Drink, Lift Dumbbell and Sit. For each action, we present two distinct generated examples to showcase the diversity and robustness of the SVAE model. 181
- 6.22 The confusion matrix compares performance when training on real samples (left) versus augmented samples with a fixed label distribution (right). The matrix consists of 12 rows and 12 columns, corresponding to the 12 action labels. Each row represents the actual class of the samples used for prediction, and each class is ranked in descending order based on their population in the test set. The results show that when the label distribution is fixed (right), the test set performance is significantly affected in classes 4, 7, and 11, which have higher ranks. 183
- 7.1 The evaluation metrics for human motion generation in this work are divided into two groups: fidelity metrics and diversity metrics. These metrics are further categorized based on their evaluation criteria, such as FID being a distribution-based metric. 186
- 7.2 Before calculating evaluation measures, two steps are followed. First, a model is trained on a supervised task using only real data and not the generated data. Second, the pre-trained encoder’s latent representation of the real data is extracted, as well as the latent representation of the generated samples. The metrics are then computed based on this latent representation. 187

- 7.3 On the left, we illustrate the energy (FID) needed to transform a **standard Gaussian distribution** into another **Gaussian distribution with a higher mean and variance**. On the right, the plot shows that as the mean (μ) and variance (σ^2) of the target distribution increase, the required transformation energy (FID) also increases progressively. 188
- 7.4 This example demonstrates the AOG metric for two generative models. **Model1** achieves a perfect AOG of 100% by accurately generating samples conditioned on three classes **red triangles**, **blue squares** and **green circles**. In contrast, **Model2** only achieves 50%, indicating it struggles with correct conditional generation. The AOG metric reflects the classification accuracy of generated samples compared to ground truth labels \hat{Y} 190
- 7.5 This example demonstrates the computation of density and precision metrics on a synthetic dataset. The left side shows the latent representation of: **real data**, **the real outlier**, generated samples **near the outlier** and **near non-outliers**. For each real sample we represent its neighborhood area. The right side depicts the original data series. The density metric, unlike precision, correctly identifies the outlier, giving a score of 1.25 instead of 1. This illustrates how density better reflects fidelity by accounting for outliers. Both metrics use 2 neighbors. 191
- 7.6 This example demonstrates the calculation of the APD metric for both **real samples** and **generated samples**. For each latent representation, two sets \mathcal{S} and \mathcal{S}' of randomly selected values, each of size S_{apd} , are created. The APD metric is then computed between these sets. This process is repeated RR times, and the final APD value is the **average of all computed APD values**. 193
- 7.7 The computation of coverage and recall metrics over a synthetic dataset is shown on the left and right side of the figure. The figure's left and right sides depict the latent space with **real samples** and generated samples both **reliable**, and **outliers**. The middle shows the original series space, highlighting the differences between the three spaces. The left plot shows neighbor areas around generated samples (recall metric), while the right plot shows neighbor areas around real samples (coverage metric). The coverage metric correctly identifies outliers, resulting in a non-perfect measure, unlike the recall metric. Both metrics use 2 neighbors. 195
- 7.8 This example illustrates the MMS metric computation on a synthetic dataset. The left side shows the latent representation of **real samples** and **generated samples**. The right side displays the original series space. First, each generated point's nearest neighbor in the real set is identified using the **Euclidean Distance**. Second, the MMS metric is obtained by averaging all these distances. 196

- 7.9 This figure demonstrates the need for a temporal distortion diversity metric. On the left side, three **real (top)** and three **generated (bottom)** human motion sequences performing the "drink-with-left-hand" action are presented. In the middle, the y -axis projection of the subject's left-hand motion is displayed **for the three samples** from both real and generated spaces. The real samples show variability in the starting frame, while the generated samples start consistently. On the right, the latent representation of **real** and **generated** samples using a pre-trained GRU classifier reveals that the model does not account for temporal distortion diversity. 197
- 7.10 The distance matrix between **two time series** is shown in a heat map where each point represents the squared difference between corresponding time stamps. The optimal **Dynamic Time Warping (DTW) path**, captures the temporal distortion between the series. The **connections** between the warping path and the **diagonal** indicate how much the two series deviate from having no temporal distortion. 198
- 7.11 Mathematical basis of the WPD metric: For **each point** on the **warping path**, the **corresponding triangle** is always a right isosceles triangle, given that the series are of equal length. Hence the **distance** from the **point** to the **diagonal** can be easily calculated with the Pythagorean theorem (Maor, 2019). 199
- 7.12 In our experiments, the CVAE undergoes two phases: training and generation. **During training**, the **Encoder** and **Decoder** are trained simultaneously. The **Encoder** extracts features from input sequences and projects them into a Gaussian latent space with a learned **mean** and **variance**, conditioned on the **action label**. The **Decoder** then reconstructs the input sequence from a **sample in this space**. **In the generation phase**, a **random sample from a Normal distribution** is fed to the **Decoder** to generate a new sequence, also conditioned on the desired **action label**. 200
- 7.13 Radar charts compare the performance of three CVAE variants across eight metrics. Each chart, labeled from **a** to **d**, represents a different (α, β) parameter set. The charts feature four polygons: one for **each CVAE variant** and one for **real data metrics**. For all metrics except FID, a higher summit indicates better performance. For FID, a higher summit means worse performance. 202
- 8.1 Warping path example between two time series from the ECGFiveDays dataset. 212

List of Tables

1	List of contributions including 11 papers and 3 open source published work with the companion GitHub repository.	24
3.1	Excluded datasets from the UCR archive in this study. Each dataset is followed by its information and a reason for its exclusion.	111
3.2	The Win/Tie/Loss count between the proposed PHIT approach and the baseline (H-InceptionTime) per dataset domain. The first column presents the number of datasets included per domain followed by the number of Wins for PHIT, number of Ties, and number of Wins for the baseline. We include as well the percentage of number of losses and the average difference in accuracy (PHIT - baseline). A positive value in the last column indicates that on average of all datasets in a specific domain, PHIT performs better than the baseline on the accuracy metric (lowest value 0.0 and highest value 1.0).	114
4.1	Comparing LITE, FCN, ResNet and Inception in terms of number of trainable parameters and number of FLoat-point Operation Per Second (FLOPS).	122
4.2	Comparison between the proposed methods with FCN, ResNet and Inception without ensemble.	124
4.3	Accuracy performance in % of LITEMVTime (LMVT), LITETime (LT), ConvTran (CT), InceptionTime (IT), Disjoint-CNN (D-CNN), FCN and ResNet on 30 datasets of the UEA archive. The datasets are ordered by their average number of training samples per class. The accuracy of the best model for each dataset is presented in bold and of the second best is underlined.	131
6.1	Accuracy of the baseline, 1-NN-DTW, three state-of-the-art deep learning models, FCN ResNet and InceptionTime compared to our LITEMVTime on the Kimore human rehabilitation exercise. We present for each of the five exercises the accuracy of the models on the test unseen split. The performance of the winning model for each exercise is shown in bold and the second best is shown in <u>underline</u>	155
6.2	The FID values of different augmentation methods and the real dataset, over different resamples of each exercise. The presented FID values include the average and standard deviation over all resamples per exercise and different initialization of the pre-trained feature extractor.	170
6.3	The APD values of different augmentation method and the real dataset, over different resamples of each exercise. The presented APD values include the average and standard deviation over all resamples per exercise, different randomly selected sets of size $S_{apd} = 20$ and different initialization of the pre-trained feature extractor.	170

6.4	MAE and RMSE errors obtained for all compared approaches on each exercise separately. Best values are emphasized in bold, while second best values are underlined.	171
6.5	The best loss function weights for the VAE, CVAE and SVAE models are as follows. For the VAE and CVAE, the classification loss weight (W_{cls}) is set to 0 due to the absence of a classifier. The generated samples maintain the same label distribution as the training set but include more samples to better estimate the statistical metrics. The best performing setup for each of the three variants is highlighted in bold	179
6.6	We compared our proposed model, the proposed SVAE, with other approaches from the literature using the FID and Diversity metrics. For each method, we reported the average \pm standard deviation of the FID and Diversity scores. For the real samples, a random split into two sets was used to calculate the FID metric. This comparison allows us to assess the effectiveness of our SVAE model in generating diverse and high-fidelity samples relative to existing methods.	182
6.7	Test accuracy values are reported for four different train/test splits: (first row) training on real samples; (second row) training on generated samples (following the same distribution as the real samples); and (third row) training on augmented samples (a combination of real and generated samples to achieve a uniform label distribution).	182
7.1	Summary of the Generative Models Metrics in this study.	200

List of theorems and definitions

1	Theorem (Increasing Trend Dection Convolution Filter)	95
2	Theorem (Decreasing Trend Dection Convolution Filter)	96
3	Theorem (Fréchet Inception Distance Interpretation)	189
4	Theorem (Average Pair Distance Interpretation)	192
5	Theorem (Warping Path Diversity's Distance To Diagonal Computation)	198

List of Abbreviations

ECG	<i>Electrocardiogram</i>
EEG	<i>Electroencephalogram</i>
TSC	<i>Time Series Classification</i>
TSCL	<i>Time Series Clustering</i>
TSP	<i>Time Series Prototyping</i>
TSER	<i>Time Series Extrinsic Regression</i>
UTS	<i>Univariate Time Series</i>
MTS	<i>Multivariate Time Series</i>
NN	<i>Nearest Neighbor</i>
DTW	<i>Dynamic Time Warping</i>
ED	<i>Euclidean Distance</i>
ShapeDTW	<i>Shape Dynamic Time Warping</i>
SoftDTW	<i>Soft Dynamic Time Warping</i>
EE	<i>Elastic Ensemble</i>
PF	<i>Proximity Forest</i>
RF	<i>Random Forest</i>
ADTW	<i>Amerced Dynamic Time Warping</i>
hctsa	<i>highly comparative time-series analysis</i>
Catch22	<i>Canonical Time Series Characteristics</i>
TSFresh	<i>Time Series Feature Extraction based on Scalable Hypothesis Tests</i>
RotF	<i>Rotation Forest</i>
CNN	<i>Convolutional Neural Network</i>
ROCKET	<i>RandOm Convolutional KERNel Transform</i>
PPV	<i>Proportion of Positive Values</i>
MPV	<i>Mean of Positive Values</i>
MIPV	<i>Mean of Indices of Positive Values</i>
LSPV	<i>Longest Stretch of Positive Values</i>
HYDRA	<i>HYbrid Dictionary-Rocket Architecture</i>
STC	<i>Shapelet Transform Classifier</i>
RDST	<i>Random Dilated Shapelet Transform</i>
SAX	<i>Symbolic Aggregate approXimation</i>
PAA	<i>Piecewise Aggregate Approximation</i>
VSM	<i>Vector Space Model</i>
SFA	<i>Symbolic Fourier Approximation</i>
MCB	<i>Multiple Coefficient Binning</i>
BOSS	<i>Bag-of-SFA-Symbols</i>
WEASEL	<i>Word Extraction for Time Series Classification</i>
TSF	<i>Time Series Forest</i>
CIF	<i>Canonical Interval Forest</i>
DrCIF	<i>Diverse Representation Canonical Interval Forest</i>
TS-CHIEF	<i>Time Series Combination of Heterogeneous and Integrated Embedding Forest</i>
RISE	<i>Random Interval Spectral Ensemble</i>

COTE	<i>Collective Of Transformation-based Ensemble</i>
CAWPE	<i>Cross-validation Accuracy Weighted Probabilistic Ensemble</i>
HIVE-COTE	<i>HIerarchical VotE Collective Of Transformation Ensemble</i>
HC	<i>HIVE-COTE</i>
RNN	<i>Recurrent Neural Network</i>
FC	<i>Fully Connected</i>
SGD	<i>Stochastic Gradient Descent</i>
SC	<i>Standard Convolution</i>
DWSC	<i>DepthWise Separable Convolution</i>
DWC	<i>DepthWise Convolution</i>
PWC	<i>PointWise Convolution</i>
BN	<i>Batch Normalization</i>
GMP	<i>Global Max Pooling</i>
GAP	<i>Global Average Pooling</i>
NLP	<i>Natural Language Processing</i>
PE	<i>Positional Encoder</i>
APE	<i>Absolute Positional Encoding</i>
LSTM	<i>Long Short-Term Memory</i>
GRU	<i>Gated Recurrent Unit</i>
MLP	<i>MultiLayer Perceptron</i>
TimeCNN	<i>Time Convolutional Neural Network</i>
FCN	<i>Fully Convolutional Network</i>
ResNet	<i>Residual Neturok</i>
IN	<i>Instance Normalization</i>
NNE	<i>Neural Network Ensemble</i>
Disjoint-CNN	<i>Disjoint Convolutional Neural Network</i>
ConvTran	<i>Convolutional Transformer</i>
RPE	<i>Relative Positional Encoding</i>
eRPE	<i>Efficient Relative Positional Encoding</i>
CART	<i>Classification and Regression Tree</i>
EBA	<i>Elastic Barycenter Averaging</i>
DBA	<i>DTW Barycenter Averaging</i>
MSM	<i>Move-Split-Merge</i>
MBA	<i>MSM Barycenter Averaging</i>
SoftDBA	<i>SoftDTW Barycenter Averaging</i>
SBD	<i>Shape Based Distance</i>
NCC	<i>Normalized Cross Correlation</i>
AE	<i>Auto-Encoders</i>
VAE	<i>Variational Auto-Encoders</i>
DRNN	<i>Dilated-RNN</i>
MSE	<i>Mean Squared Error</i>
KL	<i>Kullback-Leibler</i>
SSL	<i>Self Supervised Learning</i>
SimCLR	<i>Simple Contrastive LeaRning</i>
DCCNN	<i>Dilated Causal CNN</i>
MCL	<i>Mixup Contrastive Learning</i>
TimeCLR	<i>Time Series Self-Supervised Contrastive Learning framework for Representation</i>
NHST	<i>Null Hypothesis Significance Testing</i>
CDD	<i>Critical Difference Diagram</i>
MCM	<i>Multi-Comparison Matrix</i>
AR	<i>Average Rank</i>

CD	<i>Critical Difference</i>
DP	<i>Dirichlet Process</i>
t-SNE	<i>t-distributed Stochastic Neighbor Embedding</i>
CO-FCN	<i>Custom Only-Fully Convolutional Network</i>
H-FCN	<i>Hybrid-Fully Convolutional Network</i>
H-Inception	<i>Hybrid-Inception</i>
IT	<i>InceptionTime</i>
H-IT	<i>Hybrid-InceptionTime</i>
PHIT	<i>Pre-trained H-InceptionTime</i>
BNM	<i>Batch Normalizing Multiplexer</i>
LITE:	<i>Light Inception with boosting techniques</i>
LITEMV	<i>LITE MultiVariate</i>
FLOPS	<i>Floating Point Operations Per Second</i>
LMVT	<i>LITEMVTime</i>
LT	<i>LITETime</i>
CT	<i>ConvTran</i>
D-CNN	<i>Disjoint Convolutional Neural Network</i>
RF	<i>Receptive Field</i>
TRILITE	<i>TRIPlet Loss In Time</i>
1LP	<i>1 Linear Perceptron</i>
CAM	<i>Class Activation Map</i>
GAP	<i>Global Average Pooling</i>
FFT	<i>Fast Fourier Transform</i>
RI	<i>Rand Index</i>
ARI	<i>Adjusted Rand Index</i>
TP	<i>True Positive</i>
TN	<i>True Negative</i>
FP	<i>False Positive</i>
FN	<i>False Negative</i>
FID	<i>Fréchet Inception Distance</i>
APD	<i>Average Pair Distance</i>
Ref	<i>Reference</i>
RMSE	<i>Root Mean Squared Error</i>
SVAE	<i>Supervised Variational Auto-Encoder</i>
GAN	<i>Generative Adversarial Network</i>
MoCoGAN	<i>Motion and Content decomposed Generative Adversarial Network</i>
GPT	<i>Generative Pre-trained Transformer</i>
PoseGPT	<i>Pose Generative Pre-trained Transformer</i>
ACTOR	<i>Action-Conditioned TransfORmer</i>
UM-CVAE	<i>Uncoupled-Modulation Conditional Variational Auto-Encoder</i>
DDPM	<i>Denosing Diffusion Probabilistic Model</i>
PCA	<i>Principal Component Analysis</i>
rec	<i>reconstruction</i>
cls	<i>classification</i>
MOS	<i>Mean Opinion Scores</i>
WPD	<i>Warping Path Diversity</i>
IS	<i>Inception Score</i>
FD	<i>Fréchet Distance</i>
AOG	<i>Accuracy On Generated</i>
ACPD	<i>Average per Class Pair Distance</i>
MMS	<i>Mean Maximum Similarity</i>

CConvVAE	<i>Conditional Convolutional Variational Auto-Encoder</i>
CGRUVAE	<i>Conditional Gated Recurrent Unit Variational Auto-Encoder</i>
CTransVAE	<i>Conditional Transformer Variational Auto-Encoder</i>
KL	<i>Kullback-Leibler</i>
KAN	<i>Kolmogorov-Arnold Network</i>

Résumé des chapitres

Chapitre 1 : État de l'art pour l'analyse des séries temporelles : Apprentissage supervisé et non supervisé

Ce chapitre traite de l'état de l'art dans l'analyse des séries temporelles, avec un focus sur deux types d'apprentissage: supervisé et non supervisé. L'analyse des séries temporelles est essentielle pour les scientifiques de données, car elle permet d'extraire des informations utiles à partir de données qui évoluent dans le temps. Il existe de nombreuses techniques dans ces deux approches, chacune adaptée à des contextes et des objectifs différents. Le chapitre commence par une introduction générale de ces concepts et passe ensuite en revue les méthodes les plus avancées dans ce domaine.

Dans l'apprentissage supervisé, l'objectif principal est de prédire des valeurs futures en se basant sur des observations passées. Cela inclut des tâches comme la régression extrinsèque, où l'on cherche à prédire des valeurs continues, par exemple le prix futur des actions, ou la classification, où l'on catégorise des événements futurs en fonction des observations historiques. Un exemple serait de classer des emails comme "spam" ou "non-spam" en analysant les emails précédents. En revanche, l'apprentissage non supervisé consiste à découvrir des structures ou des motifs cachés dans les données sans utiliser de labels ou de catégories prédéfinis. Deux des tâches principales en apprentissage non supervisé sont le regroupement (clustering) et la détection d'anomalies. Ces méthodes sont utilisées pour identifier des comportements inhabituels ou des groupes de données similaires dans divers domaines, comme la segmentation des clients ou la détection de fraudes financières.

Le chapitre présente ensuite les techniques de classification des séries temporelles (*Time Series Classification, TSC*), qui ont beaucoup évolué ces dernières décennies. Parmi les approches traditionnelles, on trouve les méthodes basées sur la distance (Plus Proche Voisin), qui utilisent des mesures de similarité comme le *Dynamic Time Warping (DTW)*, une méthode capable de comparer deux séries temporelles en tenant compte des décalages temporels entre elles. Cette technique est très utile dans des domaines variés, allant de la reconnaissance d'activités humaines à la communication sans fil. Par exemple, dans une série de données temporelles, DTW permet de trouver la meilleure correspondance entre deux séries, même si elles ne sont pas parfaitement alignées dans le temps. C'est une avancée par rapport à des mesures de distance plus simples comme la distance euclidienne, qui ne tient pas compte des différences temporelles.

Un autre domaine important est celui des "shapelets" (Ye and Keogh, 2011). Ce sont des sous-séquences discriminatives d'une série temporelle qui permettent de distinguer différentes classes. Les shapelets sont souvent utilisées dans des domaines où la lisibilité et l'interprétabilité des modèles sont importantes, comme en médecine, où il est essentiel de comprendre pourquoi un certain diagnostic est fait à partir des données. Ces shapelets capturent des motifs locaux dans les séries temporelles qui sont représentatifs d'une classe spécifique.

Les approches basées sur des dictionnaires (Schäfer, 2015) sont également abordées dans ce chapitre. Elles transforment les séries temporelles en séquences de symboles,

ce qui permet de repérer des motifs répétés dans les données. L'une des techniques les plus connues dans ce domaine est SAX (*Symbolic Aggregate approXimation*) (Lin et al., 2007), qui simplifie les séries temporelles en les représentant par une séquence de symboles, rendant plus facile la détection de motifs répétitifs. Des méthodes dérivées comme BOSS (*Bag-of-SFA-Symbols*) (Schäfer, 2015) permettent d'améliorer cette approche en analysant les séries temporelles sous forme de fenêtres qui se chevauchent, et en créant des ensembles de mots qui facilitent la classification des séries temporelles.

Le chapitre aborde les méthodes hybrides qui combinent plusieurs approches pour améliorer les performances des modèles d'analyse de séries temporelles. Un modèle hybride célèbre est HIVE-COTE (Lines, Taylor, and Bagnall, 2018), qui combine des techniques basées sur les distances, les dictionnaires, les shapelets et les intervalles, en les utilisant ensemble pour créer un modèle d'ensemble puissant et robuste. Ces approches combinées permettent souvent d'obtenir des résultats plus précis que l'utilisation d'une seule méthode, en exploitant les forces de chaque approche.

Les modèles plus récents pour la classification des séries temporelles sont de plus en plus basés sur l'apprentissage profond, en particulier les réseaux neuronaux convolutifs (*Convolutional Neural Networks, CNN*). Ces réseaux utilisent des filtres qui capturent des motifs dans les données, comme des relations temporelles complexes, en parcourant les séries de manière glissante. Ils ont prouvé leur efficacité dans la reconnaissance de motifs dans les séries temporelles, souvent surpassant les méthodes traditionnelles. Le chapitre consacre également une section importante à l'apprentissage profond pour l'analyse des séries temporelles. Les réseaux neuronaux, notamment les CNN et les réseaux récurrents (RNN), sont de plus en plus utilisés dans ce domaine. Une particularité des réseaux neuronaux est leur capacité à extraire des caractéristiques complexes des séries temporelles sans nécessiter une étape explicite de sélection de caractéristiques, ce qui simplifie le processus d'apprentissage. Ces modèles peuvent paralléliser les calculs, ce qui les rend plus rapides que les approches traditionnelles pour les grands volumes de données. Les CNN, en particulier, sont efficaces pour la classification des séries temporelles, car ils permettent de détecter des motifs locaux importants dans les données.

La régression extrinsèque est une tâche importante de l'apprentissage supervisé, où l'objectif est de prédire une valeur continue à partir d'une série temporelle. Contrairement à la classification, où les résultats sont des catégories discrètes, la régression vise à estimer des valeurs numériques précises. Par exemple, elle peut être utilisée pour prédire la température d'une région en fonction des données climatiques historiques ou pour estimer les ventes futures en fonction des tendances des ventes passées. L'approche traditionnelle consiste à utiliser des modèles de régression linéaire ou d'autres techniques classiques, mais avec les récentes avancées, les méthodes basées sur l'apprentissage profond gagnent en popularité. Les réseaux neuronaux peuvent capturer les relations non linéaires entre les observations passées et futures.

L'apprentissage non supervisé pour les séries temporelles ne vise pas à prédire des valeurs futures ou à classer des événements, mais plutôt à découvrir des structures cachées dans les données. Cette partie du chapitre se concentre sur trois techniques principales: le clustering, le prototypage et l'apprentissage auto-supervisé. Ces méthodes sont particulièrement utiles lorsqu'on n'a pas, ou peu, de labels pour les données, ou lorsque les séries temporelles sont complexes et contiennent des motifs que l'on souhaite analyser sans définir de catégories précises à l'avance.

Le clustering (ou regroupement) est une méthode utilisée pour regrouper des séries temporelles similaires en fonction de leurs caractéristiques. Il permet d'organiser les données en groupes homogènes (*clusters*) où les membres d'un même groupe partagent des propriétés communes. Par exemple, dans une analyse de séries temporelles de

données clients, le clustering peut être utilisé pour segmenter les clients en fonction de leurs comportements d'achat, afin d'identifier différents types de consommateurs. Le chapitre présente plusieurs algorithmes pour le clustering, comme les méthodes basées sur la distance (ex : k -means), et explique comment ces techniques peuvent être adaptées aux séries temporelles.

L'un des défis du clustering dans les séries temporelles est de choisir la bonne mesure de similarité. Alors que les mesures comme la distance euclidienne sont simples à implémenter, elles ne prennent pas en compte les décalages dans le temps. Le *Dynamic Time Warping (DTW)*, déjà mentionné dans la section sur la classification, est souvent utilisé pour cette raison. En outre, le chapitre mentionne des méthodes plus récentes qui combinent les approches traditionnelles avec des techniques d'apprentissage profond (Lafabregue et al., 2022) pour améliorer la précision du clustering.

Le prototypage (Keogh and Pazzani, 1998) est une autre technique utile dans l'analyse non supervisée des séries temporelles, où l'objectif est de représenter un ensemble de séries temporelles par une série représentative appelée prototype. Cela permet de résumer efficacement de grands ensembles de données en une série qui capture l'essence des données. Ces prototypes peuvent être utilisés pour visualiser ou comprendre des groupes de séries temporelles, ou pour simplifier des modèles d'analyse complexes.

L'approche classique consiste à calculer une moyenne ou une médiane pour les séries temporelles d'un groupe, mais cette méthode simple peut échouer à capturer des motifs subtils. C'est pourquoi des méthodes plus sophistiquées, comme le k -means (MacQueen et al., 1967) avec le DTW ou d'autres mesures de similarité adaptées aux séries temporelles, sont utilisées pour obtenir des prototypes plus précis.

Le chapitre aborde également l'apprentissage auto-supervisé, qui est une méthode émergente dans l'analyse des séries temporelles. Contrairement à l'apprentissage supervisé classique où les modèles sont entraînés avec des labels, l'apprentissage auto-supervisé permet aux modèles d'apprendre à partir des données elles-mêmes, sans avoir besoin de labels explicites. Une technique commune consiste à créer des tâches d'apprentissage auxiliaires (par exemple, prédire une partie manquante de la série temporelle ou réorganiser des segments) pour permettre au modèle d'apprendre des représentations utiles des données. Ces représentations peuvent ensuite être réutilisées pour d'autres tâches comme la classification ou la régression.

L'apprentissage supervisé est particulièrement utile dans les situations où les labels sont rares ou coûteux à obtenir. Il permet d'exploiter efficacement les grands ensembles de données non étiquetés, ce qui est souvent le cas dans des secteurs comme la surveillance de la santé ou la gestion de grandes infrastructures industrielles.

Le chapitre conclut sur l'importance des progrès récents dans l'analyse des séries temporelles, que ce soit dans le domaine supervisé ou non supervisé. Il met en avant la richesse des méthodes disponibles et souligne que les techniques modernes, notamment celles basées sur l'apprentissage profond et l'apprentissage supervisé, sont essentielles pour résoudre les problèmes complexes que posent les séries temporelles aujourd'hui. Ces méthodes permettent de traiter des volumes de données de plus en plus importants, tout en offrant des prédictions plus précises et une meilleure capacité à identifier des comportements cachés ou inhabituels dans les données.

En résumé, le chapitre offre un panorama complet des techniques actuelles et des avancées dans l'analyse des séries temporelles. Que ce soit pour des tâches supervisées comme la classification et la régression, ou non supervisées comme le clustering et le prototypage, il souligne que la combinaison des approches traditionnelles avec les

nouvelles techniques d'apprentissage profond offre des résultats prometteurs dans de nombreux domaines.

Chapitre 2 : Évaluation comparative des modèles d'apprentissage automatique sur les données de séries temporelles

L'évaluation comparative des modèles de machine learning est une pratique cruciale pour évaluer et améliorer les algorithmes. Elle permet de comparer la performance des modèles sur plusieurs jeux de données afin d'identifier les méthodes les plus performantes et de mieux comprendre les forces et faiblesses des différents modèles. Les méthodes traditionnelles comme le *Wilcoxon signed-rank test* (Wilcoxon, 1992) et le *Nemenyi test* (Nemenyi, 1963) sont souvent utilisées, mais elles présentent des limites, par exemple elles peuvent être manipulées et ne donnent pas toujours une image complète des différences entre les modèles. Des méthodes plus récentes, comme les approches bayésiennes, sont proposées comme alternatives plus fiables pour les comparaisons multiples.

Dans ce chapitre, on se concentre sur les méthodes actuelles d'évaluation comparative, en particulier sur la tâche de classification des séries temporelles. L'un des outils les plus utilisés pour ces comparaisons est le *Critical Difference Diagram (CDD)* (Demšar, 2006; Benavoli, Corani, and Mangili, 2016). Cependant, ce diagramme présente des limites importantes, comme l'instabilité dans les classements et la possibilité de manipulation. Une méthode nouvelle, appelée *Multiple Comparison Matrix (MCM)*, est introduite pour offrir des comparaisons plus robustes et interprétables des modèles.

Le CDD résume les performances des modèles en les classant sur plusieurs jeux de données, comme les 128 de l'archive UCR (Dau et al., 2019). Cependant, cette méthode ignore la magnitude des différences et peut être instable. Par exemple, ajouter ou retirer un modèle peut changer les conclusions sur les différences significatives. Le *Friedman test* (Friedman, 1940) et le *Nemenyi test* (Nemenyi, 1963) sont souvent utilisés, mais ils ont des faiblesses similaires.

Le CDD simplifie les comparaisons, mais il présente trois problèmes majeurs :

- **Instabilité des classements:** Le classement change quand on ajoute ou retire des modèles.
- **Ignorance de la magnitude:** Le CDD ne prend pas en compte l'ampleur des gains ou pertes de performance.
- **Problèmes avec les tests statistiques:** Les *p-values* ne reflètent pas toujours les différences réelles entre les modèles.

Pour résoudre ces problèmes, la *Multiple Comparison Matrix (MCM)* est proposée dans ce chapitre comme une méthode plus fiable pour comparer les modèles. Cette méthode se concentre sur les comparaisons par paires des modèles, et elle garantit que les comparaisons restent invariantes à l'ajout ou au retrait d'autres modèles. Elle offre une vue plus détaillée des performances de chaque modèle avec des informations comme:

- La différence moyenne de performance entre deux modèles.
- Un compte des victoires, égalités et défaites pour chaque paire de modèles.

- Une p-value issue d'un test *Wilcoxon*.

En conclusion, l'évaluation comparative des modèles de machine learning joue un rôle central dans l'amélioration continue des algorithmes, en permettant d'identifier les meilleures méthodes et de mieux comprendre leurs forces et faiblesses. Bien que des approches traditionnelles comme les tests de Wilcoxon et de Nemenyi soient couramment utilisées, elles présentent des limites, notamment une instabilité dans les classements et une faible prise en compte des différences de magnitude entre les performances des modèles. Ces méthodes peuvent aussi être influencées par l'ajout ou le retrait de modèles, rendant les résultats moins fiables.

C'est dans ce contexte que des alternatives plus récentes, comme les approches bayésiennes ou la *Multiple Comparison Matrix (MCM)*, ont été proposées pour offrir des comparaisons plus robustes et pertinentes. La MCM, en particulier, se concentre sur des comparaisons par paires entre modèles et garantit une meilleure stabilité des résultats, indépendamment des changements dans l'ensemble des modèles testés. Elle fournit aussi des informations plus détaillées et descriptives, notamment sur les différences de performance moyennes, ainsi que sur les victoires et défaites entre chaque paire de modèles.

Ce chapitre a mis en évidence les limites des outils traditionnels comme le *Critical Difference Diagram (CDD)*, tout en proposant des solutions complémentaires avec la MCM pour pallier ces faiblesses. Ainsi, l'approche MCM permet d'offrir une vision plus précise et nuancée des différences entre les modèles, en garantissant des comparaisons plus cohérentes et informatives. Cela souligne l'importance de poursuivre l'exploration de méthodes d'évaluation robustes pour améliorer l'efficacité et la fiabilité des modèles de machine learning appliqués aux séries temporelles.

Chapitre 3 : Vers la recherche de modèles de fondation pour la classification des séries temporelles

Dans le domaine dynamique de la classification des séries temporelles (*Time Series Classification, TSC*), l'un des principaux défis consiste à développer des modèles robustes et adaptables à des jeux de données variés. Les modèles de fondation, qui sont de grands modèles pré-entraînés capables de généraliser sur plusieurs tâches, offrent une solution prometteuse. L'intérêt de ces modèles est qu'ils simplifient et accélèrent le processus d'ajustement pour des tâches spécifiques. Cela s'avère crucial dans des domaines comme la médecine, par exemple avec les signaux ECG, ou la gestion du trafic, où l'entraînement de modèles à partir de zéro est coûteux et long. Les modèles de fondation offrent un point de départ pré-entraîné qui comprend déjà les motifs fondamentaux, ce qui permet de gagner en temps et en précision lors de l'ajustement à des jeux de données particuliers.

Ce chapitre présente deux contributions principales pour progresser vers les modèles de fondation profonds:

1. La création de filtres convolutifs faits main pour améliorer la généralisation des modèles.
2. L'utilisation d'une méthodologie de pré-entraînement pour ajuster (*fine tune*) ces modèles à des tâches de classification spécifiques.

Ces filtres sont conçus pour se concentrer sur des caractéristiques générales des données, indépendamment du domaine spécifique, afin d'améliorer l'adaptabilité des modèles sur diverses tâches.

Les modèles de deep learning pour la TSC sont souvent confrontés à des problèmes tels que:

- Surapprentissage (*overfitting*), où les modèles deviennent trop spécialisés sur les données d'entraînement
- Complexité computationnelle
- Apprentissage de filtres redondants

Les réseaux neuronaux convolutifs (*Convolutional Neural Networks, CNNs*) traditionnels apprennent les filtres grâce à la rétropropagation (*backpropagation*), mais ce processus peut mener à des filtres trop spécifiques, manquant de généralité. Une solution consiste à créer des filtres manuellement, qui détectent des motifs génériques dans les données. Avant d'adopter cette approche, il faut supposer que les modèles CNN peuvent apprendre des filtres génériques communs à travers différents jeux de données.

Pour tester cette hypothèse, une analyse a été réalisée sur l'espace des filtres appris par les modèles CNN sur plusieurs ensembles de données ECG. L'analyse a montré qu'un certain nombre de filtres convolutifs coïncident dans l'espace, suggérant que certains filtres peuvent être partagés entre différents jeux de données.

Trois types de filtres faits main sont proposés pour capturer des motifs spécifiques dans les séries temporelles:

- Filtre de détection de tendance croissante : construit pour détecter les segments de séries temporelles où les valeurs augmentent
- Filtre de détection de tendance décroissante : construit pour détecter les segments où les valeurs diminuent.
- Filtre de détection de pics : construit pour détecter les changements brusques dans une série temporelle, comme une augmentation suivie d'une diminution rapide.

Ces filtres ne sont pas ajustés pendant l'entraînement, permettant ainsi au modèle de se concentrer sur l'apprentissage de motifs plus complexes et nuancés. Ces filtres sont similaires à ceux utilisés en vision par ordinateur, tels que les filtres Sobel (Bogdan, Bonchiş, and Orhei, 2019; Gao et al., 2010).

Pour évaluer l'impact des filtres faits main, trois architectures adaptées sont proposées :

- CO-FCN (*Custom Only-Fully Convolutional Network*): la première couche de convolution dans FCN (Wang, Yan, and Oates, 2017) est remplacé entièrement par les trois filtres créés manuellement.
- H-FCN (*Hybrid-Fully Convolutional Network*): combine les filtres créés manuellement et des filtres appris dans la première couche de convolution de FCN.
- H-Inception (*Hybrid-Inception*): intègre les filtres faits main dans l'architecture Inception (Ismail Fawaz et al., 2020), qui est connue pour ses performances sur la TSC.

Les résultats expérimentaux sur 128 jeux de données de l'archive UCR (Dau et al., 2019) montrent que les modèles avec filtres faits main surpassent souvent leurs versions originales. Par exemple, CO-FCN a mieux performé que le modèle FCN d'origine sur la plupart des jeux de données. De même, les versions hybrides H-FCN et H-InceptionTime montrent des améliorations significatives.

Dans le reste de ce chapitre, nous abordons le développement d'un modèle de fondation pour la classification des séries temporelles en utilisant une tâche prétexte. L'objectif est de pré-entraîner un modèle sur une tâche générique avant de l'adapter à des jeux de données spécifiques pour des tâches de classification particulières. Cela permet non seulement de réduire le temps d'entraînement, mais aussi d'améliorer la capacité de généralisation du modèle. Le modèle de fondation pré-entraîné tire parti de l'architecture H-Inception et intègre des filtres convolutifs faits main, qui se sont révélés utiles pour capturer des motifs généraux dans les séries temporelles.

Dans de nombreuses applications du monde réel, comme la médecine ou la gestion industrielle, il est coûteux et laborieux de collecter et d'étiqueter de grandes quantités de données pour entraîner un modèle d'apprentissage profond à partir de zéro. Par exemple, pour la détection des maladies cardiaques à partir de signaux ECG, il est nécessaire de disposer d'énormes quantités de données annotées par des professionnels de santé, ce qui n'est souvent pas réalisable. De même, dans des domaines comme la maintenance prédictive, la collecte de données de capteurs nécessite un suivi à long terme et l'expertise d'ingénieurs pour annoter les modes de défaillance.

L'idée des modèles de fondation est de pré-entraîner un modèle robuste sur un large éventail de jeux de données similaires, ce qui permet ensuite de l'adapter plus facilement et plus efficacement à de nouveaux jeux de données spécifiques. Ce processus de *fine tuning* est beaucoup plus rapide et permet d'éviter le risque de surapprentissage, un problème fréquent lorsque l'on travaille avec des ensembles de données de petite taille.

La méthode proposée dans ce chapitre repose sur une tâche prétexte construite pour entraîner un modèle à reconnaître les motifs généraux dans des séries temporelles à partir de différents jeux de données. Cette tâche prétexte consiste à apprendre au modèle à prédire le jeu de données d'origine de chaque échantillon de série temporelle. Ce processus permet au modèle de capturer des caractéristiques génériques applicables à plusieurs ensembles de données. Une fois ce modèle pré-entraîné, il est ensuite ajusté sur des tâches de classification propres à chaque jeu de données.

L'architecture choisie pour ce modèle est basée sur H-Inception, proposé dans la première contribution de ce chapitre. Le processus global peut être résumé en deux étapes principales:

- Étape 1: Pré-entraînement du modèle sur une tâche générique où il doit prédire l'origine des séries temporelles.
- Étape 2: Ajustement du modèle sur des jeux de données spécifiques pour des tâches de classification précises.

Les résultats expérimentaux montrent que le modèle proposé PHIT (*Pre-trained H-InceptionTime*) dépasse la performance des approches traditionnelles d'ajustement. Le modèle a été comparé à des approches de pointe sur l'ensemble des 88 jeux de données de séries temporelles.

Une comparaison directe entre notre approche avec pré-entraînement et un modèle sans pré-entraînement a été réalisée. Les résultats montrent que PHIT offre de meilleures performances que le modèle de base dans 48 jeux de données, tandis que le modèle de base n'en surpasse que 23. L'analyse statistique de ces résultats à l'aide

du *Wilcoxon Signed-Rank Test* (Wilcoxon, 1992) indique que l'amélioration apportée par PHIT est significative avec une p-value de 0,021 (inférieure au seuil de 0,05).

En conclusion, ce chapitre propose des avancées majeures dans la classification des séries temporelles en introduisant les modèles de fondation, qui permettent une généralisation plus efficace sur différentes tâches. Ces modèles pré-entraînés offrent un gain de temps et de précision, en particulier dans des domaines comme la médecine ou la gestion du trafic, où l'entraînement à partir de zéro est coûteux et complexe.

Les deux contributions principales de ce travail sont, d'une part, la création de filtres convolutifs créés manuellement, construits pour détecter des motifs génériques et améliorer la robustesse des modèles, et, d'autre part, l'utilisation d'une méthodologie de pré-entraînement. Cette dernière permet d'affiner les modèles sur des tâches spécifiques, en les rendant plus adaptés à chaque jeu de données sans nécessiter un long processus d'apprentissage.

Les résultats expérimentaux montrent que les architectures telles que CO-FCN et H-Inception, intégrant ces filtres faits main, surpassent souvent les versions classiques sur un large éventail de jeux de données. De plus, la méthode de pré-entraînement basée sur une tâche générique améliore significativement les performances des modèles sur des tâches spécifiques, comme l'a montré le modèle PHIT.

En résumé, ce chapitre démontre l'efficacité des modèles de fondation dans la classification des séries temporelles, en offrant une meilleure capacité de généralisation et une réduction du temps d'entraînement, ce qui les rend particulièrement utiles pour des applications nécessitant des solutions rapides et performantes.

Chapitre 4 : Réduire la complexité des modèles d'apprentissage profond pour la classification des séries temporelles

Ce chapitre explore la réduction de la complexité des modèles d'apprentissage profond dans le cadre de la classification des séries temporelles. Traditionnellement, les modèles plus complexes et volumineux, comme InceptionTime (Ismail Fawaz et al., 2020) avec ses 2,1 millions de paramètres, ont montré de bonnes performances. Cependant, leur complexité présente des défis lorsqu'il s'agit de les déployer dans des environnements à ressources limitées, comme les dispositifs embarqués ou mobiles.

Pour répondre à ces besoins, ce chapitre introduit le modèle LITE, qui vise à maintenir des performances compétitives tout en réduisant considérablement la taille et la complexité du modèle. LITE se base sur une version allégée de l'architecture Inception et intègre des techniques de boosting pour améliorer la capacité de généralisation sur divers jeux de données, tout en restant rapide à entraîner et économe en ressources.

Les principaux objectifs du modèle LITE incluent:

- Architecture Inception allégée: réduction du nombre de paramètres et de la complexité sans sacrifier la performance
- Techniques de boosting: intégration de techniques qui améliorent la généralisation, réduisent le surapprentissage, et augmentent la précision
- Efficacité et adaptabilité: offrir un modèle adapté à des environnements contraints en termes de ressources, tout en maintenant des performances élevées avec un faible coût computationnel

L'architecture LITE est une version simplifiée du réseau Inception, construit pour maximiser l'efficacité tout en minimisant la complexité. Ses principaux éléments sont:

- **Filtres créés manuellement:** Reprenant les contributions du chapitre précédent, ces filtres sont utilisés dans la première couche pour capturer des motifs génériques dès le début, tout en évitant un surapprentissage. Ils fonctionnent en parallèle avec des convolutions apprises pour maximiser l'efficacité du modèle
- **Multiplexing de convolution:** Plusieurs convolutions avec différentes tailles de filtres sont appliquées en parallèle dans les premières couches. Cela permet au modèle de capturer divers motifs dans les séries temporelles, optimisant ainsi l'extraction de caractéristiques importantes dès le début
- ***DepthWise Separable Convolutions (DWSC):*** Ces convolutions sont utilisées dans les couches profondes de l'architecture. Elles permettent de réduire drastiquement le nombre de paramètres et la charge computationnelle tout en conservant une forte capacité d'extraction de caractéristiques pertinentes (Howard et al., 2017)
- **Convolutions dilatées:** Les couches profondes utilisent des convolutions dilatées pour augmenter le champ réceptif du modèle sans ajouter de nouveaux paramètres, ce qui permet au modèle d'apprendre des dépendances à plus long terme dans les données (Dempster, Petitjean, and Webb, 2020)
- **Pooling global:** Un pooling global est appliqué dans les dernières couches pour réduire la dimension des données avant la classification finale, comme cela se fait dans les modèles classiques tels que FCN et ResNet (Wang, Yan, and Oates, 2017)

LITETime est une version ensemble du modèle LITE, similaire à InceptionTime (Ismail Fawaz et al., 2020), qui regroupe plusieurs modèles LITE pour améliorer les performances globales.

Les résultats expérimentaux montrent que LITE, avec ses moins de 10000 paramètres, surpasse des modèles bien plus volumineux comme FCN (264000 paramètres) et ResNet (504000 paramètres). Il atteint une précision de 0,8304, proche de celle des modèles plus complexes comme Inception (0,8393), tout en utilisant beaucoup moins de ressources et en étant beaucoup plus rapide à entraîner.

Lors des tests sur l'archive UCR avec 128 jeux de données (Dau et al., 2019), LITETime atteint une précision moyenne de 0,8462, tout en restant bien plus petit que InceptionTime. Il utilise seulement 2,34% des paramètres d'InceptionTime, ce qui en fait une option beaucoup plus légère et efficace pour des environnements à ressources limitées.

Dans de nombreux cas réels, les séries temporelles sont multivariées, ce qui signifie qu'elles comportent plusieurs canaux de données (comme dans la santé, où des données ECG sont mesurées sur plusieurs axes). Pour s'adapter à cela, l'architecture LITEMV a été développée, reposant sur la base du modèle LITE mais modifiée pour mieux gérer les séries temporelles multivariées. LITEMV remplace les convolutions standards dans les premières couches par des convolutions *DepthWise*, permettant de traiter chaque canal indépendamment avant de les combiner efficacement. Cela permet au modèle de mieux capturer les interactions entre les différents canaux de données.

Lors des tests sur 30 jeux de données multivariées de l'archive UEA (Bagnall et al., 2018), LITEMVTime, l'ensemble de modèles basé sur LITEMV, a surpassé

des modèles de pointe comme InceptionTime (Ismail Fawaz et al., 2020) et Disjoint-CNN (Foumani, Tan, and Salehi, 2021). Dans certains cas, comme sur le jeu de données EigenWorms, LITEMVTime a obtenu une précision impressionnante de 93,89%, contre seulement 59,34% pour ConvTran (Foumani et al., 2024a), un autre modèle de pointe pour la classification multivariée.

LITE et LITEMV représentent des avancées majeures dans la classification des séries temporelles. Grâce à leur faible complexité et leur efficacité énergétique, ces modèles sont parfaitement adaptés à des environnements à ressources limitées, tout en maintenant des performances compétitives face à des modèles bien plus complexes. De plus, l’approche d’ensemble, avec LITETime et LITEMVTime, montre que ces architectures peuvent offrir une précision encore plus élevée sans compromettre leur légèreté.

Chapitre 5 : Apprentissage semi-supervisé et auto-supervisé pour les données de séries temporelles avec un manque de labels

Ce chapitre aborde les défis liés à la classification des séries temporelles dans les cas où les données annotées sont rares. Les méthodes traditionnelles de classification supervisée nécessitent des données largement annotées, ce qui est souvent difficile à obtenir en raison de la complexité et du besoin d’expertise pour annoter ces données. En réponse à cela, l’apprentissage semi-supervisé et l’apprentissage auto-supervisé émergent comme des solutions prometteuses. Ces techniques exploitent des données non annotées pour améliorer les performances des modèles.

L’approche proposée, nommée TRILITE (*TRIPlet Loss In TimE*), repose sur le concept de perte de triplet (*triplet loss*) (Franceschi, Dieuleveut, and Jaggi, 2019), une technique utilisée pour apprendre des représentations discriminatives à partir de données non annotées. TRILITE emploie une méthode d’augmentation de données spécifiquement adaptée aux séries temporelles, permettant au modèle d’apprendre des caractéristiques utiles sans avoir besoin de beaucoup de données annotées. Deux cas d’utilisation sont explorés :

- L’amélioration des performances d’un classificateur supervisé avec peu de données annotées
- Un contexte d’apprentissage semi-supervisé où une partie des données est étiquetée et l’autre non

TRILITE est un modèle auto-supervisé qui utilise la perte de triplet pour apprendre des représentations significatives à partir de séries temporelles. Le modèle se compose de trois encodeurs partageant les mêmes poids, traitant les triplets d’entrée (référence, positif, négatif). Le mécanisme de triplet loss vise à rapprocher les échantillons similaires tout en éloignant les échantillons dissemblables (Schroff, Kalenichenko, and Philbin, 2015).

TRILITE a été testé sur 85 jeux de données de l’archive UCR (Dau et al., 2019). Les expériences ont montré que TRILITE améliore les performances des classificateurs dans les deux scénarios explorés. Dans le cas de données annotées en faible quantité, TRILITE a aidé à fournir des représentations complémentaires qui, combinées à des modèles supervisés comme FCN (Wang, Yan, and Oates, 2017), améliorent significativement la précision. De plus, dans un contexte semi-supervisé, TRILITE,

en utilisant à la fois des données annotées et non annotées, a surpassé les approches traditionnelles sur plusieurs jeux de données.

Ce chapitre montre que l'apprentissage auto-supervisé et semi-supervisé, via des approches comme TRILITE, offre des solutions efficaces lorsque les données annotées sont limitées. TRILITE utilise les données non annotées pour générer des représentations utiles, améliorant ainsi la performance des modèles de classification de séries temporelles. Ces résultats ouvrent la voie à des méthodes plus efficaces et moins dépendantes de l'annotation manuelle des données.

Chapitre 6 : Analyse de séries temporelles pour les données de mouvement humain

L'analyse des mouvements humains à partir de données de squelettes est devenue une technique couramment utilisée dans des domaines variés, tels que la reconnaissance d'actions humaines (Devanne et al., 2014), la réhabilitation (Capecci et al., 2019), et la génération de séquences de mouvements réalistes (Guo et al., 2020). Ces données sont généralement capturées à l'aide de technologies comme Microsoft Kinect (Asteriadis et al., 2013) et les systèmes de capture de mouvement (MoCap) (Vlasic et al., 2007), qui enregistrent les positions des articulations du corps humain dans un espace tridimensionnel. Chaque articulation est représentée par des coordonnées X, Y, et Z dans le temps, formant une série temporelle multivariée (MTS).

Les MTS capturant des mouvements humains présentent un intérêt particulier car elles permettent d'extraire et d'analyser des caractéristiques spatiales et temporelles simultanément. Par exemple, dans la réhabilitation, il est essentiel de comprendre non seulement le déplacement des articulations individuelles au fil du temps, mais aussi la manière dont ces articulations se coordonnent pour réaliser des mouvements complexes.

Les données de mouvements humains présentent plusieurs avantages pour l'analyse de séries temporelles:

- Elles sont souvent bien structurées et capturent les dynamiques des articulations en mouvement
- Elles peuvent être directement utilisées dans de nombreux algorithmes de l'apprentissage automatique et l'apprentissage profond pour des tâches comme la classification, la régression et la génération.
- Elles sont particulièrement adaptées aux modèles qui exploitent la relation entre les différentes dimensions des séries temporelles, comme les réseaux neuronaux convolutifs (CNN) et les réseaux neuronaux récurrents (RNN).

Les modèles d'apprentissage profond, en particulier, se sont avérés être des outils puissants pour traiter et analyser les séries temporelles multivariées provenant de mouvements humains. Les architectures de réseaux neuronaux convolutifs ont montré leur efficacité dans l'extraction automatique des caractéristiques complexes des séries temporelles, offrant ainsi des performances supérieures à celles des méthodes manuelles traditionnelles. Ce chapitre se concentre sur plusieurs méthodes avancées d'analyse des MTS, notamment dans le domaine de la réhabilitation et de la génération de mouvements.

L'un des domaines d'application les plus importants pour l'analyse des mouvements humains est la réhabilitation. Dans ce contexte, les données de séries temporelles issues des mouvements humains peuvent être utilisées pour évaluer la progression des patients au cours de leurs séances d'exercices physiques. Traditionnellement, cette évaluation est réalisée par des experts humains, qui observent et notent la qualité des mouvements. Cependant, ce processus peut être subjectif, coûteux et manquer de précision. Les modèles d'apprentissage profond, en revanche, offrent une solution pour automatiser cette évaluation, fournissant des résultats rapides, cohérents et basés sur des données objectives.

Le modèle LITEMVTime, proposé dans chapitre 4 a été testé sur le jeu de données Kimore (Capecci et al., 2019), un ensemble de données capturant des séquences de mouvements humains pendant des exercices de réhabilitation. Le jeu de données contient des enregistrements de patients sains et malades, chacun effectuant plusieurs exercices physiques sous la supervision d'experts humains. Chaque mouvement est annoté avec un score de qualité allant de 0 (très mauvaise performance) à 100 (excellente performance), attribué par des professionnels de la réhabilitation.

Le modèle LITEMVTime a été entraîné pour classer la qualité des mouvements en "bon" ou "mauvais" en utilisant les annotations d'experts comme vérité de terrain. Les résultats expérimentaux montrent que LITEMVTime surpasse d'autres architectures d'apprentissage profond telles que FCN, ResNet (Wang, Yan, and Oates, 2017) et InceptionTime (Ismail Fawaz et al., 2020), à la fois en termes de précision et de vitesse d'exécution. Grâce à sa conception légère, LITEMVTime peut être facilement intégré dans des systèmes cliniques en temps réel, fournissant ainsi des retours immédiats aux patients et aux cliniciens pendant les sessions de réhabilitation.

L'un des plus grands défis dans l'entraînement des modèles de deep learning sur des données médicales est le manque de données annotées. Les mouvements humains capturés pour des études médicales sont souvent limités, et leur annotation nécessite des experts spécialisés, ce qui en fait une ressource rare et coûteuse. Ce manque de données annotées peut entraîner des problèmes de surapprentissage, où les modèles d'apprentissage profond deviennent trop spécialisés sur les données d'entraînement et ne parviennent pas à bien généraliser sur de nouvelles données. Pour répondre à ce problème, ce chapitre propose une méthode de prototypage de séries temporelles appelée ShapeDBA (*Shape Dynamic Time Warping Barycenter Averaging*). Cette méthode permet de créer des prototypes qui représentent des moyennes barycentriques des séries temporelles, à partir desquelles de nouvelles séquences synthétiques peuvent être générées. Ces séquences synthétiques, qui conservent les propriétés essentielles des mouvements humains capturés, peuvent être ajoutées aux jeux de données d'entraînement pour augmenter artificiellement la taille du jeu de données et améliorer ainsi la généralisation des modèles.

Le prototypage de séries temporelles est une technique précieuse, en particulier pour les applications où les données réelles sont limitées. En créant des prototypes barycentriques, il est possible de générer des mouvements synthétiques qui imitent les mouvements réels des patients tout en offrant une plus grande diversité. Cela permet aux modèles de deep learning d'apprendre des motifs plus robustes et de mieux se généraliser à de nouveaux patients et à de nouvelles tâches de réhabilitation.

Les expérimentations menées sur le jeu de données Kimore (Capecci et al., 2019) montrent que l'ajout de données synthétiques générées par ShapeDBA améliore considérablement la performance des modèles d'apprentissage supervisé utilisés pour évaluer la qualité des mouvements des patients. Les modèles, lorsqu'ils sont entraînés à la fois sur des données réelles et synthétiques, produisent des prédictions plus précises sur la qualité des mouvements, réduisant les erreurs de prédiction mesurées par

la MAE (erreur absolue moyenne) et la RMSE (erreur quadratique moyenne). Cela montre que ShapeDBA est une méthode efficace pour augmenter les jeux de données limités et améliorer les performances globales des modèles de régression.

Si le prototypage de séries temporelles est une méthode efficace pour étendre les jeux de données de manière synthétique, il existe une autre approche complémentaire, basée sur l'utilisation des modèles génératifs profonds. Les modèles génératifs, tels que les Auto-Encodeurs Variationnels (*Variational Auto-Encoder, VAE*) (Kingma and Welling, 2013) et les Réseaux adverbiaux génératifs (*Generative Adversarial Networks, GAN*) (Goodfellow et al., 2014). Ces modèles peuvent apprendre des distributions complexes de mouvements et ensuite générer de nouvelles séquences qui ressemblent aux données d'entraînement d'origine.

Dans ce chapitre, on explore l'utilisation des VAE pour la génération de mouvements humains. Les VAE sont une classe de modèles génératifs qui apprennent à encoder des données d'entrée dans un espace latent de faible dimension, à partir duquel de nouvelles données peuvent être générées. Dans le cas des mouvements humains, les VAE peuvent capturer les dynamiques des articulations et générer des mouvements réalistes qui imitent les séquences observées dans les données d'entraînement.

Dans ce chapitre on propose le SVAE (*Supervised Variational Autoencoder*) est une amélioration par rapport au VAE classique, car il intègre une tâche de classification dans l'espace latent du modèle. Cela permet au modèle de non seulement générer des séquences de mouvements humains réalistes, mais aussi de les classer selon des catégories prédéfinies, ce qui renforce à la fois ses capacités génératives et discriminatives.

L'architecture du SVAE se compose de trois parties principales : l'encodeur, l'espace latent, et le décodeur, similaires à un VAE classique:

- Entrée (séquence de squelettes): Les données d'entrée sont des séquences de mouvements humaines capturées sous forme de coordonnées 3D des articulations squelettiques.
- Encodeur: L'encodeur prend les séquences de mouvements comme entrée et apprend une représentation latente sous la forme d'une distribution gaussienne (paramétrée par une moyenne et une variance). L'objectif est d'apprendre une distribution latente compacte qui capture les caractéristiques essentielles des mouvements humains.
- Supervision dans l'espace latent: Contrairement au VAE traditionnel, le SVAE introduit une tâche de classification dans l'espace latent. Cette supervision permet au modèle d'apprendre une séparation plus claire entre les différentes actions (par exemple, marcher, courir, lever les bras). Cela permet d'améliorer la cohérence entre la génération de séquences et la classe d'action correspondante.
- Décodeur: Le décodeur prend un échantillon de l'espace latent et reconstruit la séquence originale. En même temps, un classificateur est intégré dans le modèle pour reconnaître l'action à partir de la représentation latente.

Le modèle SVAE permet ainsi de réaliser deux tâches simultanées :

- Reconnaissance d'action: Prédire l'action associée à une séquence de mouvement.
- Génération de séquences réalistes: Créer des séquences de mouvements réalistes en générant des exemples à partir de l'espace latent.

Ce double usage améliore à la fois les capacités génératives du modèle (production de nouvelles séquences de mouvements) et ses capacités discriminatives (classement des séquences dans la bonne catégorie).

Les expériences se basent sur le jeu de données de reconnaissance d'action HumanAct12 (Guo et al., 2020). Ce jeu de données contient des séquences de mouvements humains où les positions des articulations sont enregistrées en 3D sur plusieurs frames.

Le modèle est testé sur sa capacité à générer des séquences de mouvements réalistes et variés à partir de l'espace latent. La qualité et diversité des séquences générées est mesurée à l'aide de metrics telles que la *Fréchet Inception Distance (FID)* et la *Average Paired Distance (APD)*, qui évalue la similitude entre les distributions des données réelles et des données générées.

Les séquences générées par le SVAE sont plus réalistes que celles générées par des modèles VAE traditionnels. Le SVAE capture mieux les variations dans les mouvements humains et évite les artefacts communs des méthodes traditionnelles. Cela est reflété par des scores FID plus bas, indiquant une plus grande similarité entre les séquences générées et réelles. Le modèle génère non seulement des séquences réalistes, mais aussi diversifiées. Cela est important pour les applications où des variations réalistes de mouvements sont requises, comme dans les jeux vidéo ou la réhabilitation médicale.

Ce chapitre a exploré plusieurs techniques avancées pour l'analyse des séries temporelles appliquées aux mouvements humains. Les modèles comme LITEMVTime ont montré leur efficacité pour évaluer la qualité des mouvements dans des contextes de réhabilitation, tandis que des approches comme ShapeDBA et le SVAE ont permis de surmonter les limites liées à la rareté des données annotées en générant des données synthétiques. Ces avancées offrent des perspectives prometteuses pour des applications en temps réel, non seulement dans le domaine médical, mais aussi dans des domaines créatifs comme le cinéma et les jeux vidéo.

Les technologies décrites dans ce chapitre démontrent que les données de mouvements humains capturées via des capteurs comme le Kinect ont le potentiel de révolutionner de nombreux domaines, en combinant l'analyse de séries temporelles avec des modèles d'apprentissage profond performants et des méthodes de génération de données synthétiques.

Chapitre 7 : Métriques d'évaluation pour la génération de mouvement humain

Ce chapitre aborde les métriques d'évaluation des modèles génératifs appliqués à la génération de mouvements humains. Contrairement aux modèles discriminatifs, où la comparaison avec des données réelles est directe, les modèles génératifs posent un défi plus complexe (Naeem et al., 2020), car il faut évaluer la fidélité des échantillons générés en fonction de leur ressemblance avec des données réelles et leur diversité. L'évaluation repose donc sur deux dimensions clés: la fidélité et la diversité. La fidélité mesure à quel point les données générées sont proches des données réelles, tandis que la diversité s'assure que le modèle génératif peut produire une variété d'échantillons.

Les méthodes traditionnelles d'évaluation, comme le *Mean Opinion Scores (MOS)* (Strejil, Winkler, and Hands, 2014), ne sont pas adaptées aux modèles génératifs, car elles présupposent une perception uniforme de l'utilisateur, ce qui est souvent irréaliste. Par conséquent, l'évaluation quantitative devient essentielle pour juger la

performance des modèles génératifs. Le chapitre souligne qu’il est difficile de trouver une métrique unique pour évaluer à la fois la fidélité et la diversité, d’où la nécessité d’un cadre unifié d’évaluation.

Un aspect crucial des données de mouvement humain est leur dépendance temporelle. Les distorsions temporelles, telles que les changements de fréquence ou les décalages dans le temps, jouent un rôle important dans l’évaluation des séquences de mouvements. Pourtant, de nombreuses métriques d’évaluation ne tiennent pas compte de ces aspects temporels, se concentrant davantage sur les caractéristiques latentes. Pour remédier à ce problème, une nouvelle métrique, appelée *Warping Path Diversity (WPD)*, est introduite. Cette métrique permet de mesurer la diversité des distorsions temporelles dans les données réelles et générées, offrant ainsi une évaluation plus précise des modèles génératifs de séquences temporelles.

Les métriques de fidélité décrites dans ce chapitre incluent la *Fréchet Inception Distance (FID)* (Heusel et al., 2017), qui évalue la différence entre les distributions des données réelles et générées. Plus la FID est basse, plus les données générées ressemblent aux données réelles. Une autre métrique importante est l’*Accuracy on Generated (AOG)*, qui mesure la capacité du modèle à générer des échantillons conformes aux étiquettes de classes définies (par exemple, générer des mouvements de course lorsque la classe “courir” est donnée). Enfin, la métrique de *Density* (Naeem et al., 2020) évalue combien d’échantillons générés correspondent aux données réelles en mesurant la proximité entre ces deux ensembles dans l’espace des caractéristiques.

Les métriques de diversité permettent d’évaluer à quel point les données générées sont variées. La *Average Pair Distance (APD)* (Guo et al., 2020), par exemple, mesure la distance moyenne entre des paires d’échantillons générés, indiquant si le modèle évite la production de résultats trop similaires (un problème appelé mode collapse). La *Coverage* (Naeem et al., 2020) est une autre métrique qui mesure la proportion d’échantillons réels couverts par les échantillons générés, assurant que les données générées couvrent bien l’ensemble de l’espace des données réelles.

Un autre concept important introduit est celui de la Mean Maximum Similarity (MMS) (Stefan, Athitsos, and Das, 2012a). Cette métrique évalue la nouveauté des échantillons générés en mesurant la distance entre les échantillons générés et les plus proches voisins dans l’ensemble des données réelles. Une valeur élevée de MMS indique que les échantillons générés sont non seulement variés, mais aussi nouveaux par rapport aux données d’entraînement.

Le *Warping Path Diversity (WPD)*, une nouvelle métrique qu’on propose, est présentée pour évaluer les distorsions temporelles. Utilisant l’algorithme *Dynamic Time Warping (DTW)* (Müller, 2007), cette métrique mesure comment les séquences générées diffèrent temporellement des séquences réelles. Par exemple, dans une séquence de mouvements comme “boire avec la main gauche”, les échantillons réels peuvent commencer à différents moments, tandis que les échantillons générés peuvent ne pas varier suffisamment en termes de timing. WPD quantifie cette diversité dans les distorsions temporelles, offrant ainsi une évaluation plus fine.

Les expériences menées dans ce chapitre reposent sur l’utilisation de modèles *Conditional Variational Auto-Encoders (CVAE)* pour la génération de mouvements humains. Ces modèles sont évalués sur plusieurs métriques en fonction de leurs architectures (CNN, RNN ou Transformer) et de différents hyperparamètres. Les résultats montrent que certains modèles, comme le CConvVAE (CVAE basé sur les CNN), excellent en termes de fidélité et de diversité, mais les performances dépendent fortement des configurations de paramètres. Par exemple, le CConvVAE obtient les meilleurs résultats en fidélité (mesurée par la FID) dans plusieurs cas, mais les résultats peuvent varier lorsque l’on change les paramètres d’entraînement ou l’architecture.

L'analyse des résultats montre qu'il est impossible de trouver un modèle unique qui surpasse tous les autres sur toutes les métriques. Chaque métrique capture un aspect différent de la qualité des échantillons générés, et en fonction des besoins (diversité dans les jeux vidéo ou fidélité dans la réhabilitation médicale), on peut être amené à privilégier une métrique sur une autre.

En conclusion, ce chapitre propose un cadre d'évaluation unifié pour les modèles génératifs appliqués à la génération de mouvements humains, avec plusieurs métriques permettant d'évaluer à la fois la fidélité et la diversité des modèles. Le *Warping Path Diversity (WPD)* ajoute une dimension temporelle essentielle à cette évaluation, en tenant compte des distorsions temporelles dans les séquences générées. Ce cadre d'évaluation contribue à améliorer la comparaison entre différents modèles génératifs et facilite l'avancement de la recherche dans le domaine de la génération de mouvements humains.

Chapitre 8 : Recherche reproductible

Ce chapitre traite de l'importance de la reproductibilité dans la recherche scientifique, en particulier dans le contexte de l'analyse des séries temporelles et de l'apprentissage profond. La reproductibilité garantit que les travaux peuvent être reproduits et adaptés par d'autres chercheurs, renforçant ainsi la confiance dans les résultats et favorisant l'innovation future. Ce chapitre met en lumière les efforts entrepris pour assurer que les travaux présentés dans cette thèse respectent les normes les plus élevées en matière de reproductibilité.

Un élément clé de ce chapitre est l'introduction du paquet *aeon* (Middlehurst et al., 2024), une bibliothèque open-source en Python construit pour effectuer diverses tâches d'apprentissage automatique sur les séries temporelles. Le développement de ce paquet a permis d'intégrer les contributions issues de cette recherche dans une plateforme accessible à la communauté scientifique. En rendant ces outils disponibles à tous, le projet encourage la reproductibilité et l'utilisation plus large des méthodes développées au cours de ce travail.

La documentation détaillée et le code ouvert jouent un rôle crucial dans la reproductibilité. Toutes les expériences décrites dans les chapitres précédents sont soutenues par du code public, permettant ainsi aux chercheurs de reproduire les expériences, de valider les résultats et de construire de nouveaux modèles basés sur ce travail. Ce code est accompagné de descriptions claires, facilitant la prise en main et l'adaptation du projet par d'autres chercheurs. En fournissant des instructions détaillées et en tenant compte des commentaires de la communauté, l'objectif est d'améliorer constamment la reproductibilité et la fiabilité des recherches.

Le paquet *aeon* (Middlehurst et al., 2024) est au cœur de cet effort, offrant des outils pour diverses tâches comme la classification, la régression, la détection d'anomalies, et la segmentation des séries temporelles. En tant que développeur principal, j'ai contribué à la conception et à l'extension de ce paquet pour intégrer des modèles d'apprentissage profond, notamment ceux utilisés dans la classification des séries temporelles. Les modèles tels que InceptionTime, H-InceptionTime, et LITETime ont été inclus, ainsi que de nouveaux modules en développement pour des tâches comme le clustering des séries temporelles.

Les efforts pour garantir la reproductibilité ne se limitent pas à la mise à disposition du code. Le maintien de ce cadre logiciel implique également la correction des bugs, l'amélioration de la documentation, et l'ajout de nouvelles fonctionnalités pour répondre aux besoins évolutifs de la communauté scientifique. Par ailleurs,

l'utilisation des tests unitaires permet de s'assurer que les nouveaux développements n'affectent pas la performance du code existant.

Une section clé du chapitre concerne les principes fondamentaux d'un travail reproductible. Cela inclut une documentation soignée, la fourniture des dépendances nécessaires, et une architecture de code claire et modulaire. Le code doit être facile à comprendre et à modifier, permettant ainsi à d'autres chercheurs de l'étendre pour ajouter de nouveaux modèles ou fonctionnalités. Des bonnes pratiques telles que l'utilisation de noms de variables explicites et une organisation efficace des fichiers sont également mises en avant pour améliorer la lisibilité et la maintenabilité du code.

On souligne également l'importance d'utiliser des outils comme Docker pour faciliter la gestion des environnements de développement et garantir que le code fonctionne de manière cohérente sur différentes machines. L'utilisation de conteneurs Docker permet de simplifier l'intégration des dépendances, notamment les configurations CUDA nécessaires pour l'utilisation des GPU, assurant ainsi une reproduction facile des expériences dans des environnements informatiques complexes.

Un autre aspect abordé dans le chapitre concerne la visualisation et la publication des résultats sous forme d'outils interactifs, tels que des pages web et des figures dynamiques. Ces outils permettent de mieux comprendre les résultats obtenus et d'interagir avec les données générées par les modèles. Par exemple, des visualisations du chemin de distorsion temporelle et de l'espace des filtres convolutifs ont été mises à disposition pour aider les chercheurs à mieux analyser les modèles de classification des séries temporelles.

En conclusion, ce chapitre met l'accent sur la nécessité de garantir la transparence et la reproductibilité dans la recherche scientifique. En publiant le code, en documentant les processus et en fournissant des outils interactifs, je contribue à renforcer la fiabilité de la recherche et à encourager la collaboration au sein de la communauté scientifique. Le développement continu de la plateforme *aeon* et la mise en place de ressources accessibles montrent un engagement fort envers la création d'un écosystème de recherche ouvert et reproductible. Ces efforts garantissent que le travail présenté dans cette thèse peut servir de base solide pour de futures avancées dans le domaine de l'analyse des séries temporelles.

Introduction

Time series refers to sequential data where data points are equally spaced in time, with each point corresponding to a specific timestamp. Time series data is prevalent across a wide range of applications, including medical fields such as electrocardiograms (ECGs) (Rajan and Thiagarajan, 2018) and electroencephalograms (EEGs) (Tripathy and Acharya, 2018), human motion (Devanne et al., 2014), stock market trends (Anghinoni et al., 2019), and telecommunications signals (Meade and Islam, 2015) between base stations and users, among others. The term “time” in time series does not imply that only temporal ordering is relevant; rather, any data with a necessary sequence or order can be treated similarly to temporal data. For instance, in applications like image contour extraction (Ye and Keogh, 2009), the data has an inherent order that, if disrupted, such as by shuffling the image into a jigsaw puzzle, would result in a loss of meaningful information. Therefore, this data is treated similarly to time series data. While time series data can, to some extent, be represented in a tabular format, where each row corresponds to a time series sample and each column represents a variable at a particular timestamp, its analysis cannot be adequately performed using standard tabular data analysis methods. Traditional tabular methods fail to consider the sequential nature of the data, focusing only on relationships between variables, rather than the critical ordering of those variables.

In 2006, time series analysis was recognized as one of the top 10 challenges in the field of data mining (Yang and Wu, 2006). This area of study involves a broad spectrum of tasks that are crucial for understanding temporal data patterns. These tasks can be effectively tackled using a variety of approaches, including traditional statistical methods, modern machine learning techniques, and advanced deep learning models.

Forecasting is a specialized regression task in the domain of time series data, aiming at predicting future segments of the input series by utilizing the temporal patterns present in the data (Godaheva et al., 2021). This task is essential to a wide range of applications, such as weather forecasting (Karevan and Suykens, 2020) and stock market prediction (Anghinoni et al., 2019).

Extrinsic regression (Tan et al., 2020), presented in Figure 1 differs significantly from time series forecasting. In this task, the goal is to predict a continuous value that is not a future point in the input series, but rather a value generated by a random variable that depends on the entire time series, including its trends and values. This type of regression is commonly used in applications such as live fuel moisture content estimation (Zhu et al., 2021; Miller et al., 2022) and human rehabilitation motion assessment (Capecci et al., 2019).

Anomaly detection (Schmidl, Wenig, and Papenbrock, 2022) in time series focuses on identifying data points or patterns that deviate from the expected norm. This task is essential for spotting unusual events that may indicate issues like system failures or fraud. It is widely applied in areas such as network security monitoring (Kim and Park, 2003) and healthcare diagnostics (Pereira and Silveira, 2019), where early detection of anomalies can prevent significant problems.

FIGURE 1: Time Series Extrinsic Regression (TSER) is the task of predicting continuous labels of the time series samples.

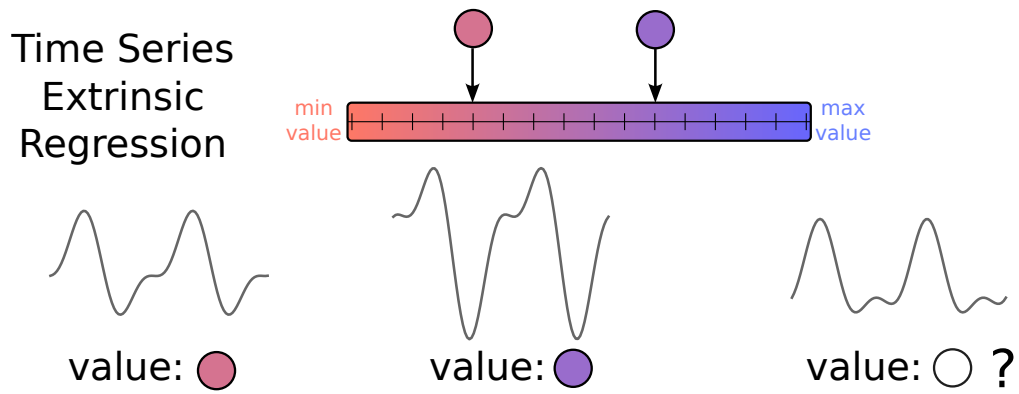


FIGURE 2: Time Series Clustering (TSCL) is the task of discovering common information between samples of time series in order to group them into clusters.

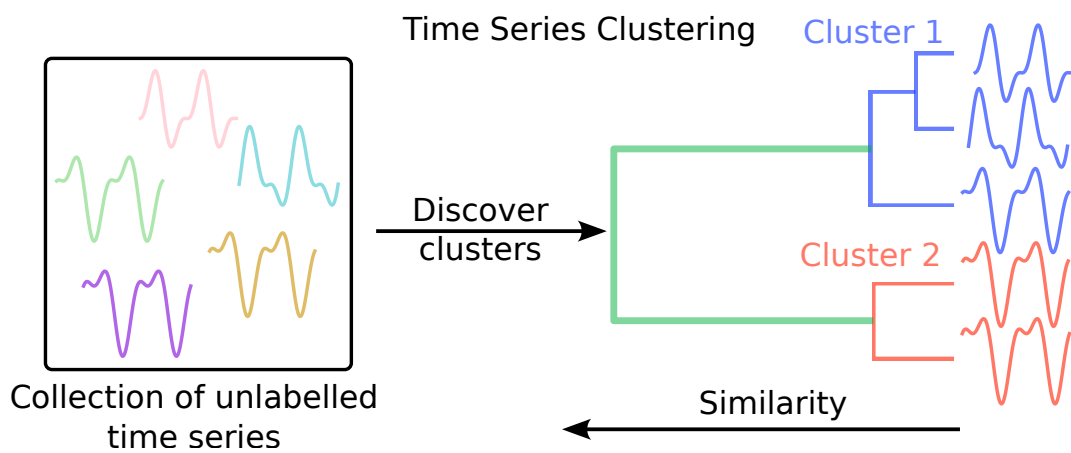


FIGURE 3: Time Series Prototyping (TSP) is the task of finding a representative of a collection of time series of a similar group.

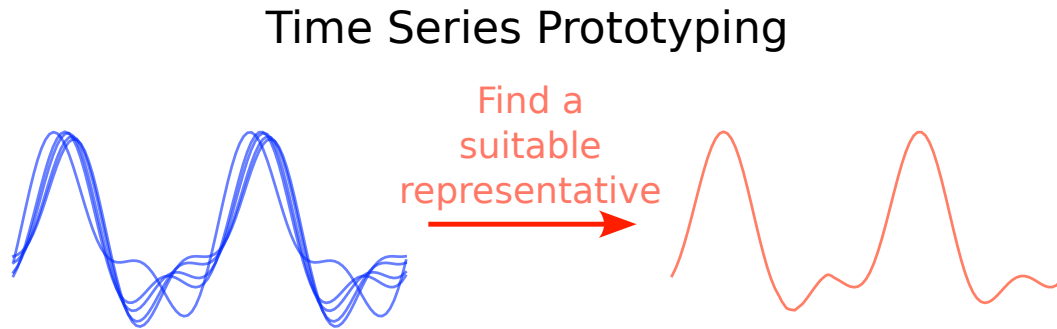
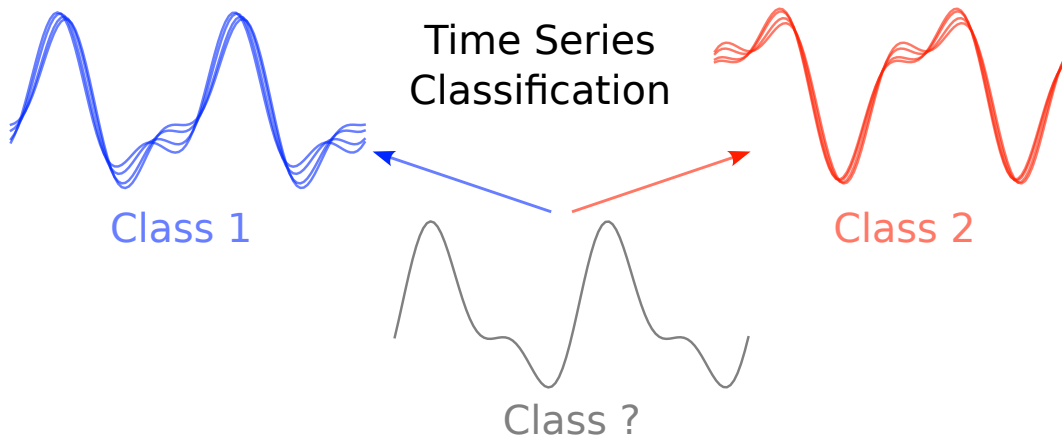


FIGURE 4: Time Series Classification (TSC) is the task of predicting a discrete label of the time series samples.



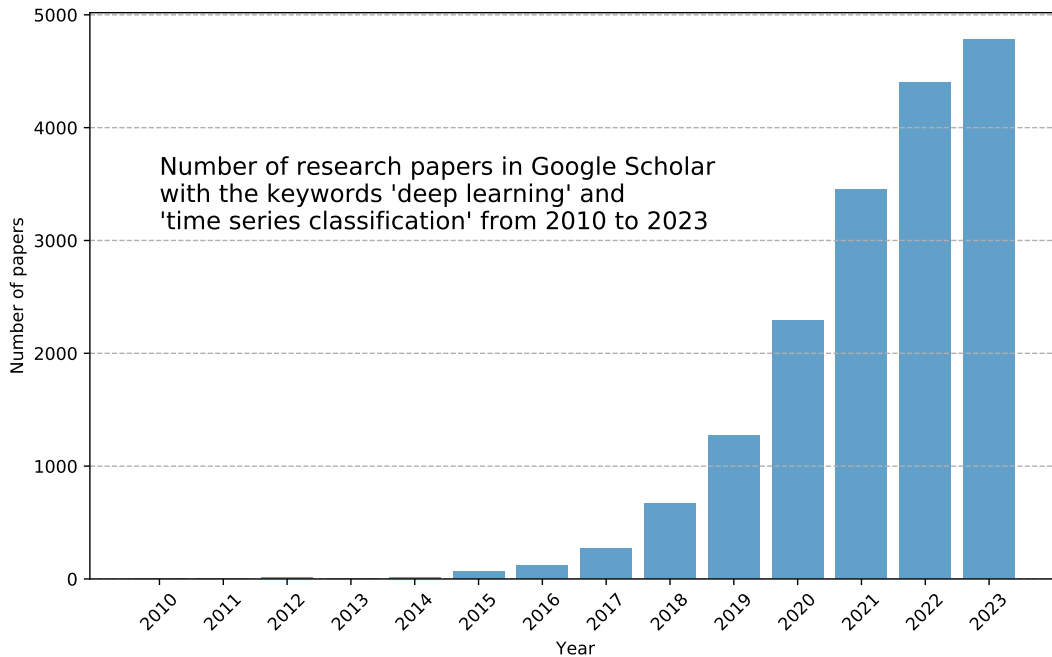
Clustering (Lafabregue et al., 2022), presented in Figure 2, involves identifying and extracting patterns within the input series to categorize them into distinct groups, which are defined by the nature of the data. This approach is applied in various fields, such as detecting daily patterns in stock market data (Sanwani and Vijayalakshmi, 2013) and identifying specific behaviors in solar magnetic wind (Pravilovic et al., 2014).

Prototyping (Petitjean, Ketterlin, and Gançarski, 2011), presented in Figure 3, is the process of identifying a representative time series from a group of similar series. This task is particularly useful in time series clustering, as it helps to summarize and simplify the data by selecting a central or typical example from each cluster. In healthcare, time series prototyping can be valuable for creating a summarized exemplar of patients with common health conditions, thereby facilitating comparisons with new patients (Imani et al., 2020).

Classification (Middlehurst, Schäfer, and Bagnall, 2024), is a discretized version of extrinsic regression as presented in Figure 4, where the goal is to predict a discrete class label for each time series with prior knowledge of the number of possible classes, which distinguishes it from clustering. This task is widely applied in various fields, including human activity recognition (Devanne et al., 2014) and medical diagnostics, such as classifying heart diseases from ECG signals (Rajan and Thiagarajan, 2018).

In this thesis, we mainly focus on four tasks for time series data: classification, clustering, extrinsic regression and prototyping. These tasks are particularly relevant

FIGURE 5: The number of research papers mentioning “deep learning” and “time series classification” increased rapidly in the last years.



to the application of human motion analysis, where the input time series consists of sequences of recorded kinematic skeleton data at each time step. Such data can be used for classification tasks to predict the activity of a subject and for extrinsic regression to predict a continuous value associated to rehabilitation motion to assess patients’ performance. More details on this application and the contributions in such domain are presented in Chapter 6.

In order to address the above mentioned applications, we addressed the approached perspective of time series analysis, starting with a study of traditional methods that have been used for years to solve Time Series Classification (TSC). However, it was shown in the first 2017 TSC bake-off (Bagnall et al., 2017) that using the traditional techniques does not achieve state-of-the-art performance, instead the authors found that hybrid approaches work much better. Moreover, the domain of TSC was then extended by different methods proposed in between, ranging from convolution methods (Dempster, Petitjean, and Webb, 2020) to bag-of-words methods (Schäfer and Leser, 2023). After the publication of the 2017 bake-off, researchers began to question the role of deep learning models in this domain, especially given their significant performance in image classification (LeCun, Bengio, and Hinton, 2015; Krizhevsky, Sutskever, and Hinton, 2012). The number of related papers in deep learning for TSC started to increase rapidly, leading to the 2019 deep learning for TSC review (Ismail Fawaz et al., 2019). The 2019 review demonstrated that the best deep learning model achieved performance comparable to the state-of-the-art non-deep learning model. Ismail Fawaz et al. (2019) paved the way for new research in deep learning for time series classification (TSC). This trend, illustrated in Figure 5, also extends to addressing other tasks within the time series domain. For instance, deep learning methods for Time Series Clustering (TSCL) was reviewed in (Lafabregue et al., 2022) showcasing that deep TSCL methods can outperform traditional elastic methods or shape based methods (Paparrizos and Gravano, 2015).

Additionally, the usage of deep learning emerged for the task of Time Series Prototyping (TSP) with the usage of multi-task Auto-Encoders (Terefe et al., 2020). Finally, Mohammadi Foumani et al. (2024) showed that numerous research papers are addressing the task of deep learning for Time Series Extrinsic Regression (TSER). A significant amount of literature work on these topics are presented in Chapter 1.

Given the growing interest and proven effectiveness of deep learning in time series analysis, we employ this approach to tackle the four tasks of TSC, TSCL, TSP, and TSER. Deep learning’s ability to capture complex patterns and dependencies in sequential data makes it well-suited for addressing these challenges. However, before presenting any contribution in this thesis in these four tasks, we start by addressing the evaluation of discriminative models. The current evaluation framework, even though having its own advantages, presents some limitations that are beneficial to any research work that want to manipulate the “view” of the results to make it seem better than other approaches. For this reason, we propose, not a replacement, but a complimentary tool for such an evaluation framework, that we present in Chapter 2.

After establishing the evaluation framework and recognizing the growing interest in developing foundation models for time series data (Goswami et al., 2024), we introduce in Chapter 3 two key contributions. These contributions converge to form a novel approach aiming at defining such a foundation model, specifically tailored for the task of TSC. Chapter 3 not only outlines the foundation model but also explains how it tackles these unique challenges through the engineering of hand-crafted features, paving the way for more robust and generalized models in this domain.

Focusing on the carbon footprint of such complex deep learning models for time series data, we propose in Chapter 4 to reduce model complexity while keeping the performance statistically non significantly worse than the state-of-the-art. This is done by the proposal of LITE, the smallest deep learning model for time series data found in the literature, that is proven to be very effective in the second TSC bake-off (Middlehurst, Schäfer, and Bagnall, 2024).

Moreover, acquiring labeled data in time series can be challenging. To address this, in Chapter 5, we propose an unsupervised framework designed to handle situations where only a limited number of labeled samples are available. This unsupervised framework, based on representation learning, can be applied to various downstream tasks involving time series data.

Given that this thesis is conducted within the framework of the ANR JCJ DEL-EGATION (more details in Section [Financing](#)), which targets the analysis of human motion, Chapter 6 addresses the specific challenges of human motion data. It highlights the unique characteristics of this data and demonstrates how our contributions are particularly effective in this domain, in line with the project’s objectives. We demonstrate how using small models like LITE, optimized for human motion, can achieve state-of-the-art performance in rehabilitation assessment within a classification framework, while also being effective in terms of medical explainability. Additionally, we introduce a novel TSP approach used as a generative method for enhancing extrinsic regression models in rehabilitation motion assessment tasks. Moreover, considering the rise generative models for human motion (Guo et al., 2020; Petrovich, Black, and Varol, 2021) and the strong performance of CNNs in the time series domain (Ismail Fawaz et al., 2020), we propose a deep generative model with a CNN backbone for human motion data that nearly matches state-of-the-art results. Given we focus on the evaluation framework for discriminative models in Chapter 2, we argue in Chapter 7 for the necessity of a unified framework specifically for generative models, particularly in the context of human motion data.

Contribution	Task	Chap.	GitHub
(Ismail-Fawaz et al., 2023a)	Evaluation	2	Multi_Comparison_Matrix
(Ismail-Fawaz et al., 2022)	Classification	3	CF-4-TSC
(Ismail-Fawaz et al., 2024e)	Classification	3	DomainFoundationModelsTSC
(Ismail-Fawaz et al., 2023c)	Classification	4	LITE
(Ismail-Fawaz et al., 2024f)	Classification	4	LITE
(Ismail-Fawaz et al., 2023b)	Self-Supervised/ Classification	5	TRILITE
(Ismail-Fawaz et al., 2023d)	Prototyping	6	ShapeDBA
(Ismail-Fawaz et al., 2024g)	Prototyping/ Regression	6	Weighted-ShapeDBA-4-Rehab
(Ismail-Fawaz et al., 2024a)	Generation/ Classification	6	SVAE-4-HMG
(Ismail-Fawaz et al., 2024c)	Generation/ Evaluation	7	Evaluating-HMG
(Middlehurst et al., 2024)	All	8	aeon
(Ismail-Fawaz et al., 2024b)	Visualization	8	Elastic_Warping_Vis
(Ismail-Fawaz et al., 2024h)	Prototyping	8	Augmenting-TSC-Elastic-Averaging
(Ismail-Fawaz et al., 2024d)	Classification	8	Simple-KAN-4-Time-Series

TABLE 1: List of contributions including 11 papers and 3 open source published work with the companion GitHub repository.

In Chapter 8, we conclude by discussing the importance of reproducible research, offering a professional perspective on this critical aspect of scientific inquiry. We highlight the contributions of this thesis to the open-source Python package *aeon* (Middlehurst et al., 2024), as well as several other open-source projects developed during the course of this research, with or without accompanying publications.

In Table 1 we present all of the contributions in this thesis, including 11 papers and 3 open source projects. All of our research work is based on using publicly available datasets, including the UCR archive (Dau et al., 2019) for univariate setups, the UEA archive (Bagnall et al., 2018) for multivariate setups and both the HumanAct12 (Guo et al., 2020) and Kimore (Capecchi et al., 2019) datasets for human motion applications of activity recognition and rehabilitation assessment.

Publications

International Journals

- Middlehurst, Matthew, **Ali Ismail-Fawaz**, Antoine Guillaume, Christopher Holder, David Guijo Rubio, Guzal Bulatova, Leonidas Tsaprounis, Lukasz Mentel, Martin Walter, Patrick Schäfer, Anthony Bagnall (2024) “aeon: a Python toolkit for learning from time series”. In *Journal Machine Learning Research (JMLR)*, open source software track. doi: <https://arxiv.org/abs/2406.14231>

International Conferences and Workshops

- **Ismail-Fawaz, Ali**, Maxime Devanne, Jonathan Weber, and Germain Forestier. (2022). “Deep learning for time series classification using new hand-crafted convolution filters”. In *IEEE International Conference on Big Data (Big*

- Data) (pp. 972-981). IEEE. doi: <https://doi.org/10.1109/BigData55660.2022.10020496>
- **Ismail-Fawaz, Ali**, Maxime Devanne, Jonathan Weber, and Germain Forestier. (2023). “Enhancing time series classification with self-supervised learning”. In *International Conference on Agents and Artificial Intelligence (ICAART)* (pp. 40-47). SCITEPRESS-Science and Technology Publications. doi: <https://doi.org/10.5220/0011611300003393>
 - **Ismail-Fawaz, Ali**, Hassan Ismail Fawaz, François Petitjean, Maxime Devanne, Jonathan Weber, Stefano Berretti, Geoffrey I. Webb, and Germain Forestier. (2023). “ShapeDBA: generating effective time series prototypes using shapeDTW barycenter averaging”. In *International Workshop on Advanced Analytics and Learning on Temporal Data; in conjunction with the European Conference on Machine Learning and Principles and Practice of Knowledge Discovery in Databases* (pp. 127-142). Cham: Springer Nature Switzerland. doi: https://doi.org/10.1007/978-3-031-49896-1_9
 - **Ismail-Fawaz, Ali**, Maxime Devanne, Stefano Berretti, Jonathan Weber, and Germain Forestier. (2023). “Lite: Light inception with boosting techniques for time series classification”. In *IEEE 10th International Conference on Data Science and Advanced Analytics (DSAA)* (pp. 1-10). IEEE. doi: <https://doi.org/10.1109/DSAA60987.2023.10302569>
 - **Ismail-Fawaz, Ali**, Maxime Devanne, Stefano Berretti, Jonathan Weber, and Germain Forestier. (2024). “Finding foundation models for time series classification with a pretext task”. In *Pacific-Asia Conference on Knowledge Discovery and Data Mining* (pp. 123-135). Singapore: Springer Nature Singapore. doi: https://doi.org/10.1007/978-981-97-2650-9_10
 - **Ismail-Fawaz, Ali**, Maxime Devanne, Stefano Berretti, Jonathan Weber, and Germain Forestier. (2024). “A Supervised Variational Auto-Encoder for Human Motion Generation using Convolutional Neural Networks”. In *4th International Conference on Pattern Recognition and Artificial Intelligence (ICPRAI)*
 - **Ismail-Fawaz, Ali**, Maxime Devanne, Stefano Berretti, Jonathan Weber, and Germain Forestier. (2024). “Weighted Average of Human Motion Sequences for Improving Rehabilitation Assessment”. In *International Workshop on Advanced Analytics and Learning on Temporal Data (AALTD); in conjunction with the European Conference on Machine Learning and Principles and Practice of Knowledge Discovery in Databases (ECML/PKDD)*. doi: https://ecml-aaltd.github.io/aaltd2024/articles/Fawaz_AALTD24.pdf

National Conferences

- **Ismail-Fawaz, Ali**, Maxime Devanne, Jonathan Weber, and Germain Forestier. (2023). “Apprentissage en Profondeur pour la Classification des Séries Temporelles à l’aide de Nouveaux Filtres de Convolution Créés Manuellement”. In *ORASIS*. doi: <https://hal.science/hal-04219450/document>
- **Ismail-Fawaz, Ali**, Maxime Devanne, Stefano Berretti, Jonathan Weber, and Germain Forestier. (2024). “LITE: Light Inception avec des Techniques de Boosting pour la Classification de Séries Temporelles”. In *Extraction et Gestion*

des Connaissances (EGC) (pp. 377-384). doi: <https://editions-rnti.fr/?inprocid=1002948>

- **Ismail-Fawaz, Ali**, Maxime Devanne, Stefano Berretti, Jonathan Weber, and Germain Forestier. (2023). “Reducing Complexity of Deep Learning for Time Series Classification Using New Hand-Crafted Convolution Filters”. *Upper Rhine Artificial Intelligence Symposium (URAI)*. doi: https://maxime-devanne.com/publis/ismail-fawaz_urai2023.pdf

Under Submission

International Journals

- **Ismail-Fawaz, Ali**, Maxime Devanne, Stefano Berretti, Jonathan Weber, and Germain Forestier. “Look Into the LITE in Deep Learning for Time Series Classification”. In *International Journal of Data Science and Analytics*. doi: <https://arxiv.org/abs/2409.02869>
- **Ismail-Fawaz, Ali**, Maxime Devanne, Stefano Berretti, Jonathan Weber, and Germain Forestier. “Establishing a Unified Evaluation Framework for Human Motion Generation: A Comparative Analysis of Metrics”. In *Computer Vision and Image Understanding*. doi: <https://arxiv.org/abs/2405.07680>

Arxiv

- **Ismail-Fawaz, Ali**, Angus Dempster, Chang Wei Tan, Matthieu Herrmann, Lynn Miller, Daniel F. Schmidt, Stefano Berretti, Jonathan Weber, Maxime Devanne, Germain Forestier, and Geoffrey I. Webb. (2023). “An approach to multiple comparison benchmark evaluations that is stable under manipulation of the compare set”. doi: <https://arxiv.org/abs/2305.11921>

Chapter 1

State Of The Art For Time Series Analysis: Supervised and Unsupervised Learning

1.1 Introduction

Time series analysis, a critical aspect of data science, leverages both supervised and unsupervised learning methods to extract meaningful insights from time-dependent data. In supervised learning, the goal is to predict future values based on past observations. This includes tasks such as extrinsic regression, where continuous future values are forecasted, and classification, where future events are categorized into predefined classes. Examples include predicting stock prices or classifying email as spam or regular based on historical data. Unsupervised learning, on the other hand, involves discovering inherent structures or patterns within the data without predefined labels. Key tasks include clustering, where similar data points are grouped together, and anomaly detection, which identifies unusual patterns that deviate from the norm. Applications of these techniques range from segmenting customers based on purchasing behavior to detecting fraudulent transactions in financial systems. By employing both supervised and unsupervised learning, time series analysis can effectively address a wide array of predictive and descriptive tasks, driving informed decision-making across various fields.

In the rest of this chapter, we will detail the state-of-the-art literature for both cases. For supervised learning, we will explore classification and extrinsic regression techniques, while for unsupervised learning, we will focus on clustering, prototyping, and self-supervised methods. This comprehensive review aims to provide a thorough understanding of the latest advancements and applications in time series analysis.

1.2 Supervised Learning: Time Series Classification and Extrinsic Regression

This subsection covers two main tasks: classification, which categorizes time series data into predefined classes, and extrinsic regression, which predicts continuous values. We will review state-of-the-art models and techniques for these tasks, discussing their applications, strengths, and limitations.

1.2.1 Time Series Classification

The task of TSC has been addressed for the last three decades in various approaches ranging from distance based approaches to recent deep learning methods.

Such type of data can be found in various domains ranging from human activity recognition (Devanne et al., 2014) to wireless communication (Bertalaníč, Meža, and Fortuna, 2022). With the availability of new TSC datasets, a significant amount of models has been proposed in the literature. Collecting such data and preprocessing them to become available for benchmarking is not a simple task, for this reason the UCR/UEA (Dau et al., 2019; Bagnall et al., 2018) archives had such a significant impact in the last decade on the amount of research in the TSC field.

In this section, we present the prerequisite definitions needed to understand all the materials. We follow these definitions by an extensive detail view over some state-of-the-art models in both deep and non deep learning methods for TSC.

Definition 1 A Univariate Time Series (UTS) $\mathbf{x} = \{x_1, x_2, \dots, x_L\}$ is a sequence of ordered real values. The length of this sequence is L .

Definition 2 A Multivariate Time Series (MTS) of M dimensions (also referred to as channels) $\mathbf{x} = \{\mathbf{x}^1, \mathbf{x}^2, \dots, \mathbf{x}^M\}$ is a set of M univariate time series of length L , where $\mathbf{x}^m = \{x_1^m, x_2^m, \dots, x_L^m\}$ is a univariate series of length L and $\mathbf{x}_t = \{x_t^1, x_t^2, \dots, x_t^M\}$ a one dimensional vector of shape $(M,)$, $m \in [1, M]$ and $t = [1, L]$.

Definition 3 A TSC dataset $\mathcal{D} = \{\mathbf{x}_i, \mathbf{y}_i\}_{i=1}^N$ is a collection of N pairs of time series and their corresponding label \mathbf{y}_i where $\mathbf{x}_i = \{\mathbf{x}_{i,1}, \mathbf{x}_{i,2}, \dots, \mathbf{x}_{i,L}\}$ is an MTS of M dimensions and length L . The label \mathbf{y}_i is a vector of length C where C is the number of possible classes in \mathcal{D} . Each element $c \in [1, C]$ in \mathbf{y}_i is one if \mathbf{x}_i belongs to class c and zero otherwise.

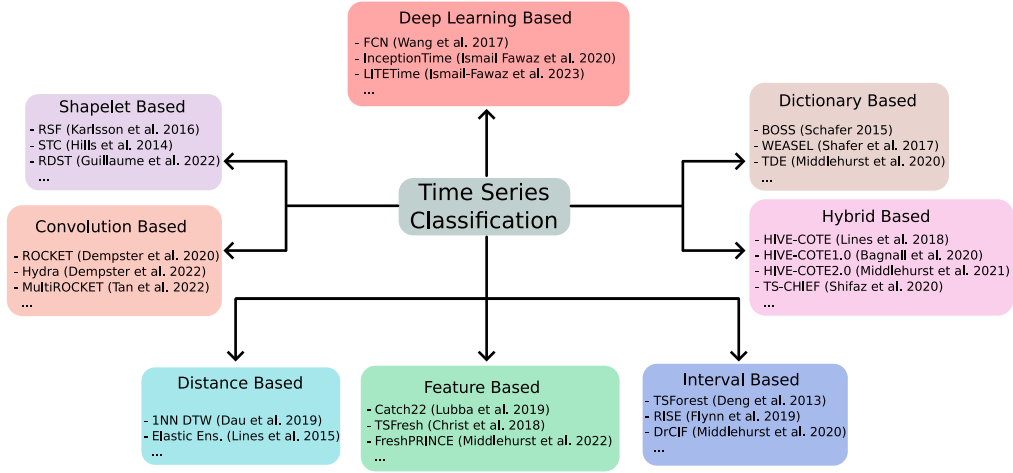
The task of TSC comes down to constructing a model \mathcal{F} that can achieve correct predictions of labels associated to each time series in the dataset. This is done by teaching the model how to predict a discrete probability distribution of C elements with the goal of having the highest probability assigned to the correct class.

$$\mathcal{F}(\mathbf{x}) = [p_1, p_2, \dots, p_C] \quad (1.1)$$

where $\sum_{c=1}^C p_c = 1$ and $0 \leq p_c \leq 1$.

For many years, the most famous approach known in the literature to address TSC was the use of Nearest Neighbor (NN) coupled with Dynamic Time Warping (DTW) similarity measure and was used as a baseline (Bagnall et al., 2017). Some work also tried to address an adaptation of Support Vector Machines (SVMs) (Vapnik, 2013) for TSC, such as the usage of edit distance kernels (Marteau and Gibet, 2014; Cuturi et al., 2007). Ever since the release of the first TSC review by (Bagnall et al., 2017), much more classifiers have been published. With the rise of available data, (Ismail Fawaz et al., 2019) presents a detailed review over all deep learning models from the literature addressed for the task of TSC and evaluated them on the UCR/UEA archives. The 2019 deep learning for TSC review (Ismail Fawaz et al., 2019) highlighted the importance of deep learning models that were missed in the TSC review of (Bagnall et al., 2017), showcasing their competitive performance with non-deep learning models. Moreover, the number of TSC models have increased significantly, which led to the second TSC review (Middlehurst, Schäfer, and Bagnall, 2024). The models in the literature can be divided into eight different sections based on the method used to solve the TSC task. These sections, presented in Figure 1.1, are: **distance based methods**, **feature based methods**, **interval based methods**, **dictionary based methods**, **convolution based methods**, **shapelet based methods**, **hybrid based methods** and **deep learning based methods**.

FIGURE 1.1: Eight sections of Time Series Classification models from the literature: shapelet based, convolution based, distance based, feature based, interval based, dictionary based, hybrid based and deep learning based.



In this section, we go through some approaches of solving the task of TSC with non-deep learning methods.

1.2.1.1 Distance Based Methods

In this section we present the distance based methods to solve the TSC task which utilizes measures such as DTW or MSM (Stefan, Athitsos, and Das, 2012b) etc.

1.2.1.1.1 k -Nearest Neighbor - Dynamic Time Warping (k -NN-DTW) and Variants As mentioned before, the most famous method to solve TSC was based on the k -NN algorithm coupled with a similarity measure. While for other types of data k -NN is coupled with the Euclidean Distance (ED) presented in Eq. 1.2, it does not capture the temporal aspect of time series.

$$ED(\mathbf{x}_1, \mathbf{x}_2) = \sqrt{\sum_{t=1}^L \sum_{m=1}^M (x_{1,t}^m - x_{2,t}^m)^2} \quad (1.2)$$

For instance if we have two time series $\mathbf{x}_1 = [1, 1, 0, 0, 0, 1, 0]$ and $\mathbf{x}_2 = [0, 1, 1, 0, 0, 0, 1]$, ED would produce a value of 2 however the series are identical with a simple shift of one time stamp between them. For this reason, DTW was proposed in order to capture this kind of temporal distortion. DTW finds the optimal alignment path between two time series before applying the Minkowski (ED if $q = 2$) over the aligned series. The mathematical formulation of DTW is as follows:

$$DTW_q(\mathbf{x}_1, \mathbf{x}_2) = \min_{\pi \in \mathcal{A}(\mathbf{x}_1, \mathbf{x}_2)} \left(\sum_{(t_1, t_2) \in \pi} \sum_{m=1}^M (x_{1,t_1}^m - x_{2,t_2}^m)^q \right)^{1/q} \quad (1.3)$$

where π is an alignment path of length L_π and is a sequence of L_π pairs of indices $[(t_{11}, t_{21}), (t_{12}, t_{22}), \dots, (t_{1,L_\pi}, t_{2,L_\pi})]$. $\mathcal{A}(\mathbf{x}_1, \mathbf{x}_2)$ is the set of all acceptable paths between the two series. A path π is considered acceptable if:

1. Start and ending point match the ones of the series:
 - $\pi_1 = (1, 1)$
 - $\pi_{L_\pi} = (L_1, L_2)$
2. The sequence is monotonically increasing:
 - $t_{1,l-1} \leq i_l \leq t_{1,l-1} + 1$
 - $t_{2,l-1} \leq j_l \leq t_{2,l-1} + 1$

where $l \in [1, L_\pi]$

The distance is usually set to the squared error so $q = 2$. A detailed view of the DTW algorithm is presented in Algorithm 1. As presented in the detailed algorithm, for each element in the distance matrix, the squared error between the current time stamps first fills the matrix's cell. Second, at each cell, the smallest element between its three neighbors is added, the upper neighbor indicates inserting a time stamp from one series to another, the left neighbor indicates deleting an element from one series and the bottom neighbor indicates that these two time stamps are aligned so no need for an operation. The time complexity of the DTW algorithm is $\mathcal{O}(L_1.L_2)$ and $\mathcal{O}(L^2)$ if both series are of the same length. This complexity is considered very high, and when coupled with NN the whole complexity is $\mathcal{O}(N_{train}.N_{test}.L^2)$, however some work has optimized such complexity by defining a lower bound for DTW (Keogh and Ratanamahatana, 2005; Webb and Petitjean, 2021).

Algorithm 1 Dynamic Time Warping (DTW)

Require: Two Time Series \mathbf{x}_1 and \mathbf{x}_2 of length L and dimension M

Ensure: DTW measure between \mathbf{x}_1 and \mathbf{x}_2

```

1:  $D = \text{array}[L + 1, L + 1]$ 
2: for  $t_1 = 1$  to  $L + 1$  do
3:   for  $t_2 = 1$  to  $L + 1$  do
4:      $D[t_1, t_2] = +\infty$ 
5:   end for
6: end for
7:  $D[0,0] = 0.0$ 
8: for  $t_1 = 2$  to  $L + 1$  do
9:   for  $t_2 = 2$  to  $L + 1$  do
10:     $cost = \sum_{m=1}^M (x_{1,t_1-1}^m - x_{2,t_2-1}^m)^2$ 
11:     $up\_insertion = D[t_1 - 1, t_2]$ 
12:     $left\_deletion = D[t_1, t_2 - 1]$ 
13:     $diagonal\_match = D[t_1 - 1, t_2 - 1]$ 
14:     $D[t_1, t_2] = cost + \min(up\_insertion, left\_deletion, diagonal\_match)$ 
15:   end for
16: end for
17: Return:  $D[L + 1, L + 1]$ 

```

An example of DTW alignment path computation between two time series of the ItalyPowerDemand dataset of the UCR archive (Dau et al., 2019) is presented in

FIGURE 1.2: Example of DTW alignment path computation between two series (in red and in blue) from the ItalyPowerDemand dataset of the UCR archive. The DTW optimal alignment path between both series is presented in gray.

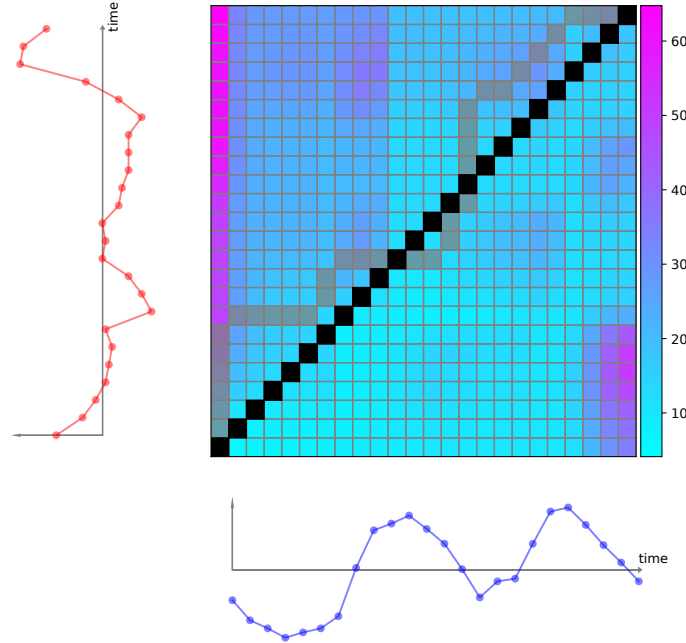


Figure 1.2. To showcase the need of a DTW alignment instead of simply using a Euclidean Distance that assume a perfect alignment, we present in Figure 1.3 for the same series used in Figure 1.2 both the perfect alignment that ED assumes vs the DTW alignment.

The DTW measure is then utilized to calculate the similarity between each testing sample to all training samples, the predicted label for the test sample is the same as its k nearest neighbors following the used similarity measure. This algorithm has been developed over the years by simply fine-tuning the parameters of DTW, or by changing the similarity measure. For instance, many versions of DTW have been proposed over the years, such as SoftDTW (Cuturi and Blondel, 2017) and ShapeDTW (Zhao and Itti, 2018).

The SoftDTW (Cuturi and Blondel, 2017) version addresses the issue of differentiability of DTW especially because of the minimization step in Algorithm 1. The authors of SoftDTW (Cuturi and Blondel, 2017) argues the need of a differentiable DTW in order to be able to construct an optimization problem used for many applications such as clustering and deep learning. SoftDTW solved this issue by replacing the *hard* – min operation by a *soft* – min operation. The *soft* – min operation is used as follows:

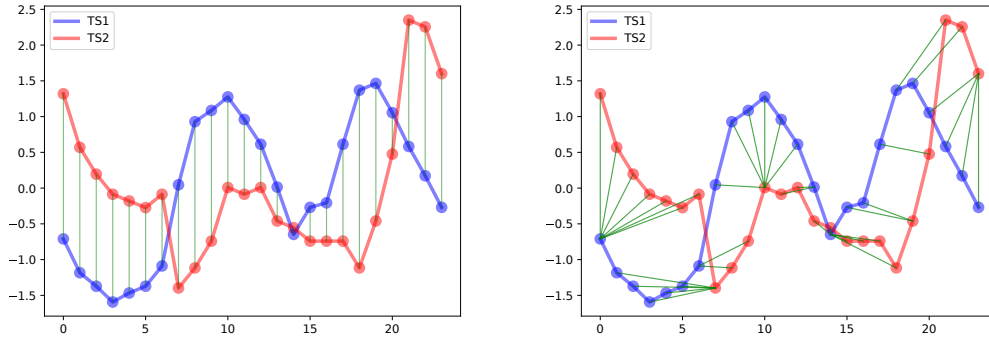
$$\text{soft-min } \gamma(a_1, a_2, \dots, a_N) = -\gamma \cdot \log \sum_{i=1}^N e^{-a_i/\gamma} \quad (1.4)$$

where γ is the smoothing factor, and as it tends to the value 0^+ , then the *soft* – min becomes the *hard* – min hence SoftDTW becomes the original DTW.

FIGURE 1.3: DTW optimal alignment vs the ED's assumption of a perfect alignment on two time series of the ItalyPowerDemand dataset of the UCR archive.

(A) Alignment using ED

(B) Alignment using DTW



In (Zhao and Itti, 2018), a variation of DTW was introduced, which aligns transformations of sub-sequences within time series instead of aligning all time series simultaneously. This approach aims to maintain the consideration of neighborhood structure when aligning timestamps across different time series. To define ShapeDTW mathematically, let \mathcal{F} be a descriptor function, \mathbf{x}_1 and \mathbf{x}_2 be two MTS of length L and dimension M . The process begins by extracting sub-sequences over all channels of length r (referred to as reach) and transform them using a descriptor $\mathcal{F} : \mathbb{R}^r \rightarrow \mathbb{R}^d$. This results in two new MTS \mathcal{D}_1 and \mathcal{D}_2 of length L and dimension $M \cdot d$, associated to \mathbf{x}_1 and \mathbf{x}_2 respectively.

The DTW alignment path is then computed on the transformed version of the series \mathcal{D}_1 and \mathcal{D}_2 , followed by the optimal path being transferred onto the original series space to calculate the measure between the original time stamps instead of the sub-sequences. In this manner, the DTW algorithm will calculate the distance between time stamps following their neighborhood alignments. The ShapeDTW measure can be formulated as the following optimization problem:

$$\text{ShapeDTW}_q(\mathbf{x}_1, \mathbf{x}_2) = \left(\sum_{(t_1, t_2) \in \pi^*} \sum_{m=1}^M (x_{1, t_1}^m - x_{2, t_2}^m)^q \right)^{1/q} \quad (1.5)$$

where π^* is the optimal path obtained by the DTW alignment path between transformed series as follows:

$$\pi^* = \arg \min_{\pi \in \mathcal{A}(\mathcal{D}_1, \mathcal{D}_2)} \left(\sum_{(\tilde{t}_1, \tilde{t}_2) \in \pi} \sum_{m=1}^M (\mathcal{D}_{1, \tilde{t}_1}^m - \mathcal{D}_{2, \tilde{t}_2}^m)^q \right)^{1/q} \quad (1.6)$$

The distance is usually set to the squared error so $q = 2$.

1.2.1.1.2 Elastic Ensemble Given the high number of similarity measures for time series data, (Lines and Bagnall, 2015) proposed to do a weighted Elastic Ensemble (EE) of 11 NN classifiers each using a different similarity measure. Below, we define what an ensemble of classifiers is, a concept that will be used throughout the rest of this work.

Definition 4 Ensembling different classifiers is motivated by the idea that combining multiple opinions often leads to a more robust decision. Since each classifier generates a probability distribution for each series across the possible classes, the ensemble method averages these probability distributions from all classifiers.

1.2.1.1.3 Proximity Forest and Proximity Forest2.0 Proximity Forest (PF) (Lucas et al., 2019) is a Random Forest (RF) (Breiman, 2001) classifier adaptation for the time series classification task. PF utilizes the same 11 similarity measures that EE (Lines and Bagnall, 2015) uses, however it randomly sets at each branch one of the similarity measures to be used for the fed time series. Until 2023, PF was the state-of-the-art distance based classifier for the task of TSC on the UCR archive (Dau et al., 2019) following the recent TSC review (Middlehurst, Schäfer, and Bagnall, 2024). However, recently, the same group that developed PF upgraded the algorithm and developed PF2.0 (Herrmann et al., 2023) and it was significantly better than PF. PF2.0 differs from the original PF by three main features: (1) being efficiently better than much faster, (2) the addition of a new similarity measure Amerced Dynamic Time Warping (ADTW) (Herrmann and Webb, 2023) and (3) tuning the parameters of the cost function.

1.2.1.2 Feature Based Methods

Using traditional machine learning classifiers such as RF (Breiman, 2001) or RIDGE classifier (Hoerl and Kennard, 1970) is insufficient on raw time series data as these classifiers are constructed to use tabular input. In order to overcome this issue, some feature based classifiers were proposed for TSC which consist of a pipeline of feature extraction methods followed by a simple classifier designed for tabular data. In what follows, we present briefly some state-of-the-art feature based methods of TSC.

1.2.1.2.1 The Canonical Time Series Characteristics (Catch22) Building on the original work of (Fulcher and Jones, 2017), which proposed the *Highly Comparative Time-Series Analysis (hctsa)* tool to extract around 7700 features from each time series, the authors in (Lubba et al., 2019) did an extensive amount of experiment in order to identify the most effective 22 *hctsa* features. This new set of features proposed in (Lubba et al., 2019) is called Catch22, which is then followed by an RF classifier (Breiman, 2001).

1.2.1.2.2 Time Series Feature Extraction based on Scalable Hypothesis Tests (TSFresh) and The FreshPRINCE TSFresh (Christ et al., 2018) is a set of around 800 features that are extracted from each time series. This set of features are not all utilized for the classification, instead, the authors in (Christ et al., 2018) proposed the usage of a feature selection method called FRESH (Christ, Kempa-Liehr, and Feindt, 2016). The selected features are then fed into an RF classifier or an AdaBoost classifier (Freund, Schapire, et al., 1996). The TSFresh features were then used recently by (Middlehurst and Bagnall, 2022) where the authors removed the feature selection method and utilize a Rotation Forest (RotF) classifier (Rodriguez, Kuncheva, and Alonso, 2006) on top of the TSFresh features, to produce the FreshPRINCE feature-based classifier.

Until now, the FreshPRINCE classifier is the state-of-the-art feature-based method for TSC on the UCR archive following the recent TSC review (Middlehurst, Schäfer, and Bagnall, 2024).

1.2.1.3 Convolutional Based Methods

Convolution based approaches have shown to be very effective on image classification since the birth of Convolutional Neural Networks (CNNs) (LeCun, Bengio, and Hinton, 2015). In the case of images, convolution filters are two-dimensional operation where the filter slides all over the image in order to extract some meaningful features. However, in the case of time series, the convolution operation is one dimensional and slides all over the temporal axis of the time series in order to extract temporal features and local dependencies.

Definition 5 A one-dimensional convolution operation over a univariate time series \mathbf{x} of length L with a kernel $\mathbf{w} = \{w_1, w_2, \dots, w_K\}$ of length K is defined as follows:

$$o_t = \sum_{k=1}^K x_{t+k-1} \cdot w_k \quad (1.7)$$

with $t \in [1, L - K + 1]$ and $\mathbf{o} = \mathbf{x} * \mathbf{w} = \{o_1, o_2, \dots, o_{L-K+1}\}$ is the output series of the one-dimensional convolution and $*$ is the convolution operator. Whenever a value in \mathbf{o} , representing a segment in \mathbf{x} of length K , is positive, it is referred to as the convolution kernel being activated at that segment in \mathbf{x} , thus a pattern is detected. *It is important to note that the above definition of a 1d convolution operation uses a stride of 1, which represents the amount of time stamps the convolutional kernel shifts when sliding on the temporal axis. By default, in the rest of this work, all convolutional operations use a stride of 1.*

In the above approach, the convolution is being applied to a consecutive set of time stamps. However, it can be interesting to extract features of time stamps with wider temporal distance between them. This can be done by simply increasing the length of the convolution kernel, however it would increase the number of parameters used. A more constructive approach is to use dilated convolution to increase the view of the kernel over the time series sample.

Definition 6 Dilated one-dimensional convolution between a series \mathbf{x} and a kernel \mathbf{w} of lengths L and K respectively with a dilation rate $d > 1$ is defined as follows:

$$o_t = \sum_{k=1}^K x_{t+(k-1) \cdot d} \cdot w_k \quad (1.8)$$

where $t \in [1, L - (K - 1) \cdot d]$ and \mathbf{o} the output series of the one-dimensional dilated convolution. If $d = 1$ then this comes down to applying the convolution as in Eq. 1.7. The dilation rate allows the convolution operation to skip some elements in the input series to detect longer patterns.

1.2.1.3.1 RandOm Convolutional Kernel Transform (ROCKET) (Dempster, Petitjean, and Webb, 2020) proposed ROCKET, a convolution based model that randomly generates a large set of kernels following a standard Gaussian distribution $\mathcal{N}(0, 1)$, with random dilation rates and random biases sampled from a uniform distribution $\mathcal{U}(-1, 1)$. This set of filters is then applied on each of training time series samples followed by two aggregation functions. The first aggregation is choosing the maximum value of the convolution output and the second is taking the Proportion of

Positive Values (PPVs). The PPV is obtained as detailed in Eq. 1.9:

$$PPV(\mathbf{o} = \mathbf{x} * \mathbf{w}) = \frac{1}{L - K + 1} \sum_{t=1}^{L-K+1} \mathbb{1}[\mathbf{o}_t > 0] \quad (1.9)$$

$\mathbb{1}[\textit{condition}]$ is the indicator function defined as:

$$\mathbb{1}[\textit{condition}] = \begin{cases} 1 & \textit{if condition is True} \\ 0 & \textit{if condition is False} \end{cases} \quad (1.10)$$

Assuming that ROCKET uses \mathcal{K} convolution filters, the output space dimension is $2\mathcal{K}$ per time series sample. This latent space of the training set is then used to optimize the parameters of a RIDGE classifier (Hoerl and Kennard, 1970). A unique feature of ROCKET, compared to other classifiers, is that it is entirely independent of the training dataset during its feature extraction phase, with its parameters being randomly generated. ROCKET’s computational runtime is significantly smaller than that of other state-of-the-art classifiers, and it has consistently been one of the top-performing models in the literature across widely used community benchmarks (Dau et al., 2019; Bagnall et al., 2018).

1.2.1.3.2 MiniROCKET & MultiROCKET The same authors of ROCKET (Dempster, Petitjean, and Webb, 2020) proposed in 2021 a new version called MiniROCKET (Dempster, Schmidt, and Webb, 2021) that is almost a deterministic version of the original model in order to reduce its randomness and add some dependency with the input data. The key differences between ROCKET and MiniROCKET can be summarized in the following:

1. MiniROCKET fixed the length of the filters to 9
2. MiniROCKET randomly generates the values of the filters from a discrete set of values $\{-1, 2\}$ instead of using a Gaussian distribution
3. MiniROCKET drops the maximum aggregation and utilizes only the PPV
4. MiniROCKET samples the bias values from the quantiles of the convolution output, making it dependent on the training data
5. MiniROCKET fixed the number of possible dilation rates from 1 to $\log_2\left(\frac{L-1}{K-1}\right)$ where L is the time series length and K the kernel length.

MiniROCKET highlights that by reducing the degree of freedom of ROCKET, than both the accuracy and efficiency can increase.

The same group proposed MultiROCKET in the following years in (Tan et al., 2022), that utilizes the MiniROCKET setup however it applies the transformation over the original time series and its first order derivative. MultiROCKET does not rely only on the PPV features however it produces three new features:

1. Mean of Positive Values (MPV) that averages the positive values of the convolution output
2. Mean of Indices of Positive Values (MIPV) that averages the indices of the positive values of the convolution output

3. Longest Stretch of Positive Values (LSPV) that finds the length of the longest subsequences containing positive consecutive values in the convolution output

MultiROCKET adds some computation complexity to MiniROCKET, however it achieved state-of-the-art results over the UCR archive for the TSC task in 2022.

1.2.1.3.3 Hybrid Dictionary-Rocket Architecture In 2023, a new adaptation of ROCKET based framework was proposed in (Dempster, Schmidt, and Webb, 2023a) called HYDRA. Unlike ROCKET, HYDRA does not rely on the actual output activation of the filter, instead it leverages over how many times a convolution kernel is activated the most between a set of kernels. In other words, HYDRA randomly defines a set of kernels, called group and applies the convolution such as in ROCKET followed by assigning each kernel in this group the number of time stamps it is activated the most in the group. HYDRA employs \mathcal{G} groups with \mathcal{K} kernels in each group, resulting in an output feature space of dimension $\mathcal{G} \times \mathcal{K}$ containing integer values. This feature space is subsequently used to train a RIDGE classifier (Hoerl and Kennard, 1970). (Dempster, Schmidt, and Webb, 2023a) concluded that by combining the feature space of HYDRA with the feature space of MultiROCKET, resulting in HydraMR (HYDRA-MultiROCKET), achieves state-of-the-art performance for the task of TSC on the UCR archive (Dau et al., 2019).

HydraMR is currently one of the state-of-the-art models for TSC, not only in convolution based methods, but overall as well.

1.2.1.4 Shapelet Based Methods

Shapelet-based time series classification methods focus on identifying and using small, discriminative subsequences, known as shapelets, to distinguish between different classes. These methods extract shapelets that capture local patterns highly indicative of the target class, providing interpretable and precise models. This approach is particularly useful in applications like medical diagnosis, where specific patterns in data can be crucial for accurate classification. Shapelet-based classifiers are valued for their robustness and interpretability, making them a powerful tool in time series analysis.

Shapelets were first introduced in (Ye and Keogh, 2009; Ye and Keogh, 2011) as discriminative subsequences used within decision tree classifiers for time series classification. Since then, the research community in TSC has extensively developed and expanded this concept, leading to a variety of advanced algorithms and applications that leverage shapelets for improved accuracy, interpretability, and computational efficiency.

1.2.1.4.1 Shapelet Transform Classifier (STC) The STC (Hills et al., 2014) is a two steps classifier. First the model searches for shapelets in the set of training samples and transforms the series to a vector of distances between the shapelet and a set of other shapelets from the series itself. Second, a decision tree classifier is trained on top of the transformed space of the series.

1.2.1.4.2 Random Dilated Shapelet Transform (RDST) The RDST model (Guillaume, Vrain, and Elloumi, 2022), motivated by ROCKET (Dempster, Petitjean, and Webb, 2020), leverages from the randomness techniques to select the shapelets from the training samples. Instead of learning the shapelets, RDST randomly selects a high number of shapelets from the training data. Similar to convolution based methods, RDST employs the dilation technique to enrich the shapelet

transform. The transformed space of RDST is then used to train a RIDGE classifier (Hoerl and Kennard, 1970).

Currently, RDST is still the state-of-the-art shapelet based methods for TSC evaluated on the UCR archive.

1.2.1.5 Dictionary Based Methods

This approach of solving TSC is based on finding discriminative patterns in the time series and counting the number of times it was repeated, followed by using this information to train a classifier. The patterns detected are not from the raw input, instead the time series is transformed first into a discrete space using a symbolic transformation. A very famous symbolic transformation proposed in (Lin et al., 2007) called Symbolic Aggregate approxImation (SAX) defines a set of discrete symbols that represent a segment of the time series. SAX employs this symbolic transformation as follows:

- **First**, each time series \mathbf{x} , supposing being univariate, of length L is z-normalized to have a zero mean and unit standard deviation.
- **Second**, the time series is divided into non-overlapping segments of length l each: $\{\mathbf{x}[(t-1).l : t.l]\}_{t=1}^{\lfloor L/l \rfloor}$
- **Third**, each segment is replaced by its mean value following the Piecewise Aggregate Approximation (PAA) (Keogh et al., 2001) dimensionality reduction technique to obtain: $\{p_t = \text{mean}(\mathbf{x}[(t-1).l : t.l])\}_{t=1}^{\lfloor L/l \rfloor}$
- **Fourth**, the dictionary of symbols $\mathcal{D}_{ict} = \{s_1, s_2, \dots, s_\alpha\}$ is defined for specific number of alphabet α (a SAX hyper-parameter) using the percent point function of the standard Gaussian distribution to obtain $\alpha - 1$ breakpoints $\{b_j\}_{j=1}^{\alpha-1}$
- **Finally**, for each segment $\mathbf{x}[(t-1).l : t.l]$ for $i \in [1, \lfloor L/l \rfloor]$ replaced by its mean value, a one-to-one mapping function is used to choose the replacement symbol from the dictionary as follows:

$$SAX(p_i) = \begin{cases} s_1 & \text{if } -\infty < p_i \leq b_1 \\ s_2 & \text{if } b_1 < p_i \leq b_2 \\ \dots & \\ s_\alpha & \text{if } b_{\alpha-1} < p_i < +\infty \end{cases} \quad (1.11)$$

The above steps can be applied in the same way on MTS data, by going through each dimension independently. The core idea of SAX is simply representing each segment of the series by a discrete symbol to form a word (sequence of symbols) that is chosen following the Gaussian distribution, this is argued by the authors in (Lin et al., 2007) by saying "... *normalized time series have a Gaussian distribution*". This symbolic representation was then used for classification in (Senin and Malinchik, 2013) with the first dictionary based classifier for time series, called SAX Vector Space Model (SAX-VSM). SAX-VSM begins by generating the Symbolic Aggregate approxImation (SAX) representation for all time series within each class, while also preserving the frequency of the symbol sequences. When presented with a new, unlabeled time series, it undergoes SAX transformation to obtain its symbolic sequence. Then, by comparing the frequencies derived from the precomputed set of

symbol sequences, the unlabeled series is assigned to the class that best matches its sequence frequencies.

In (Schäfer and Höggqvist, 2012), the authors proposed a novel version, six years after the breakthrough of SAX, called the Symbolic Fourier Approximation (SFA). First, SFA decomposes the series into segments and then z-normalize the sub-sequences instead of normalizing them prior to the decomposition. Second, SFA utilizes the Discrete Fourier Transform as a dimensionality reduction technique instead of PAA (Keogh et al., 2001). Third, SFA uses a binning technique proposed in (Schäfer and Höggqvist, 2012) called Multiple Coefficient Binning (MCB) that is based on the distributions of real and imaginary values of the Fourier Transform. Finally, Those distributions go through the binning mechanism to generate the symbols.

1.2.1.5.1 Bag-of-SFA-Symbols (BOSS) In (Schäfer, 2015), the authors proposed a novel approach for dictionary based TSC called BOSS that utilizes on SFA. BOSS applies the SFA transformation on overlapping windows of the time series instead of considering the whole time series at once. This results in a sequence of words for each series instead of producing a sequence of symbol (one word only). A BOSS classifier utilizes a non-symmetric distance in the setup of a NN classifier, and multiple BOSS classifiers are finally ensembled to form the final BOSS model. Until 2015, BOSS was the state-of-the-art dictionary based method for TSC evaluated on the UCR archive.

1.2.1.5.2 Word Extraction for Time Series Classification (WEASEL1.0 and WEASEL2.0) WEASEL1.0 is a novel dictionary based model proposed in (Schäfer and Leser, 2017) for TSC, that in contrary to BOSS, its goal is to identify meaningful words in the output transformation of SFA. This is done by applying the transformation using SFA on a large set of possible parameters, followed by a Chi-squared test to identify the words that have the highest power and discard the words that have a power lower than a specified threshold. The output space is then used to train a RIDGE classifier (Hoerl and Kennard, 1970).

Although WEASEL1.0 have seen to outperform BOSS on the UCR archive, it still however suffer from the dimensionality curse and runtime curse because of the large grid search space. The same authors (Schäfer and Leser, 2023) proposed a new version denoted by WEASEL2.0 that utilizes the randomness technique of ROCKET and randomly generate a set of parameters for the SFA transformation thus controlling the searching space. WEASEL2.0 sets a random dilation rate as well for the windowing phase of the workflow, motivated from the impact of dilation on the ROCKET transformation. WEASEL2.0 became the state-of-the-art dictionary based method for TSC in terms of both accuracy and efficiency.

1.2.1.6 Interval Based Methods

Interval based methods, first proposed in (Deng et al., 2013) as an RF (Breiman, 2001) based classifier, is a technique of ensembling different classifiers trained on different transformations of extracted intervals from the time series samples. Most approaches randomly generate the intervals' bounds that are used throughout all the samples in the dataset. The motivation of using such technique instead of feature based methods where the transformation is done over all the series at the same time, is to avoid noisy features that will lead in miss-classification and confusing the classifier.

1.2.1.6.1 Time Series Forest (TSF) The TSF (Deng et al., 2013) model employs for each decision tree \sqrt{L} intervals, where L is the time series length, of randomly selected bounds. For each of the selected intervals, TSF extracts the mean, variance and slope and concatenate them into one feature vector that is then used to build the decision tree. All the decision trees are then ensembled through a voting mechanism to form the TSF classifier.

1.2.1.6.2 Canonical Interval Forest and Diverse Representation Canonical Interval Forest (CIF and DrCIF) Similar to TSF (Deng et al., 2013), CIF (Middlehurst, Large, and Bagnall, 2020) is an ensemble of decision tree classifiers, however it utilizes the Catch22 features alongside the mean, variance and slope features of TSF. The concatenated vector is then used to build the decision tree. CIF leverages over TSF by being suitable for multivariate time series, as it the number of intervals for each tree is $\sqrt{L} \cdot \sqrt{M}$, where L and M are the length and number of channels of the time series samples respectively. In order to keep the selected intervals in the one-dimensional space, CIF randomly assigns a channel for each of the selected intervals.

In (Middlehurst et al., 2021), the same authors proposed DrCIF by incorporating two new extracted features alongside the ones of CIF: (1) the periodograms to identify and quantify the frequency components present within the time series and (2) the first order derivative.

1.2.1.6.3 QUANT In 2023, the QUANT model, as referenced in (Dempster, Schmidt, and Webb, 2023b), discarded all previously employed features identified through interval based methods. Instead, QUANT relies on quantiles that represent the empirical distribution of the intervals. However, it extracts quantiles over four different representations including the time series itself, the first and second order derivative, the Fourier transform. The choice of the intervals is not random in QUANT, instead it is fixed and dyadic (defined based on the powers of 2). For each interval of length l , QUANT defines sub-intervals of length $l/4$ and extracts two features called quantiles from each sub-interval. These two features are the median of the sub-interval and the median of zero centered sub-interval (mean of the sub-interval is extracted before finding the median). The output features of all intervals are then concatenated representing a new quantized version of the input time series. QUANT utilizes extremely randomized trees (Geurts, Ernst, and Wehenkel, 2006) for the classification task, where the transformed quantized space is used to train the tree based classifier.

In the recent TSC review (Middlehurst, Schäfer, and Bagnall, 2024), it has been shown that QUANT is the current state-of-the-art interval based method for TSC evaluated on the UCR archive (Dau et al., 2019) in both accuracy and efficiency as it is significantly faster than other interval based methods.

1.2.1.7 Hybrid Based Methods

Given that time series data does not have a unified approach to address its classification task, it is most of the time a difficult challenge to choose from the pool of methods. For this reason, hybrid models have been proposed throughout the literature in a way to combine different methods, e.g. distance based and interval based methods.

1.2.1.7.1 Time Series Combination of Heterogeneous and Integrated Embedding Forest (TS-CHIEF) TS-CHIEF (Shifaz et al., 2020) is a tree-based ensemble method where the nodes within each tree perform splits using three distinct feature criteria: distance-based, dictionary-based, and spectral interval-based. The parameters are randomly initialized to ensure diversity within the ensemble. The distance-based splits are derived from the EE(Lines and Bagnall, 2015), the dictionary-based splits are inspired by BOSS(Schäfer, 2015), and the interval-based splits are based on the Random Interval Spectral Ensemble (RISE) (Flynn, Large, and Bagnall, 2019).

1.2.1.7.2 HIVE-COTE1.0 and HIVE-COTE2.0 The HIVE-COTE (HC) method has been developed throughout the years, starting with the Collective Of Transformation-based Ensemble (COTE) (Bagnall et al., 2015) which is an ensemble of 35 time series classifiers of different approaches. This model was developed to the Hierarchical Vote Collective Of Transformation Ensemble (HIVE-COTE) (Lines, Taylor, and Bagnall, 2018) that only utilizes five classifiers and are ensembled through the Cross-validation Accuracy Weighted Probabilistic Ensemble (CAWPE) (Large, Lines, and Bagnall, 2019). HIVE-COTE utilizes a distance based, dictionary based, shapelet based, interval based and spectral based classifiers. However, the distance based model used in HIVE-COTE is computationally expensive, for this reason it was dropped in HIVE-COTE1.0 (Bagnall et al., 2020) and a more performing dictionary based classifiers is used. The most recent HC based model is HIVE-COTE2.0 (Middlehurst et al., 2021) which changed the set of classifiers to more recent ones that are much more performing. A unique feature of HC2 over HC1.0, HC and COTE, is that the classifiers used in its hybrid ensemble are suitable for multivariate datasets. HC2 is currently one of the state-of-the-art models for TSC evaluated over the UCR archive, not only in hybrid based methods, but overall as well.

1.2.1.8 Deep Learning Methods

Although the previously presented methods for TSC are performing well on the available benchmarks (Dau et al., 2019; Bagnall et al., 2018), most of them lack the capability of parallelization of their calculation over GPUs, which can decrease their efficiency. Another critical limitation of most of these classifiers is their lack of explainability, which is increasingly important for understanding model decisions, ensuring transparency, and gaining trust in applications where decision-making is crucial. For these reasons, deep learning methods can be a suitable solution, however we do not claim it should be the only solution for TSC as there are still some models that can achieve better performance compared to deep learning models but are less suitable in terms of scalability.

Deep learning (LeCun, Bengio, and Hinton, 2015) methods leverage over all the previous techniques with the ability of parallelization over multiple GPUs making them much faster during training and inference. Moreover, deep learning methods can conduct two steps including the feature extraction and the classification task at the same time instead of manually constructing the features phase and only training the classifier. Deep learning methods consist on many neural network architectures, such as Convolutional Neural Networks (CNNs), Recurrent Neural Networks (RNNs) and Transformers. However, an extensive review of deep learning methods for TSC has been conducted in (Ismail Fawaz et al., 2019) highlighted that CNNs outperform other architectures.

A deep learning model for TSC consists on applying Λ parametrized layers of different characteristics. Each of the layers λ_i where $i \in [1, \Lambda]$ represents a function f_{λ_i} parametrized by a set of parameters θ_{λ_i} . Each layer λ_i takes as input the output of the previous layer λ_{i-1} and applied a non-linear transformation over it that is controlled by θ_i . Given an input time series \mathbf{x} , feeding to a neural network of Λ layers comes down to the following pipeline:

$$f_{\Lambda}(\theta_{\Lambda}, \mathbf{x}) = f_{\Lambda-1}(\theta_{\Lambda-1}, f_{\Lambda-2}(\theta_{\Lambda-2}, \dots, f_1(\theta_1, \mathbf{x}))) \quad (1.12)$$

The above pipeline is referred to in the community as the feed-forward propagation.

Since the task at hand is classification, the last layer of the deep learning model outputs a probability distribution for each sample belonging to each of the possible classes. The parameters of all the layers are then optimized using the back-propagation algorithm (Rumelhart, Hinton, and Williams, 1986a). In what follows, we present the different types of layers than are used for time series in the literature.

1.2.1.8.1 Types of Layers In this section, we go through some layer types used in the literature's architectures. These layers are based on non-linear transformations that consists on either extracting information, detecting some patterns or combining some features in the time series samples.

Fully Connected (FC) Layers The FC layers are simply a linear transformation followed by applying a non-linear activation such as ReLU, sigmoid etc. This linear transformation is computed using matrix multiplication. For instance, if the input dimension is n and the output dimension is m , then the FC layer consists on weight matrix W of shape (m, n) and the output of the FC layer is computed as follows:

$$\mathbf{o} = \sigma(W \odot \mathbf{x} + \mathbf{b}) \quad (1.13)$$

where \mathbf{x} is the input, \mathbf{o} is the output, W is the transformation matrix, \mathbf{b} is the bias vector of dimension m , $\sigma(\cdot)$ is a non-linear activation function and \odot is the matrix multiplication operation.

This type of layer is almost always used as the last layer in a deep learning model for a classification task while setting the activation function to the softmax function and the output dimension to C , the number of possible classes. This function ensures that the output vector is a probability distribution and each element in the output vector \mathbf{o} is computed as follows:

$$o_c = \frac{e^{W[c, :] \odot \mathbf{x} + b_c}}{\sum_{\tilde{c}=1}^C e^{W[\tilde{c}, :] \odot \mathbf{x} + b_{\tilde{c}}}} \quad (1.14)$$

where o_c is the probability of \mathbf{x} belonging to class $c \in [1, C]$

In order to find the optimal weights of Eq. 1.13 and 1.14, we can use an optimization algorithm to minimize the error in the model's predictions. This error is measured through a loss function, that should be differentiable given that the optimization algorithm is gradient based. The common loss function to be used for the classification tasks is the categorical cross entropy, that measures the difference between two probability distributions, defined as follows on the i_{th} example of the dataset:

$$\mathcal{L}_i(\mathbf{y}_i, \hat{\mathbf{y}}_i) = - \sum_{c=1}^C y_{i,c} \log_2(\hat{y}_{i,c}) \quad (1.15)$$

where C is the total number of classes in the dataset, \mathbf{y}_i is the ground truth label of the i_{th} series, denoted as a one hot encoding, e.g. if the ground truth label is C_2 out of a set $\{C_1, C_2, C_3\}$ then $\mathbf{y}_i = [0, 1, 0]$ representing a discrete deterministic probability distribution. $\hat{\mathbf{y}}_i$ is a vector of length C representing a discrete probability distribution where each element $\hat{y}_{i,c}$ $c \in [1, C]$ is the probability of the i_{th} sample belonging to class c .

The total loss over a batch of N samples is the average loss over all the samples in the batch:

$$\mathcal{L} = \frac{1}{N} \sum_{i=1}^N \mathcal{L}_i(\mathbf{y}_i, \hat{\mathbf{y}}_i) \quad (1.16)$$

In order to update the weights of Eq. 1.13 and 1.14, a gradient based optimizer can be used such as Stochastic Gradient Descent (SGD) as follows:

$$W = W - \alpha \cdot \frac{\partial \mathcal{L}}{\partial W} \quad (1.17)$$

where α is the learning rate hyper-parameter controlling the step size of the optimization algorithm.

In the current literature, deep learning models consist of a very high number of layers on top of each other, in this case, the partial derivative of Eq. 1.17 cannot be calculated. Instead, for the last 20 years, neural networks utilize the derivative chain rule, the core idea of the back-propagation algorithm (Rumelhart, Hinton, and Williams, 1986b).

Convolution Layers The convolution operation, as explained in Eq. 1.7, is applied the same way in a convolution layer, where the optimization algorithm learns the best weights of the convolution kernel. A convolution layer applies \mathcal{K} filters $\{\mathbf{w}\}_{j=1}^{\mathcal{K}}$ of the same length K and same dilation rate over the input time series. If the input time series is univariate \mathbf{x} of length L , the output of the convolution layer is a multivariate time series computed as follows:

$$\mathbf{o} = \text{concat}(\{\mathbf{x} * \mathbf{w}_j\}_{j=1}^{\mathcal{K}}) \quad (1.18)$$

where *concat* is the concatenation operation and \mathbf{o} is a multivariate time series of \mathcal{K} dimensions with length $L - K + 1$ each.

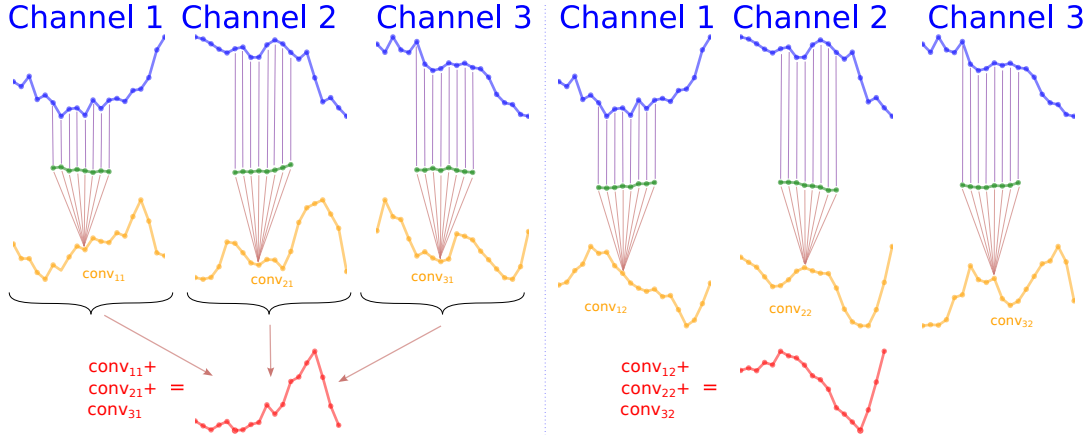
In the case \mathbf{x} is a multivariate time series of M channels of length L each, and the target output dimension is \mathcal{K} (the chosen number of filters), then in reality, the number of filters to learn is $M \cdot \mathcal{K}$. This is done by simply learn M filters, one for each of the input dimensions and summing the output. This is repeated \mathcal{K} times and the output sums are concatenated to produce the output MTS \mathbf{o} . The mathematical formulation of the above operation is defined as follows:

$$\mathbf{o} = \text{concat}(\{\sum_{m=1}^M \mathbf{x}^m * \mathbf{w}_{m,j}\}_{j=1}^{\mathcal{K}}) \quad (1.19)$$

where the above summation in Eq. 1.19 is over the temporal axis of all the series inside the sum, producing after each summation a univariate time series.

This type of convolution layer is referred to in the rest of this work as Standard Convolution (SC) layer. A visualization of the SC layer with a chosen number of filters set to 2 with a kernel size of 8 is presented in Figure 1.4 applied on an input

FIGURE 1.4: Standard Convolution applied on a multivariate input time series of dimensions 3, convoluted with two times with three different convolutional filters, producing a convolutional output per filter, that are then summed together to produce two final outputs. The convolution operation starts with an element wise multiplication followed by a summation operation.



MTS of dimension 3. It can be seen from this figure that the total number of filters to learn is 6 instead of 2 (the chosen output dimension).

DepthWise Separable Convolution (DWSC) First used for image classification in MobileNets (Howard et al., 2017), this type of convolution layer has a unique feature of having a very low number of trainable parameters. DWSCs are in fact a pipeline made of two different convolution layers: (1) DepthWise Convolution (DWC) followed by (2) PointWise Convolution (PWC). DWSC are more common to be used on MTS input data. The DWC layer (first phase of DWSCs) consists on learning M filters where M is the dimension of the input MTS, hence the reason to why DWSCs are commonly used on multivariate input, or else we learn only one filter. For instance, if the input raw MTS \mathbf{x} has M dimensions of length L , applying a DWC layer with kernel size K is defined as follows:

$$\mathbf{o} = \text{concat}(\{\mathbf{x}^m * \mathbf{w}_m\}_{m=1}^M) \quad (1.20)$$

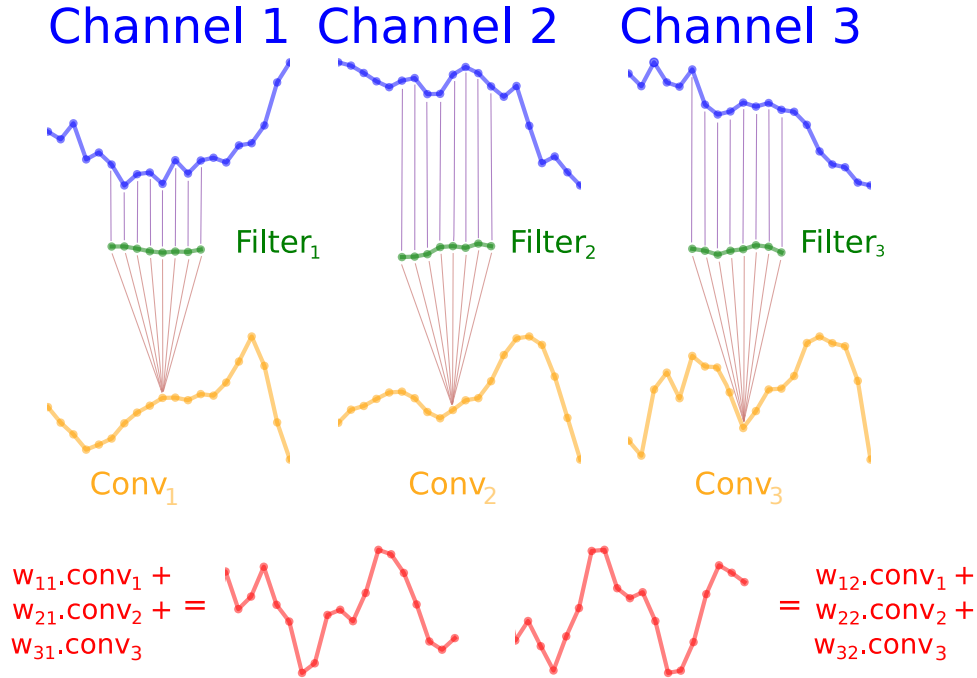
where \mathbf{o} is the output of the DWC layer, also with M dimensions of length $L - K + 1$

The PWC layer, also referred to as bottleneck layer, consists on a change of dimensionality through a standard convolution layer with a kernel size of 1. Applying a PWC layer with target dimension \mathcal{K} on an input MTS \mathbf{x} of M dimensions of length L is defined as follows:

$$\mathbf{o} = \text{concat}\left(\left\{\sum_{m=1}^M \mathbf{x}^m \cdot w_{m,j}\right\}_{j=1}^{\mathcal{K}}\right) \quad (1.21)$$

where $W = \{\{w_{m,j}\}_{m=1}^M\}_{j=1}^{\mathcal{K}}$ is a two-dimensional matrix of real values and \mathbf{o} is the output of the PWC layer with the same length as the input and \mathcal{K} dimensions.

FIGURE 1.5: DepthWise Separable convolution multivariate input time series of dimensions 3, convoluted one time with three different convolutional filters, producing a convolutional output per filter, that go through a weighted summed to produce two final outputs. The convolution operation starts with an element wise multiplication followed by a summation operation.



Finally, the pipeline of DWSC layer of kernel size K and target dimension \mathcal{K} applied on an input MTS \mathbf{x} of M dimensions of length L can be defined as follows:

$$\mathbf{o} = \text{concat}\left(\left\{\sum_{m=1}^M \text{concat}\left(\{\mathbf{x}^m * \mathbf{w}_m\}_{m=1}^M\right)^m \cdot w_{m,j}\right\}_{j=1}^{\mathcal{K}}\right) \quad (1.22)$$

where $\{\mathbf{w}_m\}_{m=1}^M$ is a set of convolution kernels of length K each and $\{\{w_{m,j}\}_{m=1}^M\}_{j=1}^{\mathcal{K}}$ is a set of real values and \mathbf{o} is the output of the DWSC layer with \mathcal{K} dimensions of length $L - K + 1$.

A visualization of the DWSC layer with a chosen number of target dimension set to 2 with a kernel size of 8 is presented in Figure 1.5 applied on an input MTS of dimension 3. It can be seen from this figure that the total number of filters to learn is 3 instead of 6 (SC layer) with additional 6 real values to learn (the chosen output dimension).

The total number of parameters learned by an SC and DWSC layers are $M \cdot \mathcal{K} \cdot K$ and $M \cdot K + M \cdot \mathcal{K}$ respectively.

Residual Connections Deep learning models sometimes suffer from a common issue referred to as the vanishing gradient. This issue is more common when the network's depth gets higher, resulting in a very deep model, and during the backward phase of the optimization, the gradient may become zero. To avoid this issue, the authors in (He et al., 2016) proposed the residual connections, where instead of having

one branch, the network gets divided into two branches. The first branch serves as the encoding and feature extraction, and the second serves as the skip branch, where it simply uses an almost identity like function. Both branches meet after a specific number of layers in an element-wise addition operation, resulting in what follows at layer λ_l :

$$f_l(\theta_l, g_{l-1}) = f_{1,l}(\theta_{1,l}, g_{l-1}) + f_{2,l}(\theta_{2,l}, g_{l-1}) \quad (1.23)$$

where g_{l-1} is the output of the $l - 1$ th layer, $f_{1,l}$ is an identity like function with parameters $\theta_{1,l}$, and $f_{2,l}$ is a stack of layers with parameters $\theta_{2,l}$.

Batch Normalization Batch Normalization (BN) is a technique used to improve the training speed and stability of neural networks by normalizing the inputs of each layer to have a mean of zero and a standard deviation of one. This is necessary in order to reduce the chance of gradient exploding due to different range of values in the features going from one layer to another. This is done by calculating the mean and variance of the inputs within each mini-batch during training and then scaling and shifting the inputs based on these statistics. In the context of time series analysis, especially when used after 1D convolution layers, batch normalization can be particularly beneficial. Since 1D convolution layers are often used to extract temporal features from the time series data, the distribution of features across different time steps may vary significantly.

Similar to other neural network layers, BN has two trainable parameters, called γ and β . Following the first z-normalization step that produces zero-mean and unit variance features, the BN layer learns how to shift and scale all the features to a new mean and variance. Supposing a batch of B MTS $\{\mathbf{x}_i\}_{i=1}^B$ produced by a convolution layer with M channels of length L , applying the BN layer with parameters $\gamma_1, \gamma_2, \dots, \gamma_M$ and $\beta_1, \beta_2, \dots, \beta_M$ is defined as follows:

$$\mathbf{o}_i = \text{concat}(\{\gamma_m \cdot \frac{\mathbf{x}_i^m - \mu_m}{\sigma_m} + \beta_m\}_{m=1}^M) \quad (1.24)$$

where $\{\mathbf{o}_i\}_{i=1}^B$ is a set of MTS of same shape as \mathbf{x}_i , μ_m is the average of the channel m of all samples in the batch over the temporal axis, and σ_m is its standard deviation.

Moreover, the BN layer also has two non-trainable parameters called μ_{mov} and β_{mov} which contains a moving average of the mean and standard deviation of the input data $\boldsymbol{\mu}$ and $\boldsymbol{\sigma}$, for each dimension separately. These two non-trainable are then used during inference to scale the features of new unseen samples. These two parameters are calculated during training as follows:

$$\mu_{mov} = \text{concat}(\{\alpha_{BN} \cdot \mu_{mov_m} + (1 - \alpha_{BN}) \cdot \mu_m\}_{m=1}^M) \quad (1.25)$$

$$\beta_{mov} = \text{concat}(\{\alpha_{BN} \cdot \beta_{mov_m} + (1 - \alpha_{BN}) \cdot \beta_m\}_{m=1}^M) \quad (1.26)$$

where α_{BN} is the moving average parameter and $0 < \alpha_{BN} < 1$.

Local Pooling (Max and Average) Pooling operations have been shown to be very effective for images throughout the years ever since the birth of deep learning (LeCun, Bengio, and Hinton, 2015). The motivation of doing local pooling operations is to reduce dimensionality resulting in a focus on more local important features extracted by the network.

There exist many local pooling layers, however two types are more common in the time series classification literature, the first being max pooling and the second being average pooling. For the max pooling layer, such as for convolution layers,

a kernel is defined with a specific length, however in this case the kernel does not have any trainable weights. Instead, the kernel slides over the temporal axis of the series, and the values seen by the kernel are replaced by their maximum value. The operation done by the max pooling layer with kernel size K is defined below on an input univariate series \mathbf{x} of dimensions (L) :

$$o_t = \max(x[t : t + k]) \quad (1.27)$$

with $t \in [1, L - K + 1]$ and $\mathbf{o} = \{o_1, o_2, \dots, o_{L-K+1}\}$ is a univariate series with length $L - K + 1$.

The average pooling layer is defined in the same way as the max pooling, however instead of choosing the maximum between the values seen by the kernel, the average value replaces them. The operation done by the average pooling layer with kernel size K is defined below on an input univariate series \mathbf{x} of dimensions (L) :

$$o_t = \frac{1}{K} \sum_{k=1}^K x[t : t + k] \quad (1.28)$$

with $t \in [1, L - K + 1]$ and $\mathbf{o} = \{o_1, o_2, \dots, o_{L-K+1}\}$ is a univariate series with length $L - K + 1$.

Similar to convolution layers, max and average pooling layers can both be applied on MTS, however in this case the operation is applied on each channel independently and the output dimension will be the same as the input. Moreover, dilation rates can also be used for local pooling layers similar to convolutions, see Eq. 1.8.

It is important to note, that by default all local pooling layers utilize a stride equals to the kernel size, unless specified to use another stride. The above output length calculations $(L - K + 1)$ is in the case where strides are set to 1, however in default mode, the output length is $\lceil \frac{L - K + 1}{K} \rceil$.

Global Pooling (Max and Average) Global pooling is a powerful technique often employed in neural network architectures for dimensionality reduction and feature summary. Unlike local pooling, which focuses on local features within specific regions, global pooling computes the summary of feature maps across the entire spatial dimensions, providing a global perspective of the input data.

Similar to local pooling, two main global pooling layers are used for time series classification in deep learning models, the first being Global Max Pooling (GMP) and the second being Global Average Pooling (GAP). In the case of time series, the global pooling layers are mostly used posterior to all the feature extraction layers.

The GMP layer receives an input dimension of (L, M) , where L is the length of the series and M is its dimensions, and outputs a vector, per series, of dimension $(M,)$, where each point of the vector is the maximum value over all the time axis of each dimension. We define below the GMP operation over an input time series \mathbf{x} of dimension (L, M) :

$$\mathbf{v} = \text{concat}(\{\max(\mathbf{x}^m[1 : L])\}_{m=1}^M) \quad (1.29)$$

where $\mathbf{v} = \{v_1, v_2, \dots, v_M\}$ is a vector of dimension $(M,)$.

Similar to the GMP layer, the GAP layer receives the same input dimension and outputs a vector \mathbf{v} also of dimension $(M,)$, however each point of the vector is the average value over the time axis of each dimension. In simpler ways, we define in what follows the operation done in the GAP layer over a series \mathbf{x} of dimensions (L, M) :

$$\mathbf{v} = \text{concat}\left(\left\{\frac{1}{L} \sum_{t=1}^L x_t^m\right\}_{m=1}^M\right) \quad (1.30)$$

where $\mathbf{v} = \{v_1, v_2, \dots, v_M\}$ is a vector of dimension $(M,)$.

As mentioned above, global pooling layers are used at the last feature extraction step of the network, this is because it can be now fed to an FC layer (see Eq. 1.13) with a softmax activation for the classification task.

Temporal Self-Attention The Self-Attention mechanism has shown to have a significant impact in Natural Language Processing (NLP) ever since the birth of Transformers for language translation in the paper *Attention Is All You Need* (Vaswani et al., 2017). The Self-Attention mechanism, adapted from the original Attention mechanism (Bahdanau, Cho, and Bengio, 2014), allows the model to learn about the dependency between features spread along a temporal axis. This information is then used to transform the input features into a new space that is more compact and contains denser information about important features.

To explain how does the Self-Attention layer is able to do the operation mentioned above, we will assume again an input time series \mathbf{x} of shape (L, M) , supposing that this time series is actually the output of previous feature extraction layers such as CNNs. We detail below each step of the Self-Attention mechanism:

First, Self-Attention mechanism has a unique feature of being order invariant, for this reason we use Positional Encoders (PEs) to add position information to each element in the sequence. Sinusoidal functions generate these encoding, which are added (element-wise) to the input embeddings, ensuring the model can use the sequence order. The PE for position $pos \in [1, L]$:

$$PE_{(pos, 2k)} = \sin\left(\frac{pos}{w_k}\right) \quad (1.31)$$

$$PE_{(pos, 2k+1)} = \cos\left(\frac{pos}{w_k}\right) \quad (1.32)$$

where $k \in [0, \frac{d_{model}}{2}]$, the frequency $w_k = 10000^{2k/d_{model}}$ and d_{model} is the dimension of the embeddings.

These encoding ensure the sequence includes both content and positional information. This type of PE is commonly referred to in the literature as Absolute Positional Encoding (APE).

Second, the Self-Attention layers transforms each time stamp of the input time series \mathbf{x} from dimension M to dimension d_{model} , a hyper-parameter of the Self-Attention layer. This first step is done three times independently to produce three different representations of the input series, referred to as: (1) Query \mathbf{Q} , (2) Key \mathbf{K} and (3) Value \mathbf{V} . The Query and Key are used to find the dependency information between time stamps in \mathbf{x} , for which this information is then used to transform the Value to a new more compact space. This is done by simply defining three FC layers (see Eq. 1.13) with weight matrices $W_{\mathbf{Q}}$, $W_{\mathbf{K}}$ and $W_{\mathbf{V}}$, for the Query, Key and Value respectively of shape (M, d_{model}) each. The three matrices are used to transform each time stamp of \mathbf{x} to a new space of different dimensions, as defined below to produce \mathbf{Q} , \mathbf{K} and \mathbf{V} of shape (L, d_{model}) each:

$$\mathbf{Q} = \text{concat}_{temporal\ axis}(\{\mathbf{x}_t \circ W_{\mathbf{Q}}\}_{t=1}^L) \quad (1.33)$$

$$\mathbf{K} = \text{concat}_{\text{temporal axis}}(\{\mathbf{x}_t \circ W_{\mathbf{K}}\}_{t=1}^L) \quad (1.34)$$

$$\mathbf{V} = \text{concat}_{\text{temporal axis}}(\{\mathbf{x}_t \circ W_{\mathbf{V}}\}_{t=1}^L) \quad (1.35)$$

where the concatenation is over the temporal axis and the matrix multiplication \circ is over the dimension axis.

Third, given that both \mathbf{Q} and \mathbf{V} are different representations but of the same input sequence \mathbf{x} , the Self-Attention layer utilizes these two sequences in order to find dependency information between each time stamp and all the other time stamps. This is done by calculating the attention score matrix as follows:

$$\text{Att} = \text{soft max}\left(\frac{Q \circ K^T}{\sqrt{d_{\text{model}}}}\right) \quad (1.36)$$

where Att is called the attention score matrix of shape (L, L) and the *soft max* operation is performed over the column's axis, producing per row a probability distribution how much the row time stamp is correlated with all the column time stamps. The scaling factor $1/\sqrt{d_{\text{model}}}$ is utilized to avoid high values produced in the dot products, resulting in values close to the *soft max* limits where the gradient can be very small.

Fourth, the above attention matrix Att is then used to transform the sequence \mathbf{V} into a new representation, making the output sequence more compact in terms of dependency information between time stamps. The transformed sequence goes through a dimension change using another FC layer with weight matrix W_{\circ} with shape (d_{model}, M) to change back to the original dimension of \mathbf{x} :

$$\mathbf{o} = (\text{Att} \circ \mathbf{V}) \circ W_{\circ} \quad (1.37)$$

where \mathbf{o} has the same dimension as \mathbf{x} .

It is common to use the concept of multi-head attention, where the same procedure described above is repeated independently H times (in parallel), where H is the number of heads. The outputs of each head are finally concatenated and the final transformation matrix W_{\circ} is used on the concatenated transformations of all heads.

Recurrent Layers Recurrent Neural Networks (RNNs) (Elman, 1990) are specialized neural networks designed for processing sequential data. They maintain a hidden state that captures information from previous inputs, making them ideal for tasks like language modeling, speech recognition (Graves, Mohamed, and Hinton, 2013), and sequence-to-sequence learning (Sutskever, Vinyals, and Le, 2014) RNNs are effective at learning patterns and dependencies in sequences, leveraging their ability to remember context over time.

There exists three different recurrent layers that have been proposed during the last three decades: (1) Simple RNN (Elman, 1990), (2) Long Short-Term Memory (LSTM) (Hochreiter and Schmidhuber, 1997) and Gated Recurrent Unit (GRU) (Cho et al., 2014). In what follows, we present each of these layers briefly with their mathematical formulation.

1. **Elman Recurrent Neural Network (Simple RNN)**, proposed in (Elman, 1990), is one of the simplest forms of RNNs. It consists of a single hidden layer that maintains a recurrent connection to itself, allowing it to capture sequential dependencies. For an input time series \mathbf{x} of length L and dimension M , applying once recurrence step t where $t \in [1, L]$ using the Simple RNN is defined as:

$$\mathbf{h}_t = \sigma(W_{hx} \circ \mathbf{x}_t + W_{hh} \circ \mathbf{h}_{t-1} + \mathbf{b}_h) \quad (1.38)$$

$$\mathbf{o}_t = \sigma(W_{oh} \circ \mathbf{h}_t + \mathbf{b}_o) \quad (1.39)$$

where \mathbf{h}_t is the hidden state of time stamp t of dimension $d_{hidden} \neq M$, W_{hx} is the input-to-hidden transformation matrix of shape (d_{hidden}, M) , W_{hh} is the hidden-to-hidden transformation matrix of shape (d_{hidden}, d_{hidden}) , b_h is the hidden layer bias vector of dimension d_{hidden} , W_{oh} is the hidden-to-output transformation matrix of shape (M, d_{hidden}) , \mathbf{b}_o is the output bias vector of dimension M , σ is the activation function commonly a sigmoid or hyperbolic tangent function and \mathbf{o} is the output series of length L and dimension M

2. **Long Short-Term Memory (LSTM)**, proposed in (Hochreiter and Schmidhuber, 1997), addresses the vanishing gradient problem faced by traditional RNNs, enabling them to capture long-range dependencies more effectively. LSTM introduces a gating mechanism that regulates the flow of information, allowing the network to selectively remember or forget information over time. The mathematical formulation of the LSTM layer is defined as follows:

$$\mathbf{f}_t = \text{sigmoid}(W_f \circ \text{concat}(\mathbf{h}_{t-1}, \mathbf{x}_t) + \mathbf{b}_f) \quad (1.40)$$

$$\mathbf{e}_t = \text{sigmoid}(W_e \circ \text{concat}(\mathbf{h}_{t-1}, \mathbf{x}_t) + \mathbf{b}_e) \quad (1.41)$$

$$\mathbf{o}_t = \text{sigmoid}(W_o \circ \text{concat}(\mathbf{h}_{t-1}, \mathbf{x}_t) + \mathbf{b}_o) \quad (1.42)$$

$$\tilde{\mathbf{C}}_t = \tanh(W_C \circ \text{concat}(\mathbf{h}_{t-1}, \mathbf{x}_t) + \mathbf{b}_C) \quad (1.43)$$

$$\mathbf{C}_t = \mathbf{f}_t \odot \mathbf{C}_{t-1} + \mathbf{e}_t \odot \tilde{\mathbf{C}}_t \quad (1.44)$$

$$\mathbf{h}_t = \mathbf{o}_t \odot \tanh(\mathbf{C}_t) \quad (1.45)$$

where \mathbf{h}_t , is the hidden state vector of dimension d_{hidden} , \mathbf{f}_t , \mathbf{e}_t and \mathbf{o}_t are the forget, input and output gates vectors respectively of dimension d_{hidden} with W_f , W_e , W_o as their respective transformation matrices of shape $(d_{hidden}, M + d_{hidden})$ each and \mathbf{b}_f , \mathbf{b}_e , \mathbf{b}_o their respective bias vectors of dimension d_{hidden} each. $\tilde{\mathbf{C}}_i$ is the candidate cell state vector, \mathbf{C}_i is the cell state vector both of dimension d_{hidden} and finally W_C is the state cell candidate transformation matrix of shape (d_{hidden}, M) and \mathbf{b}_C is the cell state bias vector of dimension d_{hidden} . \odot denotes element-wise and \circ denotes the matrix multiplication operation.

3. **Gated Recurrent Unit (GRU)**, proposed in (Cho et al., 2014), is a variation of the LSTM network that simplifies its architecture while maintaining comparable performance. The GRU combines the forget and input gates into a single update gate, reducing the number of parameters and computational complexity. The mathematical formulation of the GRU layer is defined as follows:

$$\mathbf{z}_t = \sigma(W_z \circ \text{concat}(\mathbf{h}_{t-1}, \mathbf{x}_t) + \mathbf{b}_z) \quad (1.46)$$

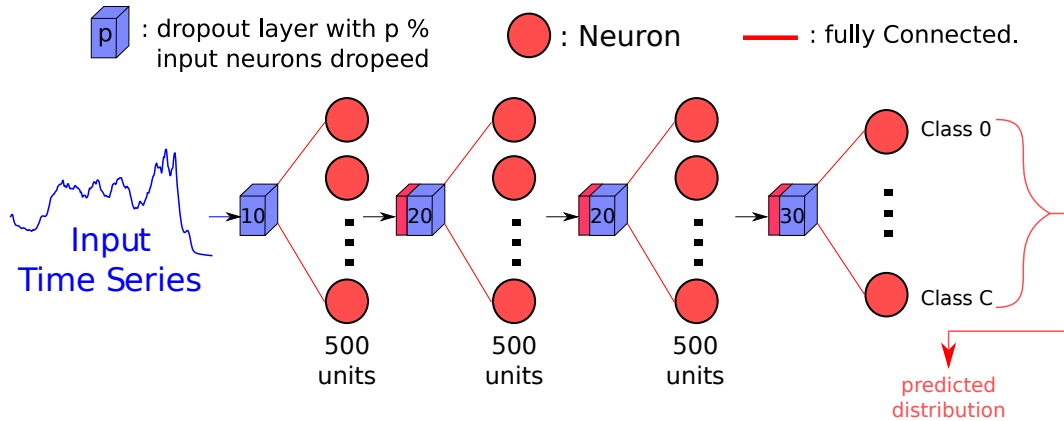
$$\mathbf{r}_t = \sigma(W_r \circ \text{concat}(\mathbf{h}_{t-1}, \mathbf{x}_t) + \mathbf{b}_r) \quad (1.47)$$

$$\tilde{\mathbf{h}}_t = \tanh(W_h \circ \text{concat}(\mathbf{r}_t \odot \mathbf{h}_{t-1}, \mathbf{x}_t) + \mathbf{b}_h) \quad (1.48)$$

$$\mathbf{h}_t = (\mathbf{1}_{d_{hidden}} - \mathbf{z}_t) \odot \mathbf{h}_{t-1} + \mathbf{z}_t \odot \tilde{\mathbf{h}}_t \quad (1.49)$$

where \mathbf{z}_t and \mathbf{r}_t are the update and reset gates respectively, $\tilde{\mathbf{h}}_t$ is the candidate activation, and \mathbf{h}_t is the hidden state, of dimension d_{hidden} . \odot denotes element-wise and \circ denotes the matrix multiplication operation. W_z , W_r , and W_h are weight matrices of shape $(d_{hidden}, M + d_{hidden})$, and \mathbf{b}_z , \mathbf{b}_r , and \mathbf{b}_h are

FIGURE 1.6: The MultiLayer Perceptron (MLP) architecture (Wang, Yan, and Oates, 2017) for Time Series Classification.

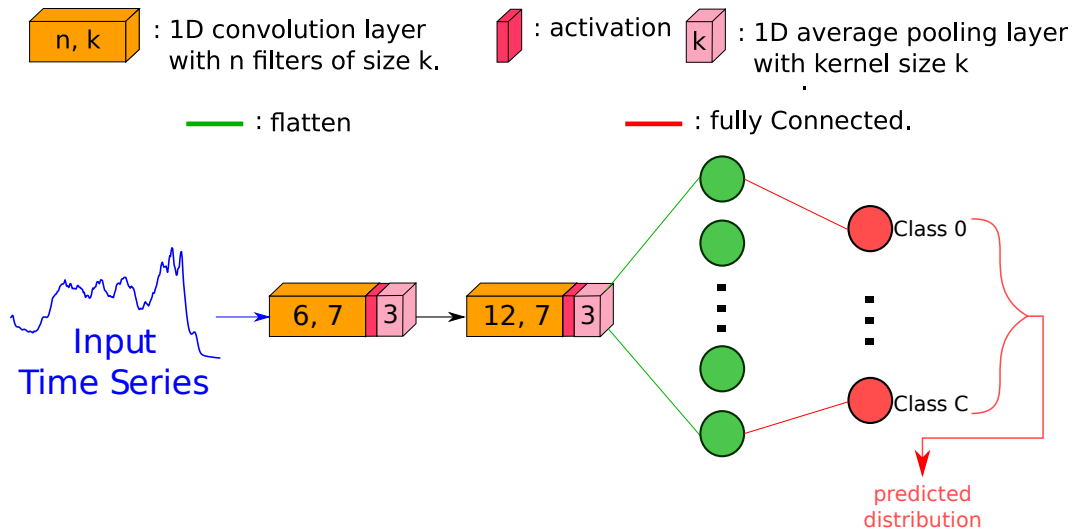


bias terms of dimension d_{hidden} . $\mathbf{1}_{d_{hidden}}$ is a column vector of 1s of dimension d_{hidden} .

1.2.1.8.2 Different Neural Network Architectures for Time Series Classification During the last decade, a significant amount of architectures has been proposed addressing the task of TSC. A detailed benchmark paper (Ismail Fawaz et al., 2019) questioned the need of a fair comparison between most of these architectures over all the datasets of the UCR/UEA archives (Dau et al., 2019; Bagnall et al., 2018). Their choice of architectures to include in the benchmark depended on their ability to reproduce the model from scratch. This benchmark, on some level, became a starting point of addressing TSC tasks with deep learning methods. In this section, we present some architectures used in this benchmark (Ismail Fawaz et al., 2019) as well as new architectures proposed for both univariate and multivariate TSC ever since 2019 (the publication year of the benchmark).

Multi Layer Perceptron (MLP) The concept of Multilayer Perceptrons (MLPs) originated from the field of artificial neural networks, where they were developed as a class of feedforward neural networks consisting of multiple layers of nodes (Minsky and Papert, 1969). Researchers began exploring the application of MLPs to time series classification due to their ability to model complex relationships between input features. The authors in (Wang, Yan, and Oates, 2017) proposed an MLP architecture, presented in Figure 1.6, for TSC. The architecture is made of three hidden FC layers each followed by a ReLU activation function and a Dropout layer. Dropout layers simply uses a random $p\%$ of the input neurons and set them to zero and scale the non-dropped input neurons by $\frac{1}{1-p}$, used to avoid overfitting the model on training data, where p is the drop rate parameter. The last Dropout layer's output is then fed to an FC layer for the classification task, see Figure 1.6 for a detailed view on the parameters of the MLP architecture. However, a significant limitation of MLPs in this context is their inability to effectively capture local temporal dependencies within the data, as they process input data in a fixed manner without considering the sequential nature of time series data. This limitation led to the exploration of other neural network architectures better suited for temporal data, such as Recurrent Neural Networks (RNNs) and Convolutional Neural Networks (CNNs).

FIGURE 1.7: Time-CNN (Zhao et al., 2017) architecture for Time Series Classification.



Time Convolutional Neural Network (TimeCNN) Ever since AlexNet (Krizhevsky, Sutskever, and Hinton, 2012) has been released in 2012 and highlighted the performance of deep CNN models on image classification (Deng et al., 2009), a significant amount of researchers started to wonder on the need to include deep learning into other applications. The authors in (Zhao et al., 2017) proposed a CNN architecture, based on the image classification CNN in (LeCun, Bengio, and Hinton, 2015), on one dimensional temporal data. The architecture, presented in Figure 1.7, consists of two convolution blocks each containing a 1D convolution layer followed by a sigmoid activation function and a local average pooling layer of default strides (see Figure 1.7 for detailed view on the parameters of TimeCNN). Following the second convolution block, the output is an MTS of 7 channels and the length depending on the input time series characteristics. This output MTS is flattened to form a large one dimensional vector that is then fed to an FC layer for the classification task.

Fully Convolutional Network (FCN) The authors in (Wang, Yan, and Oates, 2017) questioned the need of local pooling layers and proposed instead a Fully Convolutional Network (FCN), composed of three convolution blocks, each containing a one dimensional convolution layer followed by a batch normalization layer and a ReLU activation function. The FCN architecture is presented in Figure 1.8 including all the parameter setup proposed in (Wang, Yan, and Oates, 2017). The authors of FCN argues that the replacement of local pooling layers by the batch normalization not only enhances the performance given that local pooling can lose some information, but increases the speed of convergence of the model as well. The convolution layers used in FCN applies a zero-padding on the input, hence the length of the series is preserved throughout the network. This padding operation ensures that the network can detect some patterns on the edges of the series. The FCN architecture feeds the last activation layer to a global pooling layer, specifically a GAP, instead of flattening in order to reduce the number of parameters to learn in the last classification FC layer.

FIGURE 1.8: The Fully Convolutional Network (FCN) (Wang, Yan, and Oates, 2017) architecture for Time Series Classification.

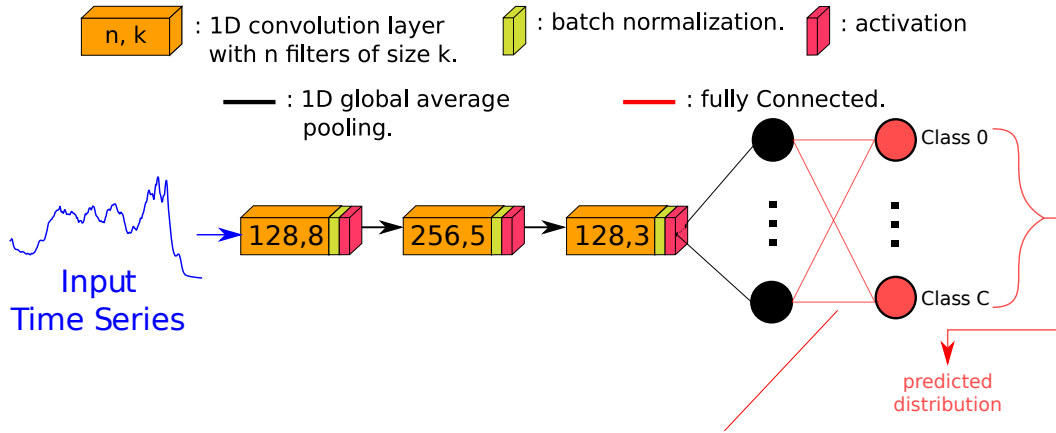
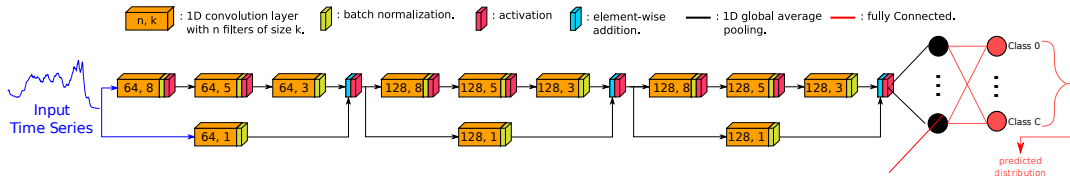


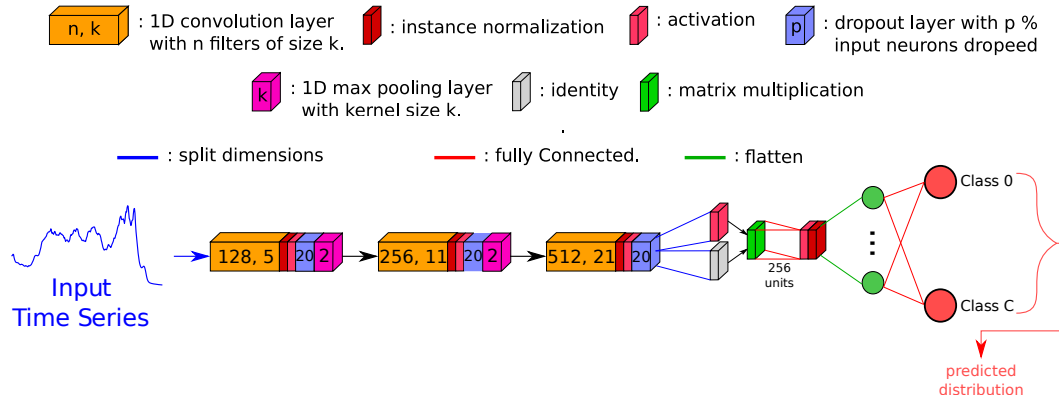
FIGURE 1.9: The Residual Network (ResNet) architecture (Wang, Yan, and Oates, 2017) for Time Series Classification.



Residual Network (ResNet) Since the impact of residual connections have been successful for image classification (He et al., 2016), the authors in (Wang, Yan, and Oates, 2017) proposed to enhance the FCN architecture with this kind of operations. The authors in (Wang, Yan, and Oates, 2017) argues the need of residual connections given that neural networks also may suffer from the vanishing gradient problem for TSC. For this reason, the authors proposed ResNet for TSC, presented in Figure 1.9 with its parameter setup. This architecture consists of three residual blocks, where each block is an FCN architecture without the GAP and classification layer. Each residual block contains an element-wise addition between its input layer and output layer, with the residual connection including a bottleneck layer (PWC see Eq. 1.21) to adjust dimensions. The convolution layers, such as in FCN, utilize a zero-padding to ensure the edge pattern detection, resulting as well in equal length input/output at the beginning and end of the network. The last activation layer of ResNet is fed to a GAP layer followed by an FC layer for classification.

Encoder Motivated by FCN (Wang, Yan, and Oates, 2017), the authors in (Serra, Pascual, and Karatzoglou, 2018) proposed a novel hybrid deep learning model, Encoder, that replaces the GAP layer by a slightly different version of Self-Attention. The Encoder architecture, presented in Figure 1.10, consists on three convolution blocks, each containing a one dimensional convolutional layer, followed by an Instance Normalization (IN) layer instead of a BN layer, a Parametric ReLU activation function, a dropout layer and finally a local max pooling layer. The IN layer consists on using the same normalization concept of BN however it is done per example in the batch instead of averaging statistics over all samples in the batch. The third convolution block however does not contain a local max pooling layer, instead the outputs are split on the dimension axis into two parts used for a Self-Attention mechanism.

FIGURE 1.10: The Encoder architecture (Serra, Pascual, and Karatzoglou, 2018) for Time Series Classification.



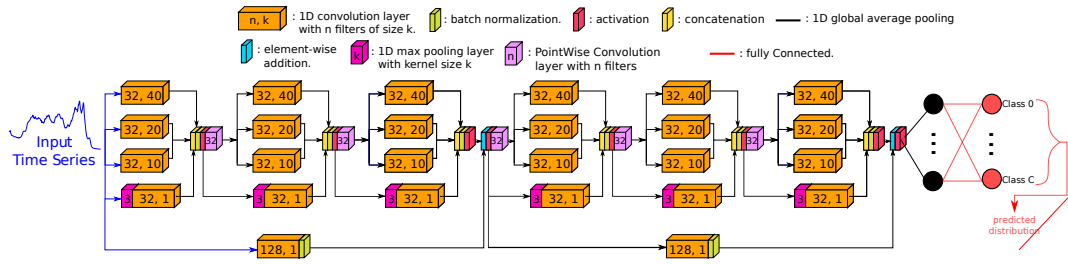
The output of the attention layer goes through an FC transformation layer followed by a flattening and the last FC classification layer.

Neural Network Ensemble (NNE) Ensemble models in machine learning (Middlehurst et al., 2021) has shown to have a significant impact, for instance until the year 2020, the state-of-the-art hybrid ensemble model, HIVE-COTE (Lines, Taylor, and Bagnall, 2018), consisted of 36 classifiers ensembled. The authors in (Fawaz et al., 2019) studied the impact of ensembling in deep learners given that HIVE-COTE (Lines, Taylor, and Bagnall, 2018) ensembles non-deep learners. In (Fawaz et al., 2019), the authors proposed the Neural Network Ensemble (NNE) consisting of 6 different deep learning architectures with 10 different initialization, hence a total of 60 models, ensembled posterior to training. NNE highlighted that it can achieve the performance of HIVE-COTE over the UCR archive as well as outperform significantly an ensemble of any other architecture alone, highlighting that the importance of hybrid ensembles.

InceptionTime In (Ismail Fawaz et al., 2020), the authors argued the need to *find the AlexNet for Time Series Classification* given the increase in number of datasets available and the high similarity that exists between them. For this reason, a deeper architecture should be proposed to outperform the current state-of-the-art deep learning model ResNet (Wang, Yan, and Oates, 2017; Ismail Fawaz et al., 2019). Motivated from the impact of Inception architecture for image classification, the authors in (Ismail Fawaz et al., 2020) proposed an adaptation of the Inception architecture for TSC, specifically the authors were based on the fourth version of Inception on image classification (Szegedy et al., 2017). The Inception architecture adapted for time series data is presented in Figure 1.11 with a detailed view on its parameters' setup.

The Inception architecture consists of two Inception-blocks each containing a residual connection (He et al., 2016) connecting their input and output. Within each Inception-block, there is three Inception-modules connected in series, each containing three convolution layers in parallel (this is referred to later as multiplexing convolution) of different kernel size applied on the same input, and a local max pooling layer followed by a PWC layer for dimension adjustment. Each Inception-module, if its input has dimension higher to 1, applies a PWC layer in order to reduce the number of filters to learn in the following convolution layers. The output of the three convolution and the max pooling layers are concatenated on the channel axis and

FIGURE 1.11: The Inception architecture (Ismail Fawaz et al., 2020) for Time Series Classification.



fed to a BN layer and a ReLU activation function. The last activation layer goes through a global pooling operation, specifically a GAP layer, before being fed to an FC classification layer.

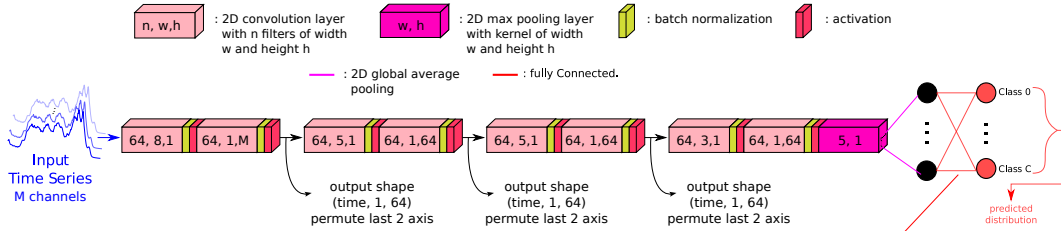
The authors in (Ismail Fawaz et al., 2020), seeing the impact of ensemble models, proposed InceptionTime, an ensemble of five Inception architectures each trained with different initialization. In 2020, InceptionTime became the state-of-the-art deep learning model for TSC and shown to have even less difference in performance, statistically, with HIVE-COTE2.0 (Middlehurst et al., 2021). InceptionTime, not only highlighted its ability to achieve HC2.0 performance, but as well as it being more efficient in terms of training runtime in function of both training dataset size and length of time series.

Disjoint Convolutional Neural Network (Disjoint-CNN) All the previously presented architectures were originally proposed for a general setup of TSC, meaning they were not constructed in a manner to address univariate time series or multivariate time series specifically, and they can be applied to both and have been evaluated on both. However, some researchers argued that handling MTS data is not the same as handling UTS data and questioned the way convolution operations are being done over MTS.

In (Foumani, Tan, and Salehi, 2021), the authors proposed the Disjoint Convolutional Neural Network (Disjoint-CNN), composed of, following the naming of the authors, 1+1D convolution layers (see Figure 1.12 for a detailed view on the architecture). The 1+1D convolution layer are two convolution operations operated in series, the first being a temporal convolution and the second being a spatial convolution. Given an input time series of M dimensions and length L , the temporal convolution layer is, in other words, a 2D convolution layer with a kernel of width $K > 1$ and height of 1. This ensures that the convolution layer will not sum up the outputs as done on MTS data with 1D convolution layers (see Eq. 1.19). The spatial convolution is as well a 2D convolution layer however with a kernel of width 1 and height M , hence learning a linear combination of temporal features over different dimensions. The core idea of 1+1D convolution blocks is very similar to what 1D DWSC does, however in this case more parameters are learned in the network.

Each of the temporal and spatial convolution layers is followed by a BN layer and an ELU activation function, forming a 1+1D convolution block. The Disjoint-CNN architecture is made of four 1+1D convolution block in series, followed by a local max pooling operation and finishing, just like Inception (Ismail Fawaz et al., 2020), by a GAP layer and an FC classifier.

FIGURE 1.12: The Disjoint-CNN architecture (Foumani, Tan, and Salehi, 2021) for Time Series Classification.



Convolutional Transformer (ConvTran) Researchers wondered the impact of Transformers and Self-Attention (Vaswani et al., 2017) when addressing the task of TSC. Although no work has been published addressing univariate data, the authors in (Foumani et al., 2024a) proposed the first working transformer on multivariate TSC. The proposed network, the Convolutional Transformer (ConvTran), consists of two phases, the time series encoder and the Self-Attention mechanism. We present in Figure 1.13 a detailed view on the ConvTran architecture with its detailed parameters' setup. The time series encoder ensures that the attention mechanism is being applied over a space in which each time stamp represents one patch of the input MTS space. The encoder used in ConvTran is a 1+1D convolution block (Foumani, Tan, and Salehi, 2021).

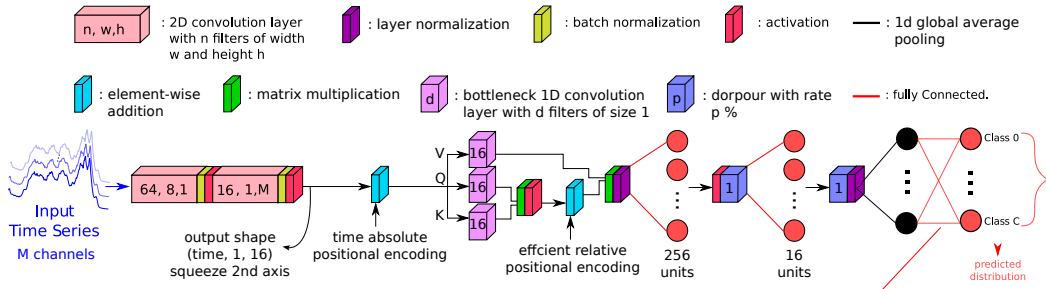
The ConvTran has two more contributions as well, as it adapts the frequency of the \sin and \cos functions of the Positional Encoder in Eqs. 1.31 and 1.32. This frequency adjustment is a form of normalization to the input length and dimension before feeding the embeddings to the Self-Attention layer. This normalization step is essential given that the original PE (Vaswani et al., 2017) was proposed for language models presenting a high dimensionality, which is not the case on average with the MTS datasets available in the literature. The authors in (Foumani et al., 2024a) showcased that the unnormalized PE suffers from its lack of ability to reflect similarity between different time stamps. The proposed normalization to the Absolute Positional Encoder (APE) is simply the following:

$$w_k = \frac{w_k \cdot d_{model}}{L} \quad (1.50)$$

where w_k is the frequency of the \cos and \sin functions in Eqs. 1.31 and 1.32, d_{model} is the dimension of the input embedding and L is the length of the series. This normalized version of APE is referred to as Time APE (tAPE).

The second contribution of the ConvTran (Foumani et al., 2024a) is an adaptation of the Relative Positional Encoding (RPE), which was first proposed on language models (Shaw, Uszkoreit, and Vaswani, 2018). The RPE is applied at the query and keys space. RPE in self-attention is motivated by the need to encode the relative positions of tokens, rather than absolute positions, to better capture the relationships between tokens irrespective of their absolute positions in the sequence. This approach improves the model's ability to generalize across different sequence lengths and better handles long-range dependencies. It enhances performance in tasks where the relative positioning of words or tokens is crucial for understanding context and meaning. ConvTran utilizes a shift based RPE instead of an index based one, taking into consideration that there should be a unique positional encoding for indices with a specific shift between them. This results in a set of scalars $w_{\delta=|i-j|}$, learnable, where i and $j \in [1, L]$ and L is the length of the embedded series. This would reduce the

FIGURE 1.13: The ConvTran architecture (Foumani et al., 2024a) for Time Series Classification.



number of parameters to learn in the RPE to $2L - 1$ instead of $(2L - 1)d_{model}$. This proposed RPE is referred to as Efficient RPE (eRPE).

In 2023, ConvTran became the state-of-the-art deep and non-deep learning model for multivariate TSC evaluated on the multivariate TSC UEA archive (Bagnall et al., 2018), outperforming the last state-of-the-art models, InceptionTime and ROCKET.

1.2.2 Time Series Extrinsic Regression

Time Series Extrinsic Regression (TSER) stands as a significant advancement in the domain of time series analysis, offering a departure from traditional intrinsic methods by focusing on predicting continuous scores rather than discrete classes. Unlike its classification counterpart, which aims to assign time series data into predefined categories, extrinsic regression is concerned with forecasting continuous values based on both temporal dynamics and external factors. In the last decade, many models have been proposed to address the task of TSER. These models leverage a variety of techniques, ranging from classical linear regression to more sophisticated algorithms such as ensemble methods and neural networks.

Extrinsic regression exhibits a wide array of applications, extending its reach across domains such as finance, healthcare, and environmental science. For example, it serves as a vital tool in satellite image analysis, where its application involves estimating live fuel moisture content in vegetation (Zhu et al., 2021) to mitigate the risk of wildfires. Additionally, in healthcare, extrinsic regression plays a pivotal role, particularly in predicting heart rates using electrocardiogram (ECG) signals (Pimentel et al., 2016) from patients, aiding in the diagnosis and management of cardiovascular conditions.

As more data becomes available and computational methods advance, extrinsic regression in time series analysis remains an active and promising field. Researchers and practitioners are constantly seeking new methods and applications, pushing the limits of predictive modeling and empirical analysis. This impact was particularly significant when Monash University published the TSER archive (Tan et al., 2020), which includes 19 different TSER datasets spanning applications from healthcare to energy monitoring. Released in 2021, the TSER archive features 4 univariate and 15 multivariate time series datasets. Similar to the UCR/UEA TSC archives, the TSER archive facilitates benchmarking, enabling researchers to evaluate their contributions in TSER across a comprehensive set of datasets.

More recently, the authors in (Guijo-Rubio et al., 2024) contributed 44 new TSER datasets including 24 univariate and 20 multivariate, resulting in a total of 63 TSER datasets when combined with the original archive (Tan et al., 2020). The authors in (Guijo-Rubio et al., 2024) adapted as well some classification based algorithms

in (Middlehurst, Schäfer, and Bagnall, 2024) to work with regression tasks. The authors concluded in (Guijo-Rubio et al., 2024) that the best regressors available now are feature based algorithms, especially DrCIF (Middlehurst et al., 2021) and FreshPRINCE (Middlehurst and Bagnall, 2022).

In this section, we define the task at hand and detail briefly some alternations done over some classification models to work with regression problems.

Definition 7 A TSER dataset $\mathcal{D} = \{\mathbf{x}_i, y_i\}_{i=1}^N$ is a collection of N multivariate time series of M dimensions and length L \mathbf{x}_i and their corresponding continuous real label y_o .

The task of TSER comes down to constructing a model \mathcal{F} that can achieve correct continuous predictions as accurate as possible. Unlike in TSC, the task is done by learning the parameters of a model \mathcal{F} to correctly predict real values instead of categorized classes.

$$\mathcal{F}(\mathbf{x}) = \hat{y} \in \mathbb{R} \quad (1.51)$$

1.2.2.1 Distance Based Methods: k -NN

Similar to classification (Section 1.2.1.1), distance based methods can be used for the task of TSER as well. For instance, the k -NN model coupled with any similarity measure, where for each new test sample, the predicted label is simply the arithmetic mean of the labels of the k nearest neighbors as follows:

$$\hat{y} = \frac{1}{k} \sum_{i=1}^k y_{neighbor_i} \quad (1.52)$$

1.2.2.2 Convolution Based Methods: ROCKET and MultiROCKET

In (Tan et al., 2020), the authors adapted the ROCKET (Dempster, Petitjean, and Webb, 2020) transformation model to work with TSER by simply replacing the RIDGE classification model by a RIDGE regression model. This was done as well for MultiROCKET (Tan et al., 2022), the newest adaptation of ROCKET for TSC (see Section 1.2.1.3), to work on TSER in the same way as ROCKET.

1.2.2.3 Feature Based Methods: FreshPRINCE

Feature based approach in the case of TSER should use an unsupervised feature extraction method as the label space, unlike in TSC in Section 1.2.1.2, is not discrete. The FreshPRINCE, consisting of a pipeline of TSFresh transformation (Christ et al., 2018) followed by a Rotation Forrest (Rodriguez, Kuncheva, and Alonso, 2006), is adapted to TSER in (Guijo-Rubio et al., 2024) by replacing the C4.5 methods of tree generation by the Classification and Regression Tree (CART) (Loh, 2011). The prediction of all trees are finally averaged and produce the predicted value for new test samples. The TSFresh phase of FreshPRINCE does not change.

1.2.2.4 Interval Based Methods: DrCIF

For TSC, interval based methods require **first** to extract phase independent intervals from the time series, **second** to extract features from each interval, **third** to train a classifier per features per interval and **fourth** to ensemble the classifiers trained. In the case of TSER, the same pipeline is used, however the interval selection must be purely unsupervised as the label space is not discrete, and the classifier is

replaced by a regressor. In the case of DrCIF (Section 1.2.1.6) the regressors used are tree regressors and the ensemble is simply the average predicted value from each tree.

1.2.2.5 Deep Learning Methods

For TSC, the deep learning models in Section 1.2.1.8 are trained to predict a discrete probability distribution of each sample belonging to each class. In the case of TSER, the label space is not discrete but rather continuous, for this reason the deep learning model should predict one real value instead of a vector of C values with a softmax activation. To make this alternation, the last FC layer in all deep learning architectures is changed to have one output neuron with no activation (linear by default) given there is no assumption of constraints over the label values.

In TSC, the cost function used to train the deep learning model's parameters is the categorical cross entropy (see Eq. 1.15) as the predicted and ground truth values are probability distributions. In the case of TSER, given the predicted and ground truth values are in fact real values, the cost function used is the Squared Error as such for sample $i \in [1, N]$ in the dataset:

$$\mathcal{L}_i(y_i, \hat{y}_i) = (y_i - \hat{y}_i)^2 \quad (1.53)$$

The total loss over a batch of N samples is simply the average loss in Eq. 1.53:

$$\mathcal{L} = \frac{1}{N} \sum_{i=1}^N \mathcal{L}_i \quad (1.54)$$

1.3 Unsupervised Learning: Prototyping, Clustering and Self-Supervised

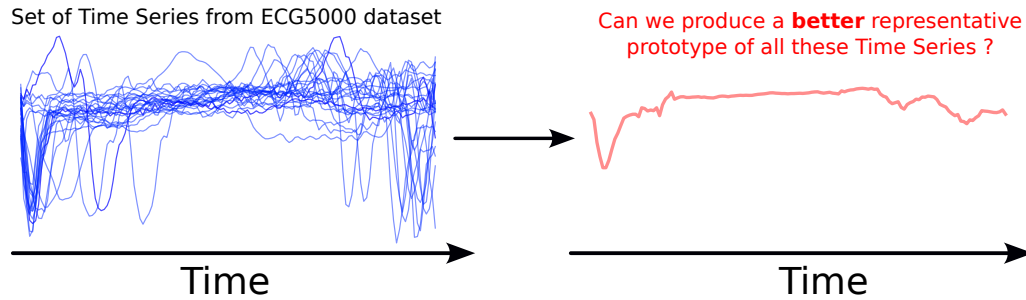
Unsupervised learning techniques are crucial in time series analysis, especially when labeled data is scarce or unavailable. These methods facilitate the discovery of inherent patterns and structures within time series data. Key approaches include prototyping, clustering, and Self-Supervised Learning (SSL). Prototyping involves creating representative samples or profiles of time series, aiding in data summarization and visualization. Clustering groups similar time series together, enabling the identification of common behaviors and anomalies. Self-supervised learning, a form of representation learning in deep learning, leverages the intrinsic structure of the data to learn meaningful features, enhancing the performance of subsequent tasks such as classification or forecasting. These techniques collectively expand the toolkit for analyzing complex time series datasets, offering valuable insights across various applications.

In this section, we explore the three aforementioned unsupervised tasks: prototyping, clustering, and SSL. We will provide the necessary background material for understanding these concepts and discuss some state-of-the-art approaches addressing each task.

1.3.1 Time Series Prototyping (TSP)

Time Series Prototyping (TSP) (Keogh and Pazzani, 1998) involves creating representative profiles or prototypes of time series data, as summarized in Figure 1.14,

FIGURE 1.14: Time Series Prototyping comes down to finding a **good representative** of the **input set of time series**. This example uses the ECG5000 dataset of the UCR archive (Dau et al., 2019).



which can simplify the analysis and interpretation of large datasets. This technique is particularly useful in applications such as anomaly detection, pattern recognition, and data summarization. For instance, in healthcare, having a representative time series for each disease based on ECG data can significantly speed up the classification of new patients. By comparing a new patient’s ECG time series to these prototypes, medical professionals can quickly identify the most likely diagnosis.

The task of finding a prototype for a group of time series involves identifying the series that minimizes the average dissimilarity to the others in the group.

Definition 8 Given a group of N time series $\{\mathbf{x}_i\}_{i=1}^N$, finding the group prototype comes down to solving the following:

$$\mathbf{x}^* = \arg \min_{\mathbf{x}} \frac{1}{N} \sum_{i=1}^N d(\mathbf{x}, \mathbf{x}_i) \quad (1.55)$$

where $d(.,.)$ represents any similarity measure between two time series.

In the rest of this section, we will present some traditional ways of prototyping as well as developed methods presented throughout the years.

1.3.1.1 Arithmetic Mean

A naive approach to time series prototyping involves calculating the arithmetic mean of corresponding data points from multiple time series. This method, often referred to as the “mean prototype” does not take into account the temporal alignment or any variations in the time series but simply averages the values at each time point.

Given a group of N time series $\{\mathbf{x}_i\}_{i=1}^N$ of M dimensions and length L , the mean prototype \mathbf{x}_p is calculated as follows:

$$x_{p,t}^m = \frac{1}{N} \sum_{i=1}^N x_{i,t}^m \quad (1.56)$$

where $t \in [1, L]$ and $m \in [1, M]$.

This method is straightforward but often fails to capture important temporal dynamics and variations in the data, making it less effective for applications where the temporal order and shape of the time series are crucial.

1.3.1.2 Piece-wise Linear Segmentation and Weighting

The approach proposed in (Keogh and Pazzani, 1998) introduces an enhanced method for time series prototyping that combines piece-wise linear segmentation with a weighting scheme to capture the importance of different segments. This method, referred to as “Weighted Piece-wise Linear Segmentation”, involves representing each time series as a series of linear segments and assigning weights to these segments based on their relevance.

Prior to prototype mining, each series \mathbf{x}_i goes through a segmentation step and S segments are extracted:

$$\{(\mathbf{x}_{t_{1l}}, \mathbf{x}_{t_{1r}}), (\mathbf{x}_{t_{2l}}, \mathbf{x}_{t_{2r}}), \dots, (\mathbf{x}_{t_{2Sl}}, \mathbf{x}_{t_{Sr}})\} \quad (1.57)$$

where $(\mathbf{x}_{t_{sl}}, \mathbf{x}_{t_{sr}})$ denotes the start (left: l) and end (right: r) of a segment under the constraint: $t_{sl} < t_{sr}$. Each segment is assigned, by the segmentation algorithm, a weight w_s and $s \in [1, S]$.

To be able to merge two series of the group: \mathbf{x}_i and \mathbf{x}_j where i and $j \in [1, N]$, the following steps are taken for each segment $s \in [1, S]$ and each dimension $m \in [1, M]$,

- **Step 1:** Compute the *sign* and *mag* (magnitude difference):

$$sign = \begin{cases} -1 & \text{if } w_{i,s} \cdot w_{j,s} < 0 \\ 1 & \text{otherwise} \end{cases} \quad (1.58)$$

$$mag = \frac{\min(|w_{i,s}|, |w_{j,s}|)}{\max(|w_{i,s}|, |w_{j,s}|)} \quad (1.59)$$

- **Step 2:** Compute the combined segment values:

$$x_{p,t_s}^m = \frac{x_{i,t_{sl}}^m \cdot w_{i,s} + x_{j,t_{sl}}^m \cdot w_{j,s}}{w_{i,s} + w_{j,s}} \quad (1.60)$$

$$x_{p,t_{s+1}}^m = \frac{x_{i,t_{sr}}^m \cdot w_{i,s} + x_{j,t_{sr}}^m \cdot w_{j,s}}{w_{i,s} + w_{j,s}} \quad (1.61)$$

- **Step 3:** Compute the weight for the segment:

$$w_{p,s} = (w_{i,s} \cdot w_{j,s}) \cdot \left(1 + \frac{sign \cdot mag}{1 + d}\right) \quad (1.62)$$

where d is a scale factor calculated as follows:

$$d = \left| \frac{(x_{i,t_{sl}}^m - x_{j,t_{sl}}^m) - (x_{i,t_{sr}}^m - x_{j,t_{sr}}^m)}{t_{sr} - t_{sl}} \right| \cdot norm \quad (1.63)$$

and *norm* is calculated as follows:

$$norm = \max(\max(\mathbf{x}_{i,l}^m), \max(\mathbf{x}_{i,r}^m)) - \min(\min(\mathbf{x}_{i,l}^m), \min(\mathbf{x}_{i,r}^m)) \quad (1.64)$$

To reconstruct the time series from the new segments, the authors in (Keogh and Pazzani, 1998) used the piece-wise linear representation created by the merging process.

1.3.1.3 Elastic Barycenter Averaging Methods

Elastic Barycenter Averaging (EBA) is a technique first addressed by (Petitjean, Ketterlin, and Gançarski, 2011) that proposed a combination between the elastic similarity measure DTW (see Alg. 1) in order to find a prototype of a group of time series. The core difference between the arithmetic Mean in Section 1.3.1.1 and the first proposed method based on EBA: DTW Barycenter Averaging (DBA) (Petitjean, Ketterlin, and Gançarski, 2011) is that DBA takes into consideration the alignment information between all samples in the group. This results in a prototype representing the *average warping* as well as the average amplitude, on contrary with arithmetic Mean which considers all series are aligned. Another powerful unique feature with EBA methods, starting with DBA in (Petitjean, Ketterlin, and Gançarski, 2011), is their ability to find prototypes over a group of unequal length time series samples.

The detailed working of DBA is presented in Algorithm 2. DBA initializes a prototype by randomly choosing one series in the group, and iteratively optimizes this prototype by finding for each of its time stamps, the aligned time stamps with all other series in the group (referred to as associates of the prototype’s time stamp). The value of the time stamp of the current prototype is then replaced by the barycenter (arithmetic mean) of the aligned values with it. Theoretically, DBA works with any value of q in DTW_q (see Eq. 1.3), however the authors in (Petitjean et al., 2014) proved that in the case of $q = 2$, DBA converges and the optimal solution is using the arithmetic mean over aligned points.

Algorithm 2 DTW Barycenter Averaging (DBA)

Require: Group of N Time Series $\{\mathbf{x}\}_{i=1}^N$ of length L and dimension M each

Require: Initial prototype series \mathbf{x}_p of length L and dimension M

Ensure: Time Series of length L and dimension M : The DBA prototype representative of the group

```

1: CountAssociates  $\leftarrow$  zeros(shape = (L,))
2: for  $i = 1 \rightarrow N$  do
3:    $\pi \leftarrow DTW_{path}(\mathbf{x}_p, \mathbf{x}_i)$ 
4:   for  $j = 1 \rightarrow len(\pi)$  do
5:      $t_1 \leftarrow \pi_{j,1}$ 
6:      $t_2 \leftarrow \pi_{j,2}$ 
7:      $\mathbf{x}_{p,t_1} = \mathbf{x}_{p,t_1} + \mathbf{x}_{i,t_2}$ 
8:     CountAssociates $_{t_1} \leftarrow$  CountAssociates $_{t_1} + 1$ 
9:   end for
10: end for
11: Return:  $\mathbf{x}_p / \text{CountAssociates}$ 

```

More recently, a new version of DBA has been proposed in (Holder, Guijo-Rubio, and Bagnall, 2023) that replaces the DTW similarity measure by the Move-Split-Merge (MSM) measure (Stefan, Athitsos, and Das, 2012b), given that it has been seen to outperform DTW for clustering (Holder, Middlehurst, and Bagnall, 2024). The proposed method, MSM Barycenter Averaging (MBA) in (Holder, Guijo-Rubio, and Bagnall, 2023) outperformed the usage of DBA for clustering.

Elastic similarity measures such as DTW, as explained in Algorithm 1, uses three moves on the cost matrix, diagonal move, horizontal move and vertical move. In terms of DTW, the algorithm penalizes a miss alignment by simply producing longer warping path with higher number of non-diagonal alignments. This can be problematic

Algorithm 3 Move-Split-Merge (MSM)**Require:** Two Time Series \mathbf{x}_1 and \mathbf{x}_2 of length L and dimension M **Require:** The cost penalty parameter c **Ensure:** MSM measure between \mathbf{x}_1 and \mathbf{x}_2

```

1:  $\tilde{D} \leftarrow \text{array}[L, L] = \{0.0\}$ 
2: for  $m = 1 \rightarrow M$  do
3:    $D \leftarrow \text{array}[L, L] = \{0.0\}$ 
4:    $D[1, 1] \leftarrow |x_{1,1}^m - x_{2,1}^m|$ 
5:   for  $t = 2 \rightarrow L$  do
6:      $D[t, 1] \leftarrow D[t-1, 1] + C(x_{1,t}^m, x_{1,t-1}^m, x_{2,1}^m, c)$ 
7:   end for
8:   for  $t = 2 \rightarrow L$  do
9:      $D[1, t] \leftarrow D[1, t-1] + C(x_{2,t}^m, x_{2,t-1}^m, x_{1,1}^m, c)$ 
10:  end for
11:  for  $t_1 = 2 \rightarrow L$  do
12:    for  $t_2 = 2 \rightarrow L$  do
13:       $\text{move} \leftarrow D[t_1-1, t_2-2] + |x_{1,t_1}^m - x_{2,t_2}^m|$ 
14:       $\text{split} \leftarrow D[t_1-1, t_2] + C(x_{1,t_1}^m, x_{1,t_1-1}^m, x_{2,t_2}^m, c)$ 
15:       $\text{merge} \leftarrow D[t_1, t_2-1] + C(x_{2,t_2}^m, x_{2,t_2-1}^m, x_{1,t_1}^m, c)$ 
16:       $D[t_1, t_2] = \min(\text{move}, \text{split}, \text{merge})$ 
17:    end for
18:  end for
19:   $\tilde{D} = \tilde{D} + D$ 
20: end for
21: Return:  $\tilde{D}[L, L]$ 

```

in some cases, as we need the algorithm to penalize directly the non-diagonal alignment itself rather than utilizing the outcome as one global penalty. Moreover, edit distances such as MSM (Stefan, Athitsos, and Das, 2012b) considers that a diagonal move is a match, and vertical/horizontal moves are considered as insertion/deletion (split/merge) and are penalized instantly when the move is made. This penalty in MSM depends on a hyper-parameter called c which represents the penalty minimum cost. For a match movement (diagonal), the MSM uses the absolute difference between matched values instead of the squared error such as in DTW. However, when two values are not matched (horizontal or vertical), the MSM uses a different functionality. For instance assuming two series \mathbf{x}_1 and \mathbf{x}_2 for which the MSM is finding the alignment path between them, the cost for a split (insertion/vertical) movement is calculated as such on dimension $m \in [1, M]$:

$$C(x_{1,t_1}^m, x_{1,t_1-1}^m, x_{2,t_2}^m, c) = \begin{cases} c & \text{if } x_{1,t_1-1}^m \leq x_{1,t_1}^m \leq x_{2,t_2}^m \\ c & \text{if } x_{1,t_1-1}^m \geq x_{1,t_1}^m \geq x_{2,t_2}^m \\ c + \min(|x_{1,t_1}^m - x_{1,t_1-1}^m|, |x_{1,t_1}^m - x_{2,t_2}^m|) & \text{otherwise} \end{cases} \quad (1.65)$$

where the above operation consists on inserting x_{1,t_1}^m between x_{1,t_1-1}^m and x_{2,t_2}^m .

For the deletion operation (horizontal movement), its the inverse of the insertion operation as the series swap in Eq. 1.65 by calling $C(x_{1,t_2}^m, x_{2,t_2-1}^m, x_{1,t_1}^m, c)$.

The MSM algorithm is detailed in Algorithm 3.

1.3.1.4 Differentiable EBA: SoftDTW Barycenter Averaging (SoftDBA)

As mentioned in Section 1.2.1.1, the authors in (Cuturi and Blondel, 2017) argue the need of a differentiable version of DTW and proposed SoftDTW. However, this is not the only contribution of (Cuturi and Blondel, 2017), as in fact the authors proposed a novel version of DBA (Petitjean, Ketterlin, and Gançarski, 2011) which does not simply replace DTW by SoftDTW, but learns the optimal barycenter using a gradient based optimization algorithm. The reason that makes this possible is the fact that SoftDTW is differentiable and the solution to Eq. 1.55 can be found through a gradient optimization approach, where the gradient to be found is the following:

$$\nabla_{\mathbf{x}}DTW^{\gamma}(\mathbf{x}, \mathbf{x}_i) \quad (1.66)$$

where \mathbf{x}_i is one series in the group of size N to be prototyped $i \in [1, N]$ and DTW^{γ} is the SoftDTW algorithm with smoothness parameter γ .

1.3.1.5 Time Elastic Kernel Averaging (TEKA)

(Marteau, 2019b) proposes a probabilistic approach, TEKA, to time series averaging and denoising based on time-elastic kernels. By interpreting kernel alignment matrices probabilistically, the method introduces a stochastic alignment automaton to compute the centroid of a set of time series. This process effectively captures both temporal dynamics and structural shape, allowing for robust averaging and noise reduction. Empirical evaluations across 45 datasets highlight its effectiveness, showing significant performance improvements for centroid-based classifiers over medoid-based counterparts. Moreover, the method proves valuable in reducing training set sizes for applications such as gesture recognition, demonstrating its utility in both denoising and efficient representation (condensing).

1.3.2 Time Series CLustering (TSCL)

Clustering is a fundamental technique in data analysis that involves grouping a set of objects in such a way that objects in the same group (or cluster) are more similar to each other than to those in other groups. This similarity is measured based on certain features or characteristics of the data. Clustering is widely used in various fields such as marketing for customer segmentation, biology for classifying species, and document clustering in text analysis. Time Series Clustering (TSCL) specifically deals with temporal data, where the objective is to group time series that exhibit similar behaviors or patterns over time. Unlike traditional clustering, time series clustering must handle the unique characteristics of time-dependent data, such as temporal ordering, trends, and seasonality. Effective clustering of time series can reveal important insights in fields like finance, healthcare, and climate science. In this section we review three common approaches in the literature of TSCL: (1) k -means clustering algorithm coupled with elastic similarity measures and EBA methods, (2) shape based algorithms and (3) deep learning methods.

1.3.2.1 k -means with Elastic Barycenter Averaging

k -means with Elastic Barycenter Averaging (EBA) is an enhanced version of the traditional k -means algorithm (MacQueen et al., 1967) designed for time series data. EBA addresses the alignment and averaging challenges of time series by allowing temporal distortions during the centroid calculation. This makes k -means more robust and accurate for clustering time series data, as it can handle shifts and variations in

the time sequences. A detailed view on how k -means work for TSCL is presented in Algorithm 4. k -means initializes random centroids $\{\mathbf{s}_j\}_{j=1}^k$ at the beginning and then updates the centroids following the set of nearest samples in the data $\mathcal{D} = \{\mathbf{x}_i\}_{i=1}^N$. This algorithm converges when the inertia presents a small non-significant change, compared to a threshold. The inertia is computed as the sum of distances between each sample and its nearest centroid:

$$inertia = \sum_{j=1}^k \sum_{\mathbf{x}_i \in NN(\mathbf{s}_j, \mathcal{D}, d)} d(\mathbf{x}_i, \mathbf{s}_j) \quad (1.67)$$

where $d(., .)$ is a similarity measure between two time series and $NN(\mathbf{s}_j, \mathcal{D})$ is the set of time series in \mathcal{D} that are nearest to centroid \mathbf{s}_j following the measure $d(., .)$.

The authors of (Petitjean, Ketterlin, and Gançarski, 2011) proposed the setup of k -means coupled with DTW similarity measure and DBA averaging method. Through extensive experiments on different datasets, the proposed setup for k -means outperformed the original setup which relies on using Euclidean Distance and Arithmetic Mean.

This setup was changed by (Cuturi and Blondel, 2017) by using the SoftDTW similarity measure and SoftDBA averaging method for k -means and showcased how it can outperform the previous setup with DBA proposed in (Petitjean, Ketterlin, and Gançarski, 2011). The authors of (Cuturi and Blondel, 2017) argue that the optimization steps of SoftDBA, facilitated by the differentiability of SoftDTW, effectively eliminate noise in the time series samples. This process yields more accurate centroids, thereby enhancing clustering performance.

Algorithm 4 k -means with Elastic Barycenter Averaging

Require: N time series samples $\mathcal{D} = \{\mathbf{x}_i\}_{i=1}^N$
Require: Number of clusters k
Require: Similarity measure $d(.,.)$ between two time series
Require: Averaging method $A()$ between a set of time series
Require: Maximum number of iterations max_{itr} in case of no convergence
Require: Threshold ϵ for inertia convergence check
Ensure: Cluster centroids $\{\mathbf{s}_j\}_{j=1}^k$ and cluster assignments

- 1: **for** $j = 1 \rightarrow k$ **do**
- 2: $\mathbf{s}_j \leftarrow \text{random_choice}(\mathcal{D})$
- 3: **end for**
- 4: $previous_inertia \leftarrow \infty$
- 5: **for** $itr = 1 \rightarrow max_{itr}$ **do**
- 6: $previous_inertia \leftarrow current_inertia$
- 7: $assigned_cluster \leftarrow \text{zeros}(size = (N,))$
- 8: **for** $i = 1 \rightarrow N$ **do**
- 9: $distances \leftarrow \text{zeros}(size = (k,))$
- 10: **for** $j = 1 \rightarrow k$ **do**
- 11: $distances[j] \leftarrow d(\mathbf{x}_i, \mathbf{s}_j)$
- 12: **end for**
- 13: $assigned_cluster[i] \leftarrow \arg \min_{j \in [1,k]} distances$
- 14: $current_inertia \leftarrow current_inertia + \min(distances)$
- 15: **end for**
- 16: **if** $|current_inertia - previous_inertia| < \epsilon$ **then**
- 17: $break$
- 18: **end if**
- 19: $previous_inertia \leftarrow current_inertia$
- 20: **for** $j = 1 \rightarrow k$ **do**
- 21: $\mathbf{s}_j \leftarrow A(\{\mathbf{x}_i \mid assigned_cluster[i] = j\})$
- 22: **end for**
- 23: **end for**
- 24: **Returns:** $\{\mathbf{s}_j\}_{j=1}^k, assigned_cluster$

1.3.2.2 Shape Based Method: k -shape

The k -shape algorithm proposed in (Paparrizos and Gravano, 2015) not only outperformed previous approaches with k -means, but also presented a significantly faster TSCL approach. For instance k -shape does not rely on using elastic similarity measures that suffer from time complexity, instead it utilizes a Shape Based Distance (SBD). Given two time series \mathbf{x}_1 and \mathbf{x}_2 of length L , the SBD used in (Paparrizos and Gravano, 2015) relies on the Normalized Cross Correlation (NCC) between \mathbf{x}_1 and the shifted version of \mathbf{x}_2 . The shifted version of \mathbf{x}_2 of shift s is computed as follows:

$$\mathbf{x}_2(s) = \begin{cases} \overbrace{\{0, \dots, 0, x_{2,1}, x_{2,2}, \dots, x_{2,L-s}\}}^{length=s} & \text{if } s > 0 \\ \{x_{2,1-s}, x_{2,2-s}, \dots, x_{2,L}, \underbrace{0, \dots, 0}_{length=s}\} & \text{if } s < 0 \end{cases} \quad (1.68)$$

And the NNC between both series is computed as follows:

$$NCC(\mathbf{x}_1, \mathbf{x}_2) = \max_{s \in \mathcal{S}} \frac{\sum_{t=1}^L x_{1,t} \cdot x_{2,t+s}}{L \cdot \text{module}(\mathbf{x}_1) \cdot \text{module}(\mathbf{x}_2)} \quad (1.69)$$

with the assumption that both series are normalized to zero mean and unit standard deviation. The $\text{module}(\cdot)$ operation is simply the sum of squares of all elements in the series and $\mathcal{S} = \{-L + 1, -L + 2, \dots, L - 2, L - 1\}$. The final SBD is calculated as follows:

$$SBD(\mathbf{x}_1, \mathbf{x}_2) = 1 - NCC(\mathbf{x}_1, \mathbf{x}_2) \quad (1.70)$$

For the case of MTS data, the SBD is simply the aggregation of SBD applied on each dimensions independently. The SBD returns as well the aligned version of \mathbf{x}_2 (referred to as \mathbf{x}'_2) following Eq. 1.68 using the optimal shift from Eq. 1.69.

The centroid finding technique used in k -shape over a set of time series $\mathcal{D} = \{\mathbf{x}_i\}_{i=1}^N$ is the solution to the following equation:

$$\mathbf{s}_j^* = \underset{\mathbf{s}_j}{\text{arg max}} \sum_{\mathbf{x}_i \in NN(\mathbf{s}_j, \mathcal{D}, SBD)} NNC(\mathbf{x}_i, \mathbf{s}_j)^2 \quad (1.71)$$

where $i \in [1, N]$ and $j \in [1, k]$.

The authors in (Paparrizos and Gravano, 2015) mentioned that the above optimization problem, after some alternations, can be solved using the problem of maximization of the Rayleigh Quotient (Golub and Van Loan, 2013). One iteration of the k -shape centroid extraction (shape extraction as referred to in the paper) phase is presented in Algorithm 5.

Algorithm 5 k -shape: Shape Extraction, One Iteration

Require: Set of Time Series in the same cluster $\mathbf{X} = \{\mathbf{x}_i\}_{i=1}^N$, assumed z-normalized

Require: The current centroid of this cluster \mathbf{s}

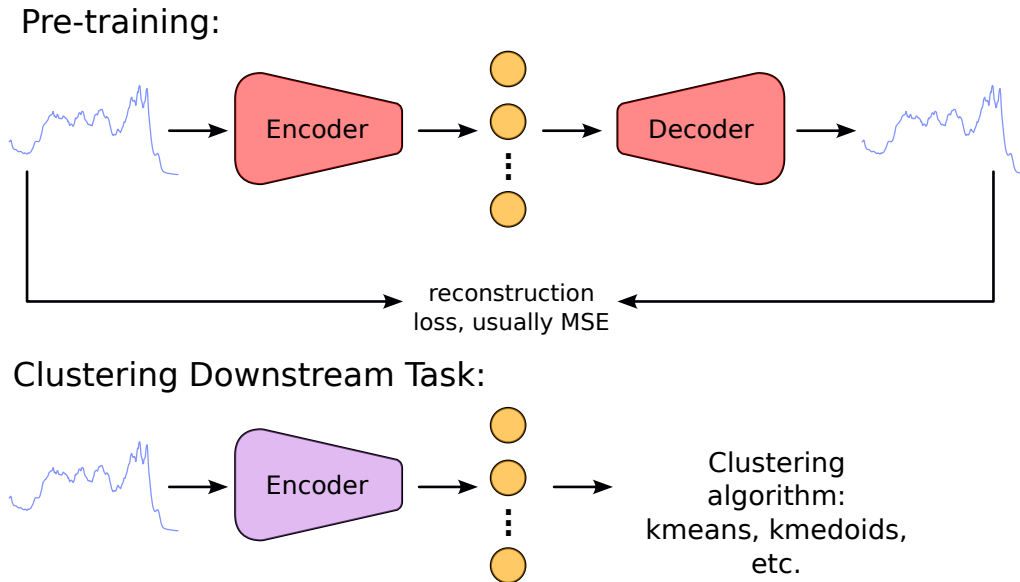
Ensure: A more accurate centroid \mathbf{s}'

- 1: $\mathbf{X}' = []$
 - 2: $\mathbf{O} \leftarrow [[1 \text{ for } o = 1 \rightarrow L] \text{ for } oo = 1 \rightarrow L]$
 - 3: **for** $i = 1 \rightarrow N$ **do**
 - 4: $\text{distance}, \mathbf{x}'_i \leftarrow SBD(\mathbf{s}, \mathbf{x}_i)$
 - 5: $\mathbf{X}' \cdot \text{append}(\mathbf{x}'_i)$
 - 6: **end for**
 - 7: $\mathbf{A} \leftarrow \mathbf{X}'^T \circ \mathbf{X}'$
 - 8: $\mathbf{Q} \leftarrow I_L - \frac{1}{L} \cdot \mathbf{O}$
 - 9: $\mathbf{M} \leftarrow \mathbf{Q}^T \circ \mathbf{A} \circ \mathbf{Q}$
 - 10: $\mathbf{s}' \leftarrow \text{EigVectors}(\mathbf{M})$
 - 11: **Returns:** \mathbf{s}'
-

1.3.2.3 Deep Learning Methods

While deep learning has revolutionized Time Series Classification (Ismail Fawaz et al., 2019), its potential for Time Series Clustering is still being explored. Recognizing the success of deep learning in classification tasks, researchers have hypothesized that it can also significantly enhance clustering methods. Consequently, various deep learning-based approaches for time series clustering have been proposed and reviewed in recent literature (Lafabregue et al., 2022). In the mentioned review (Lafabregue et al., 2022), the authors not only compared deep learning models for TSCL on the

FIGURE 1.15: AE based architecture with a reconstruction loss for Time Series Clustering. The **first step** is to train the AE architecture to reconstruction the **input time series**. The **second step** is to generate the **latent features** and apply a clustering algorithm on top of these feature.



architecture level, however they also compared different methods to train these models for better clustering downstream task.

Deep learning models, such as Recurrent Neural Networks (RNNs), Convolutional Neural Networks (CNNs), and Auto-Encoders (AEs), offer several advantages for clustering tasks. These models can automatically learn complex features and patterns directly from raw time series data, bypassing the need for manual feature extraction. RNNs, particularly Long Short-Term Memory (LSTM) networks, are adept at capturing long-term dependencies in sequential data, which are often overlooked by traditional clustering methods. CNNs, on the other hand, can efficiently process large-scale time series data in parallel, making them suitable for handling extensive datasets.

The adaptability and scalability of deep learning models make them promising for time series clustering. Their ability to model non-linear relationships and intricate temporal dependencies leads to more accurate and meaningful clustering results. As researchers continue to explore and refine these methods, deep learning is poised to offer robust solutions for clustering complex time series data, paralleling its success in classification tasks (Ismail Fawaz et al., 2019).

In this section, we will detail different architectural methods for deep clustering. Deep clustering can be performed using AEs or even standalone encoders with various pretext losses. These pretext losses include traditional reconstruction loss, multi-reconstruction (Ghasedi Dizaji et al., 2017) loss between encoder and decoder, triplet loss (Franceschi, Dieuleveut, and Jaggi, 2019), clustering losses (Xie, Girshick, and Farhadi, 2016), and more. An overview of AE architectures used for TSCL is presented in Figure 1.15. The review (Lafabregue et al., 2022) concluded that the best-performing architectures were a ResNet-based (Wang, Yan, and Oates, 2017) AE with multi-reconstruction loss and no clustering loss for univariate time series, and a non-symmetrical Dilated Recurrent Neural Network (DRNN) (Ma et al., 2019)

AE with multi-reconstruction loss and no clustering loss for multivariate time series.

1.3.2.3.1 Background on Auto-Encoders and Variational Auto-Encoders

Auto-Encoders (AEs) are a type of artificial neural network initially introduced in the 1980s by (Kramer, 1991) for the purpose of unsupervised learning, particularly for tasks like dimensionality reduction and feature learning. An AE consists of two main parts: an encoder and a decoder. The encoder maps the input series \mathbf{x} of length L and dimension M into a latent space representation \mathbf{z} , and the decoder reconstructs the input data from this latent representation. This structure allows the AE to learn efficient codings of the data by minimizing the reconstruction error between the original input and its reconstructed output. The mathematical representation is as follows:

1. Encoder: $\mathbf{z} = E_{\theta}(\mathbf{x})$
2. Decoder: $\hat{\mathbf{x}} = D_{\phi}(\mathbf{z})$

where each of the encoder $E_{\theta}(\cdot)$ and decoder $D_{\phi}(\cdot)$ is parametrized by a set of parameters for each of their layers, θ and ϕ respectively.

The objective is to minimize the reconstruction error, typically measured by the Mean Squared Error (MSE):

$$\mathcal{L}_{mse}(\mathbf{x}, \hat{\mathbf{x}}) = \frac{1}{L.M} \sum_{t=1}^L \sum_{m=1}^M (x_t^m - \hat{x}_t^m)^2 \quad (1.72)$$

However, traditional AEs face limitations in generating new data samples because they do not provide a probabilistic framework for the latent space. This is where Variational Auto-Encoders (VAEs) (Kingma and Welling, 2013) come into play. VAEs introduce a probabilistic approach to the latent space, allowing for both data reconstruction and generation of new data samples. By leveraging the principles of variational inference, VAEs model the distribution of the latent variables explicitly, which makes them highly effective for generative tasks.

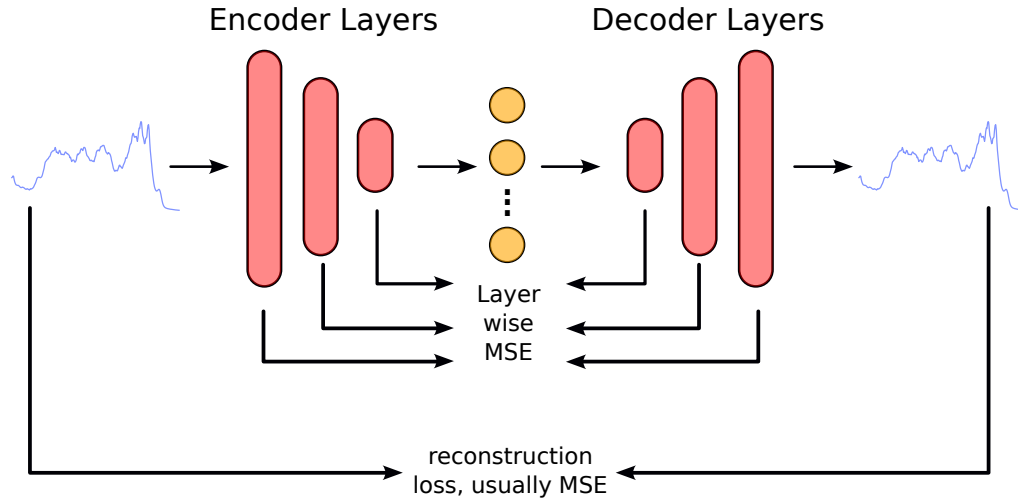
The (VAE) consists, like the traditional AE, of an encoder-decoder framework. However, unlike in AEs, the latent space in VAEs is regularized to follow a specific distribution, usually a Gaussian distribution. In traditional AEs, the latent space is not constrained to follow any distribution, which can lead to significant diversity in the placement of latent variables, potentially causing model collapse.

VAEs address this issue by incorporating a Gaussian projection step in the latent space. Specifically, the encoder in a VAE outputs two vectors: one representing the mean and the other representing the variance of a Gaussian distribution. This Gaussian distribution is then used to randomly sample points in the latent space before feeding them to the decoder. This sampling ensures continuity and smoothness in the latent space, which helps in generating coherent outputs. To prevent the encoder from producing a high-variance Gaussian distribution, which could also lead to model collapse, VAEs include a regularization loss. This regularization loss is the Kullback-Leibler (KL) divergence between the learned Gaussian distribution $q_{\theta}(\mathbf{z}|\mathbf{x})$ and the standard normal distribution $\mathcal{N}(0, 1)$. The KL divergence loss ensures that the learned distribution remains close to the prior distribution, maintaining the stability and structure of the latent space:

$$\begin{aligned} \mathcal{L}_{KL} &= D_{KL}(q_{\theta}(\mathbf{z}|\mathbf{x}), \mathcal{N}(0, 1)) \\ &= -\frac{1}{2} \sum_{d=1}^d (1 + \log \sigma_d^2 - \mu_d^2 - \sigma_d^2) \end{aligned} \quad (1.73)$$

FIGURE 1.16: AE based architecture with a multi-reconstruction loss (Ghasedi Dizaji et al., 2017) for Time Series Clustering. The first step is to train the AE architecture to reconstruction the input time series as well as each layer of the AE network. The second step is the same as in Figure 1.15

Pre-training:



where μ and $\log \sigma^2$ are both the mean and log of the variance learned by the encoder part of the VAE, and \mathbf{d} is the dimension of the latent space.

The total loss of the VAE used to optimize its parameters is a weighted sum of both the reconstruction and KL loss:

$$\mathcal{L}_{vae} = (1 - \beta) \cdot \mathcal{L}_{mse} + \beta \cdot \mathcal{L}_{KL} \quad (1.74)$$

where β is a hyperparameter between 0 and 1 used to control the amount of impact of the KL loss on the training phase, which was introduced in (Higgins et al., 2017).

1.3.2.3.2 Using AEs and VAEs for TSCL The review in (Lafabregue et al., 2022) presented multiple approaches from the literature that addressed the task of TSCL through deep learning. The best winning approaches are AE and VAE based networks that uses a multi-reconstruction loss. The multi-reconstruction loss has the same functionality as the reconstruction loss in Eq. 1.72, however it is applied between each depth of the encoder with its symmetrical depth in the decoder. This is illustrated in Figure 1.16.

In the case of univariate datasets, the review (Lafabregue et al., 2022) highlights that the winning model is an AE based architecture that utilizes ResNet (Wang, Yan, and Oates, 2017) as a backbone network. In order to define a ResNet decoder, a symmetrical architecture is defined that replaces the standard convolutions by transpose convolutions.

Definition 9 The one dimensional transpose convolution increases the length of the input series instead of decreasing it. This is done through a de-convolution step. Given an input univariate series \mathbf{x} of length L and a kernel \mathbf{w} of length K , the one

dimensional transpose convolution is applied as follows:

$$o_t = \sum_{t'=1}^L \sum_{k=1}^K x_{t'} \cdot w_k \cdot \delta(t, s \cdot t' + k) \quad (1.75)$$

where $\mathbf{o} = \{o_1, o_2, \dots, o_{(L-1) \cdot s + k}\}$ is the output series of length $(L-1) \cdot s + k$ and s is the number of strides. In the case of multivariate input series and multiple kernels used, transpose convolution follow the same protocol as standard convolutions, see Eq. 1.19.

Using the above transpose convolution, the ResNet based AE network can be defined. Posterior to training the AE network, the latent space is subsequently used to train a simple k -means cluster using the arithmetic mean and ED as parameters.

The review of deep TSCL methods (Lafabregue et al., 2022) showed however that using the VAE regularization can degrade the clustering performance.

Moreover, for multivariate datasets, the winning approach was an RNN based AE using the Dilated-RNN (DRNN) architecture (Ma et al., 2019). The DRNN AE architecture consists of three bidirectional GRU layers stacked on top of each other in the encoder part with a single GRU layer for the decoder. This architecture performed as the best deep clustering model for MTS data coupled with the reconstruction loss, unlike ResNet with the multi-reconstruction loss in the case of UTS data. The main reason to why the multi-reconstruction loss was not utilized in the case of DRNN AE network is that its a non-symmetrical AE architecture.

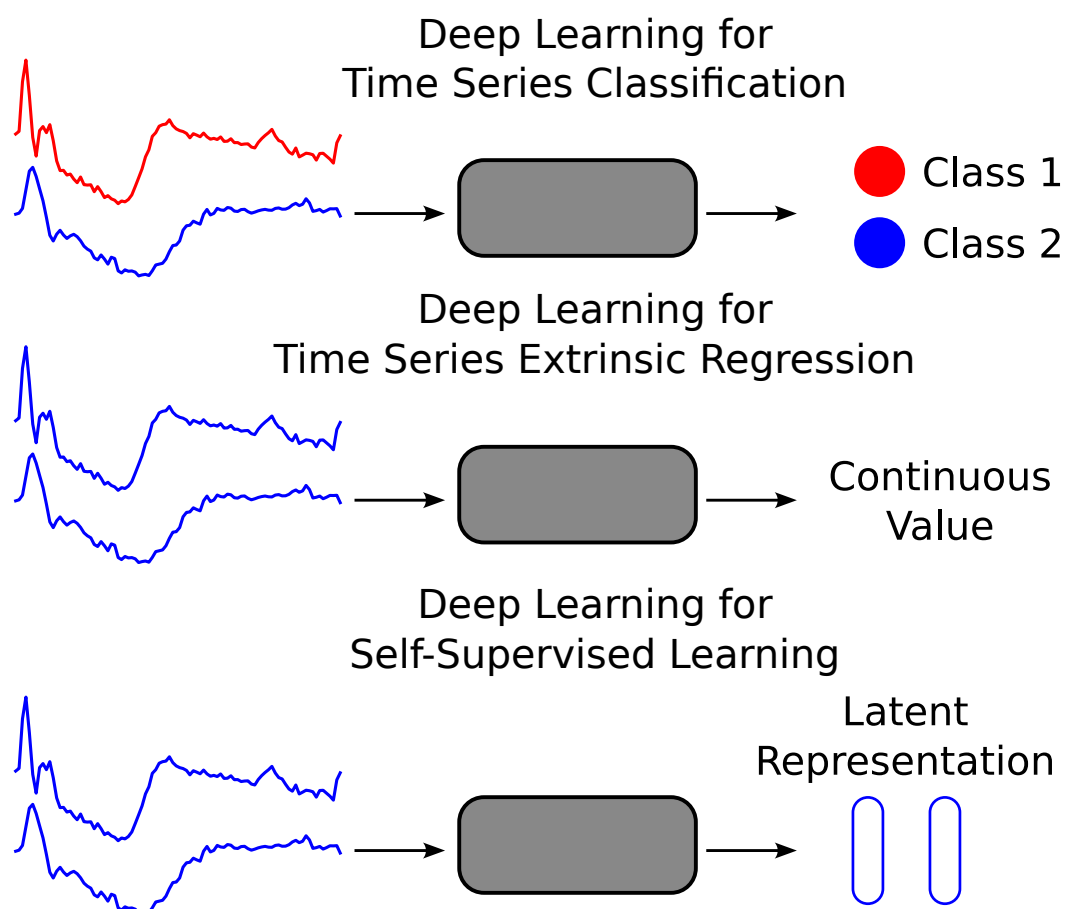
1.3.3 Self-Supervised Learning for Time Series Analysis

SSL, sometimes referred to as representation learning, is a machine learning paradigm where the model learns a compact representation of its input data without relying on labeled samples. The primary goal is to learn useful representations from the input data that can be utilized for various downstream tasks. By learning from large volumes of unlabeled data, SSL enables models to capture intricate patterns and structures, reducing the dependency on extensive labeled datasets. Figure 1.17 summarizes the pipeline of using a deep learning model for SSL, and the difference with other supervised tasks. Unlike supervised models, where deep learning models need to predict target values that are commonly known, deep learnign for SSL tries to find the best latent representation of the input data.

In the context of time series data, SSL can be particularly beneficial. Time series data, which involves patterns and dependencies over time, can be difficult to label accurately and thoroughly. By employing self-supervised techniques, models can learn to understand these patterns and temporal structures by predicting future points from past points or filling in missing data segments etc. This pre-training process results in robust feature representations that can significantly enhance the performance of downstream tasks such as forecasting, anomaly detection, and classification, even when labeled data is scarce.

Pre-trained models from SSL can greatly enhance generalization in downstream tasks, especially in scenarios with limited labeled data. These models, having been trained on large unlabeled datasets, possess a rich understanding of the underlying data distribution and can transfer this knowledge to specific tasks. This transfer learning approach is particularly useful in semi-supervised setups, where only a small fraction of the data is labeled. By fine-tuning pre-trained models on the available labeled data, we can achieve superior performance compared to training models from

FIGURE 1.17: The difference between using deep learning for Time Series Classification, Extrinsic Regression and Representation Learning (Self-Supervised Learning, SSL).



scratch. Thus, SSL not only alleviates the challenge of data scarcity but also promotes better generalization and adaptability in various real-world applications.

In this section, we present briefly some starting work of self-supervised learning for time series analysis, mostly used for downstream classification tasks.

1.3.3.1 Background on Siamese Neural Networks and SimCLR

Siamese networks, introduced in the early 1990s (Bromley et al., 1993), are a type of neural network architecture used to determine the similarity between two input samples. These networks consist of two identical subnetworks that share the same parameters and weights. They are trained using pairs of inputs, where the goal is to learn a function that can effectively distinguish between similar and dissimilar pairs. This method is particularly well-known for its application in signature verification and face verification tasks.

The original approach to training a Siamese network consists on defining for each sample a positive and negative representation of it. For instance in the case of signature verification task, it would consist on the same signature written twice, once by the same anchor subject and the second forged by a second subject. First, \mathbf{x}_1 and \mathbf{x}_2 , are fed to the same network to obtain \mathbf{z}_1 and \mathbf{z}_2 , two feature representations of the two input samples. Second, the ED is calculated between these two feature vectors. Third, the contrastive loss is computed as follows:

$$\mathcal{L}_{contrastive} = \frac{1}{2} \cdot (1 - y) \cdot ED(\mathbf{z}_1, \mathbf{z}_2)^2 + \frac{1}{2} \cdot y \cdot \max(0, \alpha - ED(\mathbf{z}_1, \mathbf{z}_2))^2 \quad (1.76)$$

where y indicates if the pair of samples are an anchor with its positive representation or an anchor with its negative representation. α is the boundary parameter that represent a penalty for the negative pairs. The goal of the Siamese network is to learn how to increase the distance between an anchor sample and its negative representation and decrease the distance between the anchor and its positive representation.

This SSL approach was then adapted in (Chen et al., 2020) to use an unlabeled setup for computing the contrastive loss. The authors in (Chen et al., 2020) proposed a Simple Contrastive LeaRning (SimCLR) self-supervised model for image representation. SimCLR does not rely on a labeled pair of samples such as in the original Siamese network. Instead, SimCLR takes as input two augmented versions of the same sample, and never the original sample, and minimizes the distance between the feature representation of the two augmented versions. This ensures that the latent space provides the same distance based information as the original space, hence can be used for downstream task e.g. simple linear classifier in the latent space for the classification task.

1.3.3.2 Self-Supervised Learning Models for Time Series Analysis

The above explained approach has been used as a base for almost all SSL research work and has been adapted to almost all domains in data science, such as time series. In what follows, we present briefly some of these adapted work in the last five years for time series data.

1.3.3.2.1 Dilated Causal CNN (DCCNN) with Triplet Loss The first ever work to address SSL for time series data was in (Franceschi, Dieuleveut, and Jaggi, 2019). The authors proposed a new architecture that they used for the self-supervised

setup. The proposed architecture, DCCNN, consists on multiple dilated causal convolutions stack on top of each other with residual networks between them. Causal convolutions are a type of convolution that ensures predictions at any point in time only use current and past data, never future data, which is important for time-based sequences. However, the main contribution of the paper was not the architecture, instead it was the proposal of a novel pretext loss, the triplet loss (Schroff, Kalenichenko, and Philbin, 2015). The triplet loss mechanism differs from the contrastive loss detailed in Eq. 1.76, by computing the loss on both positive and negative pairs at the same time, without using the labeling of positive/negative pairs y . The proposed loss in (Franceschi, Dieuleveut, and Jaggi, 2019) is computed as follows:

$$\mathcal{L}_{triplet} = -\log(\sigma(\mathbf{f}(\mathbf{x}_{ref})^T \odot \mathbf{f}(\mathbf{x}_{pos}))) - \sum_{n_{neg}=1}^{N_{neg}} \log(\sigma(-\mathbf{f}(\mathbf{x}_{ref})^T \odot \mathbf{f}(\mathbf{x}_{n_{neg}}))) \quad (1.77)$$

where σ is the sigmoid function, \mathbf{f} is a deep model used to encode feature vectors, \odot is the matrix multiplication operation, T is the transpose operation, N_{neg} is the number of negative samples $\{\mathbf{x}_{n_{neg}}\}_{n_{neg}=1}^{N_{neg}}$ per reference sample \mathbf{x}_{ref} , and \mathbf{x}_{pos} is the positive representation of \mathbf{x}_{ref} .

Given the loss defined in Eq.1.77, there should be a way to define the triplets $(\mathbf{x}_{ref}, \mathbf{x}_{pos}, \{\mathbf{x}_{n_{neg}}\}_{n_{neg}=1}^{N_{neg}})$. In (Franceschi, Dieuleveut, and Jaggi, 2019), the authors proposed the following approach to construct these triplets:

1. Choose one reference series \mathbf{r}
2. Define \mathbf{x}_{ref} as a random subsequence from \mathbf{r}
3. Define \mathbf{x}_{pos} as another random subsequence from \mathbf{r}
4. Define $\{\mathbf{x}_{n_{neg}}\}_{n_{neg}=1}^{N_{neg}}$ as being N_{neg} random subsequences from another series $\mathbf{r}' \neq \mathbf{r}$

1.3.3.2.2 Mixup Contrastive Learning (MCL) Instead of relying on subsequences, the authors in (Wickstrøm et al., 2022) proposed to use a novel approach to learn a compact representation of time series data. This approach, Mixup Contrastive Learning (MCL), does not rely on the concept of negative and positive representations directly. Instead, given two input series \mathbf{x}_1 and \mathbf{x}_2 , the proposed approach defines a weighted average $\bar{\mathbf{x}}$ of these two series as follows:

$$\bar{\mathbf{x}} = \lambda.\mathbf{x}_1 + (1 - \lambda).\mathbf{x}_2 \quad (1.78)$$

where λ is a real value between 0 and 1, representing the amount of mixing up from each of the two series. This parameter follows a beta distribution.

The self-supervised setup in Mixing Up (Wickstrøm et al., 2022) tries to predict the amount of contribution from each of the two input series. Assuming an input batch of N series, this batch is then randomly shuffled to two new batches $\{\mathbf{x}_1^{(1)}, \mathbf{x}_2^{(1)}, \dots, \mathbf{x}_N^{(1)}\}$ and $\{\mathbf{x}_1^{(2)}, \mathbf{x}_2^{(2)}, \dots, \mathbf{x}_N^{(2)}\}$. These two new batches now produces a set of weighted averages: $\{\bar{\mathbf{x}}_1, \bar{\mathbf{x}}_2, \dots, \bar{\mathbf{x}}_N\}$. The contrastive loss is then computed as follows for each sample in the batch:

$$\begin{aligned}
l_i = & -\lambda \cdot \log \frac{\exp(D_c(\mathbf{f}(\bar{\mathbf{x}}_i), \mathbf{f}(\mathbf{x}_i^{(1)}))/\tau)}{\sum_{j=1}^N (\exp(D_c(\mathbf{f}(\bar{\mathbf{x}}_i), \mathbf{f}(\mathbf{x}_j^{(1)}))/\tau) + \exp(D_c(\mathbf{f}(\bar{\mathbf{x}}_i), \mathbf{f}(\mathbf{x}_j^{(2)}))/\tau))} \\
& - (1 - \lambda) \cdot \log \frac{\exp(D_c(\mathbf{f}(\bar{\mathbf{x}}_i), \mathbf{f}(\mathbf{x}_i^{(2)}))/\tau)}{\sum_{j=1}^N (\exp(D_c(\mathbf{f}(\bar{\mathbf{x}}_i), \mathbf{f}(\mathbf{x}_j^{(1)}))/\tau) + \exp(D_c(\mathbf{f}(\bar{\mathbf{x}}_i), \mathbf{f}(\mathbf{x}_j^{(2)}))/\tau))}
\end{aligned} \tag{1.79}$$

where \mathbf{f} is the deep feature extractor, τ is the smoothness temperature parameter and $D_c(\cdot, \cdot)$ refers to the cosine similarity function. The final loss over all the batch of samples is the average loss over each sample as follows:

$$\mathcal{L}_{MixingUp} = \frac{1}{N} \sum_{i=1}^N l_i \tag{1.80}$$

The core idea of the above loss proposed in (Wickstrøm et al., 2022) is to somehow predict the amount of information each series contributed into the new weighted average series, however in the latent space instead of the original one. The backbone architecture used in the Mixing Up model is the FCN (Wang, Yan, and Oates, 2017).

1.3.3.2.3 Time Series Self-Supervised Contrastive Learning framework for Representation (TimeCLR) Instead of basing the triplet generation on subsequences or weighted averages, TimeCLR (Yang, Zhang, and Cui, 2022) defines, prior to training a self-supervised model, an AE network to be used for the generation of new samples. This AE network is trained to approximate the DTW distance between two raw series, by the ED between their latent representation extracted by the AE. The AE takes as input two series, and is trained to reconstruct both of them, such as in Eq. 1.72 using the MSE loss. However, the MSE loss is also computed between the DTW measure between those two series and the ED between their latent representation, as follows:

$$\mathcal{L}_{distance} = (DTW(\mathbf{x}_1, \mathbf{x}_2) - ED(\mathbf{z}_1, \mathbf{z}_2))^2 \tag{1.81}$$

where \mathbf{x}_1 and \mathbf{x}_2 are the two input series with their latent representations (encoder's output of the AE) \mathbf{z}_1 and \mathbf{z}_2 respectively.

This AE is then used to perform some augmentation of the input series. For instance, posterior to training the AE, each input series can now be transformed to a new series by simply extracting the latent feature vector from the encoder part of the AE, and feeding the decoder a noisy version of this vector. The output of the decoder is now an augmented version of the original input series. The above pipeline over one input series \mathbf{x} is summarized as follows:

$$\hat{\mathbf{x}} = D(E(\mathbf{x}) + \mathcal{N}(0, 1)) \tag{1.82}$$

where $E(\cdot)$ and $D(\cdot)$ are both the encoder and decoder of the pre-trained AE network.

This augmentation method is used to generated two views of each series in the dataset, for which these two views are fed to a deep learning model, with Inception (Ismail Fawaz et al., 2020) as a backbone, to be used in a contrastive learning setup. For instance, each series \mathbf{x}_i in a batch of N samples goes through the above augmentation method two times to obtain $\hat{\mathbf{x}}_i^{(1)}$ and $\hat{\mathbf{x}}_i^{(2)}$. These two augmented series are fed to the Inception network, with no final task layer, and the model's parameters

are optimized using the following contrastive loss on each sample in the batch:

$$l_i = -\log \frac{\exp(D_c(\mathbf{f}(\hat{\mathbf{x}}_i^{(1)}), \mathbf{f}(\hat{\mathbf{x}}_i^{(2)}))/\tau)}{\sum_{j \neq i} (\exp(D_c(\mathbf{f}(\hat{\mathbf{x}}_i^{(1)}), \mathbf{f}(\hat{\mathbf{x}}_j))/\tau) + \exp(D_c(\mathbf{f}(\hat{\mathbf{x}}_i^{(2)}), \mathbf{f}(\hat{\mathbf{x}}_j))/\tau))} \quad (1.83)$$

where $D_c(\cdot, \cdot)$ is the cosine similarity, \mathbf{f} is the deep learning feature extractor with the Inception architecture, and τ is the smoothness temperature parameter. The final loss over the whole batch is the average loss over all N samples:

$$\mathcal{L}_{TimeCLR} = \frac{1}{N} \sum_{i=1}^N l_i \quad (1.84)$$

The TimeCLR model learns how to represent two series that are an augmentation of the same original series, as much as close in the feature space, hence learning a compact representation space.

1.4 Conclusion

This Chapter has provided an in-depth exploration of the state-of-the-art methodologies in time series analysis, a crucial field in data science that focuses on extracting meaningful insights from time-dependent data. This chapter has navigated through both supervised and unsupervised learning techniques, each offering unique advantages and applications.

In the domain of supervised learning, we examined two primary tasks: Time Series Classification and Extrinsic Regression. Time Series Classification has seen a range of approaches over the years, from traditional distance-based methods like k-Nearest Neighbor with Dynamic Time Warping (k-NN-DTW) to modern deep learning architectures. Distance-based methods, while foundational, have evolved with innovations like SoftDTW and ShapeDTW, enhancing their ability to handle temporal distortions. Feature-based methods such as Catch22 and TSFresh have streamlined the process of extracting significant characteristics from time series data, facilitating their use in various classifiers. Interval-based methods, dictionary-based methods like BOSS and WEASEL, and convolution-based methods such as ROCKET and its variants have all contributed to the growing arsenal of tools for Time Series Classification, each addressing different aspects of the problem. Notably, hybrid models like HIVE-COTE have demonstrated the power of combining multiple approaches to achieve superior performance.

Deep learning methods have emerged as a dominant force in Time Series Classification, leveraging the parallelization capabilities of GPUs and the comprehensive feature extraction capabilities of architectures like Convolutional Neural Networks (CNNs), Recurrent Neural Networks (RNNs), and Self-Attention. These models have shown remarkable performance improvements, driven by their ability to learn complex temporal patterns directly from the data.

For unsupervised learning, the chapter covered essential tasks such as clustering, prototyping, and SSL. Clustering methods group similar time series, aiding in tasks like customer segmentation and anomaly detection. Prototyping techniques create representative examples of time series, simplifying the analysis of large datasets. SSL methods, which leverage the data itself to generate supervisory signals, have opened new avenues for extracting valuable insights without the need for labeled data.

In summary, this chapter has laid a comprehensive foundation for understanding the current landscape of time series analysis. This foundation sets the stage for the subsequent chapters, which will explore deeper into specific methodologies, their applications, and the nuances of implementing these advanced techniques in real-world scenarios. In the next chapter, we will explore the methods for comparing these models against each other by utilizing a wide range of different datasets to benchmark their performance.

Chapter 2

Benchmarking Machine Learning Models on Time Series Data

2.1 Introduction

Benchmarking machine learning models is a critical practice in the field of computer science and machine learning. This process involves comparing the performance of various algorithms across multiple datasets to determine their relative effectiveness and identify the state-of-the-art methods. Effective benchmarking is essential for understanding the strengths and weaknesses of different models, guiding future research, and improving algorithm design. In this chapter, we will explore the methodologies for benchmarking machine learning models on time series data, with a focus on the classification task.

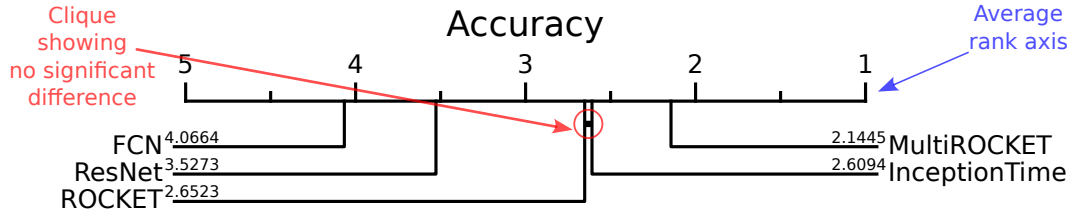
A crucial aspect of benchmarking involves hypothesis testing and the use of post-hoc tests for p-values and Null Hypothesis Significance Testing (NHST). Traditional methods like the Wilcoxon signed-rank test (Wilcoxon, 1992) and the Nemenyi test (Nemenyi, 1963) are commonly used but have significant limitations (Berrar, 2022), such as being prone to manipulation and providing limited insight into the true differences between model. Recent studies advocate for Bayesian methods (Benavoli et al., 2017) as more reliable alternatives for multiple comparisons.

We explore in this chapter the current method used for benchmarking, such as the Critical Difference Diagram (CDD) introduced by (Demšar, 2006), and discuss its evolution (Garcia and Herrera, 2008; Benavoli, Corani, and Mangili, 2016) and limitations. These traditional methods often suffer from issues such as instability in ranking and susceptibility to manipulation. To address these concerns, we will introduce the Multiple Comparison Matrix (MCM), a novel approach designed to provide more robust and interpretable comparisons.

2.2 Background and Current Benchmarking Methods

Following our exploration of the limitations inherent in traditional benchmarking methods, this section explores the current approaches used to evaluate classifiers. We address the challenge of summarizing the evaluation outcomes of m comparates $\mathcal{C} = \{c_1, \dots, c_m\}$ across multiple datasets $\mathcal{D} = \{d_1, \dots, d_n\}$ using a single performance measure $\gamma : \mathcal{C} \times \mathcal{D} \rightarrow \mathbb{R}$, that assesses the performance of a compare $c \in \mathcal{C}$ on a task $d \in \mathcal{D}$. Each task (dataset) involves training a classifier λ on a time series training set, with performance measured by the accuracy of λ on a corresponding time series test set. In this context, the comparates \mathcal{C} are the time series classifiers, the tasks \mathcal{T}

FIGURE 2.1: Critical Difference Diagram between five state-of-the-art models of TSC evaluated on 128 datasets of the UCR archive highlighting the **average rank** of each model over all datasets. If a **clique** is formed between two models it means that no conclusion can be made on the statistical significance in difference of performance between this pair of models.



are the classification problems derived from 128 datasets in the UCR archive (Dau et al., 2019), and the performance measure γ is the classification accuracy.

2.2.1 Ranking Comparates

A common approach to summarize such evaluation is through ranking each of the compare independently for each dataset for which we can produce an average rank per compare overall datasets. The Critical Difference Diagram (CDD) (Demšar, 2006) is currently the primary method used for multi-compare and multi-dataset benchmarking. This diagram provides two types of comparisons: (1) a group-wise comparison using the mean rank of each compare, and (2) a pairwise comparison indicating which pairs of compares show significant performance differences. An example is shown in Figure 2.1 where each compare is assigned an average rank overall datasets and if a clique (straight line) exists amongst a set of compares it highlights that no conclusion can be found on the statistical significance in difference of performance between these compares.

The mean rank is computed as follows. Each compare c_i is assigned a rank $R_{c_i}^{d_k}$ on each task d_k with $k \in [1, n]$ based on its relative performance score γ :

$$R_{c_i}^{d_k} = 1 + |\{c_j \in \mathcal{C} \setminus c_i : \gamma(c_j, d_k) \succ \gamma(c_i, d_k)\}| + \frac{1}{2} \cdot |\{c_j \in \mathcal{C} \setminus c_i : \gamma(c_i, d_k) = \gamma(c_j, d_k)\}|, \quad (2.1)$$

where \succ means *better than*. For example, if γ represents the accuracy on the test set, then a higher accuracy means a *better* model, however if γ represents the error rate, then a lower error rate means a *better* model. Each compare is then assigned an Average Rank (AR) by averaging its ranks over all n datasets in \mathcal{D} ,

$$\text{AR}_{c_i}^{\mathcal{D}} = \frac{\sum_{k=1}^n R_{c_i}^{d_k}}{n}. \quad (2.2)$$

The lower the AR value, the better the performance assessment relative to competing comparators. The placement of the compares in the diagram in Figure 2.1 follows their AR.

2.2.2 Pairwise Comparisons with the CDD

Originally, the CDD proposed in (Demšar, 2006) also emphasizes the significance of performance differences between each pair of compares. This significance test is crucial for determining whether it is necessary to adopt the *better* model with the

lowest AR (AR_1). However, there may be another model with an AR (AR_2) very close to AR_1 (i.e., $AR_2 = AR_1 + \epsilon$, where $0 < \epsilon \ll 1$) that is significantly faster and less complex than the *winning* model (see example between InceptionTime and ROCKET in Figure 2.1).

The method to assess this statistical significance in difference of performance has been changed throughout the years. For instance, the original CDD utilized the Nemenyi test (Nemenyi, 1963), based on the actual values of the AR. However, (Benavoli, Corani, and Mangili, 2016) argued that using a post-hoc test following the AR values may be miss-leading and proposed the usage of the Wilcoxon Signed Rank Test for pairwise significance comparison and the Friedman test (Friedman, 1940) for group-wise significance comparison.

2.2.2.1 Friedman Test

The Friedman test (Friedman, 1940) is a non-parametric statistical test used to detect differences in treatments across multiple test attempts. It is particularly useful for comparing multiple algorithms over multiple datasets. Given m algorithms and n datasets, this test ranks the performance of algorithms for each dataset and then analyzes these ranks to determine if there are statistically significant differences between the algorithms.

Let $R_{c_i}^{d_k}$ be the rank of the i_{th} compare c_i on the k_{th} dataset d_k . The test's objective is to determine if at least one of the m compares performs significantly better than all other compares. This is determined by following these steps below:

1. Compute the rank sums for each compare:

$$R_{c_i} = \sum_{k=1}^n R_{c_i}^{d_k} \quad (2.3)$$

2. Calculate the Friedman test statistic:

$$\chi_F^2 = \frac{12}{n.m.(m+1)} \sum_{i=1}^m R_{c_i}^2 - 3n.(m+1) \quad (2.4)$$

3. Determine the p-value: The test statistic χ_F^2 approximately follows a chi-squared distribution with $m.(m+1)$ degrees of freedom. The p-value is computed based on this distribution. A low p-value (typically less than $\alpha = 0.05$) indicates that at least one of the algorithms performs significantly differently from the others.

While the Friedman test is useful for identifying differences between multiple algorithms, it has several limitations:

- **Magnitude Ignored:** The test only considers the ranks of the algorithms, not the magnitude of the differences in performance. As a result, small and large differences are treated equally.
- **Instability:** The results of the Friedman test can be sensitive to the set of compares included in the analysis. Adding or removing an algorithm can change the conclusions about the relative performance of the remaining algorithms.
- **Post-hoc Analysis Needed:** To determine which specific algorithms differ from each other, a post-hoc test (such as the Nemenyi test) is required, adding complexity to the analysis.

2.2.2.2 Nemenyi Test

The Nemenyi test (Nemenyi, 1963) is a post-hoc statistical test used to determine whether the performance differences between pairs of algorithms are statistically significant. The Nemenyi test is typically applied after conducting a Friedman test, which assesses whether there are any overall differences among multiple algorithms across multiple datasets. The Nemenyi test compares the mean ranks of all pairs of algorithms and determines if the differences in their ranks exceed a critical value, which would indicate a statistically significant difference in performance. Mathematically, the Critical Difference (CD) for the Nemenyi test is calculated as follows:

$$CD = q_\alpha \sqrt{\frac{m(m+1)}{6n}} \quad (2.5)$$

where q_α is the critical value from the Studentized range distribution, which depends on the desired significance level α , usually set to 0.05 and the number of comparates m .

Two algorithms c_i and c_j are considered to have a statistically significant difference in performance if the absolute difference in their ARs exceeds the critical difference:

$$|AR_{c_i}^{\mathcal{D}} - AR_{c_j}^{\mathcal{D}}| > CD \quad (2.6)$$

where $AR_{c_i}^{\mathcal{D}}$ and $AR_{c_j}^{\mathcal{D}}$ are the ARs of both comparates c_i and c_j respectively on all datasets \mathcal{D} . If this condition is met, it can be concluded that the performance of the two algorithms differs significantly at the given significance level α . However, if the condition is not met, it does not imply that the two comparates are equivalent in performance. Rather, it suggests that, given the set of n datasets \mathcal{D} , there is insufficient evidence to conclude a statistically significant difference in performance between the two comparates.

However, this test has several limitations (Benavoli, Corani, and Mangili, 2016):

- **Rank-Only Consideration:** It only considers the ranks of the comparates, focusing solely on the number of tasks where one compare performs better or worse than others.
- **Ignoring Magnitude Differences:** The test does not take into account the magnitude of performance differences, treating small and large differences equally.
- **Results Instability:** The test's results are unstable with respect to the set of comparates included in the evaluation.
- **Sensitivity to Compare Changes:** The inclusion or exclusion of a single compare can significantly alter the pairwise conclusions drawn for the remaining comparates.

2.2.2.3 Wilcoxon Signed-Rank Test

The Wilcoxon signed-rank test is a non-parametric statistical test used to compare two related samples, matched samples, or repeated measurements on a single sample. It is the non-parametric alternative to the Nemenyi test (Section 2.2.2.2), where (Benavoli, Corani, and Mangili, 2016) questions the following: “*Should we really use post-hoc tests based on mean-ranks?*”. This test was proposed in (Wilcoxon,

1992) as a means to test for differences in the median values of two related groups without assuming that the differences follow a normal distribution.

Given n datasets, the Wilcoxon signed-rank test can be used to compare the performance of two specific comparates, c_i and c_j evaluated across these n datasets. The steps are as follows:

1. Compute the differences between the performance of the two comparates for each dataset:

$$D_k = \gamma(c_i, d_k) - \gamma(c_j, d_k) \quad \text{for } k \in [1, n] \quad (2.7)$$

where $\gamma(c_i, d_k)$ and $\gamma(c_j, d_k)$ are the performance of both comparates c_i and c_j evaluated on the test set of the k_{th} dataset $d_k \in \mathcal{D}$.

2. Rank the absolute values of the differences, ignoring the signs, and assign ranks RD_k . If there are ties, assign the average rank to both values.
3. Restore the signs to the ranks, resulting in signed ranks sRD_i
4. Calculate the test statistic W^+ , which is the sum of the positive ranks:

$$W^+ = \sum_{k: sRD_k > 0} |sRD_k| \quad (2.8)$$

5. Calculate the test statistic W^- , which is the sum of the negative ranks:

$$W^- = \sum_{k: sRD_k < 0} sRD_k \quad (2.9)$$

6. Use the smaller of the two sums, $W = \min(W^+, W^-)$ as the test statistic
7. Determine the p-value: The p-value is calculated based on the distribution of W . For large sample sizes (typically $n > 30$), the distribution of W approaches a normal distribution, and a z-score can be used. For smaller samples, exact tables or software can be used to find the p-value. If this p-value is lower than a threshold α (usually set to 0.05), then the difference of performance between both comparates c_i and c_j on the n datasets is statistically significant. However if the p-value is higher than α , then the n datasets are not enough to find a conclusion on the statistical significance in difference of performance between c_i and c_j .

While the Wilcoxon signed-rank test is robust and widely applicable, it has several limitations:

- **Sensitivity to Outliers:** Like many non-parametric tests, the Wilcoxon signed-rank test can be sensitive to outliers, which can disproportionately influence the results.
- **Dependent Observations:** The test assumes that the pairs of observations are independent of each other. If there is dependence, the results may not be valid. Such dependency exists when two comparates are the same approach but one being a weaker version than the other.

Holm Correction for Multiple Pairwise Comparison When we need to find the p-values for multiple paired comparates among m comparates, the Wilcoxon signed-rank test is often used in conjunction with the Holm correction (Holm, 1979). The Holm correction is a method for controlling the family-wise error rate when performing multiple comparisons. It adjusts the significance levels for each hypothesis test to account for the multiple comparisons being made.

Given m comparates and the significance threshold α , we have $\hat{m} = \frac{m \cdot (m - 1)}{2}$ p-values between all possible pairs of comparates: $p_1, p_2, \dots, p_{\hat{m}}$. The Holm correction is applied as follows:

1. Order the p-values from smallest to largest
2. Compute the adjusted significance level for each ordered p-value p_v as such:

$$\alpha_v = \frac{\alpha}{\hat{m} - v + 1} \quad (2.10)$$

3. Compare each ordered p-value p_v to its corresponding adjusted significance level α_v :
 - Reject the null hypothesis for p_v if $p_v \leq \alpha_v$
 - Stop testing as soon as you fail to reject a null hypothesis (i.e. when $p_v > \alpha_v$)

2.3 Limitations of the CDD

A significant benefit of the CDD is its ability to distill a large volume of information into a format that is easy to understand. However, this simplification introduces several shortcomings. We will discuss three key issues with the CDD: (1) the inconsistency of the average rank, (2) the failure to adequately account for the magnitude of performance differences and (3) the adverse effects of applying multiple testing corrections.

2.3.1 Instability of the Average Rank

The CDD arranges comparates based on their average rank (see Section 2.2.1). However, this average rank can vary with the addition or removal of comparates. The relative ranking of a group of comparates \mathcal{C} , can shift when one or more comparates are added or removed, as illustrated in Figures 2.2 and 2.3.

In particular, Figure 2.2 demonstrates that by replacing ResNet with STSF in the set of comparates, DrCIF changes its rank relative to InceptionTime, from a worse to a better rank. This shift also alters the pairwise significance between DrCIF and InceptionTime from not significant to significant. (In this scenario, ResNet is a weaker deep learning algorithm compared to InceptionTime, and STSF is a weaker interval method compared to DrCIF.)

Figure 2.3 shows how adding a weaker version of a compare (e.g., a different version of a classifier with fewer parameters or different hyperparameter tuning) can influence the mean rank and pairwise statistical significance. Adding a weaker version of a compare can significantly elevate the rank of the original compare and change the statistical significance of pairwise differences between comparates. The original

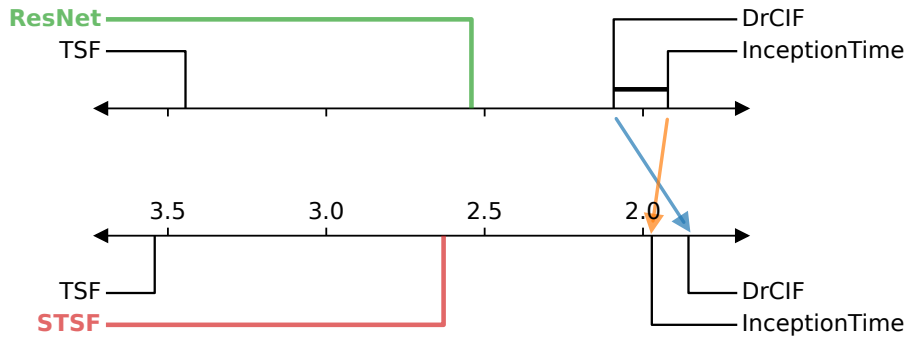


FIGURE 2.2: Manipulation of the ranks of DrCIF and InceptionTime and the statistical significance of their pairwise differences by inclusion of similar comparates. When **ResNet** is replaced by **STSF**, DrCIF moves from a “worse” to a “better” rank, and the pairwise differences between DrCIF and InceptionTime change from being not statistically significant to statistically significant.

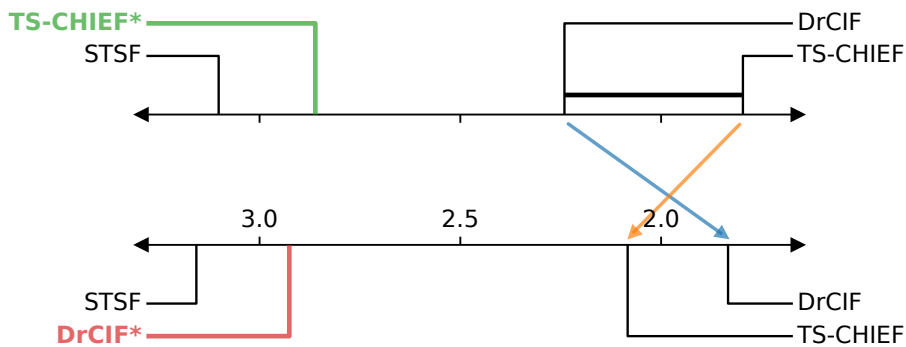


FIGURE 2.3: Manipulation of the ranks of DrCIF and TS-CHIEF and the statistical significance of their pairwise differences by inclusion of weakened comparates. When a weakened variant of TS-CHIEF (**TS-CHIEF***) is replaced by a weakened variant of DrCIF (**DrCIF***), DrCIF moves from a “worse” to a “better” rank and the pairwise differences between DrCIF and TS-CHIEF change from being not statistically significant to statistically significant.

compare, being more accurate than its weaker version, will have a better mean rank on many tasks, resulting in a lower p-value in the Wilcoxon signed-rank test, which can shift pairwise differences to become statistically significant under the Holm correction.

Therefore, we suggest that comparates should be ordered using a statistical measure that remains stable regardless of the addition or removal of other comparates. This approach ensures that the relative ranking of different comparates is consistent across studies and not susceptible to manipulation, either intentionally or unintentionally.

2.3.2 Insufficient Attention to the Magnitude of Wins and Losses

The mean rank evaluates the frequency with which a compare outperforms or underperforms others across multiple tasks, such as achieving higher or lower classification accuracy. It does not consider the extent of these performance differences. Therefore, a compare might achieve a low average rank through several minor wins while also experiencing significant losses. For instance, if a compare c_i has a 90% likelihood of a slight loss against c_j but a 10% likelihood of a substantial gain, most would prefer c_i . Nevertheless, mean rank would heavily favor c_j .

While the Wilcoxon test somewhat considers the magnitude of wins, it does not fully resolve the issue when comparisons are primarily based on rank, as illustrated in the CDD of Figures 2.2 and 2.3.

2.3.3 Null Hypothesis Significance Testing

The practice of using statistical significance tests to evaluate performance on benchmark tasks is facing growing criticism. (Benavoli et al., 2017) asserts that null hypothesis significance testing (NHST), such as the Wilcoxon test, is not optimal for benchmarking scenarios involving multiple comparates and multiple tasks for four main reasons. This viewpoint is also echoed by (Berrar, 2022).

First, Null hypothesis significance testing (NHST) does not provide the probability of the alternative hypothesis (the hypothesis that there is a difference between comparates given the observed results). Instead, NHST calculates the likelihood of observing the outcomes O assuming the null hypothesis H_0 is true, represented as $p(O|H_0)$, meaning there is no difference between comparates. (Benavoli et al., 2017) suggests that a more meaningful assessment would be $p(H_0|O)$, the probability of the null hypothesis being *true* given the observed outcomes.

Second, (Benavoli et al., 2017) highlights that the null hypothesis can always be rejected by simply increasing the number of examples, a point we revisit in Section 2.3.4.

Third, (Benavoli et al., 2017) claims that NHST fails to indicate the magnitude of differences between comparates, regardless of how small the p-value might be. For instance, if one compare's accuracy is only 10^{-4} higher than another's on most benchmark tasks, the p-value (e.g., from a Wilcoxon test) could be extremely low, misleadingly suggesting a significant difference in accuracy. However, the p-value does not provide any insight into the actual magnitude of the performance difference between comparates. This problem is related to, but separate from, the issue discussed in Section 2.3.2, where ranks do not reflect the magnitude of performance differences between comparates.

Finally, because the p-value indicates the likelihood of observing the given outcomes under the assumption that the null hypothesis is true, it does not directly reflect the probability that the null hypothesis itself is true. Therefore, a large p-value (which might suggest that differences are not statistically significant) does not actually confirm or refute the null hypothesis (Lecoutre et al., 2014).

2.3.3.1 Inferential vs Descriptive Statistics

The p-value derived from a statistical hypothesis test is often utilized as an inferential statistic rather than a descriptive one. Descriptive statistics accurately summarize the empirical properties of the results, whereas inferential statistics attempt to draw conclusions about the population from which the data was sampled. Practically, inferential statistics aim to predict or quantify how a comparee would perform on new or unseen data randomly drawn from the same source. Inferential statistics make stronger claims about the results by relying on stronger assumptions.

For instance, when applying the Wilcoxon test to two comparates c_i and c_j over n tasks $\mathcal{D} = \{d_1, \dots, d_n\}$, we obtain performance measures $\gamma(c_i, d_1), \dots, \gamma(c_i, d_n)$ and $\gamma(c_j, d_1), \dots, \gamma(c_j, d_n)$. The two-tailed Wilcoxon test returns the probability p that the differences $\gamma(c_i, d_1) - \gamma(c_j, d_1), \dots, \gamma(c_i, d_n) - \gamma(c_j, d_n)$ would be observed if these values were an independent and identically distributed (iid) sample from a distribution Ω that is symmetric around zero. As an inferential statistic, we reject the null hypothesis that the distribution of these differences is symmetric if $p\text{-value} \leq \alpha$, where α is the chosen significance level. The p-value represents the probability of obtaining a test statistic as extreme as, or more extreme than, the one observed, purely by chance, if the comparates were selected without prior knowledge of the data.

In traditional scientific experiments, this approach is feasible because data is typically collected freshly for each experiment. However, in many benchmarking scenarios, researchers select comparates based on algorithms and hyper-parameters that perform well on the given benchmark. They do not collect new benchmark data by re-sampling from the problems that define the benchmark. Therefore, it is difficult to identify a meaningful distribution from which the performance scores could be considered an iid sample, making the use of the test statistic and p-value for inferential purposes problematic.

Despite these issues, test statistics and p-values are valuable for measuring divergence between two or more sets of data points (e.g., the classification accuracies of two comparates). They provide a quantitative descriptive measure of performance differences between comparates.

2.3.4 The Use of Multiple Test Corrections

When performing multiple tests, such as Wilcoxon tests between all pairs of comparates, it is generally accepted that the significance level (typically 0.05) should be adjusted (Demšar, 2006; Benavoli et al., 2017; Berrar, 2022). Multiple test corrections aim to manage the risk of incorrectly rejecting any null hypothesis when several null hypotheses are tested simultaneously. The Holm correction (Holm, 1979) is a widely used method for this purpose (see Section 2.2.2.3 for details on the Holm correction).

We identify that it is more crucial to control the risk for each pair of comparates rather than for the entire study. We also show that multiple testing corrections can introduce undesirable effects, potentially leading to the manipulation of benchmark

results. This undermines efforts to provide a consistent and stable comparison of multiple comparates across tasks.

A significant issue is that the number of comparates in a study and the specific comparates included can affect the likelihood of one compare outperforming another (Benavoli et al., 2017). This enables the manipulation of the statistical significance of differences between comparates, whether intentionally or unintentionally, by including or excluding certain comparates from the comparison.

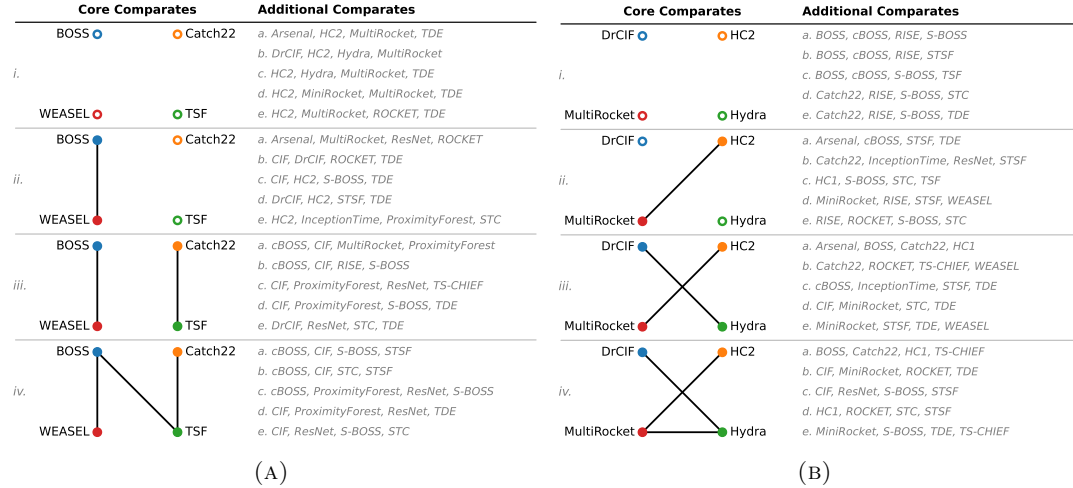


FIGURE 2.4: Two examples demonstrate the instability of pairwise significance under the Holm correction: (a) for the comparates BOSS, Catch22, TSF, and WEASEL; and (b) for the comparates DrCIF, HC2, Hydra, and MultiRocket. The statistical significance of pairwise differences between comparates is influenced by the additional comparates included in the comparison. In each case, four different patterns of statistically significant pairwise differences, (i), (ii), (iii), and (iv), are shown in the left column (pairs with non-significant differences according to the Wilcoxon signed-rank test with Holm correction are connected by a black line). Randomly chosen examples of additional comparates that result in the given pattern of statistically significant pairwise differences are shown in the right column.

To highlight the instability of pairwise significance when using the Holm correction, we illustrate how different sets of comparates influence the results. Figure 2.4 shows two examples of this instability, demonstrating how the statistical significance of pairwise differences can change with different sets of comparates. In each example, we begin with a core set of four comparates and repeatedly combine this core set with different sets of four additional comparates. For each combination, the Wilcoxon test with Holm correction was applied to all pairs, noting which pairwise differences within the core set were statistically significant. Non-significant pairwise differences within the core set are indicated by lines connecting the comparates.

Figure 2.4 presents results for core sets consisting of (a) BOSS, Catch22, TSF, and WEASEL; and (b) DrCIF, HC2, Hydra, and MultiRocket. These examples are based on results for 23 different comparates across 108 datasets from the UCR archive. For instance, in Figure 2.4(a), combining comparates BOSS, Catch22, TSF, and WEASEL with any of the five sets of comparates listed for pattern (ii), such as Arsenal, MultiRocket, ResNet, and Rocket, produces the pattern shown on the left, where the pairwise differences between BOSS and WEASEL are not statistically

significant. However, combining the same core comparates with any of the sets listed in (i), (iii), or (iv) results in different patterns of statistical significance.

The examples in Figure 2.4 illustrate that the statistical significance of pairwise differences can be influenced by adding or removing comparates, whether intentionally or unintentionally. In many instances, various different sets of additional comparates can result in the same pattern of statistical significance for pairwise differences. For instance, in Figure 2.4(b), there are 123 different sets of additional comparates that produce pattern (i), 1,876 sets that produce pattern (ii), 680 sets that produce pattern (iii), and 1,197 sets that produce pattern (iv). For simplicity, only five randomly selected combinations of additional comparates are shown for each pattern in Figure 2.4.

This issue occurs because a multiple testing correction, such as the Holm correction, adjusts the threshold for statistical significance based on the p-values of all pairs of comparates. Consequently, the significance of pairwise differences for a given pair of comparates depends on the p-values of all other pairs. Adding or removing comparates with small p-values can shift pairwise differences above or below the threshold for significance. For a given pair of comparates, including or excluding other comparates can turn an otherwise significant difference into a non-significant one, and vice versa.

Another issue is that multiple test corrections aim to prevent any algorithm from being incorrectly found superior by chance. However, this comes at the expense of increasing the risk of overlooking true findings of superiority. It is debatable why one risk should be prioritized over the other. The ability to claim that a new algorithm is not significantly less effective than the current state-of-the-art allows proponents to add enough algorithms to a comparison to achieve such a claim.

To avoid the “data dredging” problem, the adjustment for multiple testing should ideally consider the total number of comparates, including all variations of an algorithm that were tested and discarded during development. However, this is often impractical, suggesting that such efforts may be futile.

Moreover, different studies might produce varying results for pairwise comparisons of the same two competitors depending on the number of comparates included. A study with fewer comparates might reject the null hypothesis and find a significant difference between comparates c_i and c_j , whereas a study with more comparates might fail to reject the null hypothesis, finding no significant difference based on the same evidence. This inconsistency undermines the reliability of such evidence bases.

2.4 An Alternative Approach

As previously mentioned, recent studies have attempted to tackle some of these issues, especially regarding the statistical significance testing of pairwise differences between comparates. Notably, we emphasize the approach proposed by (Benavoli et al., 2017).

(Benavoli et al., 2017) argued that the Wilcoxon test, or similar tests, should be replaced by a new Bayesian test modeled after the Wilcoxon test. For comparing two comparates c_i and c_j , the Bayesian signed rank test generates a probability distribution indicating the likelihood that c_i is significantly better than c_j , c_j is significantly better than c_i , or c_i and c_j are not significantly different.

Let $\mathbf{z} = [z_0, z_1, \dots, z_i, \dots, z_q]$ be the vector of performance differences between c_i and c_j across q tasks, including a pseudo observation z_0 , a hyperparameter of the

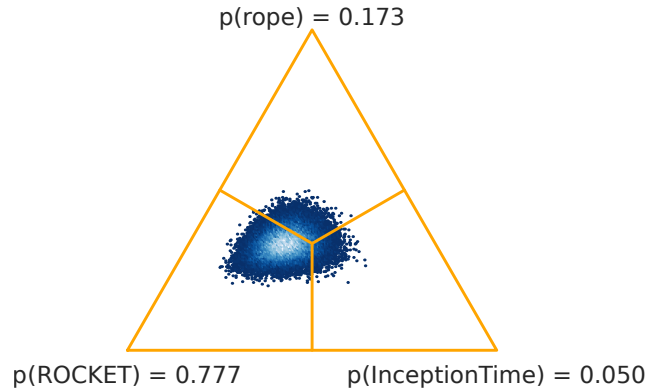


FIGURE 2.5: A visualization of the Bayesian Signed Rank Test proposed in (Benavoli et al., 2017) as a replacement for the Wilcoxon Signed Rank Test is provided. As illustrated, the Bayesian test offers information on the probability that the null hypothesis is true, given the performance metrics of both InceptionTime and ROCKET on the 108 tasks from the UCR archive.

Dirichlet Process (DP). Assuming \mathbf{z} follows a DP, the resulting probability distribution is given by:

$$\begin{aligned}
 \theta_l &= \sum_{i=0}^q \sum_{j=0}^q \omega_i \omega_j \mathbf{I}_{(-\infty, -2r)}(z_i + z_j) \\
 \theta_e &= \sum_{i=0}^q \sum_{j=0}^q \omega_i \omega_j \mathbf{I}_{(-2r, 2r)}(z_i + z_j) \\
 \theta_r &= \sum_{i=0}^q \sum_{j=0}^q \omega_i \omega_j \mathbf{I}_{(2r, \infty)}(z_i + z_j),
 \end{aligned} \tag{2.11}$$

where $\mathbf{I}_A(x) = 1$ if $x \in A$, the weights ω_i follow a Dirichlet distribution $D(s, 1, 1, \dots, 1)$ and r is the “rope” value that sets the interval of which the two classifiers have no significant difference. Given that the distribution θ_l , θ_e , and θ_r does not have a closed form solution, the probability distribution is generated using a Monte Carlo sampling on the weights ω_i .

An example of this Bayesian test is shown in Figure 2.5, comparing InceptionTime (Ismail Fawaz et al., 2020) and ROCKET (Dempster, Petitjean, and Webb, 2020) on 108 datasets from the UCR archive (Dau et al., 2019). The triangle illustrates that there is a 77.7% probability that ROCKET outperforms InceptionTime, with only a 17.3% probability that the classifiers are not meaningfully different.

Considering the limitations discussed in this chapter, there is a clear need for an alternative approach instead of the CDD. The method proposed by (Benavoli et al., 2017) highlights the importance of measuring the statistical significance of pairwise differences between classifiers as an alternative to the Wilcoxon signed-rank test. This Bayesian approach is not mutually exclusive with the method described in the following section; instead, we consider it complementary. These efforts are geared towards enhancing the robustness of statistical testing for differences between comparates. Instead of relying on p-values derived from the Wilcoxon signed-rank test, the probabilities computed via the Bayesian signed-rank test could be utilized

in the alternative approach detailed in the subsequent section.

2.5 The Multi-Comparison Matrix

Our goal is to develop methods for assessing m comparates \mathcal{C} across multiple datasets \mathcal{D} using a single performance measure γ and pairwise comparison measure δ that:

- prioritizes pairwise comparisons between comparates;
- focuses on descriptive statistics over statistical hypothesis testing;
- ensures that pairwise comparisons $\delta(c_i, c_j)$ between any two comparates $c_i \in \mathcal{C}$ and $c_j \in \mathcal{C}$ are invariant to $\mathcal{C} \setminus \{c_i, c_j\}$ (i.e., no pairwise comparison will change with the addition or deletion of other comparates, maintaining consistency across studies);
- orders comparates such that the relative order of any two comparates $c_i \in \mathcal{C}$ and $c_j \in \mathcal{C}$ is invariant to $\mathcal{C} \setminus \{c_i, c_j\}$ (i.e., the order of c_i and c_j will not change with the addition or deletion of other comparates, ensuring stability across studies);
- provides a good balance between the amount of information presented and the informativeness of that information.

To achieve this, we propose a grid of pairwise comparison statistics, as shown in Figures 2.6 and 2.7. The proposed Multi-Comparison Matrix (MCM) maintains the pairwise comparisons between each pair of comparates c_i and c_j , ordering the comparates by default based on the average performance measure γ . Each cell of this matrix contains three pairwise statistics between c_i , the compare for the row, and c_j , the compare for the column. These three statistics are:

- The mean of $\gamma(c_i, d) - \gamma(c_j, d)$ over all $d \in \mathcal{D}$;
- A Win Tie Loss count for c_i against c_j over all the tasks (datasets) in \mathcal{D} ;
- A p-value (p) for a Wilcoxon Signed Rank Test (δ).

Note that despite concerns about using statistical significance testing for benchmarking, we continue to use the Wilcoxon test and the associated p value. While there are arguments for excluding formal statistical hypothesis tests, we recognize that this may be too drastic for many. Therefore, we prioritize descriptive statistics. However, considering the issues discussed above, we encourage interpreting the p value as a *descriptive* statistic, a measure of the "strength" of the difference between comparates, rather than as an inferential statistic. In other words, the p value should not be viewed as indicating the likelihood or probability of observing a similar difference in accuracy between comparates on new or unseen data (i.e., "out of benchmark").

By default, the MCM is generated with all comparates present in both the rows and the columns, resulting in $m \times (m - 1)/2$ comparisons. Alternatively, separate lists of comparates for the rows and columns can be specified, \mathcal{C}_{row} and \mathcal{C}_{col} . In this case there are $|\mathcal{C}_{\text{row}}| \times |\mathcal{C}_{\text{col}}| - |\mathcal{C}_{\text{row}} \cap \mathcal{C}_{\text{col}}|$ comparisons.

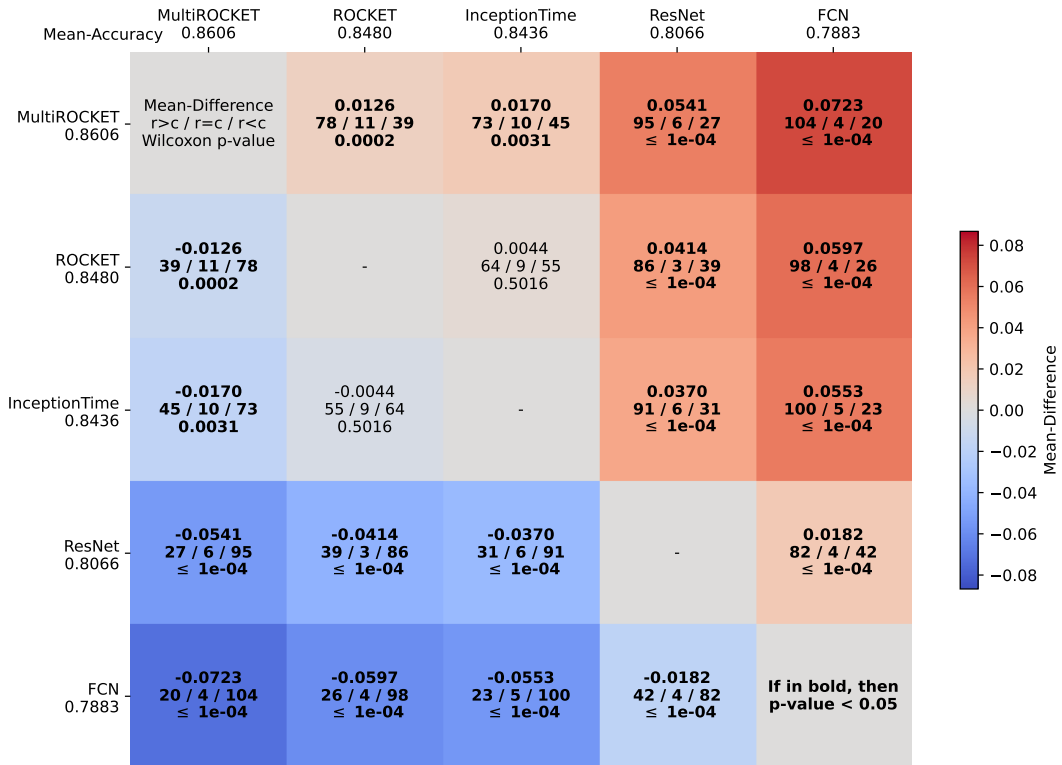


FIGURE 2.6: MCM showing all pairwise comparisons between MultiROCKET, ROCKET, InceptionTime, ResNet, and FCN on the 128 datasets of the UCR archive. In this setup, the full pairwise comparison is presented.

2.5.1 MCM Examples

By default, all pairwise comparisons between comparates are displayed. The average performance measure γ (e.g., classification accuracy) across all tasks \mathcal{D} is shown next to each compare label. An example illustrating the results for five comparates over 108 datasets from the UCR archive (Dau et al., 2019) is provided in Figure 2.6. In the Heat Map, colors represent the mean difference in γ . A positive difference (red) indicates that the row compare outperforms the column compare on average. For instance, in Figure 2.6, the top right cell is red, demonstrating that MultiROCKET (row) is generally more accurate than ResNet (column). Conversely, a negative difference (blue) means that the column compare outperforms the row compare on average. Text in each cell is in **BOLD** if the p value is below a specified threshold (e.g., 0.05).

This format of the MCM is highly effective for presenting comparisons in a benchmark review, such as in (Ismail Fawaz et al., 2019). In such reviews, detailed information on all pairwise comparisons is essential to highlight the strengths and weaknesses of each compare. For example, this MCM format can illustrate how a compare that performs poorly against the winning compare might still excel on certain datasets compared to other state-of-the-art comparates.

However, if a study focuses on a few specific comparates, such as when introducing a new algorithm, it is often more beneficial to highlight comparisons between these few and many existing alternatives. In these scenarios, the MCM can be adjusted to display only the necessary results for comparing the proposed comparates with the current state-of-the-art. This allows the reader to focus on the most pertinent

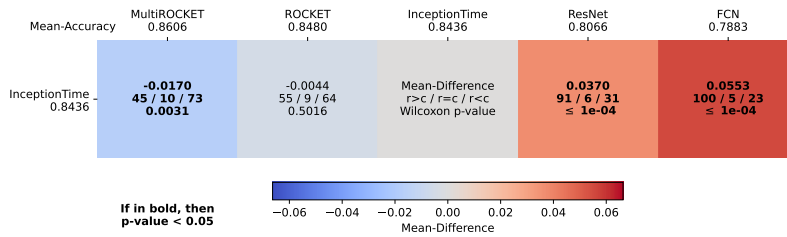


FIGURE 2.7: MCM showing pairwise comparisons between InceptionTime and each of ROCKET, MultiROCKET, FCN and ResNet on the 128 datasets of the UCR archive.

comparisons. The proposed compares are listed in either a row or a column of the matrix, as illustrated in Figure 2.7.

2.6 Conclusion

In this chapter, we have explored the critical aspects of benchmarking machine learning models on time series data. The discussion began with an examination of the significance of rigorous benchmarking and the various challenges associated with it, including the instability of pairwise comparisons and the inherent limitations of traditional statistical significance tests. These challenges highlight the necessity for developing more robust and reliable benchmarking techniques.

We detailed the Critical Difference Diagram (CDD), a widely utilized tool for visualizing the performance of multiple comparates across various tasks. While the CDD provides valuable insights, it also has significant limitations, such as its sensitivity to the addition or removal of comparates and its reliance on average ranks that may not adequately reflect performance differences.

To address these limitations, we proposed the Multi-Comparison Matrix (MCM) as a novel approach for presenting pairwise comparisons between comparates. The MCM preserves the integrity of pairwise comparisons and ensures that these comparisons remain consistent regardless of the inclusion or exclusion of other comparates. This method offers a more stable and comprehensive view of comparative performance, enabling researchers to make more informed decisions about model selection and evaluation.

The usage of MCM is not intended to act as a “replacement” for the CDD, as the CDD remains and will continue to be more “attractive” due to its simplicity. Instead, we propose that the MCM should serve as a complementary analysis tool alongside the CDD in future research, such as we do in the following Chapter.

Chapter 3

Towards Finding Foundation Models for Time Series Classification

3.1 Introduction

In the dynamic field of TSC, the quest for developing models that are robust and adaptable across diverse datasets remains a significant challenge. Foundation models, which are large pre-trained models capable of generalizing across various tasks, offer a promising solution to this problem. The necessity of foundation models arises from their ability to simplify and expedite the fine-tuning process. In many real-world applications, such as predicting heart conditions from ECG signals or forecasting traffic patterns, starting model training from scratch is time-consuming and computationally expensive. Foundation models mitigate these challenges by offering a pre-trained base that already understands the fundamental patterns within a domain. Consequently, fine-tuning becomes a matter of adapting this base model to the nuances of a specific dataset, leading to faster and more efficient training with improved performance. For instance, in the medical field, a model pre-trained on various ECG datasets can be fine-tuned to detect arrhythmias with greater accuracy and speed. Similarly, in traffic management, a model pre-trained on traffic data from multiple cities can be fine-tuned to predict congestion patterns in a specific city. This allows for more accurate and efficient traffic control solutions tailored to local conditions.

This chapter introduces two key contributions aimed at advancing towards deep foundation models: the creation of hand-crafted convolution filters to enhance model generalization, and the utilization of a pre-training methodology to fine-tune these models for specific classification tasks. These filters are designed to shift the model's focus from specific features to more fundamental, general characteristics that are independent of any particular domain. This ensures that the model can identify and leverage intrinsic patterns within the data, making it more adaptable across various tasks. Building on this, our second contribution incorporates a model that utilizes our hand-crafted filters to develop a preliminary foundation model. This model undergoes extensive pre-training on multiple datasets within the same domain, such as ECG or traffic data, aiming to predict the original dataset of each series. This pre-training equips the model with a broad understanding of domain-specific patterns, providing a strong foundation for subsequent fine-tuning. Once pre-trained, the model is fine-tuned on individual datasets to address specific classification tasks.

By combining the strengths of hand-crafted filters with a robust pre-training and fine-tuning methodology, we aim to construct a foundation model that is both versatile and powerful. These contributions not only enhance the model's performance

across varied TSC tasks but also represent a significant step towards the development of deep foundation models in this domain.

3.2 Hand-Crafted Convolution Filters

The development of deep learning models for time series classification often encounters significant challenges, such as overfitting, computational complexity, and redundancy in learned filters. Traditional CNNs (Ismail Fawaz et al., 2020) typically learn filters through back-propagation, where filters are initialized randomly and refined during training. While effective, this process can lead to several issues:

- **Overfitting:** Learned filters may become overly specialized to the training data, reducing the model’s ability to generalize to new, unseen data
- **Time Spent on Learning “Easy” Features:** During training, models may spend significant time learning simple, generic features that could have been predefined, rather than focusing on complex features that are more difficult to construct by hand.
- **Difficulty in Finding Generic Filters:** While learning simple filters from scratch is feasible, the process becomes significantly more challenging for complex filters due to error propagation, making it difficult to generalize filters that work effectively across various datasets.

3.2.1 Are There Any Common Learned Convolution Filters Between Datasets?

One approach to address issues like overfitting, excessive focus on “easy” features, and the difficulty of finding generic filters is to construct hand-crafted convolution filters that detect generic patterns in time series data. Before constructing these filters, we must assume that if such generic convolution filters can be manually created, deep CNN models should be able to learn them across different datasets.

To test this assumption, we analyzed the t-distributed Stochastic Neighbor Embedding (t-SNE) (Maaten and Hinton, 2008) two-dimensional projection of the filter space learned by CNN models, as shown in Figure 3.1. We focused on the filters from the first layer since it is more practical to identify generic patterns in raw data than in the deeper feature spaces. The t-SNE space was generated using the DTW similarity measure to ensure shift independence between the normalized filters.

Figure 3.1 shows that a significant number of convolution filters coincide in the t-SNE space across four different ECG-based datasets with varying characteristics (training size, time series length). This suggests that certain filters may be shared or common across different datasets. Furthermore, we can consider the model’s ability to find optimal solutions as having a specific amount of energy, $\mathcal{E}_{\text{total}}$. This energy is split into two parts:

$$\mathcal{E}_{\text{total}} = \mathcal{E}_1 + \mathcal{E}_2 \quad (3.1)$$

where \mathcal{E}_1 is the energy used to find a set of simple filters, and \mathcal{E}_2 is the energy used to find the remaining filters. By providing the model with some untrained hand-crafted convolution filters that it would have found on its own, we effectively set \mathcal{E}_1 to 0. This allows the model to focus all its energy \mathcal{E}_2 on finding other filters, reducing overfitting and improving performance.

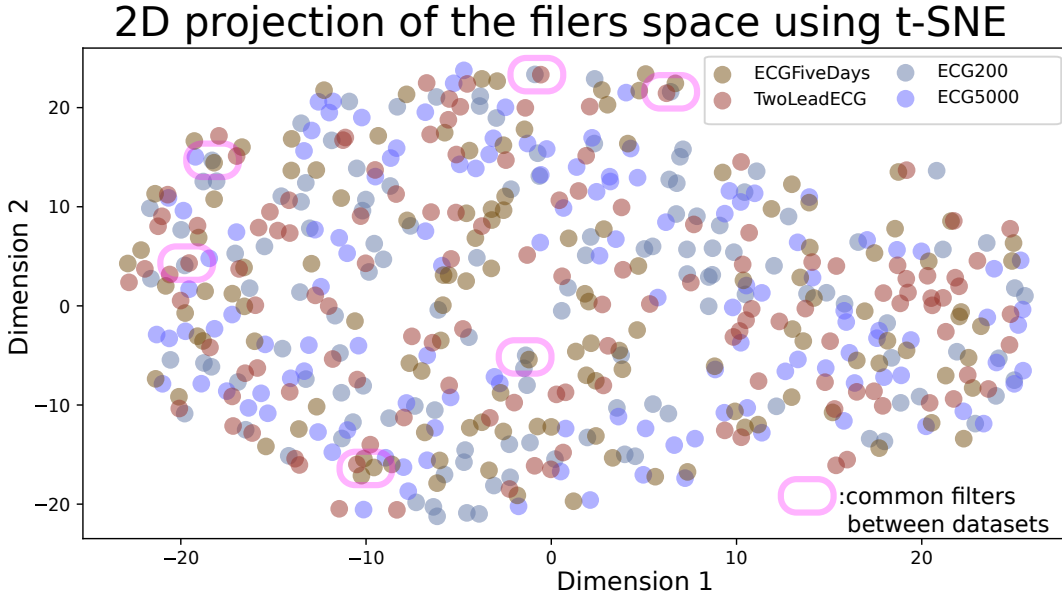


FIGURE 3.1: t-SNE two-dimensional projection of the first-layer convolution filters learned by CNN models on four ECG datasets (ECG200 , ECG5000 , ECGFiveDays , TwoLeadECG). The clustering of filters in the t-SNE space suggests that deep CNN models can identify common, generic filters across different datasets.

This idea aligns with our approach of introducing hand-crafted convolution filters specifically designed to detect fundamental patterns in time series data. These filters are fixed and not adjusted during training, allowing the model to focus on learning more complex and nuanced patterns. This approach has already been addressed in the computer vision community with the construction of untrained Sobel convolution filters (Bogdan, Bonchiş, and Orhei, 2019; Gao et al., 2010). In the following section, we detail the construction of the proposed hand-crafted convolution filters.

3.2.2 Construction of Hand-Crafted Filters

The hand-crafted filters are designed to capture specific types of patterns that are common and crucial in time series data. We propose three types of filters: (1) increasing trend detection, (2) decreasing trend detection and (3) peak detection, for which we define as such:

Definition 10 Increasing Trend Detection Convolution Filter:

An increasing trend is a sub-sequence of a time series \mathbf{x} where the values are strictly increasing in time. The filter detecting this trend is designed to detect subsequences where values are strictly increasing over time. An increasing trend detection filter of length K is defined as:

$$\mathbf{w}_{I_K} = \{(-1)^k\}_{k=1}^K \quad (3.2)$$

Theorem 1 (Increasing Trend Detection Convolution Filter) *Let K be an even positive integer, a convolutional filter $\mathbf{w}_{I_K} = [(-1)^k \text{ for } k \in \{1, \dots, K\}]$ is an increasing trend detection filter of time series, i.e. it only activates (produces positive values) on increasing trend segments.*

proof: Given a time series \mathbf{x} of length L and univariate for simplicity, that contains increasing, decreasing and stationary trends, we will prove in what follows that the increasing trend detection filter only activates on increasing trends.

For stationary trends: Suppose $\exists(t_0, t_1), \epsilon$ where $t_1 > t_0$ and $\forall t \in [t_0, t_1]$ we have $|x_{t+1} - x_t| < \epsilon$. By convolving this segment of the time series \mathbf{x} with the filter w_{I_K} we get:

$$\begin{aligned} \forall t \in [t_0, t_1], s[t] &= \sum_{k=1}^K x_{t+k-1} \cdot w_k \\ &= \underbrace{-x_t + x_{t+1}}_{< \epsilon} - \underbrace{x_{t+2} + x_{t+3}}_{< \epsilon} - \dots - \underbrace{x_{t+k-1} + x_{t+k}}_{< \epsilon} \\ &\approx 0 \text{ not activated} \end{aligned} \quad (3.3)$$

continued proof: For decreasing trends: Suppose $\exists(t_0, t_1), \epsilon$ where $t_1 > t_0$ and $\forall t \in [t_0, t_1]$ we have $x_{t+1} < x_t$. By convolving this segment of the time series \mathbf{x} with the filter w_{I_K} we get:

$$\begin{aligned} \forall t \in [t_0, t_1], s[t] &= \sum_{k=1}^K x_{t+k-1} \cdot w_k \\ &= \underbrace{-x_t + x_{t+1}}_{< 0} - \underbrace{x_{t+2} + x_{t+3}}_{< 0} - \dots - \underbrace{x_{t+k-1} + x_{t+k}}_{< 0} \\ &< 0 \text{ not activated} \end{aligned} \quad (3.4)$$

continued proof: For increasing trends: Suppose $\exists(t_0, t_1), \epsilon$ where $t_1 > t_0$ and $\forall t \in [t_0, t_1]$ we have $x_{t+1} > x_t$. By convolving this segment of the time series \mathbf{x} with the filter w_{I_K} we get:

$$\begin{aligned} \forall t \in [t_0, t_1], s[t] &= \sum_{k=1}^K x_{t+k-1} \cdot w_k \\ &= \underbrace{-x_t + x_{t+1}}_{> 0} - \underbrace{x_{t+2} + x_{t+3}}_{> 0} - \dots - \underbrace{x_{t+k-1} + x_{t+k}}_{> 0} \\ &> 0 \text{ activated} \end{aligned} \quad (3.5)$$

Definition 11 Decreasing Trend Detection Convolution Filter:

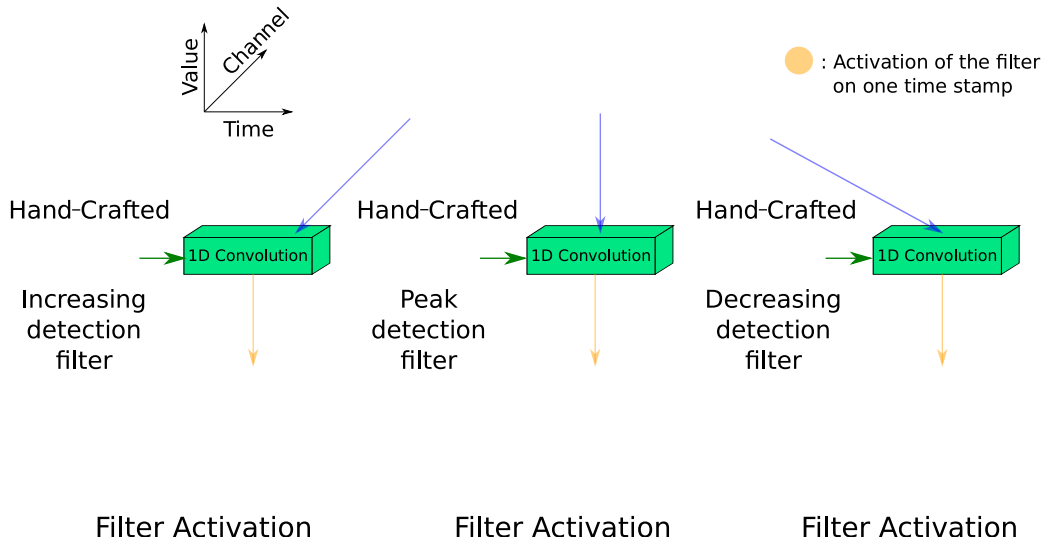
A decreasing trend is a sub-sequence of a time series \mathbf{x} where the values are strictly decreasing in time. The filter detecting this trend is designed to detect subsequences where values are strictly decreasing over time. A decreasing trend detection filter of length K is defined as:

$$\mathbf{w}_{D_K} = \{(-1)^{k+1}\}_{k=1}^K \quad (3.6)$$

Theorem 2 (Decreasing Trend Detection Convolution Filter) Let K be an even positive integer, a convolutional filter $\mathbf{w}_{D_K} = [(-1)^{k+1} \text{ for } k \in \{1, \dots, K\}]$ is a decreasing trend detection filter of time series, i.e. it only activates (produces positive values) on decreasing trend segments.

proof: The proof of Theorem 2 follows the same methodology of the proof of Theorem 1.

FIGURE 3.2: Three hand-crafted filters detecting: (1) increasing trends, (2) decreasing trends and (3) peaks in a time series. The orange points indicates on which time stamps the filters are activated after being convolved with an input time series from the Meat dataset of the UCR Archive.



Definition 12 Peak Detection Convolution Filter:

A peak is a sub-sequence of a time series \mathbf{x} where the values changed with a large variation increasingly and then decreasingly. To detect peaks, we use a filter inspired by the shape of the negative second derivative of a Gaussian function. The filter mimics this shape using a squared parabolic function divided into three parts: a negative parabolic segment, a positive parabolic segment, and another negative parabolic segment. For example, a peak detection filter of length 12 is:

$$\mathbf{w}_{P_{12}} = \{-0.25, -1, -1, -0.25, 0.5, 2, 2, 0.5, -0.25, -1, -1, -0.25\} \quad (3.7)$$

These hand-crafted filters are generic and applicable across various datasets without modification, making them robust tools for initial feature extraction in time series classification tasks. An example of these three filters can be seen in Figure 3.2 on the Meat dataset of the UCR archive (Dau et al., 2019). The output convolution between the input series and each of the hand-crafted filters go through a ReLU activation, this operation will filter out the negative outcomes, keeping the parts where the filters are activated (the target patterns).

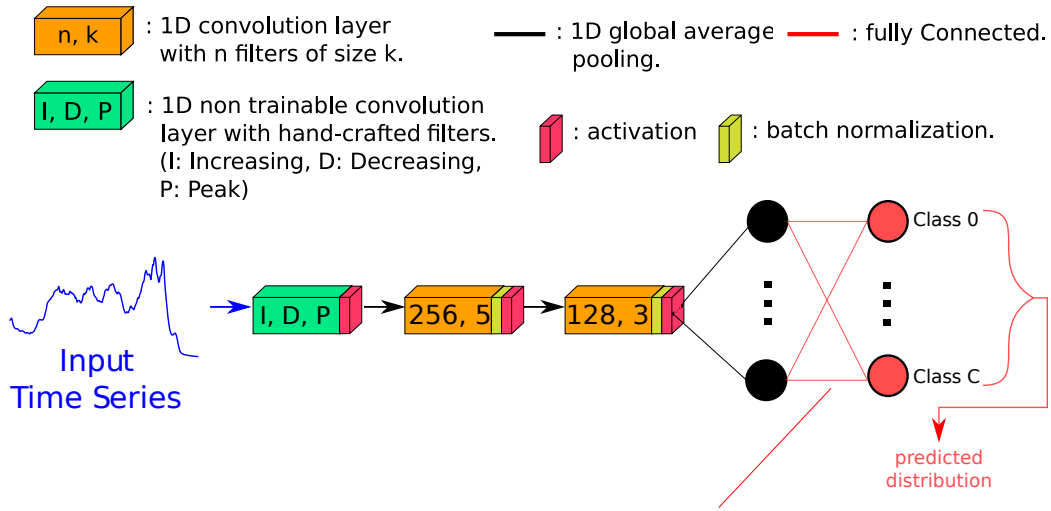
3.2.3 Integration Into Deep Learning Architectures

To evaluate the impact of these hand-crafted filters, we integrate them into existing deep learning architectures, mainly FCN (Wang, Yan, and Oates, 2017) and Inception (Ismail Fawaz et al., 2020). We propose two adapted versions for FCN and one for Inception:

3.2.3.1 Custom Only-Fully Convolutional Network (CO-FCN)

In this architecture, the first convolution layer of the standard FCN is replaced entirely by the hand-crafted filters. This adaptation ensures that the initial feature

FIGURE 3.3: The CO-FCN architecture, applied non trainable hand-crafted convolution filters on the input data, followed by the rest of the FCN architecture (Wang, Yan, and Oates, 2017).



extraction is driven by these fixed filters, allowing the subsequent layers to focus on learning more complex patterns. We refer to this architecture as Custom Only-Fully Convolutional Network (CO-FCN), which evaluates the usage of the proposed hand-crafted filters alone with no learnable layers. The details of this architecture are presented in Figure 3.3. To avoid choosing a specific length for hand-crafted filters, we apply a set of different lengths for each of the three proposed filters. We retained the parameters setup used in the last two layers of FCN as detailed in Figure 1.8 of Chapter 1.

3.2.3.2 Hybrid-Fully Convolutional Network (H-FCN)

The H-FCN architecture enhances the standard FCN by incorporating both hand-crafted and trainable filters in the first convolution layer. Features extracted by the hand-crafted filters are concatenated with those from the trainable filters, enabling the model to leverage the strengths of both approaches. The details of this architecture are presented in Figure 3.4, and such as CO-FCN, we utilize a set of different lengths for the hand-crafted filters. The rest of the FCN architecture is used, however, unlike the original FCN, given we incorporate hand-crafted filters, we reduce the number of filters throughout all the rest of the network by half. This is due to the fact that the model does not need many filters now given the presence of the hand-crafted filters, increasing the model's efficiency.

3.2.3.3 Hybrid-Inception (H-Inception)

The Hybrid-Inception (H-Inception) architecture integrates hand-crafted filters into the Inception model (Ismail Fawaz et al., 2020) (see Figure 1.11 of Chapter 1 for the network details), which is known for its superior performance in TSC. Similar to the H-FCN, the H-Inception network combines the features captured by the hand-crafted filters with those extracted by the first Inception block. This concatenation occurs before the data is processed by the remaining layers of the Inception network. Additionally, we construct H-InceptionTime which leverages an ensemble of five H-Inception models (similar to InceptionTime) to further enhance its performance. The integration of hand-crafted filters in this complex architecture allows it to maintain

FIGURE 3.4: The H-FCN architecture using non trainable hand-crafted filters in parallel to trainable convolution filters.

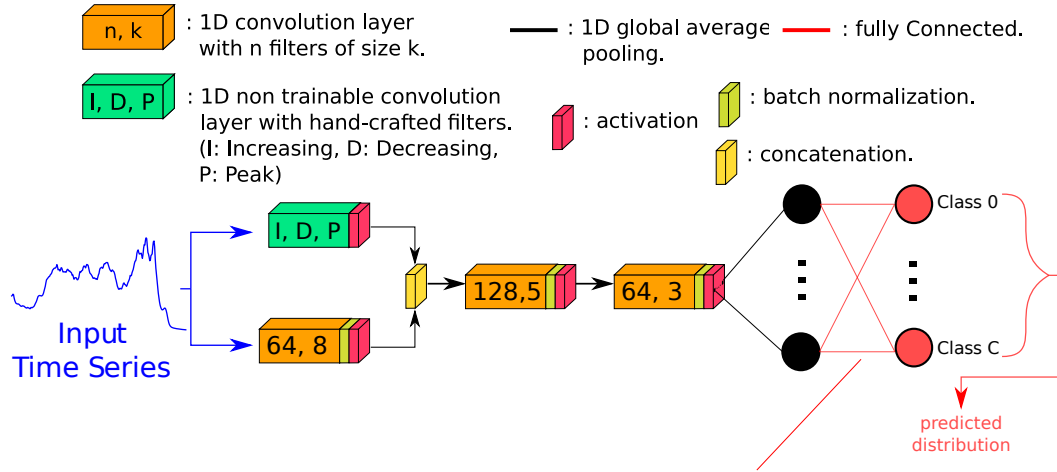
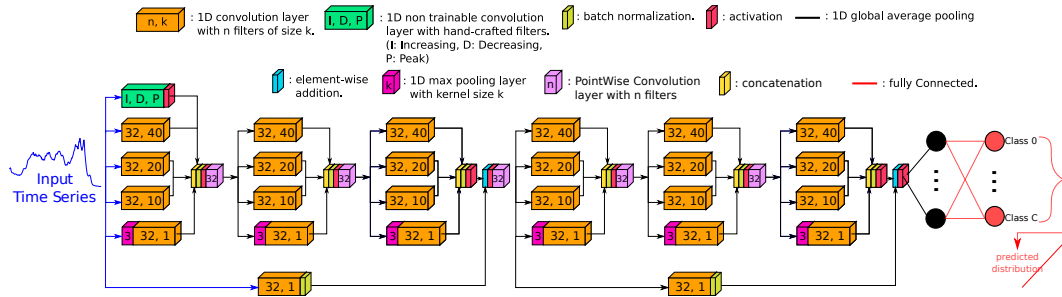


FIGURE 3.5: The H-Inception architecture using non trainable hand-crafted filters in parallel to trainable convolution filters of Inception (Ismael Fawaz et al., 2020).



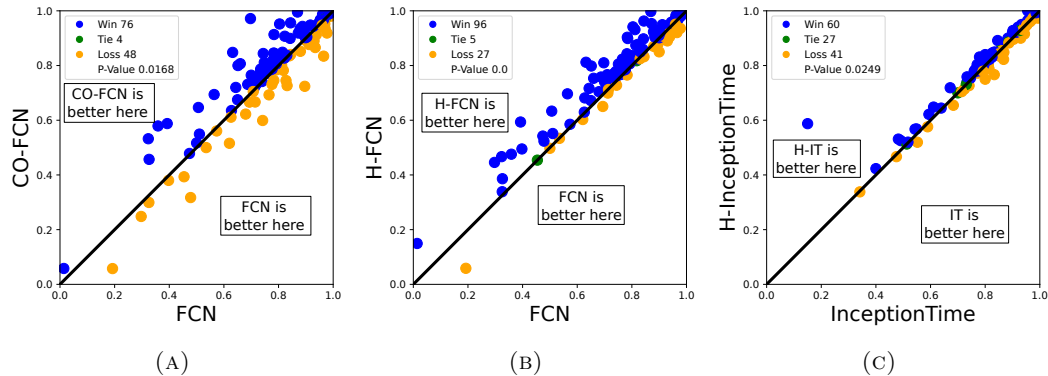
its depth and capacity to capture diverse patterns, while the ensemble approach ensures robustness and improved accuracy across various datasets. Figure 3.5 presents the detailed architecture of H-Inception. The rest of the Inception architecture and parameters are retained the same. The reason to why in H-Inception we do not reduce the number of filters to learn, is that the number of filters per convolution is small, and much smaller than the one set in FCN ($32 < 128$).

In the following section, we present a detailed evaluation of these three proposed architectures on 128 TSC datasets of the UCR archive (Dau et al., 2019), proving that the hand-crafted filters help the models to generalize, paving the way to constructing a foundation generic model for TSC tasks.

3.2.4 Experimental Setup

The evaluation of the proposed architectures was conducted using the UCR Archive, which includes 128 labeled univariate time series datasets. Each time series in these datasets undergoes z-normalization to achieve a zero-mean and unit-standard-deviation. The performance of each model was measured by comparing their accuracy on these datasets. The models were trained using the Adam optimizer with a learning rate decay, and the best-performing model based on training loss was selected for evaluation on the test set. To ensure robustness, the training process was repeated five times with different initialization, and the results were averaged.

FIGURE 3.6: Results over 128 datasets of the UCR archive (Dau et al., 2019) presented in a 1v1 scatter plot format between FCN, InceptionTime (IT) and their variants CO-FCN, H-FCN and H-InceptionTime (H-IT) using the hand-crafted convolution filters.



We compared the performance of our adapted architectures with hand-crafted filters to the original models. For each pair of models, we compared the accuracy on each dataset and computed the number of wins, ties, and losses. These comparative results are presented using Win/Tie/Loss one-vs-one plots, showing the Win/Tie/Loss count between two different classifiers on the 128 datasets of the UCR Archive. Each point in the plots represents a single dataset from the UCR Archive. The axes display the accuracy of each classifier between 0 and 1. Additionally, to assess the significance of the comparisons, the Wilcoxon Signed Rank Test (Wilcoxon, 1992) was performed for each pair of classifiers. The resulting statistical measure, the p-value, is shown in the legend of each plot. We set the α threshold for the p-values to 0.05, as done in the literature (Ismail Fawaz et al., 2019).

3.2.5 Experimental Results

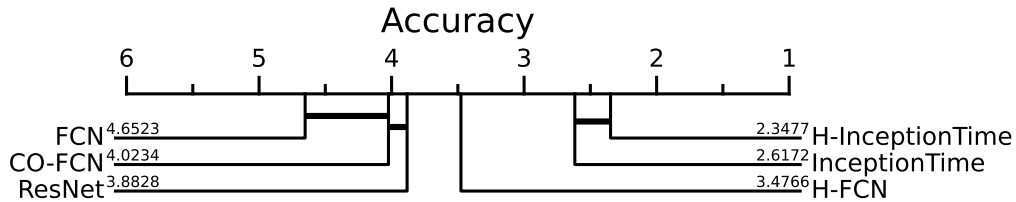
In this section we compared the proposed architectures to their original network, as well as to other deep learning models for TSC such as ResNet (see Figure 1.9). We follow this comparison by looking into the standing of our proposed models to non-deep learning state-of-the-art methods. Finally, we present a detailed analysis into the changes the FCN variants go through when using the hand-crafted filters.

3.2.5.1 Comparing To Original Networks

The CO-FCN model, which replaces the first convolutional layer of the FCN with hand-crafted filters, demonstrated improved performance over the original FCN in most cases. The Win/Tie/Loss analysis, presented in Figure 3.6a, showed that CO-FCN outperformed the original FCN on a majority of datasets, indicating that hand-crafted filters can effectively replace learned filters in the initial layer of the network. The p-value between the performances of CO-FCN and FCN is $0.0168 < 0.05$ indicating that on the 128 datasets of the UCR archive, CO-FCN outperforms FCN with a, statistically, significant difference of performance. However, there were instances where the original FCN performed better, suggesting that a hybrid approach could be beneficial, highlighting again the need to quantify the win/loss margin between two models.

The H-FCN model, which combines hand-crafted and learnable filters, showed significant improvements over the original FCN model. The Win/Tie/Loss analysis,

FIGURE 3.7: Critical Difference Diagram (Benavoli, Corani, and Mangili, 2016) presenting a comparison between three proposed networks and three state-of-the-art deep learning models for TSC, aggregated over the 128 datasets of the UCR archive.



presented in Figure 3.6b, highlighted that H-FCN achieved better accuracy in a substantial number of datasets compared to these models. The performance difference between FCN and H-FCN is statistically significant ($p\text{-value} < 0.05$), with FCN having a very small winning margin in terms of accuracy values. This demonstrates that by adding just a few hand-crafted filters, the performance of FCN can be significantly enhanced, while also being more efficient, as H-FCN (77 440 parameters) reduces the number of parameters by almost three times compared to FCN (264 704 parameters).

The H-InceptionTime model, variant of the InceptionTime model with hand-crafted filters, demonstrated significant performance improvements. As seen in Figure 3.6c, H-InceptionTime surpassed the InceptionTime ensemble in terms of accuracy, with a statistical significance in terms of difference of performance as the p -value is less than the threshold. This makes H-InceptionTime the newest state-of-the-art deep learning model for TSC.

3.2.5.2 Comparing To Other Networks

After demonstrating that hand-crafted filters can enhance a network’s performance on the UCR archive, as shown in the previous section, we now present a cross-comparison between models. For instance, Figure 3.7 illustrates the CD diagram from (Benavoli, Corani, and Mangili, 2016), implemented in¹. This CD diagram provides a multi-classifier comparison between the three proposed networks and three state-of-the-art baseline networks: FCN, ResNet, and InceptionTime.

The CD diagram highlights that H-FCN significantly outperforms ResNet, while ResNet significantly outperforms FCN, demonstrating the substantial impact of the hand-crafted filters. Furthermore, the diagram shows that, in terms of average rank on the accuracy metric, H-InceptionTime is the top performer. However, the diagram also indicates a non-significant difference in performance between H-InceptionTime and InceptionTime, which contradicts the 1v1 scatter plot in Figure 3.6c, highlighting the issues associated with Holm correction discussed in Chapter 2, Section 2.3.4. A similar argument applies to the comparison between CO-FCN and FCN. This issue can also lead to misleading conclusions about the non-significance in difference of performance between CO-FCN and ResNet, whether it exists due to Holm correction.

For these reasons, in this section and the rest of this thesis, we utilize the MCM (Chapter 2) for both 1v1 and multiple model comparisons, as shown in Figure 3.8. In this MCM, it is clear that CO-FCN significantly outperforms FCN, with no significant difference compared to ResNet. The MCM also shows that H-FCN outperforms ResNet in terms of average accuracy. These findings are crucial, as ResNet is a complex model with nearly 500,000 parameters to train, while CO-FCN and H-FCN

¹<https://github.com/hfawaz/cd-diagram>

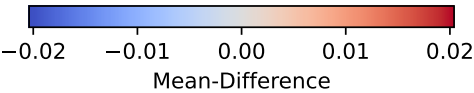
FIGURE 3.8: Multi-Comparison Matrix (Chapter 2) presenting a comparison between three proposed networks and three state-of-the-art deep learning models for TSC, aggregated over the 128 datasets of the UCR archive.

	H-InceptionTime 0.8501	InceptionTime 0.8436	H-FCN 0.8166	ResNet 0.8066	CO-FCN 0.8035	FCN 0.7883
Mean-Accuracy	0.8501	0.8436	0.8166	0.8066	0.8035	0.7883
H-InceptionTime 0.8501	Mean-Difference $r>c / r=c / r<c$ Wilcoxon p-value	0.0065 60 / 27 / 41 0.0249	0.0335 91 / 8 / 29 $\leq 1e-04$	0.0435 92 / 6 / 30 $\leq 1e-04$	0.0466 96 / 7 / 25 $\leq 1e-04$	0.0617 102 / 5 / 21 $\leq 1e-04$
H-FCN 0.8166	-0.0335 29 / 8 / 91 $\leq 1e-04$	-0.0270 33 / 9 / 86 $\leq 1e-04$	-	0.0101 73 / 6 / 49 0.0065	0.0131 74 / 8 / 46 0.0034	0.0283 96 / 5 / 27 $\leq 1e-04$
CO-FCN 0.8035	-0.0466 25 / 7 / 96 $\leq 1e-04$	-0.0401 33 / 7 / 88 $\leq 1e-04$	-0.0131 46 / 8 / 74 0.0034	-0.0031 58 / 4 / 66 0.5585	If in bold, then p-value < 0.05	0.0152 76 / 4 / 48 0.0168



FIGURE 3.9: Multi-Comparison Matrix (Chapter 2) presenting a comparison between H-InceptionTime, InceptionTime, and two state-of-the-art non-deep learning models for TSC, ROCKET and MultiROCKET, aggregated over the 128 datasets of the UCR archive.

	MultiROCKET 0.8606	H-InceptionTime 0.8501	ROCKET 0.8480	InceptionTime 0.8436
Mean-Accuracy	0.8606	0.8501	0.8480	0.8436
H-InceptionTime 0.8501	-0.0106 46 / 15 / 67 0.0397	Mean-Difference $r>c / r=c / r<c$ Wilcoxon p-value	0.0021 64 / 9 / 55 0.4725	0.0065 60 / 27 / 41 0.0249
InceptionTime 0.8436	-0.0170 45 / 10 / 73 0.0031	-0.0065 41 / 27 / 60 0.0249	-0.0044 55 / 9 / 64 0.5016	If in bold, then p-value < 0.05



have 122,496 and 77,440 parameters, respectively. This questions the direct relationship between the number of parameters and performance, indicating that adding hand-crafted filters can significantly improve a “poorly performing” model like FCN, enabling it to surpass a state-of-the-art model like ResNet.

3.2.5.3 Comparison With Non-Deep Models

This section demonstrates how hand-crafted filters boost InceptionTime to achieve better average accuracy compared to ROCKET and approach the performance of MultiROCKET. The MCM in Figure 3.9 highlights that the p-value between H-InceptionTime and MultiROCKET is closer to the threshold than the p-value between InceptionTime and MultiROCKET. We conclude that this performance boost is attributed to the hand-crafted convolution filters.

3.2.6 Analysis

To verify the hypothesis that the original models could identify shapes similar to our proposed filters, we first analyzed if the original models were able to find similar patterns. Additionally, we needed to verify that models using the hand-crafted filters did not redundantly learn the same filters, as this would be ineffective. Finally, we

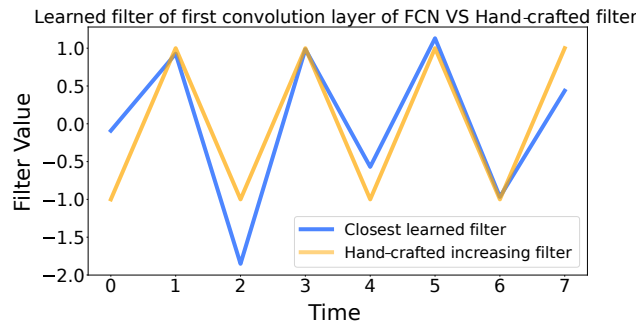


FIGURE 3.10: Hand-crafted increasing trend detection filter of size $K = 8$ and its closest learned filter on the CinCECGTorso dataset. The learned filter is from the first layer of the original FCN.

aimed to understand why the hand-crafted filters enhance model performance, specifically whether they help the model generalize better. By examining these aspects, we sought to confirm the value of hand-crafted filters in capturing critical patterns and improving the model’s robustness across different datasets.

3.2.6.1 Learned vs Hand-Crafted Convolution Filters

To evaluate the effectiveness of our hand-crafted filters, we compared them to the learned filters in the original models. Our primary goal was to determine whether the original models were learning filters similar to our hand-crafted ones. In this experiment, we analyzed the 128 filters learned by the first layer of the original FCN model on the CinCECGTorso dataset. For each hand-crafted filter, we identified the closest learned filter by computing the DTW distance for each pair, after Z-normalizing the learned filters.

For example, the hand-crafted increasing filter of size $K = 8$ and its closest learned filter on the CinCECGTorso dataset are shown in Figure 3.10. The original FCN model learned a similar filter for detecting increasing trends in the time series. The learned filter is a weighted version of our hand-crafted filter. Additionally, the first part of the learned filter resembles the peak detection filter, while the rest matches the increasing trend detection. This suggests that the FCN model learned to construct filters capturing multiple patterns simultaneously, aligning with our approach in the H-FCN model that combines hand-crafted and learned filters.

We further assessed the impact of incorporating hand-crafted filters into the H-FCN model. We compared the 64 learned filters in the first layer of H-FCN with the 128 filters in the first layer of the original FCN, including our hand-crafted increasing and decreasing filters. After computing the DTW distance for each pair of filters, we projected them into a two-dimensional space using t-SNE (Maaten and Hinton, 2008), as shown in Figure 3.11 on the CricketY dataset.

We can see that the filters learned by H-FCN (in orange) are quite similar to those learned by FCN (in blue). However, there are noticeable gaps in the H-FCN filter distribution, marked by red and green ellipsoids. These gaps correspond to the hand-crafted increasing filter (red triangle) and decreasing filter (green triangle). These hand-crafted filters serve as representative prototypes for several FCN learned filters. By integrating these hand-crafted filters, H-FCN reduces the number of learned filters needed, allowing the model to concentrate on learning other important patterns.

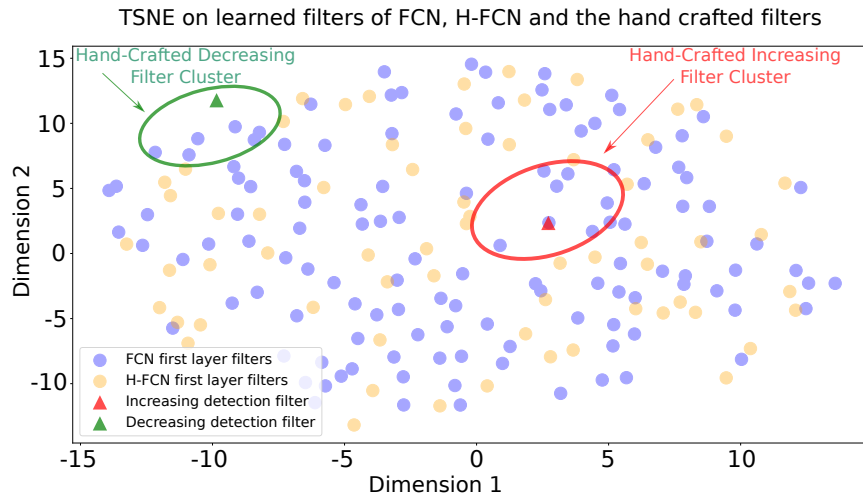


FIGURE 3.11: T-SNE two-dimensional projection of the 128 filters learned by the first layer of the original FCN and the 64 filters learned by the first layer of the H-FCN on the CricketY dataset of the UCR Archive. The two hand-crafted increasing and decreasing trend detection filters are also projected in the two-dimensional space.

In the following analysis, we examine the model’s behavior during training, both with and without our filters, to determine if the inclusion of hand-crafted filters improves the model’s ability to generalize.

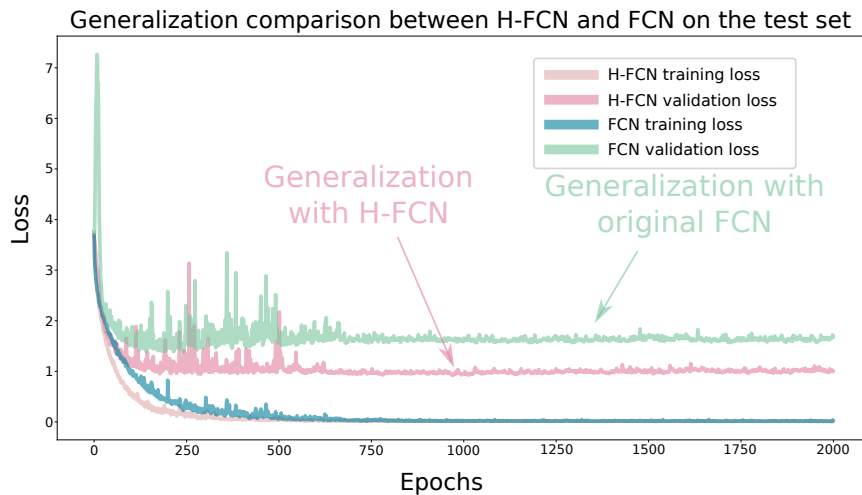
3.2.6.2 Do Hand-Crafted Filters Help Models Generalize?

Experimental results in Section 3.2.6.1 demonstrated that adding hand-crafted filters to Deep Learning models improves performance. However, as shown in Section 3.2.6.1, some of these hand-crafted filters in H-FCN resemble filters learned by the original FCN. This raises a critical question: if FCN can independently learn these filters, why does including hand-crafted filters in H-FCN enhance accuracy?

The answer likely lies in the superior generalization ability of hand-crafted filters. In models like FCN without hand-crafted filters, the optimization process focuses on fitting the training data as closely as possible, which increases the risk of overfitting, a common problem in Deep Learning for TSC. Conversely, the inclusion of generic hand-crafted filters in H-FCN helps the model capture broader patterns that are more applicable to unseen test data.

To test this hypothesis, we compared the training and validation loss curves for both FCN and H-FCN models using the FiftyWords dataset, as illustrated in Figure 3.12. Since the UCR Archive provides only training and test sets, we used the test set to compute the validation loss, solely for monitoring generalization and not for tuning hyper-parameters. The results show that the validation loss for H-FCN converges to a significantly lower value than that of FCN, indicating better generalization. This explains why H-FCN achieves a 15% higher accuracy on the test set compared to FCN.

FIGURE 3.12: Training phase of the FCN and H-FCN architectures on the FiftyWords dataset while monitoring the validation loss on the test set. The training loss of H-FCN converges faster than the training loss of FCN. Also, the validation loss of H-FCN is always below the validation loss of FCN. This shows that H-FCN generalizes better than FCN on this dataset.



3.2.6.3 Can We Use Hand-Crafted Filters To Construct Foundation Models?

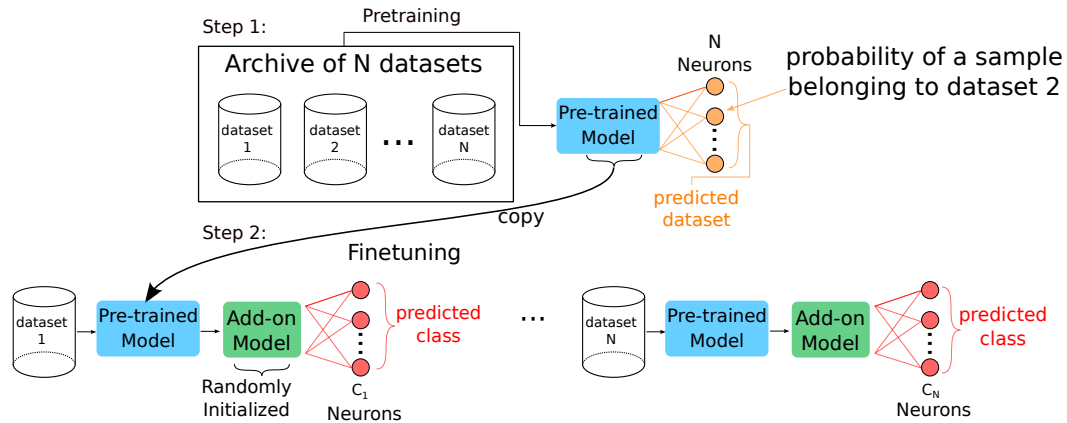
In conclusion, hand-crafted filters significantly aid in generalization because they are independent of specific datasets, allowing models to capture broad patterns applicable across various data. This approach is a step toward developing foundation models, which aim to be versatile and effective across multiple tasks and datasets. The next logical step is to explore constructing a foundation model by leveraging the new state-of-the-art model, H-InceptionTime, which incorporates hand-crafted filters. This will be discussed in the following section, where we will dig into the methodology and potential benefits of using H-InceptionTime as a foundation model.

3.3 Finding Foundation Models for Time Series Classification Using A Pretext Task

In this section, we introduce a foundation model for Time Series Classification (TSC) that leverages the H-Inception architecture, incorporating the benefits of hand-crafted filters. The core idea behind foundation models is to develop robust, pre-trained models that can generalize across diverse datasets, significantly enhancing the performance and efficiency of deep learning models in TSC.

In many real-world applications, starting from scratch with a deep learning model can be a significant downside. Collecting large amounts of labeled data is often costly and time-consuming, and in many cases, acquiring such extensive datasets is impractical. For instance, in the medical field, gathering sufficient data for training models to detect heart diseases from ECG signals involves not only extensive time and financial resources but also the expertise of medical professionals to annotate the data accurately. Similarly, in industrial applications like predictive maintenance, collecting sensor data from machinery involves prolonged monitoring periods and expert annotation to identify failure modes.

FIGURE 3.13: Summary of the proposed pretext task approach. Given an archive of N datasets, the first step is to train a **pre-trained model** on all of the datasets, where the classification task is to **predict the dataset each time series belongs to**. The second step is to copy the **pre-trained model** and follow it with an **addon model randomly initialized**. The second step is done for each of the N datasets of the archive independently. After constructing the N new models, they are fine-tuned on each dataset depending on **the task of each one**.



This is where pre-trained foundation models prove to be invaluable. By starting with a robust, pre-trained model that has already learned generalizable features from a wide array of datasets, we can significantly reduce the amount of new data needed. Fine-tuning these models on small, domain-specific datasets can lead to better performance without the risk of overfitting, which is a common issue when training from scratch with limited data.

Our foundation model, based on the H-Inception architecture, addresses these challenges effectively. The H-Inception architecture (see Section 3.2.3.3) integrates hand-crafted filters (see Section 3.2.2), which have shown strong generalization capabilities, making them independent of specific datasets. This attribute aligns well with the objective of creating foundation models that perform consistently across different data sources.

To construct our foundation model, we benefit from the extensive UCR archive (Dau et al., 2019), which includes 128 datasets divided into 8 distinct domains, such as ECG, sensor data, and motion. This diverse collection allows us to train a model on a common task across datasets within the same domain. By leveraging these varied datasets, the pre-trained model learns to identify patterns that are relevant across different, yet related, data sources. This pre-training on a broad set of tasks enhances the model's ability to generalize and perform well when fine-tuned on specific datasets within each domain.

The contribution of this part of the chapter is twofold as detailed in Figure 3.13: Firstly, we propose a novel pre-training strategy that involves a pretext task designed to predict the originating dataset of each time series sample. This approach enables the model to learn generic features that are applicable across multiple datasets. Secondly, we fine-tune the pre-trained model on specific datasets, enhancing its ability to adapt to the unique characteristics of each dataset while retaining the generalized knowledge acquired during pre-training.

After fully training the pre-trained model on the pretext task, we can proceed with fine-tuning through two different approaches. The first approach involves directly fine-tuning the pre-trained model, followed by adding a classification layer tailored to the dataset’s specific task. The second approach fine-tunes the pre-trained model by cascading it with additional deeper layers before adding the classification layer, allowing for the extraction of more intricate features. Previous research (Fawaz et al., 2018) employed the first approach to study transfer learning for TSC, but the results were suboptimal due to target datasets being highly sensitive to the source dataset used. In our work, we opted for the second approach, believing it to be more robust. This decision stems from the understanding that the first method assumes the pre-trained model has already identified the optimal convolution filters, potentially neglecting deeper, dataset-specific features during fine-tuning. By incorporating deeper layers, our approach ensures that the model refines its feature extraction capabilities, leading to better generalization and performance across diverse datasets.

3.3.1 Foundation Model Architecture Construction

Given a backbone deep learning model for TSC (H-Inception in our case) consisting of Λ layers, we divided the model into two distinct sub-models. The first sub-model, referred to as the pre-trained model, is designed to learn a pretext task. The second sub-model, which is randomly initialized, serves as an extension to the pre-trained model and focuses specifically on the TSC task.

The pretext task selected for this work involves the pre-trained model predicting the dataset of origin for each sample from a set of N datasets (see Algorithm 6). While it might seem more straightforward to combine all datasets and classes into a single large class distribution for prediction, this approach has significant limitations. When there is no correlation between classes from different datasets, the combined class distribution would lack meaningful representation. Thus, using a pretext task to first train the model ensures a more structured and effective learning process.

Algorithm 6 Train the Pre-Trained Model on pretext Task

Require: $\mathcal{D} = \{\mathcal{D}_1, \mathcal{D}_2 \dots \mathcal{D}_N\}$ N datasets where $\mathcal{D}_i = \{\mathbf{x}_{ij}, y_{ij}\}_{j=1}^{M_i}$, the number of layers for the pre-trained mode L_{PT}

Ensure: A pre-trained model $PT(\cdot)$ trained on the pretext task over all the datasets in \mathcal{D}

- 1: Define $M = \text{sum}(M_1, M_2, \dots, M_N)$
 - 2: Define $\mathcal{D}_{PT} = \text{emptyList}$
 - 3: Build $PT(\cdot)$ a neural network with Λ_{PT} layers and M output units with *softmax* activation
 - 4: **for** $i = 1$ to N **do**
 - 5: **for** $j = 1$ to M_i **do**
 - 6: $\mathcal{D}_{PT}.\text{append}([\mathbf{x}_{ij}, i])$
 - 7: **end for**
 - 8: **end for**
 - 9: $PT.\text{train}(\mathcal{D}_{PT})$
 - 10: **Return:** $PT(\cdot)$
-

Upon completing the training of the pre-trained model, we enhance it by integrating a randomly initialized sub-model. This newly constructed composite model, consisting of the pre-trained and the new sub-model, is subsequently fine-tuned for the TSC task on each dataset independently (refer to Algorithm 7).

Algorithm 7 Fine Tuning on Each Dataset

Require: $\mathcal{D} = \{\mathcal{D}_1, \mathcal{D}_2 \dots \mathcal{D}_N\}$ N datasets where $\mathcal{D}_i = \{\mathbf{x}_{ij}, y_{ij}\}_{j=1}^{M_i}$, a pre-trained model $PT(\cdot)$ of Λ_{PT} layers trained on the pretext task, the number of layers of an add-on model while fine tuning Λ_{FT}

Ensure: $\{FT_1(\cdot), FT_2(\cdot), \dots, FT_N(\cdot)\}$ N fine tuned models of $\Lambda_{PT} + \Lambda_{FT}$ layers trained on the task of each dataset independently

- 1: Build $\{FT_1(\cdot), FT_2(\cdot), \dots, FT_N(\cdot)\}$ neural networks of $\Lambda_{PT} + \Lambda_{FT}$ layers with output nodes respecting the number of classes of each dataset in \mathcal{D} respectively
 - 2: Fill the first Λ_{PT} layers in $\{FT_1(\cdot), FT_2(\cdot), \dots, FT_N(\cdot)\}$ by the learned parameters from the feature extraction part of $PT(\cdot)$
 - 3: **for** $i = 1$ to N **do**
 - 4: $FT_i.train(\mathcal{D}_i)$
 - 5: **end for**
 - 6: **Return:** $\{FT_1(\cdot), FT_2(\cdot), \dots, FT_N(\cdot)\}$
-

3.3.2 Backbone Selection

Our model is based on the state-of-the-art deep learning architecture for TSC, the H-Inception network (Section 3.2.3.3). Figure 3.14 illustrates how the H-Inception backbone is divided for our approach. The original H-Inception architecture has six Inception modules. We designate the first three modules for the pre-trained model and the last three for the fine-tuning phase. H-InceptionTime is an ensemble of five H-Inception models with different initializations. Thus, we adopt the H-Inception architecture as our backbone and use model ensemble, consistent with the original works (Ismail Fawaz et al., 2020). We call this approach Pre-trained H-InceptionTime (PHIT).

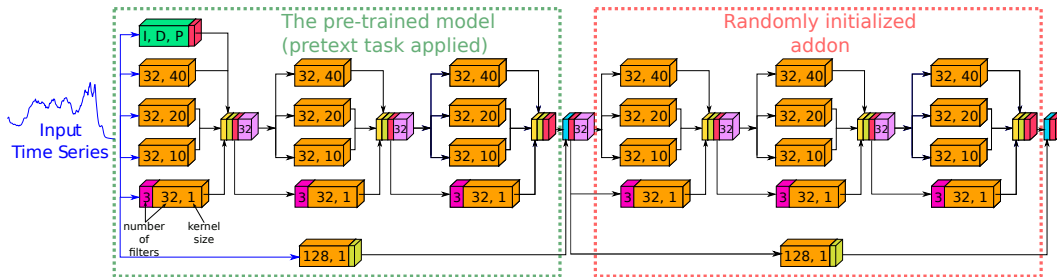
3.3.3 Does It Make Sense To Use Batch Normalization On Different Datasets?

Most cutting-edge deep learning models for TSC (Ismail Fawaz et al., 2019), which excel on the UCR archive (Dau et al., 2019), are convolution-based architectures that utilize Batch Normalization layers (Chapter 1 Section 1.2.1.8) to speed up training. In the H-Inception model we selected, each convolution layer is followed by Batch Normalization. This process adjusts the batch samples to achieve zero mean and unit variance. However, this approach can be problematic when the batch samples come from different distributions, such as different datasets, which is the scenario for our pre-trained model.

To mitigate this issue, we introduce multiple Batch Normalization layers, each dedicated to a specific dataset, instead of the single Batch Normalization layer typically used in CNN architectures for TSC. This setup requires the model to appropriately connect each sample in the batch to its corresponding Batch Normalization layer.

Our innovative Batch Normalization Multiplexer (BNM) is depicted in Figure 3.15. The BNM takes as input the output from the preceding layer, along with the dataset information for each series being processed. This dataset information, which the model is also attempting to predict, guides the control node of the BNM to select the correct Batch Normalization layer for the output node. This design ensures that proper normalization is applied, even when dealing with diverse datasets, thereby enhancing the pre-trained model’s robustness and performance.

FIGURE 3.14: The architecture of H-Inception divided into two sub-models. The **first model** is the pre-trained model, trained on the pretext task, while the second model is the **randomly initialized add-on model**. The H-Inception model is made of six Inception modules, where each module contains three **convolution layers** and a **Max Pooling layer** followed by a **concatenation**, a **batch normalization layer** and an **activation function**. Each Inception module, except the first one, is preceded by a **bottleneck layer** to reduce the dimensionality and hence the number of parameters. The first Inception module contains the hybrid addition, which is the **hand-crafted convolution filter**. **Residual connections** exist between the input and the third module, as well as between the third module and the output.



3.3.4 Experimental Setup

3.3.4.1 Datasets

To evaluate the performance of our proposed approach, we conducted a series of experiments using the UCR archive dataset, which consists of 128 datasets. Due to redundancies, we narrowed our study to 88 datasets. For example, some datasets appear multiple times with different train-test splits for various classification tasks, which could interfere with our model's objective of predicting the source dataset of a sample. Including identical series from different datasets in the training set could confuse the model. Additionally, some datasets were excluded because they only varied in class counts or were truncated versions of others. A detailed explanation of the exclusions is provided in Table 3.1.

To ensure consistency, all datasets were z-normalized before training, achieving a zero mean and unit variance. Since the sample lengths varied, we applied zero padding within each batch (instead of before training) to match the length of the longest series in that batch. This approach maintains the integrity of the model's training and evaluation processes.

3.3.4.2 Division of the Datasets into Types

The goal of using a pre-trained model is to boost the performance of deep learning classifiers on small datasets by utilizing knowledge gained from larger datasets. This strategy is particularly effective when there is some shared basic information between the large and small datasets. To explore this, we conducted eight different pretext experiments, each corresponding to a different type of dataset in the UCR archive. For each experiment, we trained a pre-trained model using all datasets of a specific type, such as ECG, and then fine-tuned the model on each dataset individually. The eight dataset types and their corresponding numbers of datasets are as follows:

FIGURE 3.15: An example using the proposed **Batch Normalizing Multiplexer (BNM)** that solves the problem of learning a batch normalization layer on multiple samples of different distributions (datasets). The BNM is made of **multiple batch normalization layers** (with **blue** and **red** contours) preceded by a multiplexer. This multiplexer has three different nodes: (a) input node, where the input time series goes through, (b) the control node, where the information about the dataset this input time series belong to goes through, and (c) the output node. The path selected for the output node is controlled by the node (b). It is important to note that the BNM, such as the traditional batch normalization layer, learns on the whole batch. The only difference is that more than one batch normalization layer will be fed by parts of this batch, which intuitively means the flow of information is slower when using the BNM.

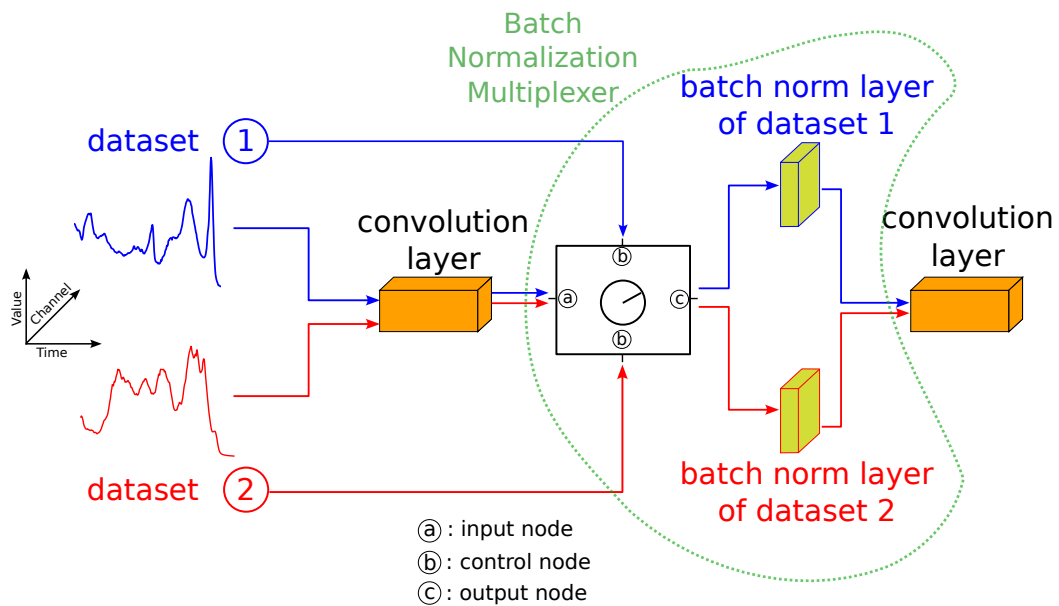


TABLE 3.1: Excluded datasets from the UCR archive in this study. Each dataset is followed by its information and a reason for its exclusion.

Type	Dataset	Train Samples	Test Samples	Length	reason (if excluded)
EOG	EOGHorizontalSignal	362	362	1250	same datasets multivariate with 2 channels divided into 2 univariate datasets
	EOGVerticalSignal	362	362	1250	
EPG	InsectEPGRegularTrain	62	249	601	same test set, different train set size, a combination of both train sets is better than doing a pretext task
	InsectEPGSmallTrain	17	249	601	
Hemodynamics	PigAirwayPressure	104	208	2000	correlation unclear between these three datasets
	PigArtPressure	104	208	2000	
	PigCVP	104	208	2000	
HRM	Fungi	18	186	201	Only one dataset in this type
Image	DistalPhalanxOutlineAgeGroup	400	139	80	same samples as DistalPhalanxTW with different classification and train test split
	DistalPhalanxOutlineCorrect	600	276	80	
	FaceAll	560	1690	131	same as FacesUCR with different train test split
	FiftyWords	450	455	270	same as WordSynonyms with more classes
	MiddlePhalanxOutlineAgeGroup	400	154	80	Same reason as DistalPhalanx
	MiddlePhalanxOutlineCorrect	600	291	80	
	ProximalPhalanxOutlineAgeGroup	400	205	80	Same reason as DistalPhalanx
	ProximalPhalanxOutlineCorrect	600	291	80	
Motion	MixedShapesRegularTrain	500	2425	1024	Bigger version of MixedShapesSmallTrain
	GunPoint	50	150	150	GunPointAgeSpan is the new version with more samples
	WormsTwoClass	181	77	900	Same as Worms with different number of classes
	GunPointMaleVersusFemale	135	316	150	Same as AgeSpan version with different train test split
GunPointOldVersusYoung	136	315	150		
Power	PowerCons	180	180	144	Only one dataset for this type
	AllGestureWiimoteX	300	700	Vary	
Sensors	AllGestureWiimoteY	300	700	Vary	too much Variable length datasets to handle in this type for the pretext task which already has the variable length issue/instability
	AllGestureWiimoteZ	300	700	Vary	
	DodgerLoopDay	78	80	288	
	DodgerLoopGame	20	138	288	All dodger datasets are the same with different train test split with too many missing values
	DodgerLoopWeekend	20	138	288	
	FreezerRegularTrain	150	2850	301	Same as FreezerSmallTrain with more training examples
	GesturePebbleZ1	132	172	Vary	too much Variable length datasets to handle in this type for the pretext task which already has the variable length issue/instability
	GesturePebbleZ2	146	158	Vary	
	PickupGestureWiimoteZ	50	50	Vary	
Spectrum	ShakeGestureWiimoteZ	50	50	Vary	Not a time series
	Rock	20	50	2844	
	SemgHandGenderCh2	300	600	1500	
	SemgHandMovementCh2	450	450	1500	
Trajectory	SemgHandSubjectCh2	450	450	1500	Same datasets different split if we include one of them we end up with one dataset for this type
	GestureMidAirD1	208	130	Vary	
	GestureMidAirD2	208	130	Vary	
	GestureMidAirD3	208	130	Vary	

- Electrocardiogram (ECG): 7 datasets
- Sensors: 18 datasets
- Devices: 9 datasets
- Simulation: 8 datasets
- Spectrogram: 8 datasets
- Motion: 13 datasets
- Traffic: 2 datasets
- Image Contours: 23 datasets

3.3.4.3 Implementation Details

We maintained the same parameters for the H-Inception model as in the original study (first contribution of this chapter). Each experiment was conducted with five different initializations, covering both the pre-trained and fine-tuned models. We aggregated the results from these multiple runs, selecting the best-performing model based on training loss for evaluation.

To optimize training, we utilized a learning rate decay with the ReduceLROnPlateau function in Keras (Chollet, 2021), which halves the learning rate when the training loss stabilizes. All models were trained with a batch size of 64. Both the pre-trained and fine-tuned models were trained for 750 epochs each, ensuring that the total training duration did not exceed the 1500 epochs used for the baseline model in the original study (first contribution in this chapter).

3.3.5 Experimental Results

In this section, we present the results of PHIT compared to the baseline model, followed by a comparison with state-of-the-art deep and non-deep models for TSC on the UCR archive.

3.3.5.1 Comparing With Baseline With No Pre-Training

In this section, we present a direct comparison between our pre-training approach using the H-Inception architecture and the baseline model, both evaluated in their ensemble forms. Figure 3.16 illustrates this comparison with a scatter 1v1 plot. The x-axis indicates the accuracy of H-InceptionTime, while the y-axis shows the accuracy of PHIT, both measured on the test sets. Our findings show that PHIT outperforms on average the baseline across 88 datasets, with PHIT achieving higher accuracy in 48 datasets compared to the baseline's 23. To assess the statistical significance of this difference, we used the Wilcoxon Signed-Rank Test to produce a p-value reflecting the confidence level of the performance difference. With a p-value of approximately $0.021 < 0.05$, it is clear that PHIT significantly outperforms the baseline. This demonstrates that the pre-trained model was able to generalize to the test set better, a result that we will analyze in more detail in Section 3.3.6.

FIGURE 3.16: A 1v1 scatter plot that compares the performance of H-InceptionTime (baseline) and PHIT following the accuracy metric.

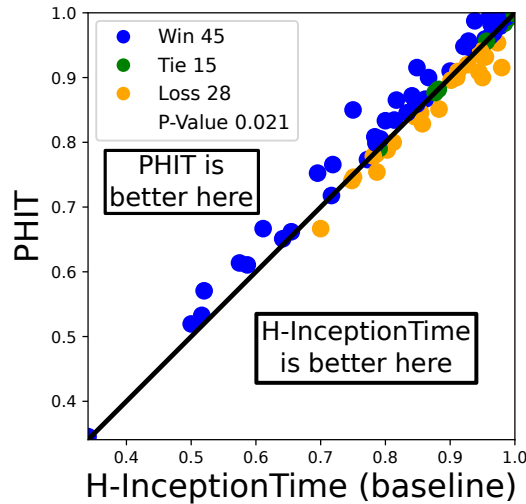


FIGURE 3.17: A Multi-Comparison Matrix (MCM) representing the comparison between the proposed approach PHIT with the state-of-the-art approaches. The winning approach following the average performance is MultiROCKET and in second comes our approach. No conclusion can be found on the difference of performance between MultiROCKET and PHIT given the high p-value.

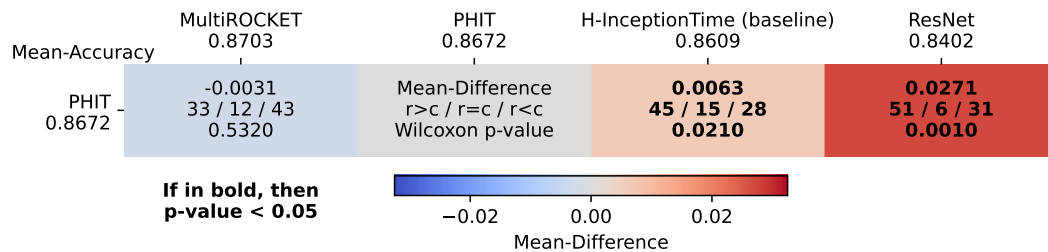


TABLE 3.2: The Win/Tie/Loss count between the proposed PHIT approach and the baseline (H-InceptionTime) per dataset domain. The first column presents the number of datasets included per domain followed by the number of Wins for PHIT, number of Ties, and number of Wins for the baseline. We include as well the percentage of number of losses and the average difference in accuracy (PHIT - baseline). A positive value in the last column indicates that on average of all datasets in a specific domain, PHIT performs better than the baseline on the accuracy metric (lowest value 0.0 and highest value 1.0).

Dataset Type	Number of Datasets	Wins of PHIT	Ties of PHIT	Losses of PHIT	Difference in Average Accuracy (PHIT - Baseline)	Percentage of Losses
Devices	9	4	0	5	+0.0046	55.55 %
ECG	7	3	2	2	+0.0012	28.57 %
Images	23	14	2	7	+0.0087	30.43 %
Motion	13	11	1	1	+0.0179	07.69 %
Sensors	18	7	5	6	+0.0002	33.33 %
Simulation	8	3	3	2	+0.0051	25.00 %
Spectro	8	3	2	3	+0.0115	37.50 %
Traffic	2	0	0	2	-0.0333	100.0 %

3.3.5.2 Comparing To State-Of-The-Art

Figure 3.17 presents the MCM (Chapter 2 Section 2.5) comparing PHIT with state-of-the-art approaches, encompassing both deep and non-deep learning models. The results demonstrate that PHIT outperforms all deep learning approaches based on the average performance metric across the 88 datasets in the UCR archive. Moreover, the MCM also reveals that there is no statistically significant difference in performance between PHIT and the state-of-the-art MultiROCKET model, indicating that while PHIT shows strong performance, it matches rather than surpasses MultiROCKET in statistical significance.

3.3.6 Analysis

In this section, we present a detailed analysis aimed at understanding why the pre-training phase was able to outperform the baseline model. We achieve this by examining the performance differences between the pre-trained model and the baseline across various domains. Additionally, we analyze the impact of training set size for each dataset within these domains. Finally, we visualize the filter space to observe the effects of training for the three methods: baseline, pre-trained, and fine-tuned.

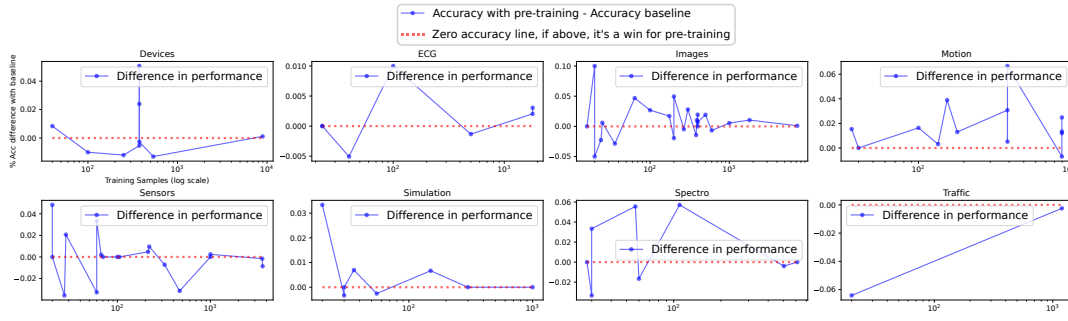
3.3.6.1 Analysing Performance Per Domain

In Table 3.2, we provide a comprehensive analysis of the PHIT approach’s performance compared to the baseline across different dataset domains. For each domain in the UCR archive, we list the total number of datasets, the Win/Tie/Loss count, and the average difference in performance in the final column. A positive value in this column indicates that, on average, PHIT surpasses the baseline in terms of accuracy. Additionally, the last column shows the percentage of datasets where PHIT performed worse than the baseline.

The table reveals that the percentage of losses for PHIT exceeds 50% in only two instances, and the average performance difference is positive for all domains except Traffic, which contains only two datasets. These results highlight that PHIT generally outperforms the baseline across most domains in the UCR archive.

FIGURE 3.18: Comparing the performance of the proposed approach and its change with respect to the training set size. The curve represents the difference in performance between the proposed approach and the baseline.

A positive value (above the tie line) represents a win for the pre-training approach. For each plot, we show this comparison on the datasets of the same type in the UCR archive. The x -axis represents the number of training examples (in \log_{10} scale). The y -axis represents the difference of accuracy between the usage of our pre-training approach and the baseline.



This analysis demonstrates that fine-tuning a pre-trained model on a common task shared by multiple datasets is significantly more effective than the traditional approach. In the following section, we will investigate deeper into the scenarios where the pre-trained model outperforms the baseline by examining the size of the training sets.

3.3.6.2 Larger Datasets Helping Smaller Datasets

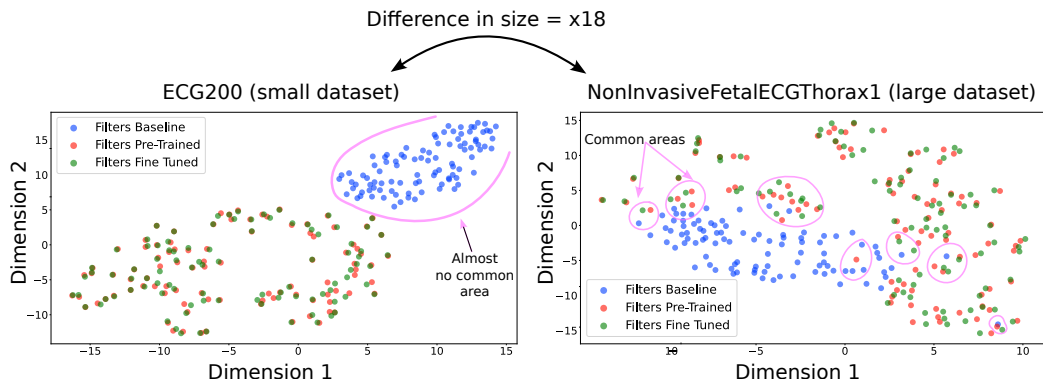
As outlined earlier (Section 3.3), the primary aim of the pretext task is to enhance the performance of deep learning models on TSC tasks, particularly when faced with datasets that have a limited number of training samples. In this section, we explore the effect of the pretext task on each of the 8 dataset types, considering the number of training samples available. This analysis is illustrated in Figure 3.18, where the y -axis represents the difference in accuracy between PHIT and the baseline, and the x -axis (in \log_{10} scale) denotes the training set size. The study is presented across 8 distinct plots, one for each dataset type. Positive values in the blue curves indicate that PHIT outperforms the baseline.

Our observations reveal that, on average, the pretext task significantly benefits datasets with fewer than 10^3 training samples. This is evident in most cases, though not in every case. We hypothesize that this effect arises because the pretext task allows the model to glean more knowledge from larger datasets, which can then be effectively transferred to smaller ones. This transfer process provides the fine-tuning stage with rich, informative data for small datasets while introducing a degree of noise for larger ones. Larger datasets require the model’s full attention on their specific tasks, whereas smaller datasets gain a crucial boost from the additional information, which the model alone might struggle to learn without external guidance.

3.3.6.3 Analyzing The Filters Space

Given our focus on CNNs, we can compare the learned filter spaces to understand the impact of our pre-training approach. To visualize this, we employed the t-SNE

FIGURE 3.19: A two dimensional representation of the filters coming from the first Inception module of the baseline, pre-trained and fine tuned models. The used datasets in this study are ECG200 (left) and NonInvasiveFetalECGThorax1 (right). The two dimensional representation is done using t -SNE coupled with DTW to as a distance measure. Some areas can be seen to be in common between the three models in the case of large datasets (right) however it is not the case for small datasets (left).



technique (Maaten and Hinton, 2008), reducing the dimensionality of the filters to a two-dimensional space. We used DTW for the t -SNE technique as explained before, to have a shift-invariant two-dimensional projection. We visualized the filters from the first Inception module of the baseline, pre-trained, and fine-tuned models in Figure 3.19, focusing on the ECG datasets: ECG200 and NonInvasiveFetalECGThorax1 from the UCR archive (Dau et al., 2019). These datasets were chosen deliberately due to their differing training set sizes, with ECG200 having 100 training examples and NonInvasiveFetalECGThorax1 having 1800.

Figure 3.19 displays the filter distributions for the baseline, pre-trained, and fine-tuned models for each dataset. One prominent observation is that the blue points (baseline filters) are markedly different from the red and green points (pre-trained and fine-tuned filters). This demonstrates that the pre-training followed by fine-tuning leads to the learning of different convolution filters compared to the traditional baseline approach. Another key observation is the variation between the two plots. For ECG200 (left plot), there is minimal overlap between the filters of the three models, indicating distinct learning outcomes. In contrast, for NonInvasiveFetalECGThorax1 (right plot), there are numerous overlapping areas among the filters of different models. This supports our earlier argument in Section 4.3 that larger datasets tend to refine existing knowledge rather than discovering new features. However, the presence of new regions for the pre-trained and fine-tuned filters (green and red) indicates that even large datasets can benefit from the new filters explored during pre-training, leveraging insights gained from other datasets.

In summary, the filter distributions show that pre-training allows models to learn different and sometimes more complex filters than the baseline approach. While smaller datasets like ECG200 encourage the discovery of new, unique features, larger datasets like NonInvasiveFetalECGThorax1 tend to refine knowledge, though they can still benefit from the exploration of new filters during pre-training.

3.4 Conclusion

In this chapter, we have explored the integration of hand-crafted convolution filters into deep learning architectures for time series classification (TSC). We started by examining the rationale and construction of these filters, demonstrating their potential to improve model performance significantly. Our experiments showed that hand-crafted filters could generalize across various datasets, enhancing the robustness and accuracy of the state-of-the-art deep learning model InceptionTime by proposing its new hybrid version H-InceptionTime.

We then introduced a pre-training approach using the H-Inception architecture, leveraging the generalization capabilities of hand-crafted filters. The pretext task, designed to predict the dataset of origin for each time series, proved effective in transferring knowledge from larger to smaller datasets. This methodology helped mitigate the common issue of overfitting, particularly when dealing with limited training samples.

The experimental results validated our approach, with the Pre-trained H-InceptionTime (PHIT) model consistently outperforming the baseline across different dataset domains. Our analysis also highlighted the importance of fine-tuning with additional layers to capture deeper features, further boosting performance.

In summary, this chapter demonstrates that incorporating hand-crafted filters and a strategic pre-training approach can significantly enhance the performance of deep learning models for TSC. These findings pave the way towards developing foundation models that can generalize well across diverse datasets, reducing the need for extensive data collection and training from scratch.

One of the key insights from this chapter was that simply adding hand-crafted filters to the FCN "poorly performing" model enabled it to achieve state-of-the-art performance. This raises an intriguing question as we move forward: can we reduce the complexity of all these models while maintaining or even enhancing their performance? This question will be the focus of the next chapter.

Chapter 4

Reducing Complexity in Deep Learning Models for Time Series Classification

4.1 Introduction

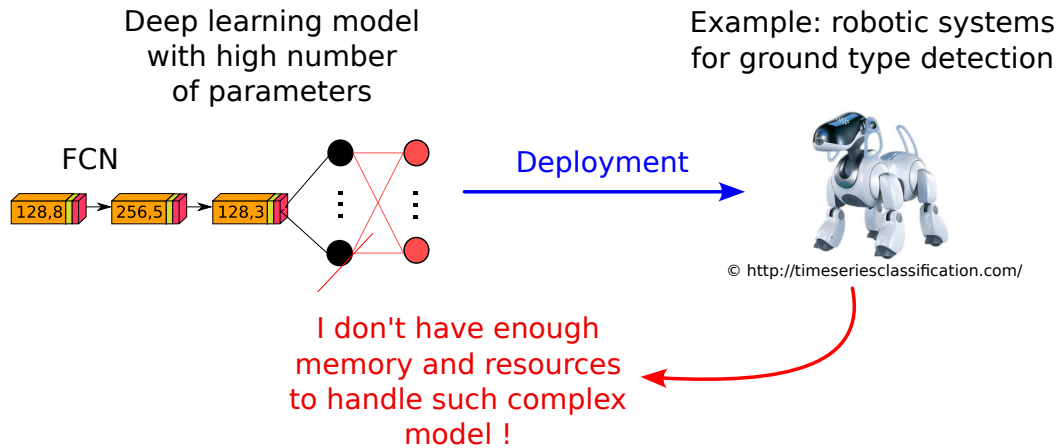
In Chapter 3, we explored the significant impact of integrating hand-crafted filters into small, non-complex models in terms of number of parameters (FCN), demonstrating that such models can outperform more complex, state-of-the-art models (ResNet), as presented in Section 3.2.5.2. This finding challenges the conventional wisdom that increasing model complexity and the number of parameters inherently leads to better performance. Instead, it suggests that strategic simplicity and careful feature engineering can yield superior results. For instance, the groundbreaking work presented in (Ismail Fawaz et al., 2020) introduced an innovative deep learning model, InceptionTime (Chapter 1 Section 1.2.1.8), for TSC, significantly advancing the role of Convolutional Neural Networks (CNNs) in this field. Despite its impressive performance, InceptionTime, with nearly 2.1 million parameters distributed across five Inception models, exemplifies a large and complex architecture. This complexity poses challenges for deployment in real-world applications, particularly those requiring small, resource-constrained devices.

Building on these foundations, this chapter introduces and looks into the innovative approach presented in here. The core motivation behind this work is to develop a more efficient and effective model, LITE, for TSC by leveraging lightweight Inception-based architectures and boosting techniques. This results in a model that is not only powerful but also efficient and adaptable.

The key contributions of the LITE approach are multifaceted:

- **Lightweight Inception Architecture:** The LITE model employs a streamlined version of the Inception (Figure 1.11) architecture, designed to reduce computational complexity without compromising performance. This makes the model more accessible for applications with limited computational resources.
- **Boosting Techniques:** To further enhance performance, LITE integrates boosting techniques that improve the model's ability to generalize across diverse datasets. Boosting helps in mitigating overfitting, enhancing its predictive accuracy.
- **Efficiency and Adaptability:** The combination of a lightweight architecture and boosting techniques results in a model that is both efficient and adaptable, capable of performing well across various TSC datasets with reduced training times, lower computational demands and carbon footprint.

FIGURE 4.1: Difficulties in deploying a high-parameter deep learning model, such as FCN, on a Sony robot for ground type classification. The extensive computational resources and memory required by FCN present significant challenges for resource-constrained devices.



In real-world scenarios, the LITE model has significant implications. For example, in the healthcare sector, it can be utilized for rapid and accurate diagnosis of heart conditions from ECG signals, even in resource-constrained environments. In traffic management, LITE can be deployed to predict congestion patterns and optimize traffic flow with minimal computational overhead. Figure 4.1 illustrates a real-world scenario where deploying a model with over 200,000 parameters, such as FCN, on a Sony robot for ground type classification encounters significant difficulties. The high parameter count not only demands substantial computational resources but also strains the device's memory and processing capabilities. To address this issue, we propose constructing a lightweight model: LITE.

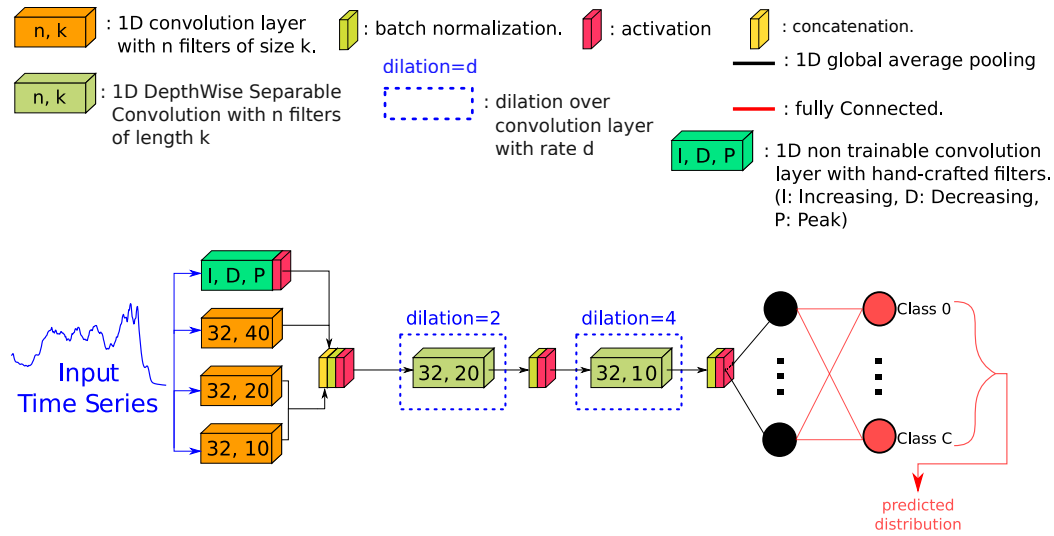
This chapter will provide an in-depth exploration of the LITE model, discussing its architecture, the integration of boosting techniques, and its performance across different TSC tasks. By building on the insights gained from the previous chapter regarding the efficacy of hand-crafted filters in simplifying and enhancing model performance, we will see how the LITE approach takes these principles further to achieve state-of-the-art results in a lightweight and efficient manner. We also propose an adaptation of the proposed LITE network specifically for the case of multivariate time series, LITE MultiVariate (LITEMV). We support the findings of this chapter with extensive experiments on both the UCR and UEA archives (Dau et al., 2019; Bagnall et al., 2018).

4.2 The LITE Architecture

The LITE architecture is a streamlined version of the Inception network (Figure 1.11), designed to maintain high performance while significantly reducing computational overhead. The LITE architecture, presented in Figure 4.2 with a detailed parametric view, includes:

- **Hand-Crafted Convolution Filters:** Recognizing the significant impact of hand-crafted filters (Chapter 3 Section 3.2.2) on the performance of the simple FCN network, we employ these filters in the first layer of LITE. This approach mirrors the implementations in H-FCN and H-Inception (Chapter 3

FIGURE 4.2: The proposed LITE architecture for Time Series Classification.



Section 3.2.3). This is the **first** boosting technique used by LITE.

- Multiplexing Convolution:** The core of the LITE architecture is built upon Inception modules, which apply multiple convolution operations with different filter sizes simultaneously. This allows the model to capture various types of patterns within the time series data. This is referred to as multiplexing convolution, the **second** boosting technique used in LITE, and it is used only on the raw data and not in the rest of the network such as in Inception (Ismail Fawaz et al., 2020). The convolution layers used in this part of the network are the standard convolution operations. The output convolution of these three layers, as well as the hand-crafted filters (with an activation), are concatenated on the channels axis and go through a Batch Normalization layer and an activation layer.
- Efficient Convolutions:** The architecture employs efficient convolution techniques, DWSCs (Chapter 1 Section 1.2.1.8), in the second and third layers of the LITE network. This approach drastically reduces the computational cost and memory footprint while maintaining the model's ability to extract meaningful features from the data. It is important to notice that for the first layer, standard convolutions are used instead of DWSC. This is due to the fact that as the input time series is univariate, DWSC will learn only one filter. The output of these DWSC layers go through a Batch Normalization layer and an activation layer.
- Dilation:** The LITE network uses a dilation rate for the DWSC layers in the second and third depths. This increases the receptive field without increasing the kernel size, thus reducing parameters, unlike Inception, which does not use dilation. This is the **third** boosting technique used by LITE. Notably, dilation is not used in the first standard convolution layers to avoid missing crucial input data.
- Global Average Pooling:** Similar to the state-of-the-art networks, e.g. FCN, ResNet and Inception, the LITE network applies a GAP operation over the last

TABLE 4.1: Comparing LITE, FCN, ResNet and Inception in terms of number of trainable parameters and number of FLOat-point Operation Per Second (FLOPS).

	FCN	ResNet	Inception	LITE
Number of trainable parameters	264,704	504,000	420,192	9,814
FLOPS	266,850	507,818	424,414	10,632

activation layer, transforming the output MTS to a vector, before being fed to the classification FC layer.

Table 4.1 highlights how much LITE is less complex than the three state-of-the-art networks: FCN, ResNet and Inception, in terms of both number of trainable parameters and the number of FLOat-point Operation Per Second (FLOPS). The number of parameters shown is the number of trainable parameters of the architecture without the last classification Fully Connected layer because it depends on each dataset (number of classes). The table shows that the smallest model in terms of number of parameters is the LITE with 9,814 parameters. This is mainly due to the usage of DWSC instead of standard ones.

4.2.1 LITETime: An Ensemble Approach

Similar to InceptionTime, which is an ensemble of five Inception models, we propose LITETime, an ensemble of five LITE models. The goal of an ensemble is to reduce the variance in the model’s performance. Thus, the more sensitive a model is, the greater the impact an ensemble will have.

Given the compact architecture of LITE, with approximately $10k$ parameters compared to the nearly $400k$ parameters of Inception, we believe that ensembling multiple LITE models will have a significantly higher impact. This approach leverages the efficiency and simplicity of LITE, amplifying its performance through ensembling to achieve robust and reliable results.

4.2.2 Experimental Setup

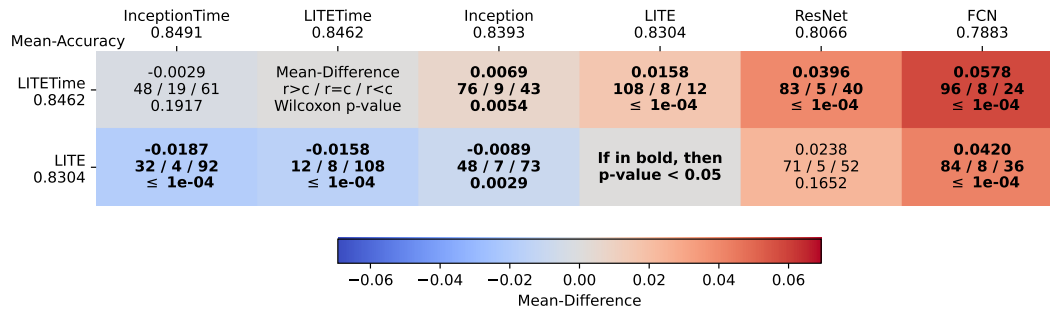
We utilize the 128 datasets of the UCR archive (Dau et al., 2019) to evaluate the performance of LITE and LITETime compared to existing deep learning models. All datasets were z-normalized prior to training and testing.

We meticulously measured the training time, inference time, CO2 emissions, and energy consumption using the CodeCarbon python package (Courty et al., 2024). The best-performing model during training, determined by monitoring the training loss, was selected for testing. The Adam optimizer with Reduce on Plateau learning rate decay method was employed, using TensorFlow’s (Abadi et al., 2015) default parameter settings. Each LITE model in the LITETime ensemble was trained with a batch size of 64 for 1500 epochs, similarly to Inception.

4.2.3 Experimental Results

In this section, we present the experimental results of LITE in terms of performance and efficiency compared to other complex deep learning models, notably FCN, ResNet, and Inception.

FIGURE 4.3: MCM (Chapter 2) showing the comparison between (LITE, LITETime) and the rest of the state-of-the-art deep learning models for time series classification.



4.2.3.1 Comparing To State-Of-The-Art

Our proposed LITE model and its ensemble, LITETime, demonstrate competitive performance on the UCR archive, particularly when considering their significantly smaller size compared to other deep learning models. The LITE model, with approximately $10k$ parameters, and LITETime, which ensembles five LITE models, show impressive results in terms of accuracy, as presented in Figure 4.3.

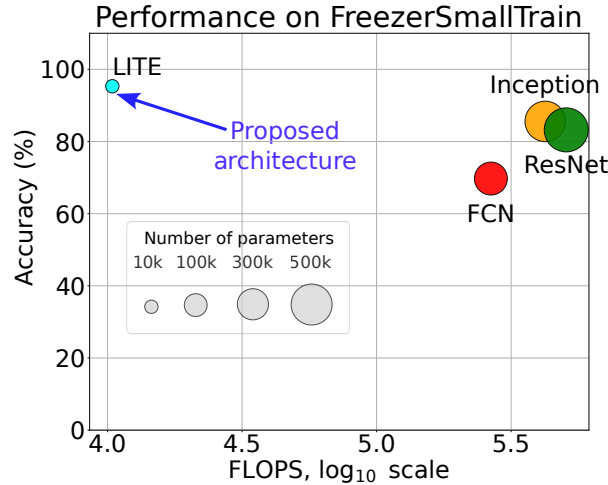
LITE achieves a mean accuracy of 0.8304, outperforming traditional models such as ResNet (0.8066) and FCN (0.7883), which have considerably more parameters. Notably, LITETime further improves this performance, reaching a mean accuracy of 0.8462. While slightly below the performance of InceptionTime (0.8491), the advantage of LITE and LITETime lies in their efficiency and lower computational requirements.

Examining the significance in performance differences, it is noteworthy that LITE alone significantly outperforms FCN and shows no significant difference in performance compared to ResNet. This is a revolutionary finding given that LITE has a significantly smaller number of parameters compared to these two models. Furthermore, LITETime presents no significant difference in performance compared to InceptionTime, despite having only 2.34% of the parameters of InceptionTime. This underscores the efficiency and effectiveness of LITE and LITETime, demonstrating that smaller, well-optimized models can achieve competitive results with much lower computational requirements.

The smaller parameter size of LITE compared to InceptionTime, which has nearly 400,000 parameters, highlights the effectiveness of our approach. The compact architecture of LITE, combined with boosting techniques and the efficiency of ensembling in LITETime, allows for robust performance with reduced computational costs. This makes LITE and LITETime particularly suitable for deployment in resource-constrained environments, where model size and inference time are critical factors.

Overall, the results validate the hypothesis that smaller, well-optimized models like LITE can achieve high performance comparable to larger models, offering a viable and efficient alternative for TSC tasks. An example showcasing the trade off between performance, FLOPS and number of parameters can be seen in Figure 4.4. In this figure we present the performance of LITE, FCN, ResNet and Inception over the test set of the FreezerSmallTrain dataset (Dau et al., 2019), as well as the number of FLOPS needed for one inference of each model per sliding window. We also present each model in a form of circle where its radius represents the number of trainable parameters of each model. It can be seen from Figure 4.4 that LITE is the most

FIGURE 4.4: For each model, the y-axis shows accuracy on the FreezerSmallTrain dataset, and the x-axis shows FLOPS in a \log_{10} scale. Circle diameter represents the number of trainable parameters. The smallest model, LITE (ours), has 10k parameters and the lowest FLOPS (4 in \log_{10} scale), while achieving the highest test accuracy.



accurate model in terms of performance as well as the most efficient in terms of FLOPS and number of parameters, with a large gap in difference of efficiency with the other deep learning models.

4.2.3.2 Efficiency Comparison

Models	Number of parameters	FLOPS	Training Time	Testing Time	CO ₂ (g)	Energy (Wh)
Inception	420,192	424,414	145,267 seconds 1.68 days	81 seconds 0.0009 days	0.2928 g	0.6886 Wh
ResNet	504,000	507,818	165,089 seconds 1.91 days	62 seconds 0.0007 days	0.3101 g	0.7303 Wh
FCN	264,704	266,850	149,821 seconds 1.73 days	27 seconds 0.00031 days	0.2623 g	0.6176 Wh
LITE	9,814	10,632	53,567 seconds 0.62 days	44 seconds 0.0005 days	0.1048 g	0.2468 Wh

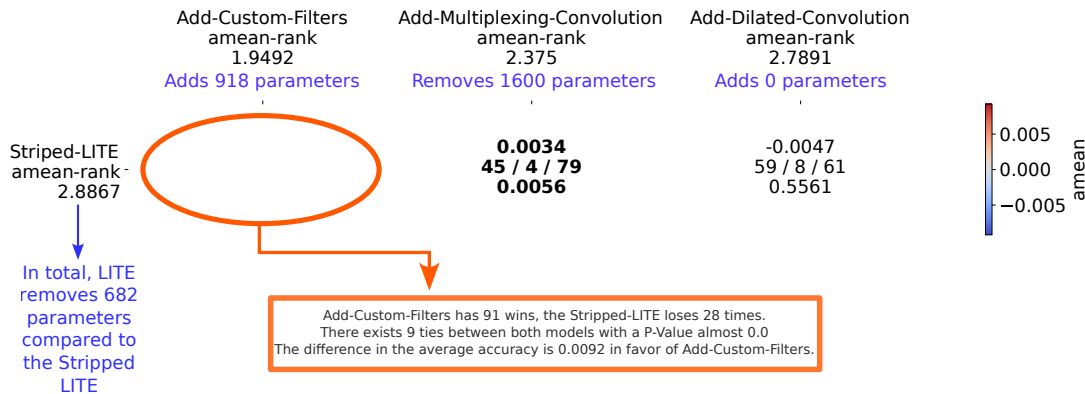
TABLE 4.2: Comparison between the proposed methods with FCN, ResNet and Inception without ensemble.

Table 4.2 summarizes the number of parameters, the number of (FLOPS), training time, inference time, CO₂, and power consumption using CodeCarbon (Courty et al., 2024) across the 128 datasets of the UCR archive (Dau et al., 2019). The values are aggregated over the 128 datasets and averaged over five different runs.

Compared to FCN, ResNet, and Inception, LITE has only 3.7%, 1.95%, and 2.34% of their respective number of parameters. Moreover, LITE is the fastest model during the training phase, with a training time of 0.62 days. This makes LITE 2.79, 3.08, and 2.71 times faster than FCN, ResNet, and Inception, respectively.

Additionally, LITE consumes the least amount of CO₂ and energy, at 0.1048 g and 0.2468 Wh, respectively. This demonstrates that LITE is not only the fastest but

FIGURE 4.5: The Heat Map shows the one-vs-one comparison between the Striped-LITE and the three variants: (1) Add-Custom-Filters, (2) Add-Multiplexing- Convolution and (3) Add-Dilated-Convolution. The colors of the Heat Map follow the value of the first line in each cell. This value is the difference between the value of the first line (average accuracy when winning/losing). The second line represents the Win/Tie/Loss count between the models in question (wins for the column model). The last line is the statistical P-Value between the two classifier using the Wilcoxon Signed Rank Test



also the most environmentally friendly model for TSC compared to FCN, ResNet, and Inception. Given these factors, we believe that LITE is highly suitable for deployment in small devices, such as mobile phones.

4.2.4 Ablation Studies

In this section, we present an extensive study on the various features of the LITE-Time classifier. LITETime leverages three key features: (1) boosting techniques in each LITE model, (2) Depthwise Separable Convolution layers, and (3) the ensemble approach. In the following three sections, we examine the significance of each of these features, providing a detailed analysis of their contributions to the overall performance of LITETime.

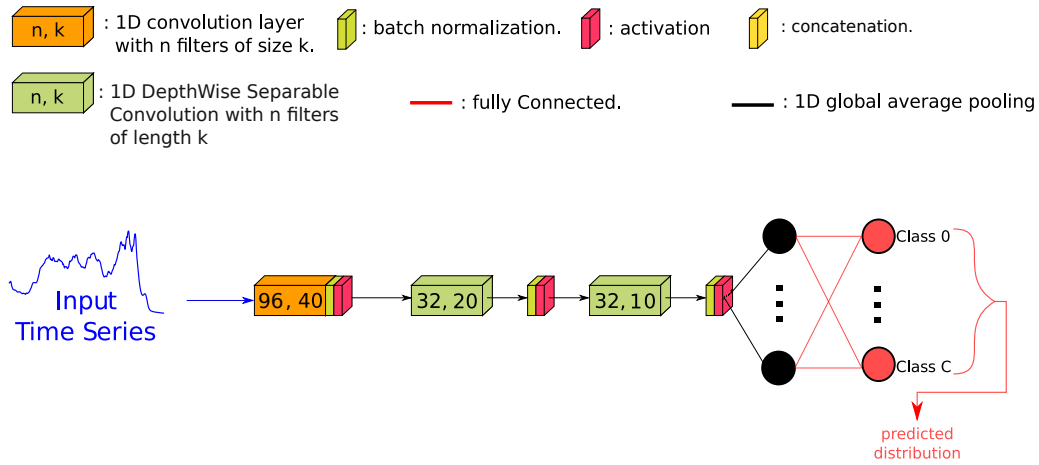
4.2.4.1 Impact Of Boosting Techniques

The LITE architecture leverages several advanced techniques to boost its performance. To demonstrate the individual impact of each technique, we conduct a comprehensive ablation study.

Initially, we strip the LITE model of its three key techniques: dilation, multiplexing, and hand-crafted filters. In the multiplexing convolutions performed in the first layer, there are three layers with 32 filters, resulting in the stripped-down LITE learning a total of $96 = 3 \times 32$ filters for the first depth. The remaining architecture is kept the same, utilizing DWSCs without dilation. The detailed architecture of the Striped-LITE is presented in Figure 4.6.

Following this, we reintroduce each boosting technique one at a time to the stripped LITE model and evaluate its performance. The results of this ablation study are illustrated in Figure 4.5 using an MCM. The results demonstrate that integrating hand-crafted filters in the first layer and utilizing multiplexing convolutions significantly enhance the LITE model's performance. The MCM shows that hand-crafted

FIGURE 4.6: The stripped version of the LITE architecture for Time Series Classification.



filters positively impact average accuracy, although they do introduce additional parameters. In contrast, multiplexing convolutions achieve minor performance gains. The minor average impact of 0.34% is outweighed by the benefits, as multiplexing significantly reduces the number of parameters and consistently outperforms across the majority of datasets.

While the addition of dilated convolutions does not yield statistically significant improvements (p -value > 0.05), the average accuracy differences indicate that dilated convolutions generally enhance performance. This is particularly relevant for large datasets, as dilation expands the receptive field without increasing parameter count. Occasionally, dilation may negatively affect performance on datasets that do not require an extensive receptive field.

In summary, the LITE model, equipped with these boosting techniques, features fewer parameters than the stripped-down version while delivering performance on par with state-of-the-art models. The reduction in parameter count is primarily due to multiplexing, which offsets the additional parameters introduced by hand-crafted filters.

Figure 4.5 also presents the average rank of the models, similar to the CD Diagram. The model with custom filters ranks the highest, indicating the best performance, while the stripped LITE ranks the lowest, marking it as the least effective. Thus, the Stripped-LITE model, without any boosting techniques, is the weakest among the configurations shown in the MCM.

4.2.4.2 Impact Of DepthWise Separable Convolutions

To further investigate the impact of DepthWise Separable Convolutions (DWSC), we replaced them with standard convolutions followed by a Bottleneck layer. The reason we add a bottleneck layer is it simulates the reduction of number of filters needed to learn, as motivated from the Inception architecture (Ismail Fawaz et al., 2020). To ensure a fair and accurate comparison, we employed ensemble techniques, which are crucial in this context due to the significant disparity in the number of parameters, LITE has only about 11% of the parameters compared to the alternative model. Since the alternative model has about 85,000 parameters, LITE would have around 9,350 parameters (11% of 85,000).

FIGURE 4.7: One-vs-one comparison between LITETime and LITETime with Standard convolutions over the 128 datasets of the UCR archive (Dau et al., 2019).

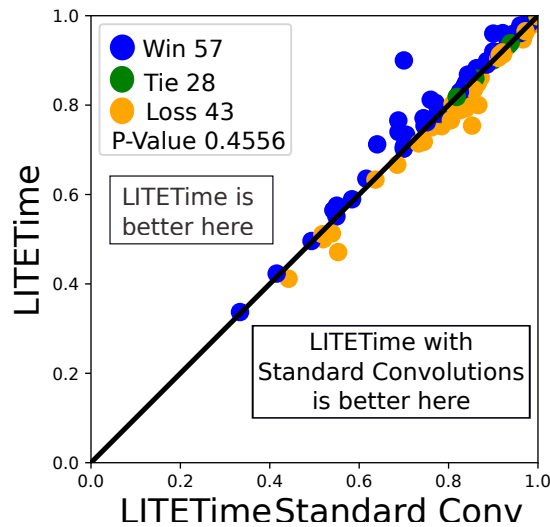


FIGURE 4.8: A Critical Difference diagram showcasing the comparison of performance of LITETime when more or less LITE models are used in the ensemble.

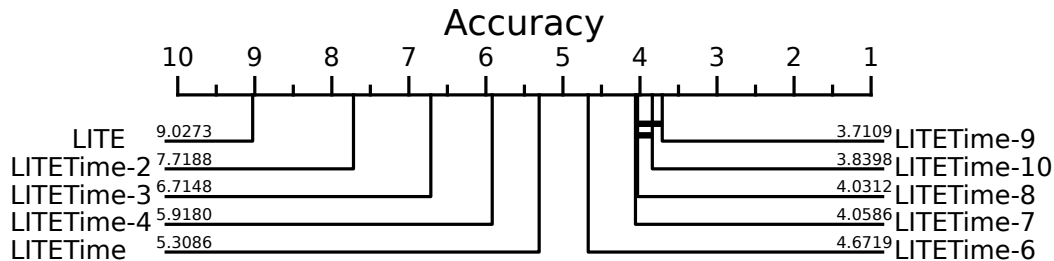


Figure 4.7 showcases a one-on-one comparison between LITETime and LITETime utilizing standard convolutions. The findings reveal that incorporating DWSC does not substantially influence performance, as indicated by a high P-Value of 0.4556. This high p-value suggests that the performance difference is not statistically significant, highlighting that DWSC can achieve comparable results with a significantly reduced parameter count.

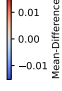
4.2.4.3 Impact Of Number of LITE Models in the Ensemble

In previous experiments, we used five LITE models in LITETime to ensure a fair comparison with InceptionTime, which is an ensemble of five Inception models. The original work of InceptionTime (Ismail Fawaz et al., 2020) has shown that no significant performance improvement is observed on the UCR archive when the ensemble size of InceptionTime exceeds five models. However, due to the smaller and more lightweight architecture of LITE, it may exhibit greater variance and reduced robustness compared to Inception.

To address this, we believe that increasing the number of LITE models in the LITETime ensemble could enhance performance. To test this hypothesis, we trained ten different LITE models on the UCR archive and constructed ensembles of varying sizes (from 1 to 10 models) by averaging all possible ensemble combinations. For

FIGURE 4.9: A Multi-Comparison Matrix (Chapter 2) showcasing the comparison of performance of LITETime-10,9 and 8 with other LITETime models with varying number of LITE heads.

	LITETime-9 0.7832	LITETime-10 0.7830	LITETime-8 0.7830	LITETime-7 0.7829	LITETime-6 0.7825	LITETime 0.7819	LITETime-4 0.7810	LITETime-3 0.7797	LITETime-2 0.7769	LITETime-1 0.7705
Mean-Accuracy	0.7832	0.7830	0.7830	0.7829	0.7825	0.7819	0.7810	0.7797	0.7769	0.7705
LITETime-9 0.7832	Mean-Difference 0.0002 Frac / Freq / frac Wilcoxon p-value	0.0002 42 / 31 / 55 0.3664	0.0002 66 / 21 / 41 0.0479	0.0003 68 / 22 / 38 0.0183	0.0006 73 / 18 / 37 0.0018	0.0013 83 / 14 / 31 ≤ 1e-04	0.0021 84 / 14 / 30 ≤ 1e-04	0.0035 90 / 14 / 24 ≤ 1e-04	0.0063 96 / 11 / 21 ≤ 1e-04	0.0127 101 / 11 / 16 ≤ 1e-04
LITETime-10 0.7830	-0.0002 55 / 31 / 42 0.3664	-	-0.0000 69 / 18 / 41 0.0679	0.0001 66 / 20 / 42 0.0707	0.0004 75 / 17 / 36 0.0079	0.0011 80 / 14 / 34 0.0018	0.0019 82 / 14 / 32 0.0001	0.0033 83 / 13 / 32 ≤ 1e-04	0.0061 89 / 11 / 28 ≤ 1e-04	0.0125 96 / 10 / 22 ≤ 1e-04
LITETime-8 0.7830	-0.0002 41 / 21 / 66 0.0479	0.0000 41 / 18 / 69 0.0679	If in bold, then p-value < 0.05	0.0001 61 / 18 / 49 0.0976	0.0005 74 / 16 / 38 0.0004	0.0011 80 / 15 / 33 ≤ 1e-04	0.0020 87 / 11 / 30 ≤ 1e-04	0.0034 89 / 11 / 28 ≤ 1e-04	0.0062 92 / 15 / 21 ≤ 1e-04	0.0125 103 / 8 / 17 ≤ 1e-04



example, to create LITETime-3 (an ensemble of three LITE models), we combined all possible sets of three models from the ten trained models. The results are displayed in the CD diagram in Figure 4.8 and the detailed MCM in Figure 4.9.

As illustrated in Figure 4.8, LITETime-5 (LITETime) (an ensemble of five LITE models) is not the optimal limit for LITE. Instead, LITETime-7 proves to be more effective. This is due to LITE’s compact size, approximately 42 times smaller than Inception, which allows for greater scalability within the ensemble framework. Consequently, LITETime can enhance accuracy while maintaining significantly lower complexity compared to InceptionTime. Specifically, LITETime-5, with five models, utilizes only about 2.34% of InceptionTime’s trainable parameters, and LITETime-7 increases this to just 3.27%. However, the MCM in Figure 4.9 demonstrates that LITETime-9 significantly outperforms LITETime-8, which contrasts with the conclusions drawn from the CD diagram in Figure 4.8. Additionally, LITETime-10 does not show a significant difference compared to LITETime-9, indicating that the optimal ensemble size for LITETime lies between nine and ten models. Remarkably, even with ten models, LITETime-10 remains approximately 21 times smaller than the ensemble InceptionTime.

Moreover, Figure 4.10 provides a concrete example using the Beef dataset from the UCR archive, illustrating how the performance on unseen data varies with the number of models in both the LITETime and InceptionTime ensembles. This figure underscores the scalability and efficiency of the LITETime approach, highlighting its potential for superior performance with minimal computational overhead.

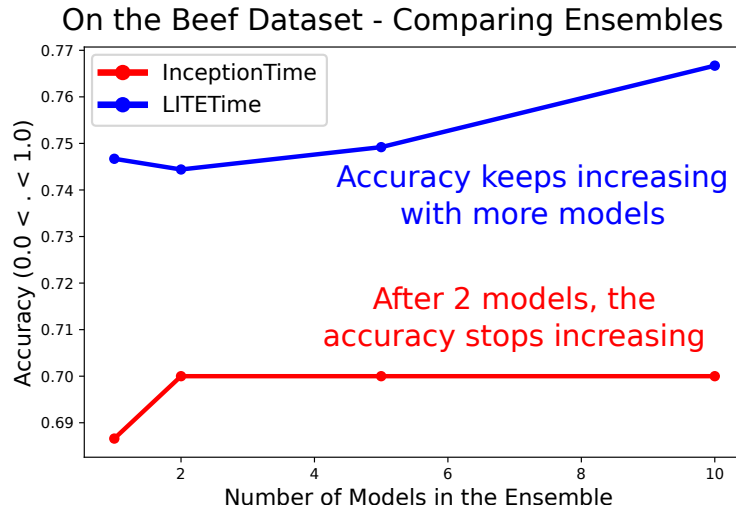
LITETime for Multivariate Time Series? Given the groundbreaking findings of this study with LITETime, its suitability for real-world applications becomes evident due to its remarkably small parameter count and memory footprint. However, practical applications often involve multivariate TSC tasks. This raises an important question: Can LITETime be effectively applied to multivariate scenarios, or does it require adaptation?

In the following section, we address this question by introducing a novel multivariate deep learning model, LITEMV (LITE MultiVariate). This new model is specifically designed to extend the capabilities of LITETime to handle the complexities of multivariate TSC, ensuring its applicability across a broader range of real-world tasks.

4.3 LITEMV: Addressing Multivariate Time Series Classification

As we explore the potential applications of the LITE architecture, it becomes evident that many real-world scenarios involve multivariate time series data and not

FIGURE 4.10: A Comparison on the Beef dataset of the UCR archive (Dau et al., 2019) between the ensemble of LITE and Inception models. The x -axis represents the number of models used in each ensemble and the y -axis the performance of the ensemble on the test set of the Beef dataset.



only univariate data. Examples include medical diagnostics using multiple biosignals, financial forecasting with various economic indicators, and industrial monitoring with multiple sensor readings. Efficient and effective handling of multivariate data is essential for advancing the applicability of TSC models where channel dependency is crucial for capturing discriminative patterns.

While the LITE model has demonstrated exceptional performance and efficiency for univariate TSC, its design requires adaptation to fully leverage the information contained in multivariate datasets. The standard convolution approach used in the first layer of LITE for univariate data does not fully exploit the potential of multivariate inputs, where interactions between different channels can provide critical insights.

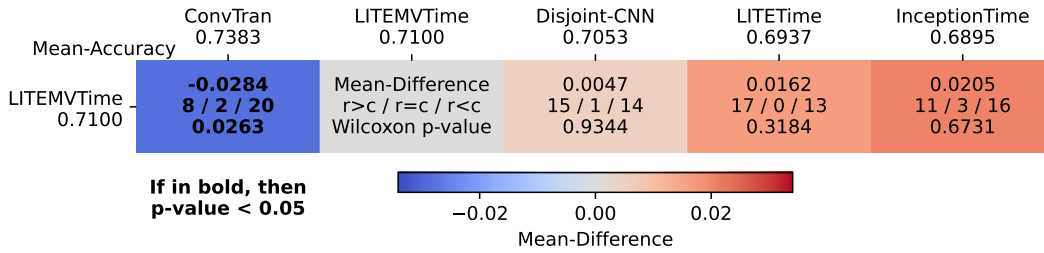
The proposed LITEMV (LITE MultiVariate) architecture is designed to address these challenges. By learning a filter per channel and combining them effectively, LITEMV ensures that the unique contributions of each channel are preserved and utilized to enhance classification performance. This adaptation allows LITEMV to maintain the efficiency and performance advantages of LITE while being optimized for the complexities of multivariate time series data.

4.3.1 Model Adaptation For Multivariate Time Series

To address the issue of effectively handling MTS data, we propose adapting the LITE architecture by replacing the three standard convolution layers at the beginning of the network with DWSC layers. DWSCs allow each channel to be processed independently, preserving the unique information in each channel before combining them.

Additionally, the hand-crafted convolution filters used at the beginning of the network, originally implemented as standard convolutions, are also replaced with DepthWise Convolutions (DWCs, Chapter 1 Section 1.2.1.8). While we continue to use the same hand-crafted filters, the outputs of these DWCs are concatenated rather

FIGURE 4.11: A Multi-Comparison Matrix (MCM) showcasing the performance of LITEMVTime, LITETime, InceptionTime, Disjoint-CNN and ConvTran on the 30 datasets of the UEA archive.



than summed. This ensures that the information from each channel is retained and effectively utilized in the subsequent layers of the network.

This adaptation enhances the model’s ability to manage the complexities of multivariate time series data, leading to improved overall performance and accuracy. We refer to this enhanced multivariate version of LITE as LITEMV and its ensemble version LITEMVTime.

In what follows we present extensive experiments to highlight the contribution of this adaptation and its placement compared to the state-of-the-art deep learning models for multivariate TSC tasks, notably ConvTran (Foumani et al., 2024a) and Disjoint-CNN (Foumani, Tan, and Salehi, 2021) (Chapter 1 Section 1.2.1.8).

4.3.2 Experimental Setup

We utilize the 30 datasets of the UEA archive (Bagnall et al., 2018) to evaluate the performance of LITETime and LITEMVTime compared to existing deep learning models for multivariate TSC. All datasets were z-normalized prior to training and testing independently on each channel. The best-performing model during training, determined by monitoring the training loss, was selected for testing. The Adam optimizer with a Reduce on Plateau learning rate decay method was employed, using TensorFlow’s (Abadi et al., 2015) default parameter settings. Similar to LITE, each LITEMV model in the LITEMVTime ensemble was trained with a batch size of 64 for 1500 epochs.

4.3.3 Experimental Results

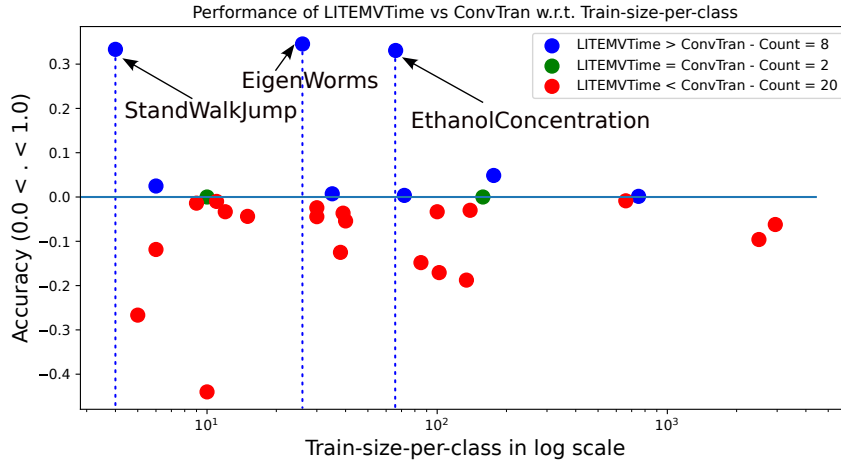
In Table 4.3, we compare the accuracy performance of LITEMVTime, LITETime, and five other leading models: ConvTran, InceptionTime, Disjoint-CNN, FCN, and ResNet. The accuracy metrics for these competitors are sourced from the ConvTran paper (Foumani et al., 2024a). LITEMVTime shows a significant performance edge when it surpasses other models, as evidenced by the substantial gaps in accuracy. This is further illustrated in the MCM plot in Figure 4.11, where LITEMVTime’s performance is benchmarked against the other models.

LITEMVTime ranks second in overall performance, outperforming LITETime, Disjoint-CNN and InceptionTime. Although LITEMVTime does not exceed ConvTran on more than eight datasets, a detailed examination of Table 4.3 reveals that its victories are often by a wide margin. For example, on the EigenWorms dataset, ConvTran achieves a top accuracy of 59.34%, whereas LITEMVTime attains an impressive 93.89%, and LITETime achieves an even higher accuracy of 95.42%. In the following section, we dig into the analysis into the common characteristics of the

TABLE 4.3: Accuracy performance in % of LITEMVTime (LMVT), LITETime (LT), ConvTran (CT), InceptionTime (IT), Disjoint-CNN (D-CNN), FCN and ResNet on 30 datasets of the UEA archive. The datasets are ordered by their average number of training samples per class. The accuracy of the best model for each dataset is presented in bold and of the second best is underlined.

Dataset	Train Size per Class	LMVT	LT	CT	IT	D-CNN	FCN	ResNet
FaceDetection	2945	61.01	62.37	67.22	58.85	56.65	50.37	59.48
InsectWingbeat	2500	61.72	39.79	71.32	69.56	63.08	60.04	65.00
PenDigits	750	98.86	98.83	98.71	97.97	97.08	98.57	97.71
SpokenArabicDigits	660	98.59	98.77	99.45	98.72	98.59	98.36	98.32
LSST	176	66.42	<u>62.85</u>	61.56	44.56	55.59	56.16	57.25
FingerMovements	158	56.00	44.00	56.00	56.00	54.00	53.00	54.00
MotorImagery	139	53.00	51.00	56.00	53.00	49.00	<u>55.00</u>	52.00
SelfRegulationSCP1	134	73.04	75.09	91.80	86.34	<u>88.39</u>	78.16	83.62
Heartbeat	102	61.46	67.80	78.53	62.48	71.70	67.80	<u>72.68</u>
SelfRegulationSCP2	100	<u>55.00</u>	53.89	58.33	47.22	51.66	46.67	50.00
PhonemeSpectra	85	15.81	17.45	30.62	15.86	28.21	15.99	15.96
CharacterTrajectories	72	99.58	99.51	99.22	98.81	99.45	98.68	99.45
EthanolConcentration	66	69.20	67.30	36.12	34.89	27.75	32.32	31.55
HandMovementDirection	40	35.14	21.62	<u>40.54</u>	37.83	54.05	29.73	28.38
PEMS-SF	39	79.19	82.66	82.84	89.01	89.01	<u>83.24</u>	73.99
RacketSports	38	73.68	78.29	86.18	82.23	<u>83.55</u>	<u>82.23</u>	82.23
Epilepsy	35	99.28	98.55	<u>98.55</u>	99.28	88.98	99.28	99.28
JapaneseVowels	30	96.49	97.30	98.91	97.02	<u>97.56</u>	97.30	91.35
NATOPS	30	90.00	88.89	94.44	91.66	<u>92.77</u>	87.78	89.44
EigenWorms	26	<u>93.89</u>	95.42	59.34	52.67	59.34	41.98	41.98
UWaveGestureLibrary	15	84.68	85.00	89.06	90.93	89.06	85.00	85.00
Libras	12	<u>89.44</u>	87.78	92.77	87.22	85.77	85.00	83.89
ArticulatoryWordRecognition	11	97.33	97.67	<u>98.33</u>	98.66	98.66	98.00	98.00
BasicMotions	10	100.0	<u>95.00</u>	100.0	100.0	100.0	100.0	100.0
DuckDuckGeese	10	18.00	24.00	62.00	36.00	<u>50.00</u>	36.00	24.00
Cricket	9	<u>98.61</u>	97.22	100.0	<u>98.61</u>	97.72	93.06	97.22
Handwriting	6	40.00	36.82	37.52	30.11	23.72	<u>37.60</u>	18.00
ERing	6	84.44	89.63	96.29	<u>92.96</u>	91.11	90.37	<u>92.96</u>
AtrialFibrillation	5	13.33	06.67	40.00	20.00	40.00	<u>33.33</u>	<u>33.33</u>
StandWalkJump	4	66.67	<u>60.00</u>	33.33	40.00	33.33	40.00	40.00

FIGURE 4.12: Difference of performance between LITEMVTime and ConvTran with respect to the number of training samples in log scale.



datasets where LITEMVTime wins with a significant margin compared to ConvTran. Moreover, a crucial limitation of ConvTran is its sensitivity to the length of the input series. As a Self-Attention based network, ConvTran must store an attention score matrix of size (L, L) , where L is the length of the input series, with a runtime complexity of $\mathcal{O}(L^2)$. This can create issues for long time series, as the model may face out-of-memory errors during training despite its architectural simplicity.

4.3.4 Analysis On Dataset Characteristics When Comparing LITEMVTime and ConvTran

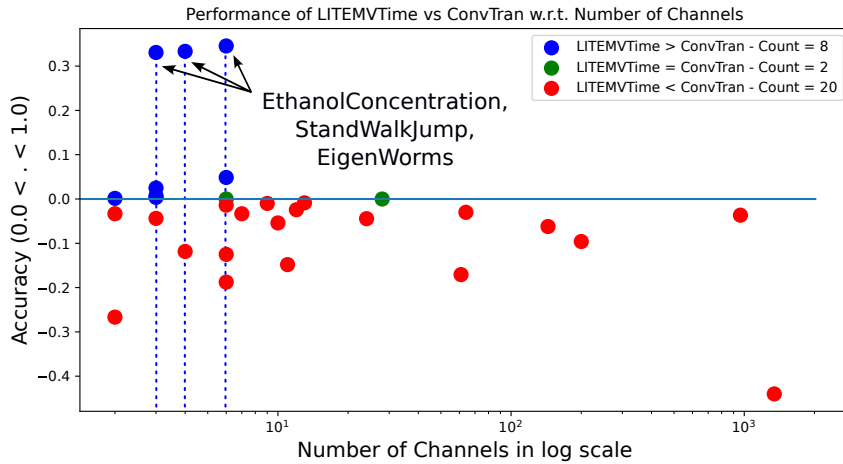
To gain a deeper understanding of the scenarios where LITEMVTime significantly outperforms ConvTran, we analyzed the performance differences between these two models in relation to the number of training samples per class. This analysis aims to uncover any patterns or commonalities in the datasets where LITEMVTime demonstrates superior performance.

Figure 4.12 illustrates the performance gaps between LITEMVTime and ConvTran. The most pronounced differences are observed in three datasets: StandWalkJump, EigenWorms, and EthanolConcentration. These datasets exhibit considerable variation in the number of training examples. For instance, StandWalkJump has a small training set with only 4 samples per class and a total of 12 training samples. On the other hand, the EthanolConcentration dataset contains 66 training samples per class, amounting to 261 samples in total.

This analysis indicates that LITEMVTime's enhanced performance is not confined to datasets with a specific size but extends across datasets with varying numbers of training examples. This highlights LITEMVTime's robustness and versatility in handling diverse dataset conditions, making it a reliable choice for a wide range of time series classification tasks.

To further investigate why LITEMVTime performs better than ConvTran on certain datasets, we can analyze the impact of the number of dimensions in multivariate time series data. Figure 4.13 illustrates the same performance differences shown in Figure 4.12, but this time as a function of the number of dimensions in the datasets. The analysis highlights that the datasets where LITEMVTime shows significant superiority, StandWalkJump, EigenWorms, and EthanolConcentration, all have a relatively

FIGURE 4.13: Difference of performance between LITEMVTime and ConvTran with respect to the number of channels in log scale.



small number of dimensions. However, ConvTran consistently outperforms LITEMVTime as the number of dimensions increases.

Figures 4.12 and 4.13 illustrate that LITEMVTime is more suitable for scenarios with small training data and a limited number of channels. This limitation of ConvTran was also discussed in the original paper (Foumani et al., 2024a).

4.4 Discussion Over Limitations of LITE and LITEMV

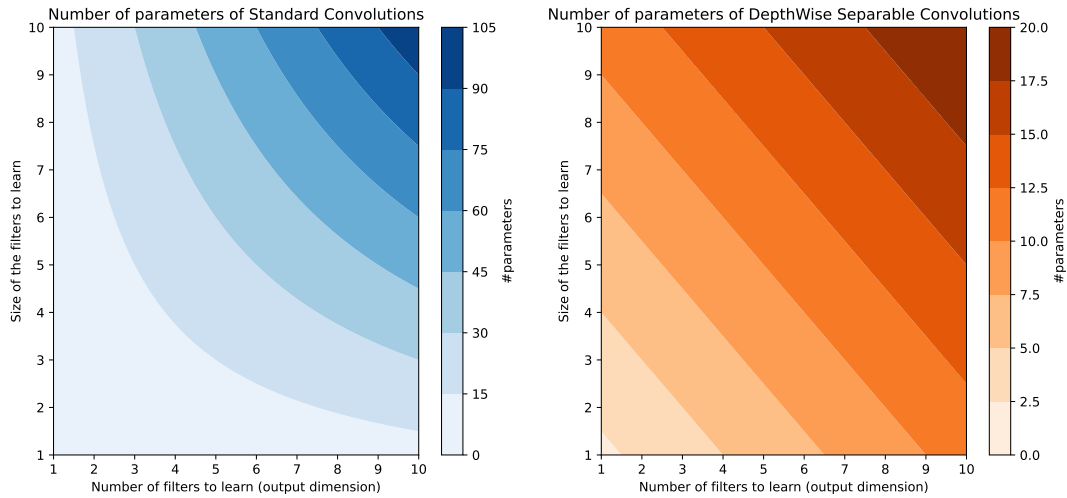
LITE and LITEMV are designed with low complexity, making them efficient compared to other architectures. However, this simplicity may pose a limitation when dealing with very large datasets. For instance, these models might not perform optimally with training sets comprising millions of samples. This limitation can be mitigated by increasing the number of filters in the DWSC layers, which, thanks to the efficient convolution application of DWSCs, would result in only a slight increase in computational cost. Assuming an input MTS of M channels and the output target dimension we want is M' produce by a convolution layer with kernel size K , then the ratio between number of parameters needed in the cases of standard and DWSC layers is:

$$\begin{aligned}
 \text{Ratio} &= \frac{\text{number of parameters standard}}{\text{number of parameters DWSC}} \\
 &= \frac{M \cdot M' \cdot K}{M \cdot K + M \cdot M'} \\
 &= \frac{M' \cdot K}{K + M'}
 \end{aligned} \tag{4.1}$$

As seen in Eq. 4.1 and illustrated in Figure 4.14, independently of the number of input channels M , the number of parameters of the Standard Convolutions increases much faster compared to DWSCs. For instance, the number of parameters in Standard Convolutions increases quadratically, while Depthwise Separable Convolutions (DWSCs) exhibit a linear increase.

A second limitation common to all architectures discussed in this work relates to the length of the time series samples. This can be addressed by enhancing the CNN's Receptive Field (RF), which determines the length of the input visible to the CNN

FIGURE 4.14: Number of parameters of Standard Convolutions and DWSCs in function of number of convolution filters to learn and their kernel size.



at the last layer. For a CNN with Λ convolution layers, each with kernel size K_i and dilation rate d_i where $i \in [1, \Lambda]$, the RF is calculated as:

$$RF = 1 + \sum_{i=1}^{\Lambda} d_i \cdot (K_i - 1) \quad (4.2)$$

The RF varies between different CNN models. For example, the RF for FCN (Wang, Yan, and Oates, 2017) is $14 = 1 + 7 + 4 + 2$, which is relatively small compared to the time series lengths in the UCR archive. In contrast, ResNet has an RF of 40, and Inception extends this to 235. For LITE and LITEMV, the RF is 114, which is sufficient for state-of-the-art performance on the UCR archive. However, for datasets with much longer time series, this RF needs to be increased.

The RF can be expanded by either increasing the filter lengths or adding more layers to deepen the model. While this typically leads to a substantial increase in network complexity for conventional CNNs, LITE and LITEMV can accommodate these adjustments without significant complexity increases, making them well-suited for handling longer time series while maintaining their efficiency and performance.

4.5 Conclusion

In this chapter we introduced LITE: a lightweight, Inception-based architecture enhanced with boosting techniques for TSC. Through rigorous experimentation and analysis, we demonstrated that LITE achieves competitive performance while maintaining a significantly lower number of parameters compared to more complex models like Inception, FCN, and ResNet.

The ensemble approach, LITETime, further capitalizes on the strengths of LITE, reducing variance and enhancing robustness. We explored the impact of boosting techniques such as hand-crafted convolution filters, multiplexing convolutions, and dilated convolutions through comprehensive ablation studies, confirming their contributions to the model's overall efficacy.

Moreover, recognizing the importance of multivariate time series classification in real-world applications, we introduced LITEMV. This adaptation preserves the

efficiency of LITE while extending its capabilities to handle the complexities of multivariate data. Our experiments confirmed that LITEMV performs exceptionally well in its ensemble version LITEMVTime, often surpassing more memory-intensive models like ConvTran in various scenarios.

We also addressed the limitations of our proposed architectures, particularly in handling extremely large datasets. We discussed potential solutions such as increasing the number of filters in DWSC layers and expanding the receptive field, which LITE and LITEMV can achieve with minimal increase in complexity.

In summary, LITE and LITEMV present a significant advancement in time series classification, offering a balance of efficiency, performance, and adaptability. These models are well-suited for deployment in resource-constrained environments, making them practical for a wide range of real-world applications.

Chapter 5

Semi-Supervised and Self-Supervised Learning for Time Series Data with a Lack of Labels

5.1 Introduction

The challenge of effectively classifying time series data has garnered significant attention within the field of machine learning. Previous chapters have discussed traditional approaches, which most of the time primarily rely on supervised learning techniques demanding the availability of labeled data. However, acquiring sufficient labeled time series data is often prohibitively difficult due to the need for expert annotation and the inherent complexity of the data itself. Consequently, there is a growing interest in methodologies that can leverage limited labeled data while making the most of the abundant unlabeled data available.

This chapter explores semi-supervised and self-supervised learning techniques as promising methods to address the issue of time series classification when labeled data is scarce. Semi-supervised learning and self-supervised learning methods aim to reduce the dependency on labeled data by utilizing unlabeled data to improve model performance. These techniques have shown considerable potential in various domains, and are becoming increasingly popular within the time series data mining research community.

In this chapter, we propose a novel self-supervised approach for enhancing TSC. Our method, named TRIPlet Loss In TimE (TRILITE), is built upon the concept of triplet loss, a mechanism traditionally used in tasks like face recognition to learn effective representations without the need for extensive labeled data (see Chapter 1 Section 1.3.3.2). TRILITE employs a specialized augmentation technique adapted to the characteristics of time series data, allowing the model to learn discriminative features from unlabeled data.

We investigate two specific use cases to evaluate the efficacy of TRILITE. The first scenario considers the augmentation of a supervised classifier's performance when only a small amount of labeled data is available. Here, TRILITE acts as a booster, enhancing the classifier by providing additional, meaningful representations. The second scenario addresses a semi-supervised learning context, where the dataset comprises both labeled and unlabeled samples. In this scenario, TRILITE is utilized to effectively harness the unlabeled data, resulting in improved overall classification accuracy.

Through extensive experiments conducted on 85 datasets from the UCR archive, we demonstrate the potential of TRILITE in both scenarios. The results indicate that our approach not only boosts performance in low-labeled data settings but also effectively incorporates unlabeled data to create more robust classifiers. This chapter outlines the methodology, experimental setup, and findings, contributing to the broader understanding of semi-supervised and self-supervised learning in time series classification.

By addressing the limitations of traditional supervised learning models and harnessing the power of unlabeled data, this work paves the way for more efficient and scalable solutions in the analysis and classification of time series data.

5.2 TRILITE: TRIPlet Loss In TimE

This section presents the proposed self-supervised learning approach for time series classification, named TRIPlet Loss In TimE (TRILITE). Our approach leverages triplet loss to learn meaningful representations from time series data without requiring extensive labeled data. We describe the architecture of the TRILITE model, the triplet loss mechanism, and the specific data augmentation techniques employed to generate effective triplets. The term *data augmentation* in this chapter does not mean training on more samples, it simply means transforming the input series to a new series that is somehow similar to the reference series.

5.2.1 Model Construction

Our TRILITE model features a trio of encoders, all sharing identical weights to ensure consistency. This configuration effectively functions as a single encoder processing the generated triplets. We have adopted the FCN architecture (Wang, Yan, and Oates, 2017), but modified it by removing the classification layer to suit our self-supervised learning framework. Each component of the triplet, the reference *ref*, positive *pos*, and negative *neg* samples, is input into the model, producing their respective latent representations (ref_l , pos_l , and neg_l). In this case, positive and negative samples refer to similar and dissimilar representations of the anchor (reference) sample. These representations are streamlined to a fixed size of 128 dimensions, enabling robust and efficient feature extraction. The three representations are then used to calculate the triplet loss, defined in the following section, as presented in Figure 5.1.

5.2.2 Triplet Loss

The core of our approach is the triplet loss (Schroff, Kalenichenko, and Philbin, 2015), which is designed to create a discriminative latent space by minimizing the distance between a reference sample and its positive representation while maximizing the distance between the reference and a negative representation. Formally, the triplet loss for a given triplet (reference, positive, and negative) is defined as:

$$\mathcal{L}_{triplet}(ref_l, pos_l, neg_l) = \max(0, \alpha + d(ref_l, pos_l) - d(ref_l, neg_l)) \quad (5.1)$$

where $d(.,.)$ is the Euclidean Distance and α is a margin hyperparameter that controls the separation between positive and negative pairs. The loss encourages the model to learn embeddings where similar samples are close together, and dissimilar samples are far apart.

FIGURE 5.1: Overview of our TRILITE model with a triplet input example taken form the Beef dataset of the UCR archive (Dau et al., 2019).

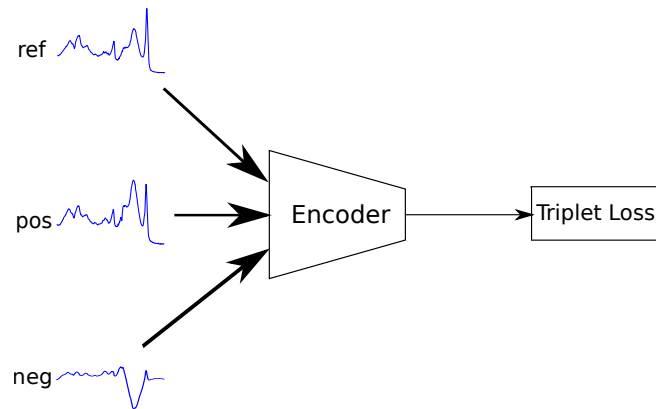
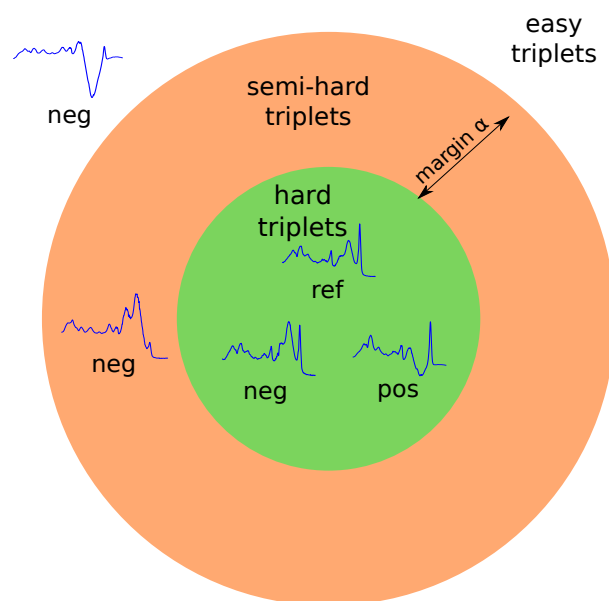


FIGURE 5.2: Schema of the relaxed spaced controlled by the margin α with an input example taken form the Beef dataset of the UCR archive (Dau et al., 2019).



The objective of the triplet loss function is to maximize the distance between the reference latent representation ref_l and the negative latent representation neg_l , while minimizing the distance between the reference and positive latent representations pos_l . Consequently, we can identify three situations for triplets as illustrated in Figure 5.2:

- **Easy Triplet:** The loss equals 0 because $d(ref_l, pos_l) + \alpha < d(ref_l, neg_l)$
- **Hard Triplet:** The negative representation is closer to the reference than the positive representation, i.e. $d(ref_l, neg_l) < d(ref_l, pos_l)$
- **Semi-Hard Triplet:** The positive representation is closer than the negative, i.e. $d(ref_l, pos_l) < d(ref_l, neg_l)$, but there is still a strictly positive loss.

Setting α to 0 would limit us to identifying only easy and hard triplets. Exclusively using easy triplets would likely cause the model to overfit, while relying solely on hard triplets could lead to underfitting. Therefore, the introduction of the α hyperparameter is crucial, as it facilitates the creation of semi-hard triplets, striking a balance between these extremes. Moreover, the incorporation of the max operation in the loss function ensures that the optimization problem remains convex, promoting more effective and stable training.

In the following section, we detail the proposed method of generating these triplets ref , pos and neg .

5.2.3 Triplet Generation

Algorithm 8 Triplet_Generation

Require: A time series dataset \mathcal{D} of N samples of length L each

Ensure: Three sets of triplets ref , pos and neg of same shape as \mathcal{D} each

```

1:  $shuffle(\mathcal{D})$ 
2:  $w \leftarrow random(0.6, 1)$ 
3: for  $i : 0 \rightarrow N$  do
4:    $ref[i] \leftarrow data[i]$ 
5:    $ts_1 \leftarrow random\_sample(data)$ 
6:    $ts_2 \leftarrow random\_sample(data)$ 
7:    $pos[i] \leftarrow w.ref[i] + (\frac{1-w}{2}).(ts_1 + ts_2)$ 
8:    $ts_3 \leftarrow random\_sample(data)$ 
9:    $ts_4 \leftarrow random\_sample(data)$ 
10:   $ts_5 \leftarrow random\_sample(data)$ 
11:   $neg[i] = w.ts_3 + (\frac{1-w}{2}).(ts_4 + ts_5)$ 
12:   $pos[i], neg[i] \leftarrow Mask(pos[i], neg[i])$ 
13: end for
14:  $pos \leftarrow Znormalize(pos)$ 
15:  $neg \leftarrow Znormalize(neg)$ 
16: Return  $ref, pos, neg$ 

```

Generating effective triplets is crucial for the success of the TRILITE model. We combine two main strategies for triplet generation: mixing up and masking. In (Wickstrøm et al., 2022), a mixing-up strategy is employed, while in (Franceschi, Dieuleveut, and Jaggi, 2019), a masking approach is utilized. The proposed triplet generation setup is detailed in Algorithms 8 and 9.

Algorithm 9 Mask**Require:** Two input time series x and y of length L **Ensure:** Masked version of x and y

- 1: $l \leftarrow \text{len}(x)$
- 2: $\text{start} \leftarrow \text{random_randint}(0, L - 1)$
- 3: $\text{stop} \leftarrow \text{random_randint}(\text{start} + \frac{L-1-\text{start}}{10}, \text{start} + \frac{L-1-\text{start}}{2.5})$
- 4: $x[0 : \text{start}] \leftarrow \text{noise}$
- 5: $x[\text{stop} + 1 :] \leftarrow \text{noise}$
- 6: $y[0 : \text{start}] \leftarrow \text{noise}$
- 7: $y[\text{stop} + 1 :] \leftarrow \text{noise}$
- 8: **Return** x, y

First, we generate a positive sample pos by computing a weighted sum of three time series, including the reference ref . For the negative sample neg , the reference is excluded from the weighted sum. We limit the mixed samples to three, ensuring each sample contributes significantly. The process can be represented by the following equations:

$$pos = w.ref + \frac{1-w}{2} \cdot (ts_1 + ts_2) \quad (5.2)$$

$$neg = w.ts_3 + \frac{1-w}{ts_4 + ts_5} \quad (5.3)$$

where ts_1 and ts_2 are randomly selected time series distinct from the reference, and the contribution weight w is randomly chosen between 0.6 and 1.0. This ensures the positive sample has a greater influence from the reference compared to ts_1 and ts_2 . For the negative sample, three distinct samples, ts_3 , ts_4 and ts_5 are randomly chosen from the training dataset excluding the ref sample.

Next, we apply a random-length mask to both the positive and negative samples. This masking strategy simplifies the training process by allowing the model to focus on learning specific segments of the representations rather than the entire sequence.

Finally, the unmasked segments of the time series are replaced with random Gaussian noise, enhancing the robustness of the model. Figures 5.3 and 5.4 provides a visualization of the positive and negative samples generation. Importantly, triplet generation occurs online during each training epoch, promoting better generalization of the model.

5.3 Experimental Setup

For our experiments, we utilized 85 datasets from the UCR archive (Dau et al., 2019)¹. All datasets were z-normalized prior to training. We employed the Adam optimizer with an initial learning rate of 10^{-3} . Triplet generation occurred online for each epoch to ensure robust generalization. For evaluation on the test set, we used the final trained model. The models were trained for 1000 epochs with batch size 32.

To identify the optimal hyperparameter α , we conducted a thorough exploration across a range of values: $\{10^{-6}, 10^{-5}, 10^{-4}, 10^{-3}, 10^{-2}, 10^{-1}\}$. By meticulously visualizing the resulting latent representations, we discerned that modifying α primarily affected the scale of these representations without altering the fundamental classification of triplet types (as elaborated in Section 5.2.2 of this chapter). This nuanced

¹More experiments will be done for this technique.

FIGURE 5.3: A **mixed up pos** is built from **three time series including the ref**. The resulting time series is close to the *ref* except some areas as highlighted in the **red circle**. A **mask** is then applied on the **mixed up pos** to generate the **final sample**, where the unmasked parts are replaced by a Gaussian noise.

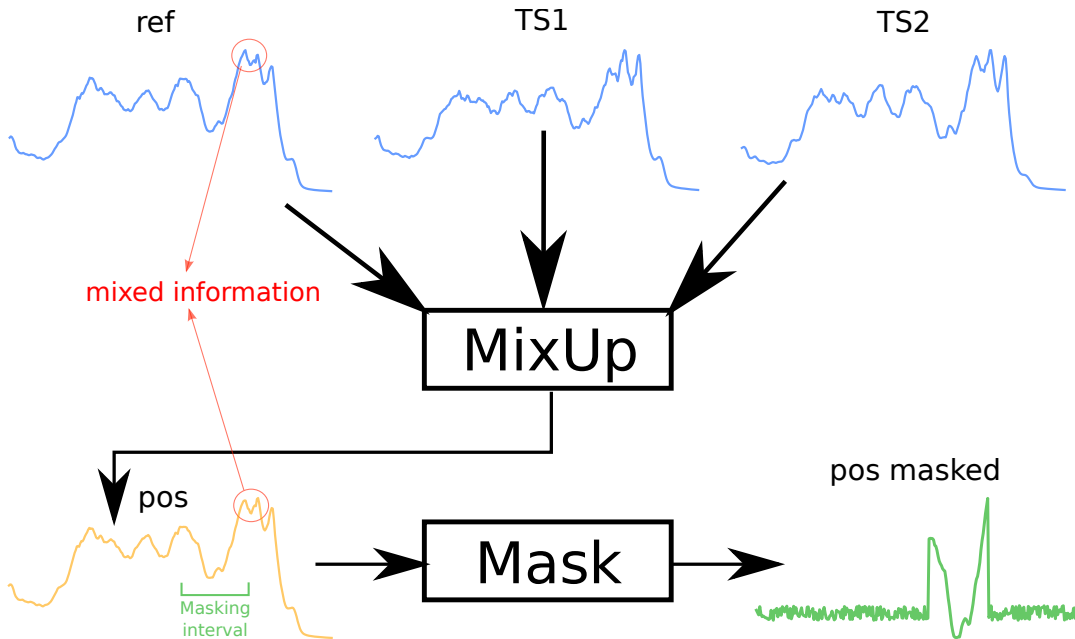


FIGURE 5.4: A **mixed up neg** is built from **three time series excluding the ref** used to generate the *pos* sample. The resulting time series is close to the *not ref* except some areas as highlighted in the **red circle**. A **mask** is then applied on the **mixed up neg** to generate the **final sample**, where the unmasked parts are replaced by a Gaussian noise.

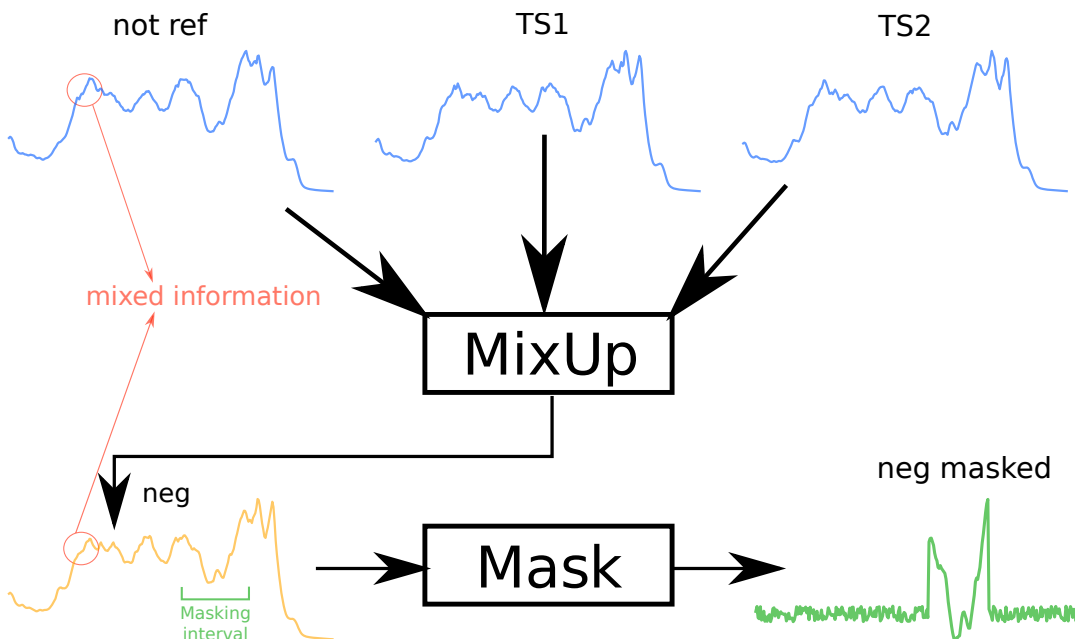
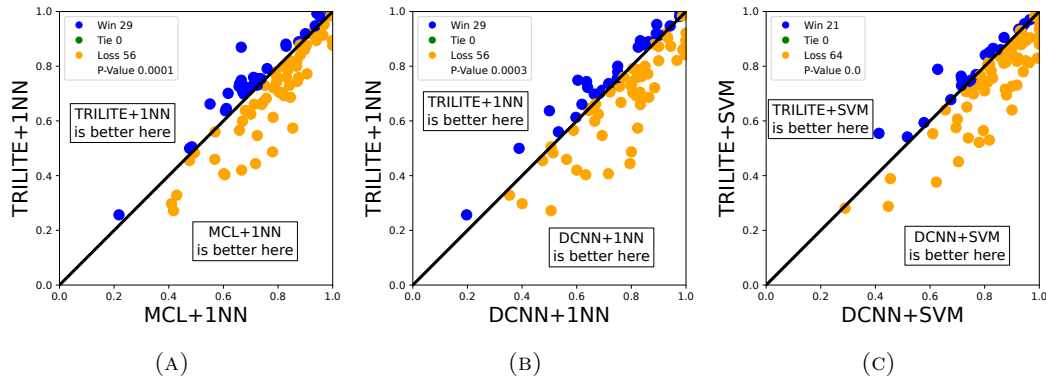


FIGURE 5.5: Comparing the proposed TRILITE approach to two state-of-the-art SSL models: DCNN (Franceschi, Dieuleveut, and Jaggi, 2019) and MCL (Wickstrøm et al., 2022). We compare the classification of TRILITE latent spaces to MCL’s latent space using a 1NN and to DCNN’s latent space using both 1NN and a Support Vector Machine classifier (Vapnik, 2013) following the original work of both comparates.



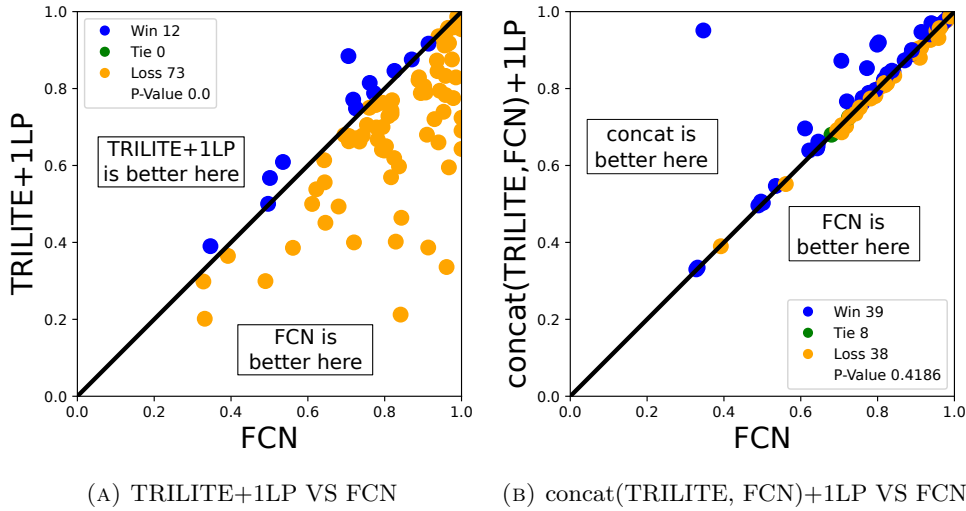
understanding led us to conclude that an α value of 10^{-2} struck the right balance. This value was meticulously fine-tuned using a representative subset of the UCR archive, ensuring robustness and generation in our model’s performance.

5.4 Experimental Results

5.4.1 Comparing To State-Of-The-Art

Comparing our approach to the two state-of-the-art models, Dilated Convolutional Neural Network (DCNN) with its version of triplet loss (Franceschi, Dieuleveut, and Jaggi, 2019) and Mixup Contrastive Learning (MCL) (Wickstrøm et al., 2022), is essential as this work draws significant motivation from their methodologies. However, the goal was not to outperform these models as our objectives differ. In this study, the aim is to demonstrate how self-supervised models can enhance supervised learning, particularly in scenarios with limited data and a lack of labeled data. For each self-supervised model, DCNN, MCL, and TRILITE (ours), we applied a classifier to their latent features to evaluate performance, posterior to training. Specifically, we compared TRILITE and MCL using a 1NN classifier with Euclidean distance, consistent with the evaluation method used in (Wickstrøm et al., 2022). Additionally, we compared TRILITE and DCNN with both 1NN and SVM classifiers, as presented in (Franceschi, Dieuleveut, and Jaggi, 2019). The choice of classifier when comparing to each of the two comparators aligns with those used in the original experiments of DCNN and MCL. We present in Figure 5.5 the three 1v1 scatter plots illustrating these comparisons. Although our model does not consistently surpass the performance of DCNN and MCL across all datasets, it does perform comparably on several datasets. This indicates that TRILITE has potential. Now, we will present the two cases addressing the challenges of small labeled datasets and the lack of labeled samples. In scenarios with small labeled datasets, the primary challenge is that models tend to overfit, as they struggle to learn patterns that generalize well beyond the limited training data. Such scenario results in poor performance on unseen data,

FIGURE 5.6: Scatter plots comparing the proposed TRILITE model to FCN.



limiting the model’s utility. Moreover, the lack of labeled samples poses a significant challenge in training supervised models, as they rely on labeled data to learn associations between inputs and outputs. Without sufficient labeled data, models cannot effectively learn or make accurate predictions, leading to unreliable outcomes in practical applications.

5.4.2 Use Case 1: Small Annotated Time Series Datasets

To address the first case of having a small annotated time series dataset, we compared the TRILITE model, followed by a fully connected layer with *softmax* activation (denoted as TRILITE+1-LP), against the fully supervised FCN model. It is important to note that the TRILITE+1LP approach is a two step training, first the TRILITE is trained on the self-supervised task and this is subsequently followed by training a 1LP classifier on the pre-trained TRILITE’s latent space. The 1v1 scatter plots are reported in Figure 5.6a. As expected, the supervised model generally outperforms the self-supervised one. However, for certain datasets, the self-supervised features notably improve classification accuracy. This observation motivated us to explore the contribution of self-supervised features within a supervised learning context.

To do this, we concatenated the latent representations from the self-supervised TRILITE model (each of size 128) with those from the supervised FCN model (also of size 128) for both the training and test sets. The concatenated features were then used to train a classifier comprising a single fully connected layer with softmax activation (1LP). Subsequently, this pipeline is evaluated on the concatenated features of the test set. We compared this approach, denoted as concat(TRILITE,FCN)+1LP, against the fully supervised FCN in Figure 5.6b. This Win-Tie-Loss comparison highlights that the concatenation method is never significantly worse than the single FCN, in terms of magnitude of accuracy difference. This can be attributed to the fact that supervised features are not negatively impacted by the SSL features; in the worst case, the linear classifier can simply ignore the SSL features if they do not aid classification.

Furthermore, we present in Figure 5.7 the MCM comparing the three models: TRILITE+1LP, FCN, and the concatenation method concat(TRILITE, FCN)+1LP.

FIGURE 5.7: The MCM (Chapter 2) comparing `concat(TRILITE,FCN)+1LP` to FCN and TRILITE+1LP over the 85 datasets of the UCR archive.

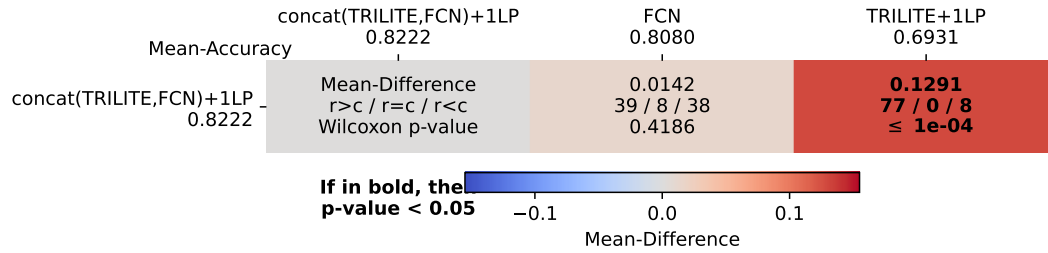
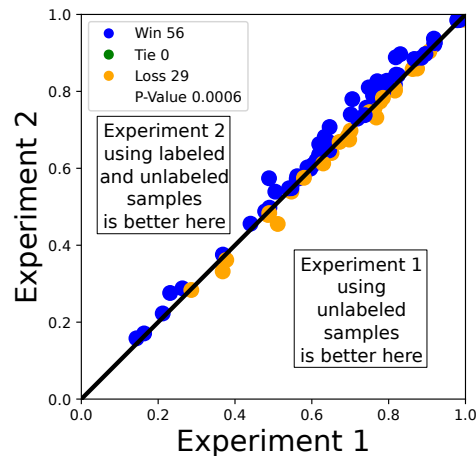


FIGURE 5.8: Comparison of experiment 1 and experiment 2. In experiment 1, the TRILITE model is trained only on the labeled subset (30% of the data). On the contrary, in experiment 2, the TRILITE model is trained on the whole train set. The evaluation is done on the whole test set.



The MCM highlights that the concatenation method is nearly 2% better in terms of average accuracy, demonstrating the boosting effect. This indicates that SSL generates features distinct from those produced by supervised learning. Consequently, the combination of both sets of features enhances classification performance. Notably, the peaks in performance improvement are observed in datasets with a small number of samples, such as `DiatomSizeReduction`, which has only 16 samples in the training set.

5.4.3 Use Case 2: Partially Annotated Time Series Datasets

In this second case, we explore a semi-supervised scenario where only a portion of the data is labeled. Our objective is to assess how self-supervised learning can address the challenge of limited labels. Assuming that only 30% of the training set is labeled, we proceed with the following steps:

1. **Self-supervised training:** We generate self-supervised latent representations by training our TRILITE model:
 - **Experiment 1:** Training is conducted solely on the labeled subset.
 - **Experiment 2:** Training is conducted on the entire training set, including both labeled and unlabeled data.

2. **Supervised learning:** The latent representations derived from the labeled set (from either Experiment 1 or Experiment 2) are fed into a Ridge classifier (Hoerl and Kennard, 1970).
3. **Evaluation:** The performance of the trained classifier is then evaluated on the test set.

To ensure the reliability and robustness of our results, these steps are repeated across 25 runs, with the average accuracy calculated for each run. The high number of experiments motivated the usage of Ridge classifier instead of SVM as proposed by (Franceschi, Dieuleveut, and Jaggi, 2019) given its fast training time. The same labeled subset is utilized for both experiments within each run. The 1v1 scatter plot comparison between **Experiment 1** and **Experiment 2** is illustrated in Figure 5.8.

The comparison reveals that Experiment 2 outperforms **Experiment 1** more frequently. On average, when **Experiment 2** prevails, the accuracy difference is 2.12 ± 2.13 . Conversely, when Experiment 1 has better performance, the accuracy difference averages 1.17 ± 1.21 . This disparity underscores the effectiveness of self-supervised learning in cultivating more nuanced and comprehensive latent representations. By integrating both labeled and unlabeled data, **Experiment 2** is able to capture a wider spectrum of underlying patterns and structures within the data. This setup not only enhances the overall performance of the model but also demonstrates that self-supervised methods contribute to greater stability and adaptability across diverse datasets. These findings emphasize the potential of self-supervised learning to bridge gaps in data quality and quantity, leading to models that are better equipped to generalize across different tasks and challenges.

5.5 Conclusion

In this chapter, we have explored innovative approaches in semi-supervised and self-supervised learning for TSC. The primary goal of our research was to utilize self-supervised models to enhance supervised models in two specific cases: first, when there is a lack of data but all available data is labeled, and second, when there is a scarcity of labeled data in a semi-supervised learning context.

Our TRILITE model, based on triplet loss, was developed to generate meaningful latent representations from time series data. We conducted extensive experiments comparing TRILITE with state-of-the-art models such as DCNN (Franceschi, Dieuleveut, and Jaggi, 2019) and MCL (Wickstrøm et al., 2022). While TRILITE did not consistently outperform these models, it demonstrated competitive performance on several datasets. This indicates the potential of self-supervised learning in improving TSC, particularly in challenging scenarios with limited labeled data.

In the first use case, where only a small annotated time series dataset is available, we showed that incorporating self-supervised features with supervised learning models can enhance classification accuracy. Specifically, by concatenating the latent representations from the TRILITE model with those from a supervised FCN model, we observed significant improvements in performance. This approach, termed `concat(TRILITE, FCN)`, consistently achieved comparable results to the single FCN model and better performance on small datasets, showcasing the complementary nature of self-supervised and supervised features.

In the second use case, involving a semi-supervised scenario with only a portion of the data labeled, we demonstrated how self-supervised learning can effectively address the lack of labels. By training the TRILITE model on both the labeled subset and

the entire training set, we obtained more robust latent representations that improved the performance of the downstream classifier. The results from repeated experiments confirmed that leveraging unlabeled data in self-supervised training leads to more meaningful feature extraction, which in turn enhances classification accuracy.

The findings in this chapter underscore the importance of integrating self-supervised learning techniques to enhance supervised learning models, especially in the context of time series data with limited labeled samples. The potential of TRILITE to generate useful features from both labeled and unlabeled data opens new avenues for future research. Moving forward, further refinement of these techniques could lead to more robust and efficient models, advancing the field of TSC, and potentially other tasks, addressing the persistent challenges of data scarcity and annotation costs.

Chapter 6

Time Series Analysis For Human Motion Data

6.1 Introduction

Human motion data, particularly skeleton-based data, plays a crucial role in various applications such as action recognition (Devanne et al., 2014), rehabilitation assessment (Capecci et al., 2019), prediction/forecasting (Martinez, Black, and Romero, 2017), and generation (Petrovich, Black, and Varol, 2021) for cinematic and gaming systems. This chapter digs into the unique aspects of Multivariate Time Series (MTS) analysis when applied to skeleton-based human motion sequences.

Skeleton-based human motion data is primarily extracted using advanced sensing technologies like the Microsoft Kinect (Asteriadis et al., 2013; Lun and Zhao, 2015), which captures 3D spatial coordinates of body joints. This data provides a simplified yet informative representation of human motion by tracking the positions of key skeletal joints over time. Other technologies, such as motion capture systems (Vlasic et al., 2007), also offer detailed skeletal data by using markers placed on the body to record joint movements with high precision. These datasets are invaluable for various tasks due to their ability to encapsulate the complexity of human motion in a structured format. One significant advantage of Kinect sensors over traditional MoCap technologies is their inherent synchronization. With Kinect, all joints are detected through a single camera operating at a consistent sampling frame rate, ensuring uniformity and temporal coherence in the captured data. In contrast, MoCap systems assign individual sensors to each joint, which can lead to potential desynchronization issues between the sensors. Moreover, Kinect sensors offer the benefits of being both low-cost and non-intrusive, enhancing their accessibility and ease of use. These attributes make Kinect an ideal choice for our study, and hence, we have exclusively utilized Kinect-based data in this chapter. An example of such sequences are presented in Figure 6.1.

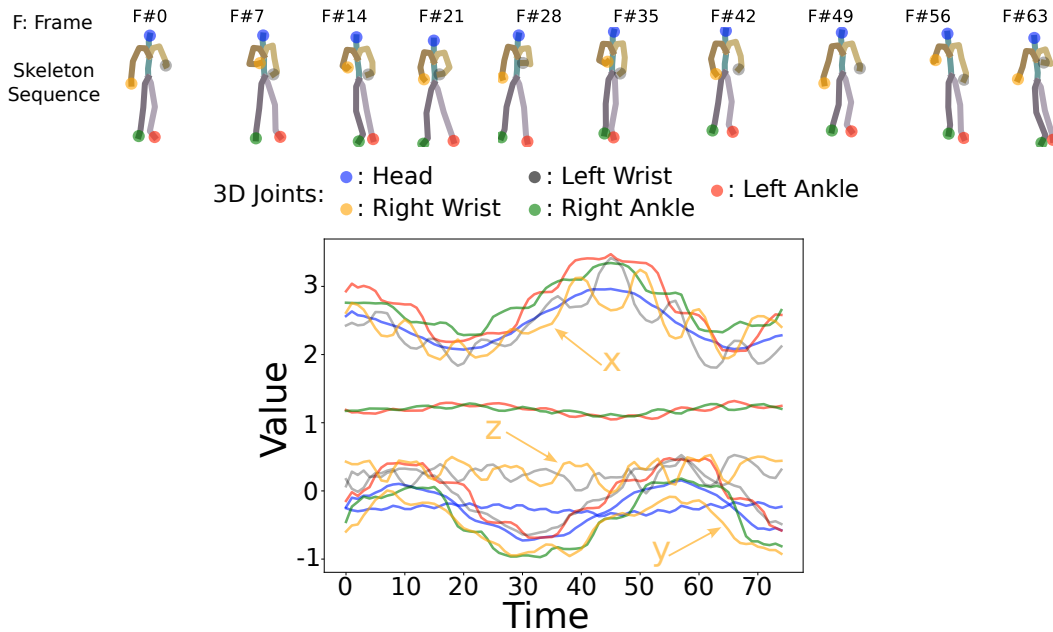
The versatility of skeleton-based human motion data lends itself to numerous tasks:

- **Action Recognition:** Identifying specific actions or activities performed by individuals.
- **Motion Assessment:** Monitoring and analyzing patient movements to aid in physical therapy and recovery.
- **Prediction:** Forecasting future movements based on past motion patterns.
- **Generation:** Assessment Creating realistic human movements for use in cinematic productions, gaming environments, medical research etc.

FIGURE 6.1: Example of one sample per action (12 total) taken from the HumanAct12 action recognition skeleton based dataset (Guo et al., 2020). Each skeleton is made of five body parts, **right arm**, **left arm**, **spine & neck**, **right leg** and **left leg**.



FIGURE 6.2: Example of one sample taken from the HumanAct12 action recognition skeleton based dataset (Guo et al., 2020) represented as a Multivariate Time Series. For the sake of visualization we consider only five joints: head, left wrist, right wrist, left ankle, and right ankle, each in a 3D space, resulting in an MTS of 15 dimensions.



Skeleton-based human motion sequences can be effectively represented as MTS. Typically, a skeleton sequence has a shape of $(time, number\ of\ joints, dimensions\ per\ joint)$. For instance, with 25 joints tracked in 3D space (x, y, z coordinates), each time step is characterized by a 75-dimensional vector. This structure can be transformed into a more conventional MTS format of $(time, 75)$. This transformation enables the application of standard time series analysis techniques to the data. An example of this representation is illustrated in Figure 6.2.

In previous chapters, we have explored various deep learning methodologies for time series analysis. This chapter will extend that exploration to the domain of skeleton-based human motion data. We will assess the effectiveness of deep learning models in addressing specific tasks related to this type of data.

In this chapter, we will explore several key contributions related to the analysis of skeleton-based human motion data. **First**, we will investigate the use of deep learning models to assess the quality of a patient's movement for rehabilitation exercises. **Second**, to mitigate overfitting, we will explore techniques to prototype and extend medical datasets, ensuring robust model performance. This will be done through a novel Time Series Prototyping (TSP) approach, notably ShapeDBA (ShapeDTW Barycenter Average). **Third**, the chapter will cover the use of deep generative models to create new, realistic motion sequences, expanding the potential applications in action recognition tasks by proposing a novel CNN-based VAE model.

We will use two publicly available datasets for all our work in this chapter, notably the HumanAct12 (Guo et al., 2020) dataset for action recognition and the Kimore (Capecci et al., 2019) dataset for the medical rehabilitation assessment.

6.2 Advancing Human Motion Rehabilitation Assessment with LITEMVTime

In the domain of rehabilitation assessment, accurately evaluating a patient’s performance during physical exercises is paramount. Traditional methods often rely on subjective judgments or handcrafted features, which can be both time-consuming and inconsistent. The advent of deep learning models, particularly for time series classification, has opened new avenues for enhancing the precision and efficiency of these assessments.

Deep learning techniques, such as Convolutional Neural Networks (CNNs) and Recurrent Neural Networks (RNNs), have shown remarkable success in classifying time series data, including human motion sequences captured via 3D skeleton tracking (Jiang and Yin, 2015). These methods leverage the sequential and spatial characteristics of the data, providing a more nuanced understanding of the movements.

In this section, we utilize LITEMVTime, the multivariate extension of the previously developed LITETime model (Chapter 4). LITEMVTime has been specifically designed to address MTS data for classification tasks, such as the task of human motion rehabilitation assessment. It is lightweight in terms of both the number of parameters and computational requirements, making it highly suitable for real-time applications in medical settings. This efficiency is crucial for deployment in clinical environments, where timely and accurate feedback is essential for both patients and medical practitioners.

We showcase in this section that LITEMVTime outperforms other architectures on this task. The model’s superior performance is attributed to its innovative architecture, which effectively captures the temporal dynamics and spatial configurations of the human skeleton during rehabilitation exercises. Unlike conventional models that may require extensive computational resources, LITEMVTime’s streamlined design ensures it can operate on standard medical clinic hardware without compromising on performance.

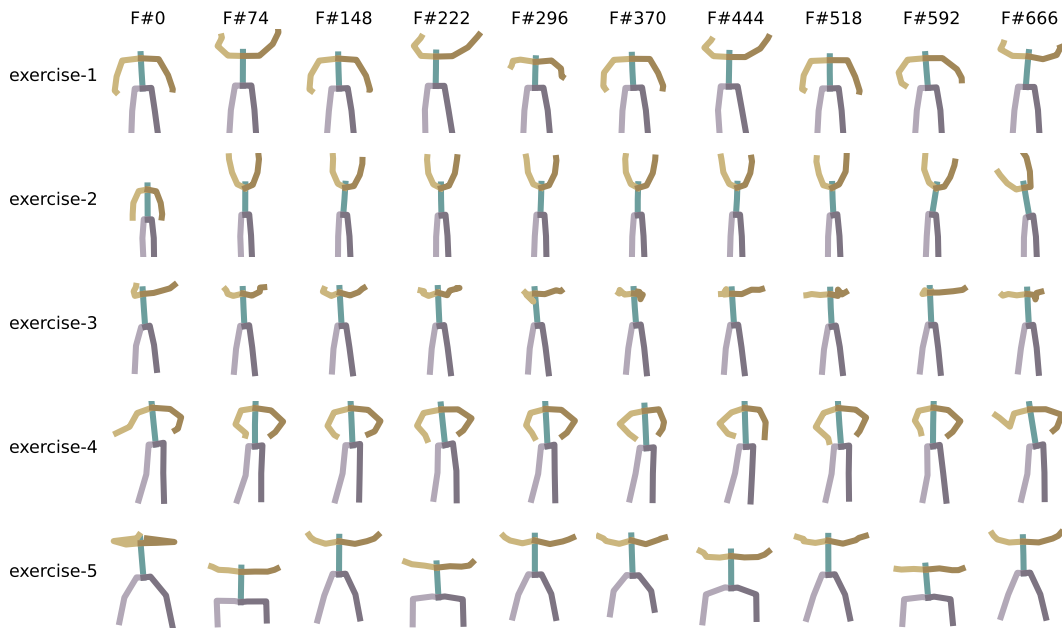
Furthermore, the model’s efficiency ensures that it can be integrated into existing clinical workflows without the need for extensive computational infrastructure. This integration can enhance the overall quality of care by enabling more frequent and detailed assessments, ultimately contributing to better patient outcomes (Muro-De-La-Herran, Garcia-Zapirain, and Mendez-Zorrilla, 2014; Nweke et al., 2018).

A crucial aspect of deploying machine learning models in medical applications is the explainability of their decisions. Medical doctors often pose the question, “*Why should I trust you?*” (Ribeiro, Singh, and Guestrin, 2016) when presented with automated assessment results. To address this concern, we have integrated Class Activation Maps (CAMs) (Zhou et al., 2016) into our framework. CAMs help in visualizing the regions of the input data that are most influential in the model’s decision-making process, thereby providing insights into which features are most impactful for a given prediction. This is particularly important for our CNN-based LITEMVTime model.

6.2.1 Experimental Setup & Dataset Preprocessing

For this experiment, we utilized the Kimore dataset (Capecci et al., 2019), which includes video sequences of patients performing rehabilitation exercises, captured and converted into numerical 3D sequences using Kinect v2 sensors (Asteriadis et al., 2013). The dataset comprises recordings from both healthy and unhealthy subjects executing five distinct rehabilitation exercises. These exercises are the following: (1) lifting of the arms, (2) lateral tilt of the trunk with the arms in extension, (3) trunk

FIGURE 6.3: Visualization of one sample from the Kimore skeleton based human rehabilitation dataset (Capecci et al., 2019), per exercise.



rotation, (4) Pelvis rotations on the transverse plane and (5) Squatting. An example sequence of each exercise is represented in Figure 6.3. The skeletons contain 18 joints each in a three dimensional space x , y and z .

Each sequence of patient’s movement in every exercise is evaluated by a human expert, who assigns a quality score ranging from 0 (poor performance) to 100 (excellent performance). The dataset comprises 71 subjects, with 40 being healthy and 31 unhealthy. Each subject performs at least five repetitions of each exercise, and all repetitions are recorded as individual samples, resulting in 71 samples per exercise.

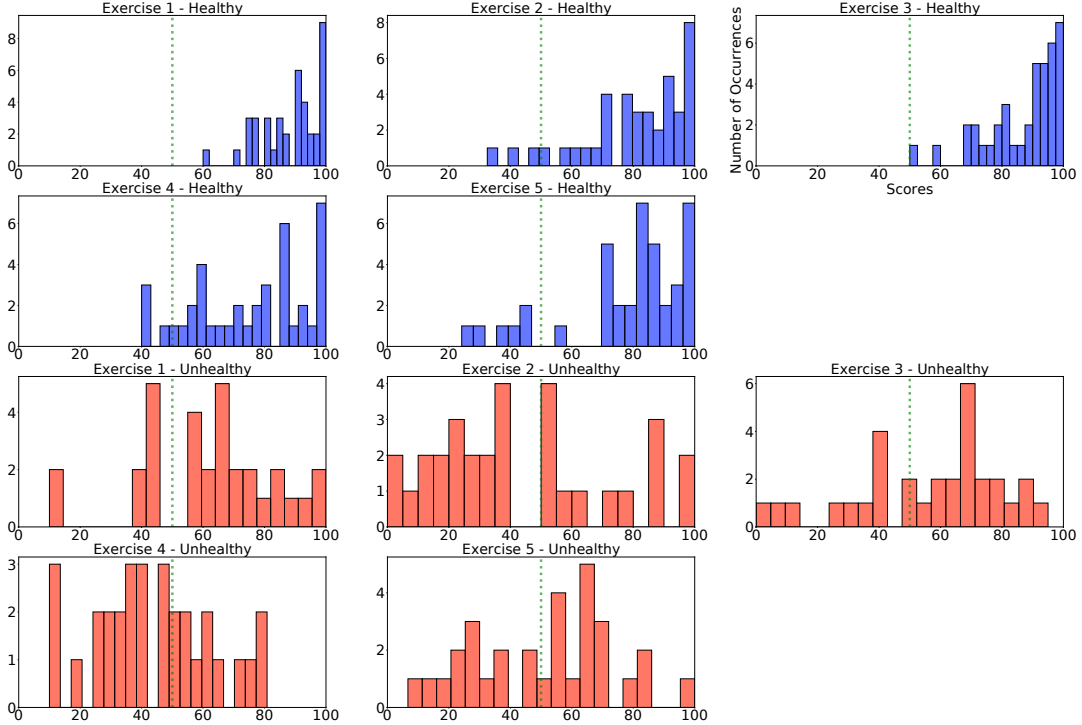
Figure 6.4 illustrates the distribution of performance scores for each exercise, differentiated between healthy and unhealthy subjects. Typically, unhealthy subjects tend to receive lower scores, whereas healthy subjects achieve higher scores. However, this is not always the case, as seen in Figure 6.4. This discrepancy arises because even if some subjects are considered as unhealthy in the dataset, their injury could not limit to perform some exercise. Despite the regression nature of the dataset, we reframed the task to evaluate the performance of subjects irrespective of their health status. The evaluation criteria are defined as follows:

- Scores below 50 indicate a poorly performed exercise.
- Scores above 50 indicate a well-performed exercise.

The dataset features sequences of varying lengths, which necessitated resampling all sequences to a common length, determined to be 748 frames (the average length) using the Fourier resampling method in *scipy* Python package (Virtanen et al., 2020). This is due to the fact that skeleton-based motion sequences extracted using kinect cameras are sampled using a uniform sample rate, which is a condition to be able to use this resampling approach. We split the dataset into an 80% – 20% train-test set, ensuring stratification to maintain a balanced representation of good and bad performances in both sets.

Each 3D human motion sequence is transformed to an MTS and each exercise is utilized as an independent dataset, given that one score value does not represent

FIGURE 6.4: The distribution of the scores given by experts to healthy and unhealthy patients when performing each of the five different exercises. The threshold set to discretize these scores is chosen to be the middle point posed at 50.



the same thing from one exercise to another. The dataset were z-normalized prior to training and testing independently on each channel. The best-performing model during training, determined by monitoring the training loss, was selected for testing. The Adam optimizer with a Reduce on Plateau learning rate decay method was employed, using TensorFlow’s (Abadi et al., 2015) default parameter settings. The same parameters are used as presented in Chapter 4 for LITEMV, as well as its ensemble version LITEMVTime.

6.2.2 Competitor Models

We evaluated the performance of various deep learning models on this dataset, including Fully Convolutional Networks (FCN), ResNet, and InceptionTime, along with our proposed model, LITEMVTime. Additionally, we included a baseline classifier, 1-Nearest Neighbor Dynamic Time Warping (1-NN-DTW) following (Middlehurst, Schäfer, and Bagnall, 2024). For all the competitors we utilize the same parameter setup used in (Ismail Fawaz et al., 2019).

6.2.3 Experimental Results

The results, summarized in Table 6.1, indicate that LITEMVTime outperforms the other models in both average performance and average rank across all exercises. This demonstrates that LITEMVTime, despite its small size, is highly effective in classifying the quality of exercise performance based on recorded sequences. Consequently, LITEMVTime proves to be a valuable tool for assessing patient rehabilitation exercises, providing reliable classifications that can support clinical decision-making.

TABLE 6.1: Accuracy of the baseline, 1-NN-DTW, three state-of-the-art deep learning models, FCN ResNet and InceptionTime compared to **our** LITEMVTime on the Kimore human rehabilitation exercise. We present for each of the five exercises the accuracy of the models on the test unseen split. The performance of the winning model for each exercise is shown in **bold** and the second best is shown in underline.

Kimore Exercise	1-NN-DTW	FCN	ResNet	InceptionTime	LITEMVTime
Exercise 1	60.00	84.00	<u>85.33</u>	78.67	86.67
Exercise 2	46.67	72.00	69.33	<u>78.67</u>	80.00
Exercise 3	86.67	92.00	86.67	<u>88.00</u>	86.67
Exercise 4	66.67	<u>65.33</u>	60.00	57.33	66.67
Exercise 5	73.33	66.67	<u>81.33</u>	84.00	80.00
Average Accuracy	66.67	76	<u>76.53</u>	<u>77.33</u>	80.00
Average Rank	3.6	2.8	2.8	<u>2.6</u>	1.8

6.2.4 Enhancing Trust and Transparency in Human Rehabilitation Assessment With LITEMV

In the field of rehabilitation assessment, achieving high performance with deep learning models is essential. However, the ability to understand the decision-making process of these models is equally important, especially in medical applications where the stakes are high. Over the past decade, there has been a significant focus on model interpretability, particularly in Time Series Classification (TSC) over the last five years (Theissler et al., 2022).

Class Activation Maps (CAM) are a powerful technique for interpreting the decisions of deep Convolutional Neural Networks (CNNs), which are often perceived as black-box models. Initially introduced by (Zhou et al., 2016) for image data, CAMs have since been adapted for time series data, providing a way to visualize which parts of the input data contribute most to the model’s decisions. This technique got first adapted to time series classification in (Wang, Yan, and Oates, 2017).

CAMs require a global representative layer before the softmax classification layer, such as Global Average Pooling (GAP). This setup is used in various architectures including FCN, ResNet, Inception, LITE, and LITEMVTime. In the context of TSC, the output of a CAM is a univariate time series where each timestamp indicates the importance of that specific point in the input series for the model’s decision.

Mathematically, CAM is defined as follows:

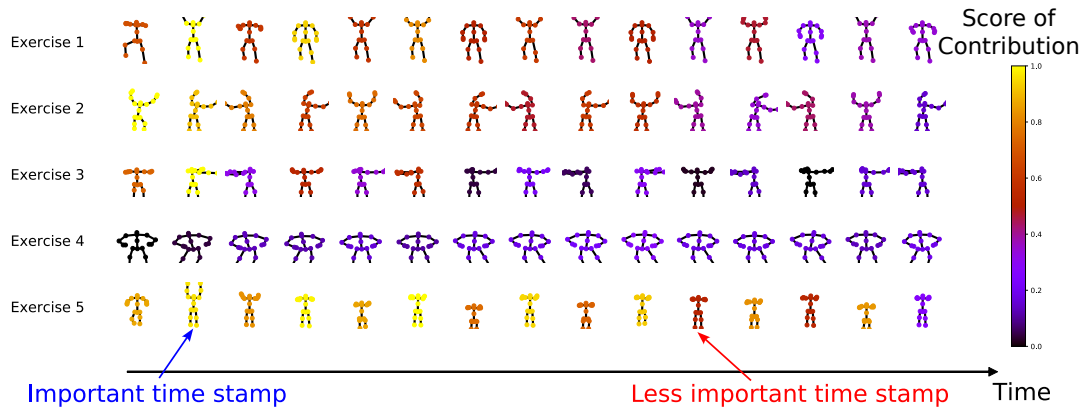
- Let $\mathbf{O}(t) = \{\mathbf{o}^1(t), \mathbf{o}^2(t), \dots, \mathbf{o}^M(t)\}$ represent the output of the last convolutional layer, an *MTS* with M variables (the number of filters). Thus, $\mathbf{o}^m(t)$ is the output univariate time series of filter $m \in [1, M]$.
- Let $\mathbf{w}^c = \{w_1^c, w_2^c, \dots, w_M^c\}$ be the weight vector connecting the GAP output to the neuron of the winning class c (the class with the highest probability value).

The CAM output is then:

$$CAM(t) = \sum_{m=1}^M w_m^c \cdot \mathbf{o}^m(t) \quad (6.1)$$

This output is normalized using min-max normalization. For two given timestamps, the one with the highest CAM score has contributed more significantly to the decision of the black-box model.

FIGURE 6.5: Explainability of the LITEMV model using the Class Activation Map (CAM) on the feature of the last DWSC layer. The colorbar values represent the normalized (between 0 and 1) scores of the CAM. Five samples each from one of the five exercises are presented with the CAM scores on different time stamps. A higher CAM score indicates the importance of a time stamp for the decision making of LITEMV.



In our study, we apply CAM to the LITEMVTime model to interpret its decisions on the Kimore dataset, which includes human rehabilitation exercises. We analyze five different examples from each exercise and generate CAM outputs using a LITEMVTime model trained for each exercise classification task presented in Figure 6.5.

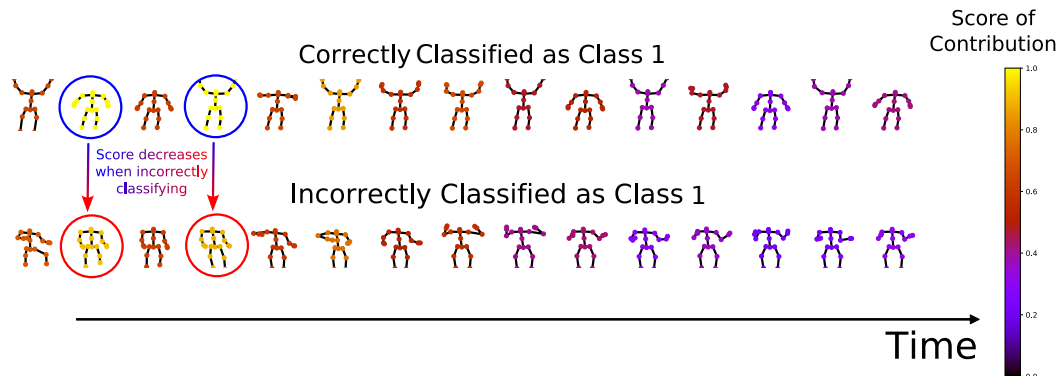
Given that human skeleton data forms a multivariate time series, the CAM values represent the temporal axis, with each timestamp's CAM score indicating the contribution of that particular pose to the classification. To further explore the variability in CAM scores, we compare two CAM explanations for two samples of the same exercise in Figure 6.6: one correctly classified as class 1 ($score > 50$) and another incorrectly classified as class 1 when it should be class 0 ($score < 50$). The higher intensity of CAM colors for the correctly classified sample indicates higher contribution of important timestamps, while the misclassified sample shows lower scores, reflecting the influence of the incorrect class weights.

By utilizing CAM, we can provide clear explanations for the LITEMVTime model's decisions, demonstrating the specific data points that influenced its classifications. This transparency is crucial for integrating deep learning models into clinical workflows, ensuring that healthcare professionals can rely on these tools with confidence.

6.3 Extending Human Motion Rehabilitation Data With Time Series Prototyping

Human motion rehabilitation data is inherently sensitive and challenging to acquire, particularly due to privacy concerns and the complex nature of medical data. This scarcity often results in limited datasets that can lead to overfitting in machine learning models used for patient assessment, whether for classification or regression tasks. To mitigate this issue, we propose generating synthetic data using time series prototyping techniques (Petitjean, Ketterlin, and Gançarski, 2011). By creating

FIGURE 6.6: Explainability of the LITEMV model using the Class Activation Map (CAM) on the feature of the last DWSC layer. Two samples from the test split of the same exercise are presented, the first (top) having a ground truth of class 1, and the second (bottom) having a ground truth of class 0. LITEMV correctly classifies the first sample but incorrectly the second. It can be seen that the important time stamp in the case of the correctly classified sample has higher color intensity, so higher CAM score, compared to the same time stamp from the incorrectly classified sample.



synthetic data, we can extend existing datasets, making models more resilient to overfitting and improving their generalization.

One effective approach for generating synthetic data is through time series prototyping. We introduce an innovative approach called ShapeDBA (Shape Dynamic Time Warping Barycenter Average) for time series prototyping (Chapter 1 Section 1.3.1). Following its application in standard prototyping, we leverage ShapeDBA for advanced weighted prototyping. This method builds upon the sophisticated principles of weighted elastic averages as delineated by (Forestier et al., 2017). This method involves creating prototypes that capture the essential characteristics of a set of time series data, which can then be used to generate new, synthetic sequences.

In the following sections, we will present the ShapeDBA method in detail and provide extensive experimental results to demonstrate that it is now the state-of-the-art prototyping method for time series data. Subsequently, we will introduce the weighted ShapeDBA setup tailored for regression tasks, specifically focusing on human rehabilitation assessment using the Kimore dataset (Capecci et al., 2019). We will extend the Kimore dataset with synthetic data generated by the ShapeDBA method and demonstrate that this augmented dataset significantly enhances the performance of deep supervised regression models compared to using the original dataset alone.

6.3.1 Generating Effective Time Series Prototypes With ShapeDBA

Prototyping time series data is a critical task in various domains, including medical diagnostics, human motion analysis, and satellite imagery interpretation. Traditional methods for generating time series prototypes often fall short in preserving the inherent patterns and nuances of the data, leading to out-of-distribution artifacts. This discrepancy is primarily due to the reliance on conventional DTW measure (Petitjean, Ketterlin, and Gançarski, 2011), which emphasize absolute similarities over neighborhood similarities. These artifacts can significantly impact the accuracy and reliability of subsequent analyses, such as clustering (Holder, Middlehurst, and Bagnall, 2024), classification (Petitjean et al., 2014) or explainability (Gee et al., 2019).

Therefore, there is a pressing need for a more robust and representative method to generate prototypes that faithfully capture the underlying data distribution, ensuring more accurate and meaningful insights from time series analysis.

6.3.1.1 ShapeDBA Methodology

Our proposed prototyping method, ShapeDBA (Shape Dynamic Time Warping Barycenter Averaging), is an advanced method designed to generate more accurate and representative time series prototypes. The key innovation in ShapeDBA is the integration of the ShapeDTW (Zhao and Itti, 2018) (Chapter 1 Section 1.2.1.1) measure, which considers the structural similarities within the neighborhoods of time series data points, thus overcoming the limitations of traditional DTW methods.

The ShapeDBA algorithm follows these steps:

1. **Initialization:** Start with an initial average time series, which can be randomly selected from the dataset.
2. **Alignment:** For each time stamp in the average time series, find the aligned points (using ShapeDTW measure) in all the time series samples. This involves creating a set of associated time stamps $assoc_t$ for each time stamp t in the average series.
3. **Averaging:** Calculate the barycenter for each time stamp t by averaging all the aligned points in $assoc_t$. The barycenter is computed as:

$$ShapeDBA_{barycenter}(assoc_t) = \frac{1}{|assoc_t|} \sum_{i=1}^{|assoc_t|} assoc_t^i \quad (6.2)$$

4. **Iteration:** Repeat steps 2 and 3 until convergence, i.e. until the changes in the average time series are minimal.

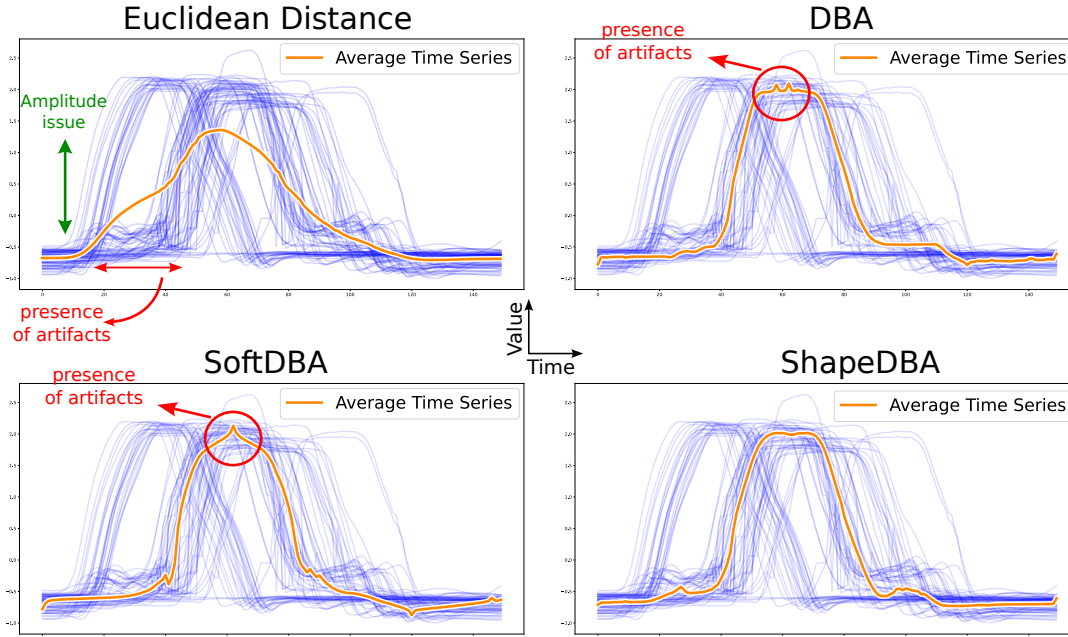
6.3.1.2 Reach Value Control

The “reach” hyperparameter in ShapeDTW defines the neighborhood size around each time stamp for alignment purposes. By adjusting this parameter, ShapeDTW can emulate different similarity measures. When the reach is set to 1, ShapeDTW operates like traditional DTW, focusing solely on individual time stamps. However, when the reach is set to a very large value, it behaves similarly to the Euclidean distance, as the neighborhood extends across the entire time series. This flexibility allows ShapeDTW, and consequently ShapeDBA, to balance between local and global alignment, adapting to the specific requirements of the data.

6.3.1.3 Qualitative Evaluation

In the literature, the arithmetic mean and two notable TSP approaches with elastic measures, DBA (Petitjean, Ketterlin, and Gançarski, 2011) and SoftDBA (Cuturi and Blondel, 2017). Figure 6.7 compares prototype calculations using these methods and our ShapeDBA on the GunPoint dataset of the UCR archive (Dau et al., 2019). The figure reveals that the arithmetic mean is unsuitable for temporal data, particularly when samples are shifted. It introduces spatial and temporal artifacts; the temporal placement of the prototype skews toward the most frequent occurrence, and the amplitude values become out-of-distribution due to averaging misaligned values. DBA and SoftDBA improve temporal alignment but still produce peak artifacts because of

FIGURE 6.7: A qualitative evaluation of the proposed average technique compared to other approaches on a GunPoint dataset. The ShapeDBA algorithm is the only approach to not generate out-of-distribution artifacts.



the rigid point-to-point alignment of DTW and SoftDTW, which do not account for amplitude differences. ShapeDBA, however, offers the best of both worlds. It leverages DTW’s temporal alignment and ShapeDTW’s neighborhood alignment (Zhao and Itti, 2018), avoiding point-to-point issues. Consequently, the prototype generated by ShapeDBA in Figure 6.7 is free from peak out-of-distribution artifacts.

6.3.1.4 Quantitative Evaluation

To quantitatively evaluate the effectiveness of ShapeDBA in time series prototyping, we coupled ShapeDBA and ShapeDTW as the averaging method and distance measure in the k -means algorithm for clustering. Clustering, particularly using the k -means algorithm, serves as a robust evaluation metric for TSP methods based on elastic similarity measures (Holder, Middlehurst, and Bagnall, 2024).

We compared ShapeDBA against four distance-based methods: (1) k -means with the default setup (arithmetic mean and Euclidean Distance), referred to as MED; (2) k -means with SoftDBA and SoftDTW; (3) k -means with DBA and DTW; and (4) k -shape. Given that all other methods iteratively find prototypes, we applied the same iterative approach to the MED method. Instead of using a simple arithmetic mean of all samples, we iteratively calculated the mean over aligned points for each time stamp in the prototype, similar to DBA. However, for MED, we assumed ideal alignment without any warping.

6.3.1.4.1 Experimental Setup We conducted our experiments on 123 datasets from the UCR archive (Dau et al., 2019). Out of the 128 available datasets since 2018, five were excluded due to their high time series length, which would have been computationally prohibitive given the quadratic time complexity of the considered algorithms. All samples in each dataset were z-normalized to ensure a zero mean and unit standard deviation. The clustering algorithms were trained on the combined

train-test splits of these 123 datasets. While some UCR datasets are merely different train-test splits of the same original dataset, this occurs infrequently, so the same data might be clustered multiple times. We set the value of the “reach” hyperparameter to 15 resulting in a sliding window size of 31, following the original work of ShapeDTW (Zhao and Itti, 2018).

In machine learning, non-deterministic estimators often suffer from performance biases related to their initial setup, such as the initialization of weights in deep learning models. This bias is particularly relevant in clustering tasks, where the starting positions of clusters can significantly influence the results. To address this in our experiments, we ran each clustering algorithm five times, each with different initial cluster configurations, and averaged the results. However, using different initial clusters for each method could introduce another layer of bias. To ensure a fair comparison, we used the same set of five initial clusters across all clustering algorithms for each dataset. This approach eliminated variability due to initial cluster selection and allowed us to present unbiased average performance metrics, accurately reflecting the effectiveness of each clustering method.

6.3.1.4.2 Evaluation Metric: Adjusted Rand Index (*ARI*) The Adjusted Rand Index (*ARI*) (Hubert and Arabie, 1985) is an enhanced version of the Rand Index (*RI*), addressing the limitations of the original metric. The *RI* measures the similarity between true labels \mathbf{y} and predicted labels $\hat{\mathbf{y}}$ from a clustering algorithm using the formula:

$$RI(\mathbf{y}, \hat{\mathbf{y}}) = \frac{TP + TN}{TP + FP + FN + TN} \quad (6.3)$$

Here, *TP* (True Positive) and *TN* (True Negative) denote correctly clustered pairs, while *FP* (False Positive) and *FN* (False Negative) denote incorrectly clustered pairs. The *RI* calculates the proportion of pairwise agreements between the true and predicted clusters. However, the *RI* can be misleading because it may indicate high similarity for clusters that are randomly generated, particularly when the number of clusters is large. This occurs because the expected *RI* value varies between random clusters.

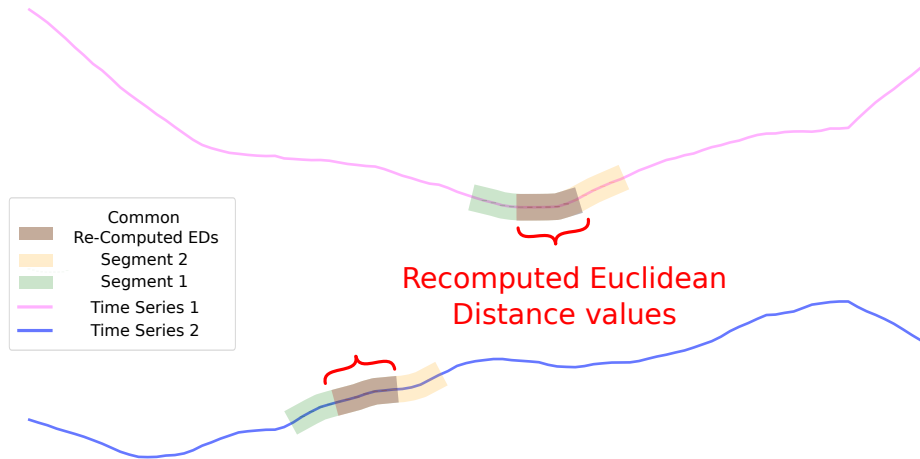
To overcome this, the *ARI* adjusts the *RI* to account for chance, normalizing the score so that random clustering yields an *ARI* of 0.0. The *ARI* is defined as:

$$ARI(\mathbf{y}, \hat{\mathbf{y}}) = \frac{RI(\mathbf{y}, \hat{\mathbf{y}}) - E[RI]}{1.0 - E[RI]} \quad (6.4)$$

where $E[RI]$ is the expected value of the *RI* for random clustering. The *ARI* ranges from -0.5 (indicating no similarity) to 1.0 (indicating perfect agreement), providing a more reliable measure of clustering performance by correcting for random chance.

6.3.1.4.3 Implementation Efficiency The ShapeDTW algorithm modifies the original DTW similarity measure by transforming the input time series into a multivariate format. In the univariate case with the “identity” descriptor, each time stamp’s neighborhood is converted into a Euclidean vector, creating a multivariate time series. Applying DTW to this transformed series involves computing the Euclidean distance between the channel vectors of paired time stamps, which can lead to computational inefficiency when sliding the reach window, as depicted in Figure 6.8. This inefficiency is specific to the identity transformation.

FIGURE 6.8: Calculation of the ShapeDTW measure between two time series. The overlapping area between the two sliding windows is recomputed.



To optimize this process, we first calculate the Euclidean pairwise distances between the two time series, resulting in a distance matrix. This matrix is then padded with edge values equal to half the reach. A window, with dimensions matching the length of the time series, slides diagonally across the distance matrix. The results are accumulated into a zero-initialized matrix. The DTW algorithm is subsequently applied to this new matrix, thereby avoiding unnecessary computations and improving efficiency. Figure 6.9 illustrates this streamlined implementation of ShapeDTW.

6.3.1.4.4 Experimental Results In Figure 6.10 we present the MCM (Chapter 2) between ShapeDBA, k -shape and its competitors when coupled with k -means following the ARI metric on 123 datasets of the UCR archive (Dau et al., 2019). The MCM showcases that our proposed ShapeDBA outperforms MED and the original DBA work (Petitjean, Ketterlin, and Gançarski, 2011), significantly, as well as significantly outperforming k -shape, the fastest TSCL algorithm in the literature. The winning approach in terms of average performance ranking is SoftDBA (Cuturi and Blondel, 2017). However, comparing ShapeDBA and SoftDBA showcases that no conclusion can be made between the performance of both algorithms given the high p-value. We show however in Section 6.3.1.4.5 that ShapeDBA is way faster than SoftDBA.

A detailed 1v1 scatter plot of the comparisons between ShapeDBA and the three other comparates is presented in Figure 6.11. Certain outliers in the One-vs-One scatter plots distinctly favor either ShapeDBA or the other methods. For example, ShapeDBA shows lower performance (low ARI) compared to k -shape on the ShapeletSim and ECGFiveDays datasets. The ShapeletSim dataset, being a simulation of random data, does not provide meaningful conclusions. However, the ECGFiveDays dataset, as shown in Figure 6.12, uniquely illustrates a limitation of ShapeDBA. The ECGFiveDays dataset consists mainly of noisy time stamps, with critical information compressed into the middle segments of the time series, as depicted in Figure 6.12. This noise introduces challenges during the optimization steps of ShapeDTW. On the

FIGURE 6.9: A more efficient implementation of the ShapeDTW measure with the identity descriptor involves sliding a window over the time stamp pairwise Euclidean matrix between the two time series, instead of applying DTW directly on their multivariate transformation. The data from each window position is collected into a zero-initialized matrix, which is then processed using the DTW algorithm, significantly reducing computational overhead.

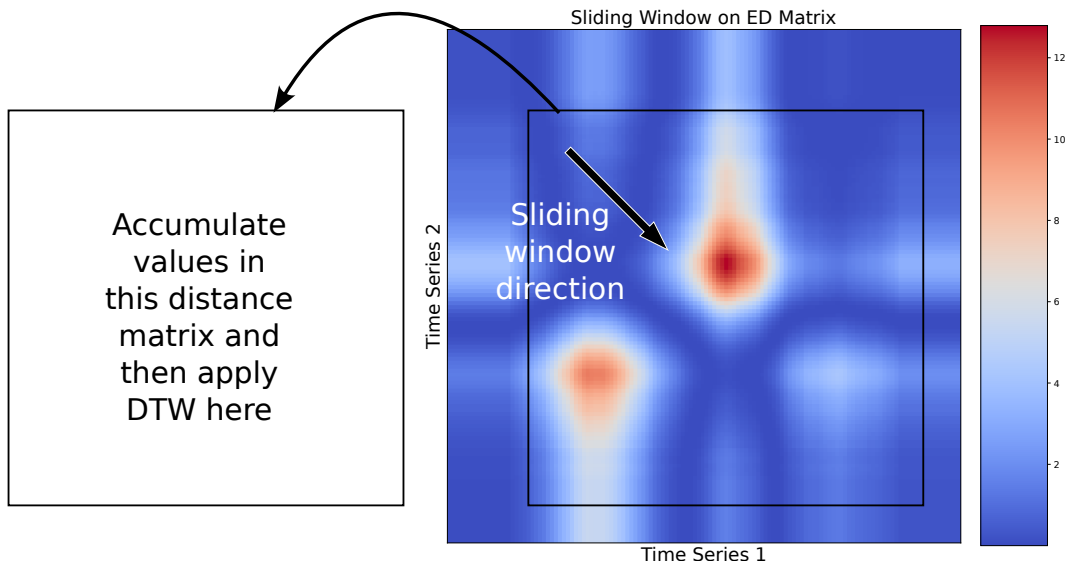
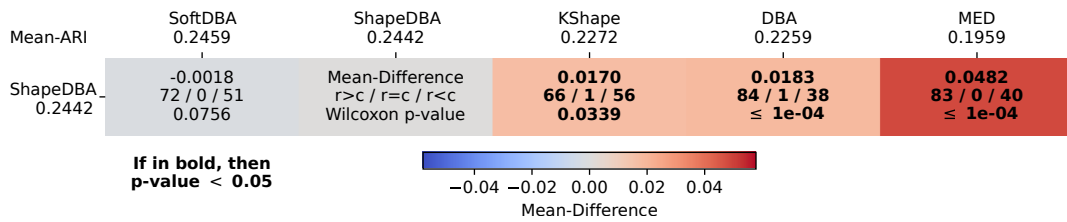


FIGURE 6.10: An MCM comparing ShapeDBA to other averaging approaches, coupled with k -means and their associated similarity measure, and k -shape, on the ARI metric.



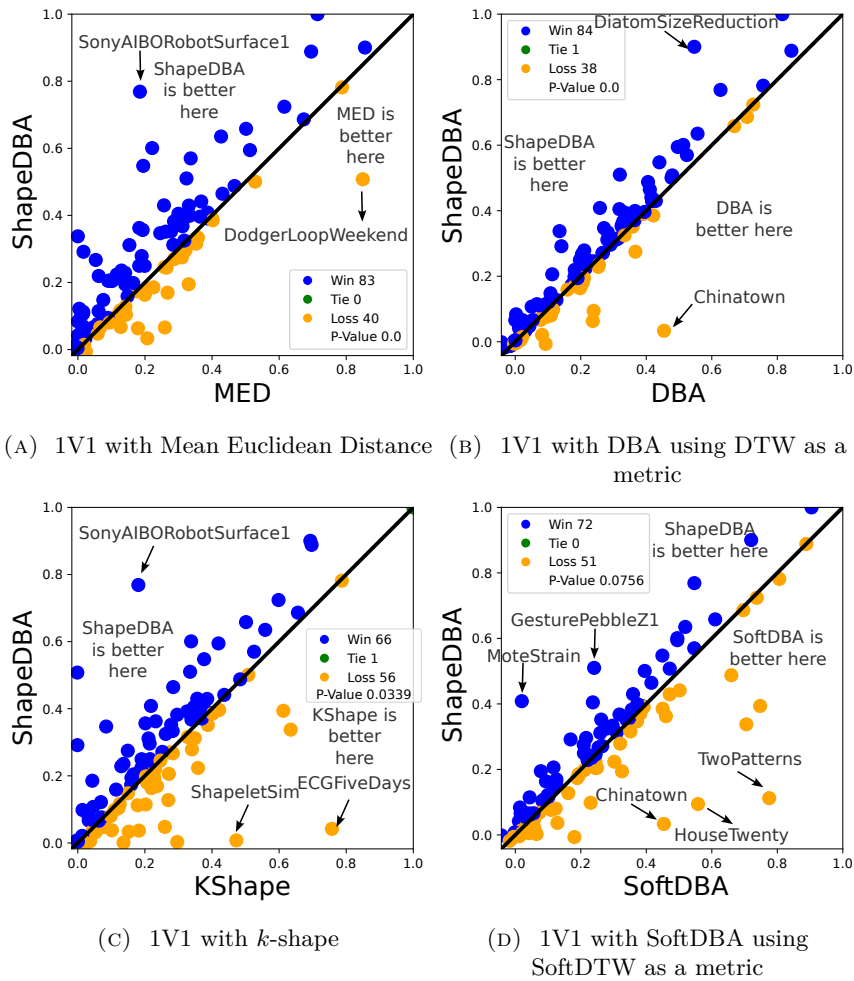


FIGURE 6.11: 1v1 Comparison between using k -means with ShapeDBA-ShapeDTW and other approaches from the literature using the Adjusted Rand Index clustering metric.

FIGURE 6.12: The ECGFiveDays dataset from the UCR archive provides two examples from each class. In this dataset, the majority of the time stamps are noisy, with the critical information localized in the central section of the time series. ShapeDBA does not perform well on this dataset, with an ARI score of almost 0.042.

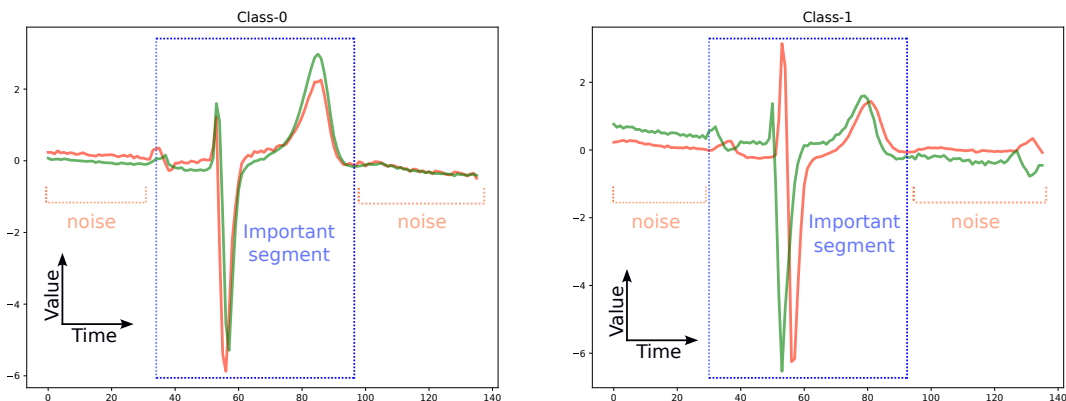
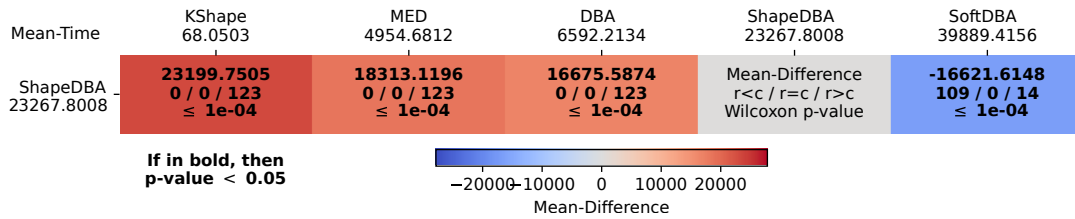


FIGURE 6.13: An MCM (Chapter 2) showing ShapeDBA’s (ours) duration (in seconds) compared to other approaches to finalize the clustering task on 123 datasets of the UCR archive (Dau et al., 2019).



other hand, ShapeDBA significantly outperforms k -shape on the SonyAIBORobot-Surface1 dataset, with an ARI difference of nearly 0.6. However, it is important to note that this might reflect k -shape’s underperformance since MED, DBA, and SoftDBA also show better results on this dataset. When comparing ShapeDBA to DBA, ShapeDBA exhibits a distinct advantage on the DiatomSizeReduction dataset, which struggles with having only four samples per class label. This highlights ShapeDBA’s effectiveness in handling datasets with sparse training data.

6.3.1.4.5 Computational Runtime All experiments were conducted on the same machine and under identical conditions, ensuring a fair comparison of computational times. We recorded the total computation time for each clustering method, averaging the results over five initializations. This approach allowed us to apply the same comparison techniques as for the ARI. In Figure 6.13, the MCM from Chapter 2 illustrates the computational runtime comparison between ShapeDBA and the other comparates. To maintain consistency, we inverted the values (multiplying by -1) since lower times are preferable. The MCM reveals that k -shape is the fastest method, primarily due to its use of the Fast Fourier Transform (FFT) for cross-correlation, while SoftDBA is the slowest because of its computational gradient based optimization step. Across 123 datasets, ShapeDBA is on average 1.7 times faster than SoftDBA, with 109 wins in terms of computational runtime. Given that no definitive conclusion can be drawn regarding the performance difference between ShapeDBA and SoftDBA, and considering that ShapeDBA is significantly faster, these extensive experiments highlight ShapeDBA as the more suitable state-of-the-art method for the task of TSP.

In the following section, we propose using ShapeDBA in a weighted setup to generate new synthetic samples. In this approach, weights determine the amount of information drawn from each sample. This method will be applied to human motion data, specifically in the medical field of human rehabilitation, with the goal of extending a regression dataset.

6.3.2 Weighted Average of Human Motion Sequences for Improving Rehabilitation Assessment

The collection and annotation of rehabilitation sequences (Capecchi et al., 2019) are complex, time-consuming, and require clinical expertise, which limits the size of available datasets. Conventional data augmentation methods for human motion data, simply adding noise, (Xin et al., 2024), although beneficial in other areas, tend to produce unrealistic motion sequences that do not capture the intricate temporal dynamics of human movement. This inadequacy necessitates innovative approaches to data generation that can create meaningful and representative synthetic sequences.

Another approach to generating synthetic sequences is the use of deep generative models (Petrovich, Black, and Varol, 2021), which have shown success in creating

realistic sequences for human motion tasks. However, these models face a significant challenge: the lack of sufficient data to train a deep supervised model also means inadequate data for training a deep generative model. To address this issue, researchers in the time series domain often turn to prototyping techniques (Forestier et al., 2017). These techniques create representative average sequences from existing training samples, offering a practical solution for augmenting datasets when data availability is limited.

Incorporating our previously proposed prototyping method, we propose to utilize a weighted version of ShapeDBA presented in the previous section, tailored to multivariate time series representing rehabilitation motions. By incorporating weights, this method ensures that the generated synthetic sequences maintain the essential characteristics of the original data, enhancing the realism and variability of the dataset. Our approach not only compensates for the limited data but also improves the generalization capability of models trained for rehabilitation assessment. This study utilizes the Kimore regression dataset (Capecchi et al., 2019) to validate our method, highlighting its effectiveness in producing coherent synthetic data that can significantly aid in the evaluation and personalization of rehabilitation treatments.

Moreover, we employ a weighted version of the ShapeDBA approach to generate diverse synthetic average sequences, subsequently used to enhance the training phase of deep learning models for downstream tasks. Due to the time-consuming nature of this averaging method, it cannot be computed at each epoch of the training phase, as is common in data augmentation. Instead, we generate several average sequences beforehand to expand the original training dataset, a process we refer to as data extension to distinguish it from traditional data augmentation.

Finally, we address the challenge of rehabilitation assessment, which is often approached as an extrinsic regression problem. The goal is to predict a continuous performance score for each rehabilitation sequence. Current state-of-the-art methods primarily use data augmentation or data extension for classification tasks, where synthetic samples are given discrete labels matching the original samples. However, assigning continuous labels to synthetic data presents a more complex problem. To overcome this, we propose a novel approach that employs a weighting strategy to calculate weighted continuous labels based on the true labels of a set of samples. This method enhances the realism and accuracy of the generated data, as detailed in Figure 6.14, for which we detail in the following section.

6.3.2.1 Methodology

Since rehabilitation motion sequences can be sparse, using the original ShapeDBA method to compute an average may lead to meaningless or incoherent results. To better capture the distribution of these sequences, a weighted average is more suitable (Forestier et al., 2017).

For each reference motion sequence, we generate a synthetic version by considering a neighborhood of N motion sequences. The reference sequence S_{ref} is given a weight of 1, while each neighboring sequence S_i is weighted based on its similarity to the reference. The weight w_i for each neighbor is calculated as follows:

$$w_i = e^{\ln(0.5) \cdot \frac{DTW(S_i, S_{ref})}{d_{NN}}} \quad (6.5)$$

where d_{NN} is the DTW distance between S_{ref} and its nearest neighbor. This weighting emphasizes the influence of sequences that are more similar to the reference.

FIGURE 6.14: We determine the N nearest neighbors for each reference in the dataset using Dynamic Time Warping (DTW). Each neighbor is assigned a weight according to its DTW distance from the reference. These weights are then utilized to compute a weighted average sequence through ShapeDBA. Subsequently, a weighted score is calculated, allowing us to expand the regression training dataset with this new synthetic sample.

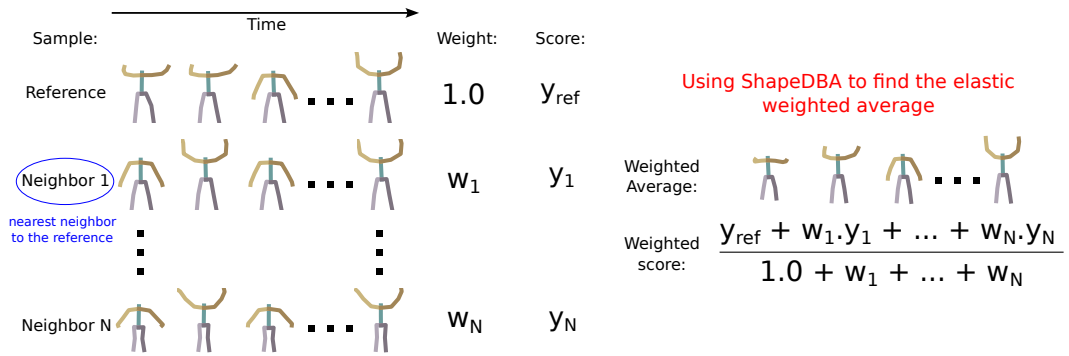


FIGURE 6.15: Averaging six human motion sequences (Examples 0 to 5 shown on the top left/right) with uniformly distributed weights results in an unrealistic example (bottom right skeleton sequence). The 2D t-SNE (Maaten and Hinton, 2008) projection of these sequences (bottom left) illustrates that the averaged sequence falls outside the manifold of the original sequences.

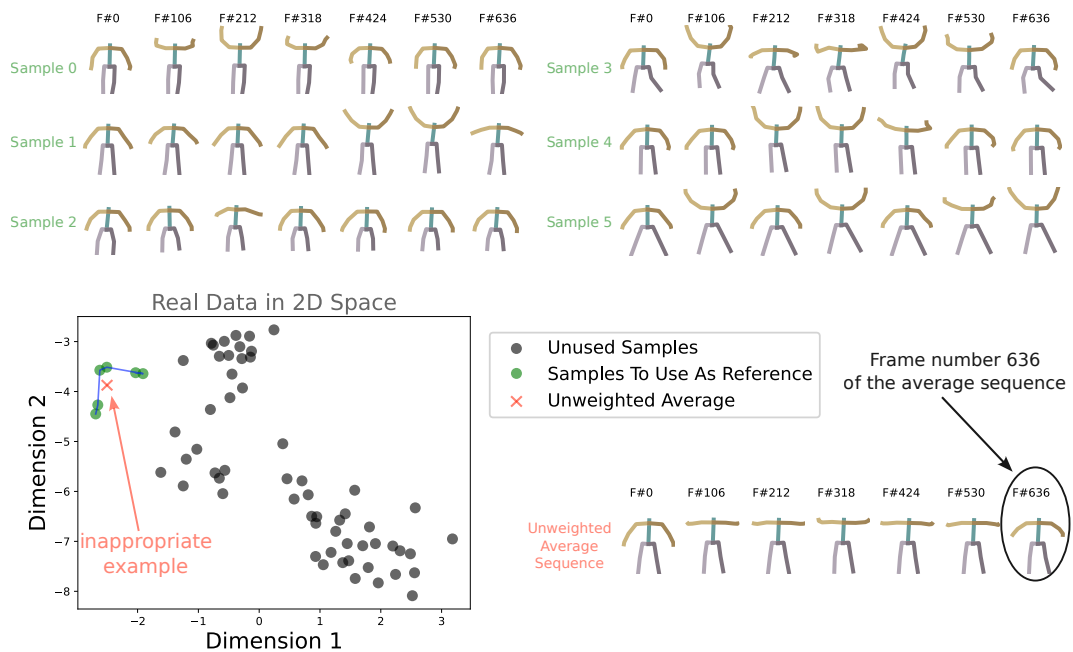


Figure 6.15 demonstrates the significance of using a weighted average in cases where the data manifold is sparse and the distribution is non-spherical.

For each reference sequence S_{ref} , the weighted ShapeDBA computation produces a corresponding synthetic sequence \hat{S} . To assign a continuous label (score) to the synthetic sequence, the same weights are normalized using min – max normalization, ensuring the labels remain within the original range of 0 to 1. The continuous label \hat{y} for the synthetic sequence \hat{S} is calculated as:

$$\hat{y} = \sum_{i=1}^{N+1} \bar{w}_i \cdot y_i \quad (6.6)$$

where \bar{w}_i is the normalized weight of the i_{th} sequence in the set of the $N + 1$ samples (including the reference and its N nearest neighbor sequences).

6.3.2.2 Experimental Evaluation

6.3.2.2.1 Experimental Setup We conducted a two-fold evaluation of our proposed approach. First, we examined the coherence of the synthetic sequences through both qualitative and quantitative analyses. Second, we investigated the utility of these synthetic sequences in improving a deep learning model’s performance in extrinsic regression, aiming to predict continuous scores for rehabilitation sequences.

Dataset We utilize the Kimore dataset (Capecci et al., 2019), for which the pre-processing of the sequences are presented in Section 6.2.1, however we use the regression task here. We implemented a 5-fold cross-validation protocol with a unique adaptation to more accurately reflect real-world scenarios by including only unhealthy subjects in the test phase. Unlike the standard approach, we divided the sequences of unhealthy subjects into 5 folds. For each iteration, all sequences from healthy subjects and 4 folds of unhealthy subjects were used for training, while the remaining fold of unhealthy subjects was reserved for testing. This method ensures that the evaluation is focused on the performance for unhealthy subjects, providing a more realistic assessment.

Comparative Sets of Rehabilitation Sequences Our comparative study involves several sets of rehabilitation sequences. The reference set, consisting of D sequences, includes the original sequences from the Kimore dataset. As a baseline, we introduced random noise $\mathcal{N}(0, 0.1)$ to each reference sequence, creating a noisy set of the same size. Beyond this, we generated five additional sets of synthetic sequences using our proposed weighted ShapeDBA method. For each reference sequence, we created synthetic versions by applying weighted ShapeDBA with neighborhood sizes ranging from $N = 1$ to $N = 5$. This process resulted in five distinct sets, each containing D sequences, which we labeled as *ShapeDBANN1*, *ShapeDBANN2*, *ShapeDBANN3*, *ShapeDBANN4*, and *ShapeDBANN5*.

6.3.2.2.2 Evaluation of Synthetic Data Coherence Evaluating generative models typically requires multiple methods. For human motion data, one way is to visually inspect the realism of the generated sequences. However, visual inspection alone is not enough, as it lacks quantitative objectivity, as argued in (Naeem et al., 2020). Thus, it is crucial to use specific metrics to assess the reliability of the generated samples. In this section, we introduce a comprehensive evaluation strategy that

FIGURE 6.16: Visualization of three examples: the top row shows a real sample, the middle row displays a noisy sample, and the bottom row features a sample generated using the weighted ShapeDBA method. Each sequence is represented by 10 frames, arranged sequentially from left to right.

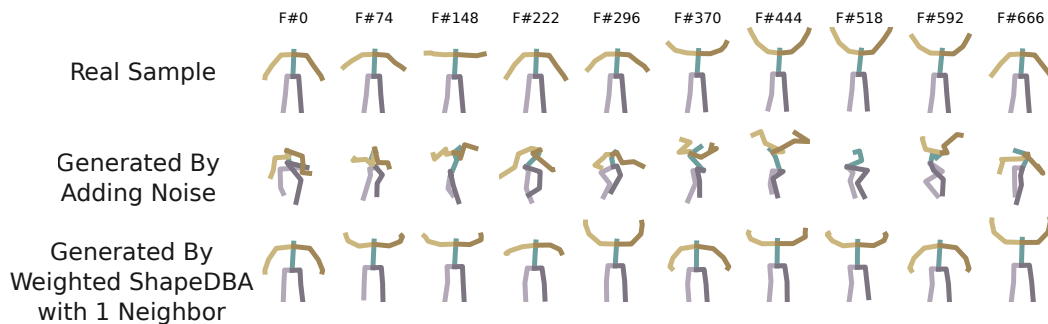
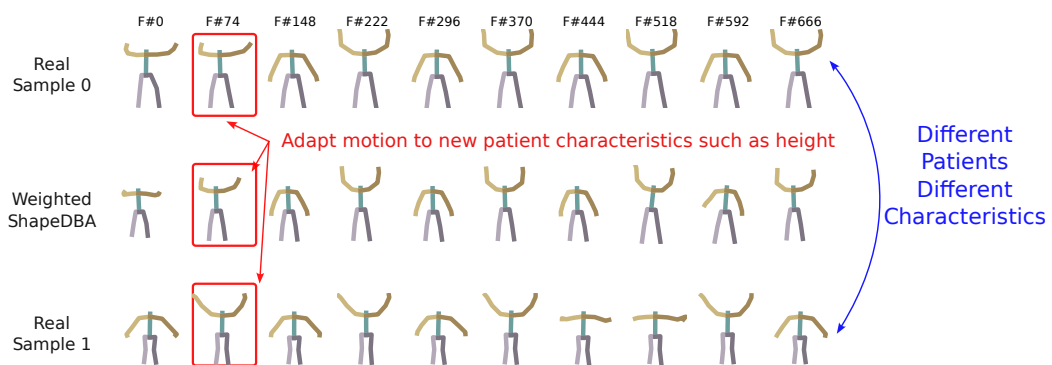


FIGURE 6.17: Visualization of two real sequences (top and bottom) and their corresponding weighted ShapeDBA sequence (middle). The generated average sequence preserves the temporal alignment of the top sequence, which has a higher weight, while also incorporating features like the patient's height from the bottom sequence.



includes both visual and numerical assessments to ensure a thorough analysis of the generated sequences.

Qualitative Analysis: Visualizing Real vs Generated Figure 6.16 showcases three sequences: the first is an original sequence from the Kimore dataset, the second is created by adding random noise to this original sequence, and the third is generated using our weighted ShapeDBA method. Visually, the noisy sequence appears less realistic compared to the sequence produced by the weighted ShapeDBA approach.

To illustrate the effectiveness of weighted ShapeDBA, Figure 6.17 presents two sequences and their resulting weighted ShapeDBA sequence. The higher weight given to the first sequence (the reference) ensures that the temporal motion aligns closely with it. Simultaneously, the weighted ShapeDBA sequence incorporates attributes from the second sequence, such as the patient's height and form, effectively blending characteristics from both sequences to create a more coherent and realistic synthetic sequence.

Quantitative Analysis: Fidelity and Diversity When extending a dataset, even using non-deep learning methods, it is crucial to evaluate both the fidelity and diversity of the generated samples. Fidelity metrics determine how closely the generated samples match real ones, with higher fidelity indicating more reliable samples for real-world use. Diversity metrics, on the other hand, assess the variability among samples, ensuring that both real and generated samples are distinct from one another. The goal of a generative model is typically to create a generated space that is as diverse as the original data.

In this study, we used two common metrics to evaluate fidelity and diversity: the Fréchet Inception Distance (FID) and the Average Pair Distance (APD), define below:

- *Fréchet Inception Distance (FID)*: The FID metric evaluates the similarity between the distributions of real and generated samples. To compute FID, both real and generated samples first undergo latent feature extraction using a pre-trained deep learning model \mathcal{F} (in this study, trained on a regression task). The mean and covariance of these latent features are then calculated for both sets of samples. FID measures the distance between these distributions by assuming they follow a Gaussian distribution. The mathematical formula for FID is:

$$FID(\mathcal{P}_1, \mathcal{P}_2)^2 = \text{trace}(\Sigma_1 + \Sigma_2 - 2(\Sigma_1 \Sigma_2)^{1/2}) + \sum_{i=1}^f (\mu_{1,i} - \mu_{2,i})^2 \quad (6.7)$$

where, \mathcal{P}_1 and \mathcal{P}_2 represent the distributions of real and generated samples, respectively. f is the dimension of the latent space of \mathcal{F} . μ_1 and μ_2 are vectors of dimension f , representing the means of the real and generated samples' feature spaces, respectively. Σ_1 and Σ_2 are the covariance matrices of dimensions (f, f) for the real and generated samples, respectively.

- *Average Pair Distance (APD)*: The APD metric evaluates the average Euclidean Distance (ED) between randomly selected samples from both real and generated data within the feature space, utilizing \mathcal{F} as the latent feature extractor. To compute APD, two randomly selected sets of samples, \mathcal{S}_1 and \mathcal{S}_2 , each containing S_{apd} samples, are defined. The average distance between these sets is calculated as:

$$APD(\mathcal{S}_1, \mathcal{S}_2) = \frac{1}{S_{apd}} \sum_{i=1}^{S_{apd}} \sqrt{\sum_{j=1}^f (\mathcal{S}_{i,j} - \mathcal{S}'_{i,j})^2}, \quad (6.8)$$

This process is repeated across multiple random sets of \mathcal{S}_1 and \mathcal{S}_2 where the final APD value is the average of these calculations, which helps to eliminate bias from set selection.

In this study, we utilized open-source software to compute the FID and APD metrics. The results were averaged over different initializations of our pre-trained deep regression model, which was trained solely on the training set. For the APD metric, we used $S_{apd} = 20$ for the size of the randomly selected sets.

For each augmentation method—noisy and weighted ShapeDBA, we present the average FID and APD values along with their standard deviations. These metrics are calculated over various resamples of the dataset for each exercise, as well as different initializations of the pre-trained deep regression model.

TABLE 6.2: The FID values of different augmentation methods and the real dataset, over different resamples of each exercise. The presented FID values include the average and standard deviation over all resamples per exercise and different initialization of the pre-trained feature extractor.

	Exercise 1	Exercise 2	Exercise 3	Exercise 4	Exercise 5
Real	$02.18E^{-6} \pm 06.66E^{-7}$	$02.48E^{-6} \pm 09.82E^{-7}$	$02.19E^{-6} \pm 08.18E^{-7}$	$05.00E^{-6} \pm 02.09E^{-6}$	$03.06E^{-6} \pm 01.30E^{-6}$
Noisy	00.07 ± 00.03	00.08 ± 00.03	00.09 ± 00.03	00.24 ± 00.10	00.07 ± 00.03
ShapeDBA NN1	01.94 ± 00.81	04.12 ± 01.86	02.28 ± 01.10	04.19 ± 02.95	03.39 ± 01.92
ShapeDBA NN2	03.15 ± 01.06	06.62 ± 02.56	04.01 ± 02.70	05.95 ± 04.07	05.75 ± 02.34
ShapeDBA NN3	03.77 ± 01.21	07.98 ± 02.59	05.16 ± 03.39	07.16 ± 04.51	07.34 ± 02.91
ShapeDBA NN4	04.31 ± 01.24	09.38 ± 03.05	05.96 ± 03.52	08.01 ± 04.64	08.51 ± 03.76
ShapeDBA NN5	04.62 ± 01.28	10.21 ± 03.34	06.45 ± 03.69	08.90 ± 05.07	09.23 ± 04.12

TABLE 6.3: The APD values of different augmentation method and the real dataset, over different resamples of each exercise. The presented APD values include the average and standard deviation over all resamples per exercise, different randomly selected sets of size $S_{apd} = 20$ and different initialization of the pre-trained feature extractor.

	Exercise 1	Exercise 2	Exercise 3	Exercise 4	Exercise 5
Real	06.09 ± 00.63	06.61 ± 00.83	05.95 ± 00.78	08.24 ± 01.24	07.10 ± 01.10
Noisy	06.05 ± 00.57	06.55 ± 00.79	05.90 ± 00.78	08.14 ± 01.18	07.00 ± 01.03
ShapeDBA NN1	05.21 ± 00.68	05.32 ± 00.63	05.06 ± 00.68	07.14 ± 01.12	06.11 ± 01.08
ShapeDBA NN2	04.93 ± 00.69	04.96 ± 00.66	04.77 ± 00.65	06.90 ± 01.16	05.70 ± 00.98
ShapeDBA NN3	04.78 ± 00.75	04.64 ± 00.54	04.53 ± 00.66	06.84 ± 01.20	05.52 ± 00.96
ShapeDBA NN4	04.67 ± 00.74	04.47 ± 00.55	04.34 ± 00.63	06.59 ± 01.16	05.35 ± 00.91
ShapeDBA NN5	04.61 ± 00.67	04.35 ± 00.53	04.30 ± 00.61	06.50 ± 01.13	05.31 ± 00.90

Table 6.2 displays the FID values for each exercise using the noisy augmentation method and five variations of our weighted ShapeDBA (with neighborhood sizes ranging from 1 to 5). The FID for real samples is also included as a baseline. Ideally, the FID of any generative method should be close to, but slightly higher than, the FID of the real data, as generated samples cannot exceed the fidelity of the actual data. As seen in Table 6.2, the noisy method has a lower FID compared to the weighted ShapeDBA method. On one hand, this difference can be explained by the fact that the dataset exists in a sparse space. Adding a small amount of noise generates a point in the encoder’s latent space that is very close to the real sample. On the other hand, generating data with ShapeDBA introduces new points into this sparse space. Given the small amount of data, the FID metric may appear “better” with noise augmentation. Despite this, Figure 6.16 clearly shows that the noisy augmentation produces unrealistic sequences. This highlights the importance of using multiple evaluation methods to draw comprehensive conclusions about generative models, as there is no single best approach.

The same trend is observed with the APD values in Table 6.3. The noisy method has an APD closest to that of real samples, outperforming the weighted ShapeDBA method in quantitative evaluations.

6.3.2.2.3 Evaluation of Synthetic Sequences for Data Extension In our second experiment, we assess the effectiveness of the proposed method as a data extension technique for rehabilitation assessment. This task is framed as an extrinsic regression problem, where the aim is to predict a continuous performance score associated with each rehabilitation sequence. We use the Fully Convolutional Network (Chapter 1 Figure 1.8) as our backbone model (same used as feature extractor for generation metrics in previous section).

TABLE 6.4: MAE and RMSE errors obtained for all compared approaches on each exercise separately. Best values are emphasized in bold, while second best values are underlined.

Training Set	Exercise 1	Exercise 2	Exercise 3	Exercise 4	Exercise 5
MAE					
Ref.	0.206 ± 0.069	0.202 ± 0.037	0.204 ± 0.055	0.184 ± 0.068	0.224 ± 0.058
Ref. + Noise	0.186 ± 0.065	0.172 ± 0.040	0.203 ± 0.045	0.185 ± 0.073	0.229 ± 0.069
Ref. + ShapeDBA NN1	0.167 ± 0.070	0.175 ± 0.030	0.182 ± 0.051	0.141 ± 0.062	0.208 ± 0.079
Ref. + ShapeDBA NN2	0.169 ± 0.057	0.177 ± 0.041	0.194 ± 0.041	0.168 ± 0.056	0.226 ± 0.066
Ref. + ShapeDBA NN3	0.173 ± 0.063	0.183 ± 0.047	0.199 ± 0.058	0.168 ± 0.083	0.225 ± 0.055
Ref. + ShapeDBA NN4	0.168 ± 0.059	0.179 ± 0.043	0.199 ± 0.043	0.180 ± 0.080	0.231 ± 0.060
Ref. + ShapeDBA NN5	0.166 ± 0.067	0.185 ± 0.043	0.201 ± 0.050	0.182 ± 0.089	0.226 ± 0.061
RMSE					
Ref.	0.251 ± 0.083	0.247 ± 0.045	0.248 ± 0.065	0.230 ± 0.083	0.267 ± 0.073
Ref. + Noise	0.203 ± 0.078	0.226 ± 0.043	0.238 ± 0.046	0.227 ± 0.090	0.274 ± 0.092
Ref. + ShapeDBA NN1	0.199 ± 0.087	0.226 ± 0.036	0.214 ± 0.054	0.178 ± 0.074	0.251 ± 0.094
Ref. + ShapeDBA NN2	0.203 ± 0.075	0.232 ± 0.052	0.226 ± 0.044	0.210 ± 0.074	0.268 ± 0.083
Ref. + ShapeDBA NN3	0.205 ± 0.082	0.235 ± 0.050	0.240 ± 0.062	0.214 ± 0.105	0.268 ± 0.066
Ref. + ShapeDBA NN4	0.198 ± 0.071	0.235 ± 0.050	0.234 ± 0.048	0.230 ± 0.105	0.279 ± 0.070
Ref. + ShapeDBA NN5	0.202 ± 0.079	0.230 ± 0.049	0.244 ± 0.057	0.231 ± 0.109	0.280 ± 0.080

To compare the predicted scores from our models with the clinical scores provided by experts, we used two metrics as outlined by (Capecci et al., 2018): the Root Mean Square Error (RMSE) and the Mean Absolute Error (MAE). Given two sets of N scores, \mathbf{y} (the ground truth) and $\hat{\mathbf{y}}$ (the predictions), the MAE and RMSE are calculated as follows:

$$MAE(\mathbf{y}, \hat{\mathbf{y}}) = \frac{1}{N} \sum_{i=1}^N |y_i - \hat{y}_i|, \quad (6.9)$$

$$RMSE(\mathbf{y}, \hat{\mathbf{y}}) = \sqrt{\frac{1}{N} \sum_{i=1}^N (y_i - \hat{y}_i)^2}. \quad (6.10)$$

We evaluated the performance of the FCN model for extrinsic regression by training it on various sets of rehabilitation sequences combined with the reference set. The average MAE and RMSE errors (\pm standard deviation) are reported in Table 6.4.

Our first observation is that adding noisy sequences to the training set (*Ref.* + *Noise*) generally leads to better performance compared to using only the original training set (*Ref.*). This suggests that the FCN model tends to overfit the original data, and incorporating noisy sequences helps to improve its generalization capabilities.

Moreover, Table 6.4 highlights that the best error values for both metrics are achieved when the FCN model is trained on the rehabilitation set extended with ShapeDBA-generated averages. This indicates that synthetic average sequences not only mitigate overfitting but also capture realistic rehabilitation motion patterns, allowing the FCN model to more effectively learn the variations in rehabilitation exercises.

Finally, we note that for three out of five exercises, the optimal performance is obtained when the training data includes average sequences computed using a single neighbor (*Ref.* + *ShapeDBANN1*). This suggests that using a larger neighborhood may sometimes result in less coherent average sequences, as the neighbors might not reside within a continuous subspace.

The experiments demonstrated that incorporating synthetic sequences generated by the weighted ShapeDBA method significantly enhances the performance of rehabilitation assessment models. This approach mitigates overfitting and captures realistic motion patterns, leading to more accurate predictions. However, the reliance on real data distribution and the computational expense of finding nearest neighbors and

applying ShapeDBA can be problematic in real-world scenarios where instant generation is required. In the next section, we address this challenge by exploring the use of deep learning models for generation tasks, aiming to mitigate the limitations of dataset distribution and provide a more efficient solution.

6.4 Exploring Deep Generative Models for Human Motion Generation

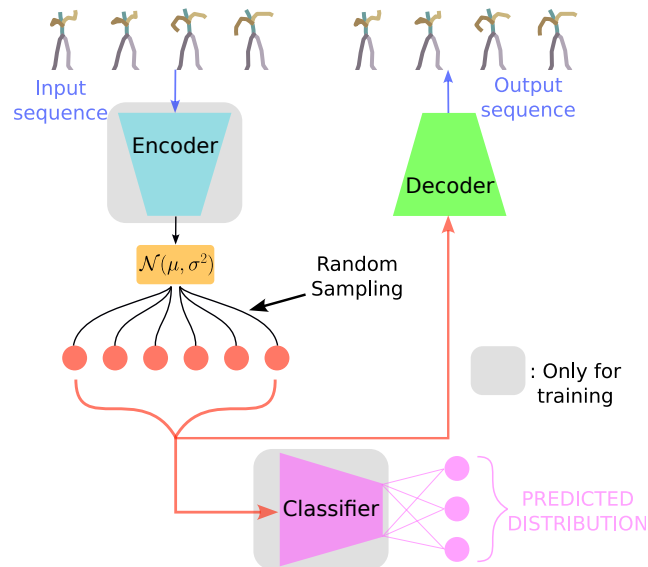
In this section, we investigate the application of deep generative models for the task of human motion generation. The need for generating realistic and diverse motion sequences efficiently has spurred significant interest in this domain. Traditional prototyping methods, such as ShapeDBA, though effective, can be computationally intensive and time-consuming, particularly during the inference (generation) phase. This limitation makes them less suitable for real-time applications where quick data generation is crucial. Deep generative models, on the other hand, offer a substantial advantage in terms of speed and efficiency during the inference phase, making them highly suitable for these scenarios.

Generative models can revolutionize various fields, including the cinematic and gaming industries, by enabling the creation of lifelike and varied character animations (Cao et al., 2020; Evin, Hämäläinen, and Guckelsberger, 2022). In medical rehabilitation (Li and Vakanski, 2018), these models can assist in creating realistic motion sequences for better patient assessment and treatment planning. The flexibility and scalability of deep generative models allow them to generate large volumes of high-quality motion sequences, essential for these applications. Additionally, fine-tuning these models (Zhang et al., 2024b) on small datasets helps avoid overfitting, ensuring the generated sequences are diverse and realistic without requiring extensive training data.

Convolutional Neural Networks (CNNs) have proven highly effective in TSC, as seen in chapters 3 and 4, yet their application to human motion generation remains relatively unexplored. Despite this, CNNs offer distinct advantages over Recurrent Neural Networks (RNNs) (Guo et al., 2020) and Transformers (Petrovich, Black, and Varol, 2021), particularly regarding inference time and computational efficiency (measured in FLOPS). To harness these benefits, we propose a CNN-based Variational Auto-Encoder (VAE) generative model tailored for human motion data, specifically for action recognition tasks as it is directly conditioned with labels. The traditional approach to incorporating a conditioning aspect into a VAE model is by simply concatenating a one-hot encoded vector, representing the action label, with the latent space before feeding it to the decoder. However, this technique may have limitations in terms of sensitivity, as the model is not explicitly trained to recognize that the action label is significantly different from another. To improve the conditioning and effectively separate the latent space, we introduce a classification task within the latent space by proposing a Supervised VAE (SVAE), summarized in Figure 6.18. Our model demonstrates competitiveness with state-of-the-art methods in terms of fidelity and diversity metrics. Additionally, we address the challenge of balancing training datasets concerning class label distribution, thereby enhancing downstream classification performance.

In the following sections, we detail some of the background work on human motion generation using deep learning models, the proposed architecture and its specific features, followed by the experimental results using the publicly available HumanAct12 dataset (Guo et al., 2020) (Figure 6.1).

FIGURE 6.18: Summary of our proposed Supervised VAE (SVAE) architecture: The input skeleton sequences are processed by the encoder to learn a Gaussian distribution in the latent space. From this distribution, a random sample is drawn and utilized in two ways: it is fed into a classifier for the action recognition task and also into the decoder to reconstruct the original sequence. This dual functionality enhances both the generative and discriminative capabilities of the model.



6.4.1 Background Work

Recent advancements in deep generative models have brought significant improvements in the generation of human motion sequences. This subsection provides an overview of the key state-of-the-art models, highlighting their unique contributions and advantages. The current state-of-the-art in this field lies within the capabilities of VAEs, GANs, and diffusion models.

6.4.1.1 Generative Adversarial Networks (GANs)

Generative Adversarial Networks (GANs) (Goodfellow et al., 2014) employ a dual-network structure consisting of a generator and a discriminator. The generator creates synthetic data, while the discriminator evaluates the authenticity of the generated data against real data. Through this adversarial process, GANs learn to produce highly realistic data that can often be indistinguishable from real samples. The ability to generate high-quality data quickly makes GANs especially appealing for applications requiring rapid generation of human motion sequences, such as in real-time game character animation or virtual reality environments. Before the availability of 3D human motion datasets, researchers addressed the motion generation problem at a 2D level. One notable approach is the two-stage Generative Adversarial Network (GAN) introduced in (Cai et al., 2018), which generates 2D videos of human motion. This model works in two phases: first, it creates a human skeleton from random noise, and then it transforms this skeleton into an image, repeating this for multiple frames to produce a coherent video sequence. Another significant model is MoCoGAN (Tulyakov et al., 2018), a GAN-based approach that generates motion

by conditioning on specific content, learning two distinct spaces—one for content representation and the other for frame sequences. These innovative models, Two-Stage GAN and MoCoGAN, were later adapted for 3D human motion sequences, as demonstrated in (Guo et al., 2020), paving the way for more advanced and realistic 3D human motion generation techniques.

6.4.1.2 Variational Auto-Encoders (VAEs)

Variational Auto-Encoders (VAEs) (Chapter 1 Section 1.3.2) learn to encode data into a Gaussian latent space and then decode it back into the data space, effectively capturing the underlying distribution of the training data. This allows VAEs to generate new data points that are coherent and representative of the original data distribution. The capability of VAEs to produce high-quality, diverse data points makes them particularly useful in applications such as the cinematic and gaming industries, where creating lifelike and varied character animations is essential. With the availability of 3D human motion datasets, researchers in (Guo et al., 2020) highlighted the limitations of existing datasets and introduced HumanAct12, a new dataset derived from the PHSPD dataset (Zou et al., 2020; Zou et al., 2020), which utilizes a polarization camera and three Kinect v2 cameras (Asteriadis et al., 2013). Additionally, the authors in (Guo et al., 2020) proposed Action2Motion, a VAE model, called Action2Motion, designed to generate skeleton-based human motion sequences. This auto-regressive VAE consists of two encoders, a prior and a posterior encoder, and one decoder. The model approximates a latent representation of the prior and posterior time frames while minimizing the Kullback-Leibler (KL) divergence between their distributions to ensure regularization. Importantly, Action2Motion is a conditional VAE, with conditioning based on the action label and the timestamp to differentiate between prior and posterior pose frames. Other researchers have also explored conditional VAE modeling. For example (Aliakbarian et al., 2021) introduced a conditional VAE that learns a latent representation of the condition instead of adding the label directly. This model comprises two VAEs, CS-VAE and LCP-VAE, one encoding the prior knowledge (condition) and the other encoding the future sequence (posterior knowledge). The model can be applied in two ways: using the action label as prior knowledge or using a part of the training sequence as prior knowledge. The latter approach has shown better performance, as using a real human motion sequence as prior knowledge increases the diversity of the generated samples. Transformers have recently shown significant impact in translation models (Vaswani et al., 2017) and image recognition (Dosovitskiy et al., 2020). Building on this, the authors in (Petrovich, Black, and Varol, 2021) developed ACTOR, a Transformer-based VAE model to generate 3D human motion sequences. Moreover, (Lucas et al., 2022) introduced a Quantized VAE (Van Den Oord, Vinyals, et al., 2017) to generate 3D human motion sequences. This model employs a Generative Pre-trained Transformer (GPT)-like model (Radford et al., 2018) in the latent space after quantization to predict latent indices. More recently, researchers in (Zhong et al., 2022) proposed a VAE that encodes the input human motion sequence in two streams simultaneously, resulting in action-agnostic and action-aware representations, known as UM-CVAE.

6.4.1.3 Denoising Diffusion Probabilistic Models (DDPMs)

Recently, the advancement of Denoising Diffusion Probabilistic Models (DDPMs) (Ho, Jain, and Abbeel, 2020) has added another dimension to the field of generative models. DDPMs gradually transform simple initial data, such as Gaussian noise, into complex data distributions through a series of steps. This approach

allows for high-quality data generation and has shown impressive results in generating detailed and realistic motion sequences. Diffusion models have advanced the field by providing a robust framework for generating complex data, further enhancing the ability of generative models to create lifelike human motion sequences efficiently. For instance, (Zhang et al., 2024a) introduced MotionDiffuse, a DDPM for human motion generation. This diffusion model employs an attention mechanism architecture for the denoising process, incorporating residual connections instead of the U-Net (Ronneberger, Fischer, and Brox, 2015) architecture used in the original DDPM model (Ho, Jain, and Abbeel, 2020).

6.4.2 Proposed Model

In this section, we introduce our proposed Supervised VAE (SVAE) architecture, which builds upon the original Variational Auto-Encoder (VAE) model by incorporating an associated classification task. Both models utilize a Fully Convolutional Network (FCN) architecture (Wang, Yan, and Oates, 2017) as the backbone. The encoder employs one-dimensional convolutions for down-sampling, while the decoder uses transposed one-dimensional convolutions for up-sampling. Below, we present the original VAE and the Supervised VAE, both based on CNN architecture, as illustrated in Figure 6.19.

6.4.2.1 Original Variational Auto-Encoder (VAE)

The VAE architecture, initially proposed in (Kingma and Welling, 2013), has been adapted for time series data, specifically targeting human motion sequences. The optimizer in this model minimizes two key losses: the reconstruction loss and the Kullback-Leibler (KL) divergence, as detailed in Chapter 1 Section 1.3.2. Notably, the reconstruction loss deviates from the standard Mean Squared Error loss by excluding the averaging over the time dimension, as shown below:

$$\mathcal{L}_{rec}(\mathbf{x}, \hat{\mathbf{x}}) = \frac{1}{J.D} \sum_{t=1}^L \sum_{m=1}^{J.D} (x_t^m - \hat{x}_t^m)^2, \quad (6.11)$$

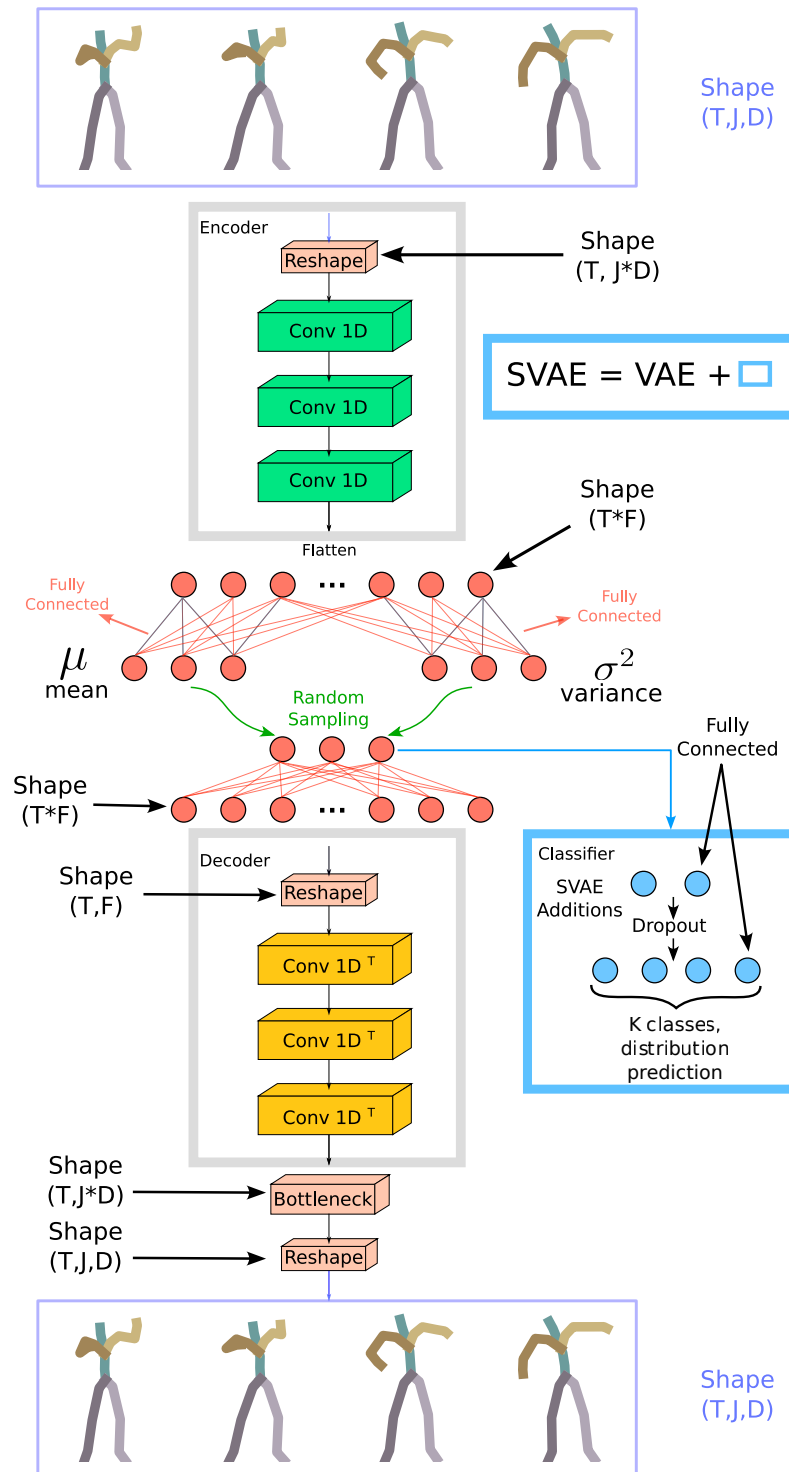
where \mathbf{x} and $\hat{\mathbf{x}}$ are the MTS representation of the input skeleton sequence and the reconstructed one, both of length L and JxD dimensions, and J is the number of joints on the recorded skeleton each in a space of D dimensions. This modification prevents the model from converging to the average sequence during training, which would lead to underfitting due to reduced dimensionality in the optimization problem.

The KL divergence loss aligns the Gaussian distribution in the latent space to a standard normal distribution with zero mean and unit variance, such as Eq. 1.73 in Chapter 1:

$$\begin{aligned} \mathcal{L}_{KL} &= D_{KL}(q_{\theta}(\mathbf{z}|\mathbf{x}), \mathcal{N}(0, 1)) \\ &= -\frac{1}{2} \sum_{d=1}^{\mathbf{d}} (1 + \log \sigma_d^2 - \mu_d^2 - \sigma_d^2) \end{aligned} \quad (6.12)$$

where \mathbf{d} is the dimension of the latent space, specific to the architecture of the VAE, $\boldsymbol{\mu}$ and $\log \boldsymbol{\sigma}^2$ are the mean and log variance vectors of the latent space features.

FIGURE 6.19: The Variational Auto-Encoder (VAE) model for human motion generation leverages an FCN backbone in both the Encoder and Decoder. In the Decoder, **standard one-dimensional convolutions** are replaced with **transposed convolutions**. Each convolution layer is followed by batch normalization and a ReLU activation function. The SVAE model further includes **Fully Connected layers** to enhance its functionality.



6.4.2.2 Supervised Variational Auto-Encoder (SVAE)

To enhance the VAE with conditioning capabilities, we introduce a classification task within the latent space. The SVAE model integrates an MLP based classifier (Wang, Yan, and Oates, 2017) within the latent space. Both the classifier and the decoder utilize a randomly sampled vector from the Gaussian distribution produced by the encoder. This additional classification task brings a Cross Entropy (CE) loss into the optimization process, alongside the reconstruction and KL divergence losses:

$$\mathcal{L}_{CE}(\mathbf{y}, \hat{\mathbf{y}}) = - \sum_{c=1}^C y_c \cdot \log_2(\hat{y}_c) \quad (6.13)$$

where \mathbf{y} and $\hat{\mathbf{y}}$ represent the true and predicted class distributions, respectively, and C denotes the number of classes.

Inspired by the β -VAE (Higgins et al., 2017), each loss in the SVAE model is weighted. In β -VAE, the total loss is modulated by a hyperparameter β :

$$\mathcal{L}_{\beta\text{-vae}} = (1 - \beta) \cdot \mathcal{L}_{mse} + \beta \cdot \mathcal{L}_{KL} \quad (6.14)$$

The β parameter balances the emphasis between reconstruction quality and latent space disentanglement. Higher β values prioritize learning disentangled latent features, while lower values focus on achieving better reconstruction quality. In our SVAE model, the total loss is calculated as:

$$\mathcal{L}_{total} = \lambda_{rec} \cdot \mathcal{L}_{rec} + \lambda_{KL} \cdot \mathcal{L}_{KL} + \lambda_{CE} \cdot \mathcal{L}_{CE}. \quad (6.15)$$

For the original VAE architecture, the CE loss weight λ_{CE} is set to zero. The optimal values for these weights were determined through extensive experiments, detailed in the experimental section.

6.4.3 Experimental Setup

6.4.3.1 Dataset

To evaluate our proposed model, we employ the open-source HumanAct12 dataset as described in (Guo et al., 2020). This dataset consists of 1,191 human motion sequences, each depicting one of 12 different actions. Each frame in these sequences represents a 3D skeleton composed of 24 joints, for a total of 72 dimensions. To manage the variation in sequence lengths, we apply a resampling algorithm that adjusts all sequences to a uniform target length of 75, which corresponds to the average length of the input sequences. This resampling process is based on the Fourier Transform and is implemented using the SciPy Python module (Virtanen et al., 2020). Prior to training, we normalize the skeleton sequences using min – max normalization, which is applied separately to each dimension. Let \mathcal{S} represent the dataset of skeleton sequences, organized into four dimensions: number of samples, sequence length, number of joints, and dimension of each joint. The normalization process is defined as follows:

$$\mathcal{S}[:, :, :, d] = \frac{\mathcal{S}[:, :, :, d] - \min(\mathcal{S}[:, :, :, d])}{\max(\mathcal{S}[:, :, :, d]) - \min(\mathcal{S}[:, :, :, d])}, \quad (6.16)$$

In scenarios involving a train/test split, the test set is normalized using the min and max values derived from each dimension of the training set. This ensures consistency in the data preprocessing steps and enhances the model’s performance by standardizing the input data.

6.4.3.2 Model Architecture

For the Encoder and Decoder architecture in our model (Figure 6.19), we have employed the following configurations:

- Each convolutional layer in the network uses 128 filters.
- The kernel sizes for the filters are 40, 20, and 10 for the three layers in the Encoder, respectively, and these sizes are reversed in the Decoder.
- The dimension of the latent space is set to 16.

The classifier architecture within the SVAE model comprises an FC layer with 8 units, followed by a 50% dropout, and then two fully connected layers with C units each, where C represents the number of classes. The generative models are trained for 2000 epochs with a batch size of 32, using the Adam optimizer with a learning rate decay. We monitor the training loss to select the best model for evaluation.

6.4.3.3 Evaluation Metrics

For the evaluation metrics, we utilize the FID and APD fidelity and diversity metrics, detailed in the previous Section 6.3.2.2.2. For feature extraction during evaluation, we adhere to the methodology in (Guo et al., 2020), employing a GRU-based classifier.

6.4.4 Experimental Results

In this section, we present the experimental results on the HumanAct12 dataset. We start with a parameter search to determine the optimal weights for the different losses in SVAE while comparing its performance to the standard VAE model and the CVAE. Next, we compare our SVAE model with state-of-the-art models. Finally, we conduct an experiment on label distribution balancing using data generation.

6.4.4.1 Weight Losses Parameter Search

To determine the optimal set of hyperparameters for the loss function, we performed an ablation study using a grid search. During this process, we tracked the FID and APD metrics to evaluate performance for the VAE, CVAE and SVAE models. The results of this ablation study are detailed in Table 6.5, with the best-performing model highlighted in bold.

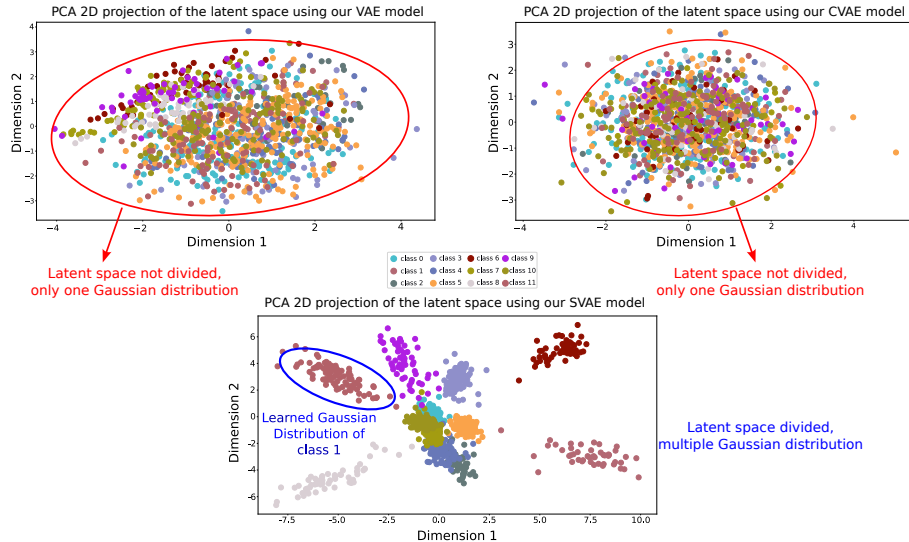
In this study, the SVAE model achieved optimal performance with loss function weights of 0.4995 for the reconstruction loss, 0.001 for the KL loss, and 0.4995 for the CE loss. Reflecting the principles of the β -VAE model, this configuration minimizes the weight of the KL loss while equally weighting the reconstruction and classification losses. This setup ensures that the SVAE model strikes a balance between achieving an optimal latent space representation, maintaining high reconstruction quality, and effectively separating classes in the latent space.

The SVAE model outperforms the traditional VAE model, though it does not surpass the best setup of the CVAE model. However, the SVAE model is less sensitive to changes in the loss parameters. This stability is due to the explicit training setup, which ensures that the action labels effectively distinguish between samples in the latent space. In order to highlight such ability, a 2D visualization of the training samples' latent space, created using Principal Component Analysis (PCA), is shown

TABLE 6.5: The best loss function weights for the VAE, CVAE and SVAE models are as follows. For the VAE and CVAE, the classification loss weight (W_{cls}) is set to 0 due to the absence of a classifier. The generated samples maintain the same label distribution as the training set but include more samples to better estimate the statistical metrics. The best performing setup for each of the three variants is highlighted in **bold**.

Model	W_rec	W_kl	W_cls	FID	APD
VAE	0.99900	1E-03	0.00000	01.38 ^{+0.37}	06.42 ^{+0.10}
VAE	0.99990	1E-04	0.00000	01.20^{+0.10}	06.46^{+0.10}
VAE	1.00000	1E+00	0.00000	45.03 ^{+1.90}	00.07 ^{+0.07}
VAE	0.99999	1E-05	0.00000	01.23 ^{+0.09}	06.45 ^{+0.10}
VAE	0.99000	1E-02	0.00000	01.80 ^{+0.38}	06.39 ^{+0.10}
CVAE	0.99900	1E-03	0.00000	00.55 ^{+0.13}	06.62 ^{+0.11}
CVAE	0.99990	1E-04	0.00000	01.35 ^{+0.22}	06.39 ^{+0.13}
CVAE	1.00000	1E+00	0.00000	05.83 ^{+1.95}	06.15 ^{+0.20}
CVAE	0.99999	1E-05	0.00000	04.65 ^{+1.85}	05.84 ^{+0.23}
CVAE	0.99000	1E-02	0.00000	00.38^{+0.14}	06.71^{+0.11}
SVAE	0.70000	1E-04	0.29000	00.59 ^{+0.11}	06.64 ^{+0.10}
SVAE	0.49950	1E-03	0.49950	00.53^{+0.15}	06.65^{+0.11}
SVAE	0.49995	1E-04	0.49995	00.72 ^{+0.23}	06.62 ^{+0.11}
SVAE	1.00000	1E+00	1.00000	45.56 ^{+1.85}	00.05 ^{+0.07}
SVAE	0.29000	1E-04	0.70000	00.64 ^{+0.09}	06.64 ^{+0.10}
SVAE	0.30000	1E-02	0.70000	00.86 ^{+0.30}	06.62 ^{+0.12}
SVAE	1.00000	1E-04	1.00000	00.79 ^{+0.15}	06.59 ^{+0.11}
SVAE	0.70000	1E-04	0.30000	00.80 ^{+0.22}	06.61 ^{+0.10}
SVAE	0.29000	1E-02	0.70000	00.73 ^{+0.27}	06.63 ^{+0.13}
SVAE	0.30000	1E-04	0.70000	00.68 ^{+0.13}	06.63 ^{+0.10}

FIGURE 6.20: The 2D projection of the latent space (using PCA) for the VAE, CVAE and SVAE models on the training samples shows distinct separation of latent points corresponding to each action label in the case of SVAE compared to no separation in the cases of VAE and CVAE.



in Figure 6.20 for the three models VAE, CVAE and SVAE. This visualization highlights the SVAE model’s ability to clearly separate multiple classes within the latent space, providing better control over generation conditioned on the label, which is not provided by both the VAE and the CVAE models. A visualization of several generated samples is shown in Figure 6.21, demonstrating that the quality of the generated sequences appears visually satisfactory. However, visual inspection alone is not sufficient to fully assess the model’s performance. Therefore, quantitative evaluations are necessary to objectively measure the fidelity and diversity of the generated samples.

6.4.4.2 Comparison With State-Of-The-Art

To evaluate our proposed SVAE architecture against state-of-the-art models on the HumanAct12 dataset, we present the results in Table 6.6, focusing on our best SVAE model. To ensure fair metric evaluation, the generated samples maintain the same label distribution as the training set, for instance if the real data contains 10 samples of class 1 and 5 samples of class 2, then the generated data should follow the same label distribution. This is followed by extracting the features of both real and generated samples using the GRU classifier, i.e. extracting the output of the layer before the classification one. The results reveal that our SVAE model surpasses the Action2Motion model in fidelity (FID) and performs closely to the leading state-of-the-art models. Moreover, the diversity of samples generated by the SVAE is similar to that of the real samples, indicating that the model effectively preserves diversity while maintaining high fidelity.

The results demonstrate that the SVAE model can generate high fidelity human motion sequences, as illustrated by the examples in Figure 6.21. This indicates that the convolution filters effectively extract temporal features from the input sequences. Consequently, this confirms that human motion skeleton sequences can be accurately represented as Multivariate Time Series (MTS).

FIGURE 6.21: Generated samples from the proposed SVAE models are conditioned on four different actions: **Warm Up**, **Drink**, **Lift Dumbbell** and **Sit**. For each action, we present two distinct generated examples to showcase the diversity and robustness of the SVAE model.

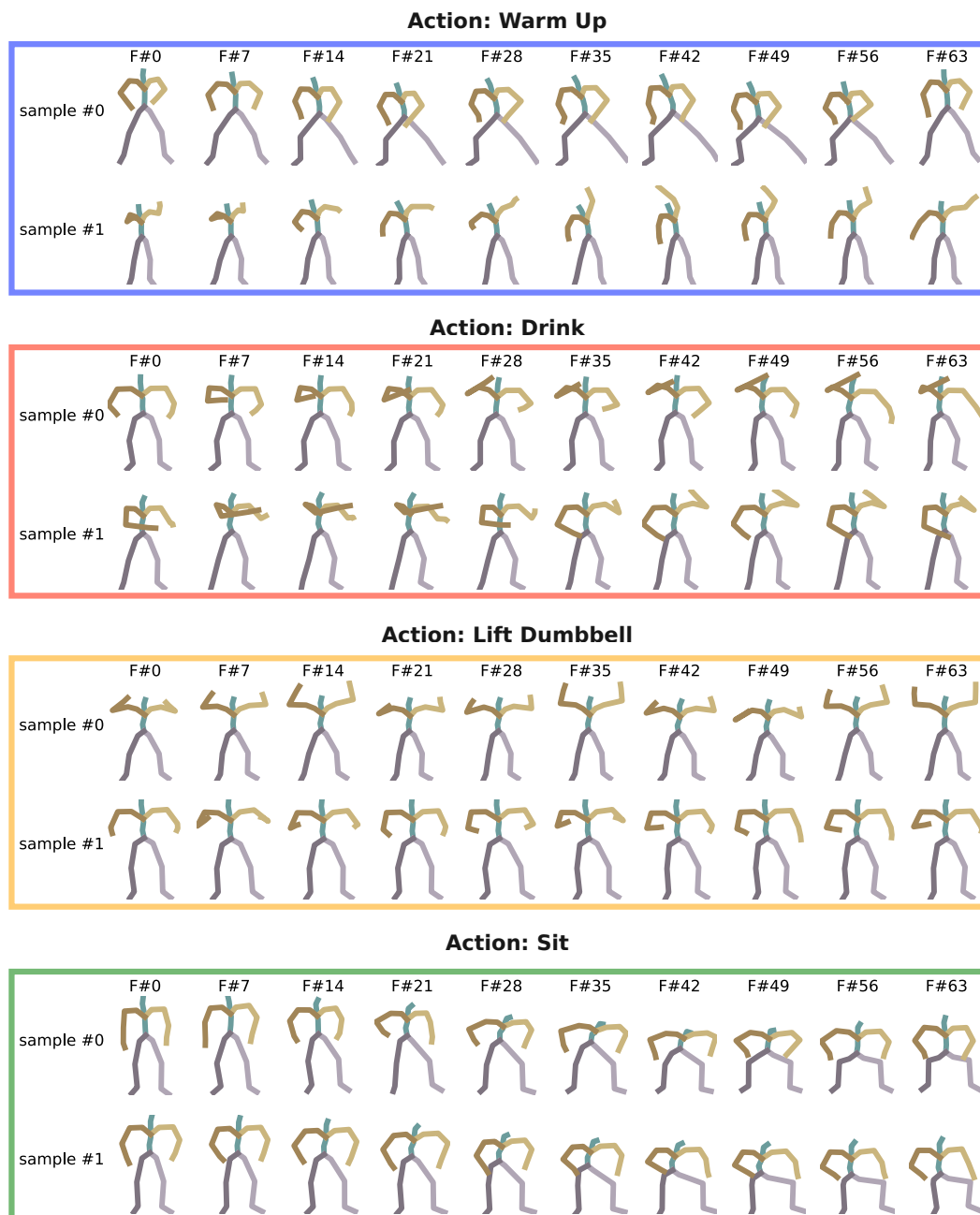


TABLE 6.6: We compared our proposed model, the proposed SVAE, with other approaches from the literature using the FID and Diversity metrics. For each method, we reported the average \pm standard deviation of the FID and Diversity scores. For the real samples, a random split into two sets was used to calculate the FID metric. This comparison allows us to assess the effectiveness of our SVAE model in generating diverse and high-fidelity samples relative to existing methods.

Model	FID \downarrow	Diversity \uparrow
Real	00.030 ^{+0.005}	06.860 ^{+0.070}
Two-stage GAN (Guo et al., 2020)	10.480 ^{+0.089}	05.960 ^{+0.049}
Act-MoCoGAN (Guo et al., 2020)	05.610 ^{+0.113}	06.752 ^{+0.071}
Action2Motion (Guo et al., 2020)	02.458 ^{+0.079}	07.032 ^{+0.038}
ACTOR (Petrovich, Black, and Varol, 2021)	00.120 ^{+0.000}	06.840 ^{+0.030}
PoseGPT (Lucas et al., 2022)	00.080 ^{+*.***}	06.850 ^{+*.***}
UM-CVAE (Zhong et al., 2022)	00.090 ^{+0.000}	06.810 ^{+0.020}
MotionDiffuse (Zhang et al., 2024a)	00.070 ^{+0.000}	06.850 ^{+0.020}
SVAE (ours)	00.560 ^{+0.170}	06.640 ^{+0.100}

TABLE 6.7: Test accuracy values are reported for four different train/test splits: (first row) training on real samples; (second row) training on generated samples (following the same distribution as the real samples); and (third row) training on augmented samples (a combination of real and generated samples to achieve a uniform label distribution).

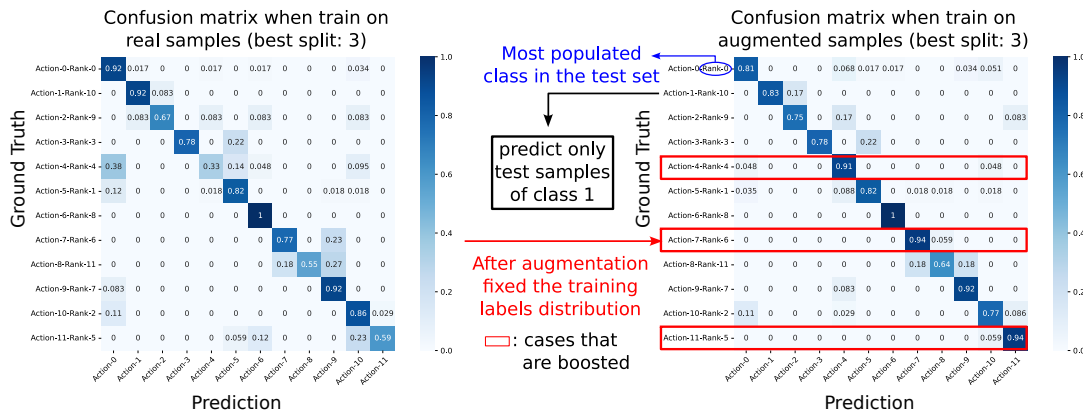
Train On	Split 0	Split 1	Split 2	Split 3
real	87.77 ^{+1.55}	76.47 ^{+2.23}	87.78 ^{+1.40}	77.43 ^{+2.54}
generated	72.47 ^{+2.91}	64.39 ^{+2.42}	77.37 ^{+4.32}	69.75 ^{+7.31}
augmented	86.07 ^{+2.10}	73.51 ^{+1.32}	89.34 ^{+1.77}	78.71 ^{+2.53}

6.4.4.3 Fixing Labels Distribution With SVAE’s Generations

As previously discussed, utilizing data extension with deep generative models can present a paradoxical challenge. In this section, we aim to address the impact of the class balancing problem. By examining the effects of balancing class distributions in the training data, we seek to understand how this approach influences model performance and the quality of generated samples. We implemented our method by balancing the label distribution in the training set, after applying four different train/test splits with a cross subject setup. Specifically, for each training set per split, we generated new human motion sequences using our SVAE model to augment each class, aiming for a uniform label distribution while keeping the most populated class unchanged. Additionally, we trained the model on generated samples that maintained the same number of samples and label distribution as the training set. The results, presented in Table 6.7, indicate that the performance is comparable to training on real samples, showing no significant differences. This demonstrates that the generated samples possess sufficient quality. Furthermore, using data generation to balance the label distribution enhances the model’s performance.

To further examine the fourth split and understand the impact on each action class, we present a confusion matrix in Figure 6.22. The row ticks include the rank of each action class, which represents the population of each class in the test set,

FIGURE 6.22: The confusion matrix compares performance when training on real samples (left) versus augmented samples with a fixed label distribution (right). The matrix consists of 12 rows and 12 columns, corresponding to the 12 action labels. Each row represents the actual class of the samples used for prediction, and each class is ranked in descending order based on their population in the test set. The results show that when the label distribution is fixed (right), the test set performance is significantly affected in classes 4, 7, and 11, which have higher ranks.



listed in descending order. The confusion matrix reveals that our data generation for label distribution balancing technique effectively boosted the performance of some intermediate and low-rank action classes. This demonstrates that the quality of the generated samples is sufficient to enhance the performance of underrepresented classes.

6.5 Conclusion

In this chapter, we explored several advanced methodologies for improving human motion analysis represented as time series data.

Firstly, we discussed the usage of LITEMVTime, a powerful model designed for human rehabilitation assessments. LITEMVTime not only enhances performance but also offers explainability, making it highly suitable for clinical applications where understanding model decisions is crucial.

Next, we introduced ShapeDBA, a novel prototyping method. ShapeDBA was used in a weighted setup to perform data extension for human rehabilitation, effectively boosting regression models. This approach demonstrated significant improvements in handling sparse training data, enhancing the overall quality and robustness of the rehabilitation assessments.

Additionally, we proposed a deep generative model, the Supervised Variational Auto-Encoder (SVAE), for human motion generation. This CNN-based model competes well with state-of-the-art models. The SVAE model integrates classification tasks within the latent space, achieving a balance between reconstruction quality and class separation, ultimately generating high fidelity and diverse human motion sequences.

Throughout this chapter and all previous chapters, we have extensively discussed discriminative tasks such as classification, regression, and clustering, noting that the evaluation methods for these tasks are now well-established and widely adopted by the community. In contrast, the evaluation of generative models is more complex and

diverse, with metrics like FID and APD being commonly used, but many new metrics being proposed each year. It is common in generative model studies, especially in applications like human motion generation, to use fewer than five datasets for evaluation. This limitation makes it impractical to use techniques such as the Critical Difference Diagram and the Multi-Comparison Matrix. Currently, each paper often proposes a new metric with different settings, leading to inconsistent and unfair comparisons. This inconsistency is due to the lack of a standardized framework, which the next chapter aims to address. The next chapter addresses the need to unify the evaluation metrics for human motion generation.

Chapter 7

Evaluation Metrics For Human Motion Generation

7.1 Introduction

Evaluating generative models presents unique challenges (Naeem et al., 2020) that are not as prevalent in discriminative models, where comparisons to ground truth data are straightforward. For generative models, the evaluation involves measuring the validity of generated samples against real ones. Traditional human judgment metrics, such as Mean Opinion Scores (MOS) (Streijl, Winkler, and Hands, 2014), often fall short as they assume a uniform user perception of ideal generation, which is unrealistic. Therefore, quantitative evaluation is essential, focusing on two key dimensions: fidelity and diversity. Fidelity assesses the similarity between the distributions of real and generated data, while diversity measures the variety within the generated samples, ensuring they reflect the range present in real data sets.

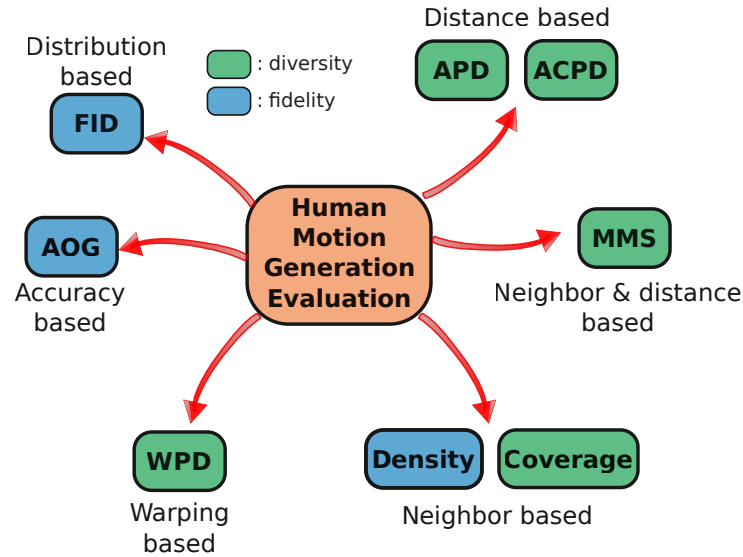
In the previous chapter, we reviewed existing works on human motion generation, which typically use standard evaluation methods and sometimes introduce new metrics. The main challenge is defining fidelity and diversity metrics, as no single optimal solution exists, *No Metric To Rule Them All*. Consequently, numerous approaches and novel metrics have been developed to address this issue. However, evaluating these metrics alone is insufficient, and inconsistencies in generation setups and frameworks post-training across different studies make model comparisons problematic. This complexity underscores the need for a unified and detailed evaluation framework.

A crucial aspect of evaluating human motion data is its temporal dependency (Dau et al., 2019). Temporal distortion, which includes time shifts, frequency changes, and warping, is vital for assessing multivariate time series (Bagnall et al., 2018) such as human motion sequences. Existing metrics often overlook this, focusing instead on latent representations. To address this gap, we introduce a novel metric called Warping Path Diversity (WPD). WPD measures the diversity of temporal distortions in both real and generated data, scoring models based on their ability to produce varied temporal sequences, thus ensuring a more comprehensive evaluation.

Unifying the evaluation process is essential. This work consolidates evaluation metrics from the literature into a unified framework for fair comparisons, providing a helpful resource for newcomers. Our experiments highlight the difficulty of identifying a universally superior model, as small changes in architecture and hyperparameters can significantly impact metric values. We conduct detailed experiments with three CVAE model variants on the same dataset, offering an in-depth analysis of each metric.

Figure 7.1 presents a brief summary of all the metrics used in this work, categorized into fidelity and diversity. The metrics are further organized into sub-categories

FIGURE 7.1: The evaluation metrics for human motion generation in this work are divided into two groups: fidelity metrics and diversity metrics. These metrics are further categorized based on their evaluation criteria, such as FID being a distribution-based metric.



based on their evaluation approach: accuracy-based, distribution-based, distance-based, neighbor-based, neighbor/distance-based, and warping-based.

In this chapter, we propose a clear, user-friendly evaluation framework for newcomers to the field. By establishing standardized practices, we aim to facilitate more consistent and meaningful comparisons of generative models, ultimately contributing to the advancement of human motion generation research.

7.2 Generative Models Metrics

The evaluation metrics for generative models are categorized into fidelity and diversity. Fidelity metrics evaluate how well generated samples mirror the real distribution, making it harder to distinguish between real and generated data, thus ensuring reliability. Diversity metrics assess the variation among generated samples, indicating the model’s ability to produce a wide range of outputs. Higher diversity means the model isn’t limited to a narrow segment of the real distribution.

This section first defines key concepts, then thoroughly reviews the main metrics used for assessing both fidelity and diversity.

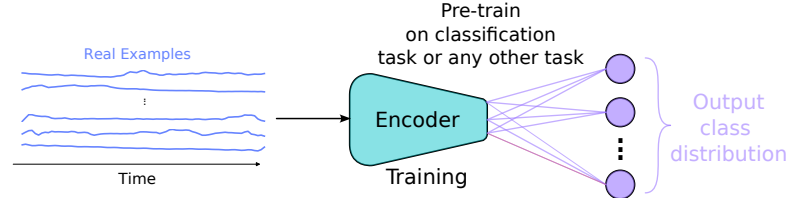
7.2.1 Definitions

To understand the metrics that follow, it’s necessary to establish some definitions:

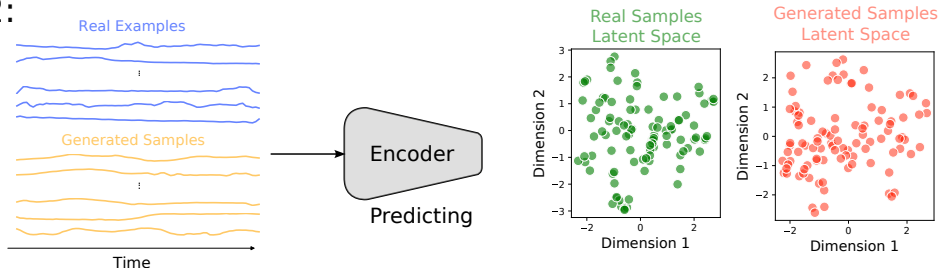
Definition 13 Real set of samples: a set of N real samples is referred to as $\mathcal{X} = \{\mathbf{x}_i\}_{i=1}^N$ and follows a distribution $\mathcal{P}_{\mathcal{R}}$; where \mathbf{x}_i is an MTS of length L and dimensions $M = JxD$, with J being the number of skeleton joints and D the dimension of each joint.

FIGURE 7.2: Before calculating evaluation measures, two steps are followed. First, a model is trained on a supervised task using only real data and not the generated data. Second, the pre-trained encoder's latent representation of the real data is extracted, as well as the latent representation of the generated samples. The metrics are then computed based on this latent representation.

Step 1:



Step 2:



Definition 14 Generated set of samples: a set of G generated samples is referred to as $\hat{\mathcal{X}} = \{\hat{\mathbf{x}}_j\}_{j=1}^G$ and follows a distribution $\mathcal{P}_{\mathcal{G}}$.

Definition 15 A pre-trained deep learning model $\mathcal{G} \circ \mathcal{F}(\cdot)$ is made of a feature extractor \mathcal{F} and a last layer \mathcal{G} achieving the desired task (e.g. classification).

To compute most metrics, we first train a deep learning model $\mathcal{G} \circ \mathcal{F}$ on a specific task, typically classification, using real data. Here, \mathcal{G} is a *softmax* layer. The feature extractor is then used to project both real data \mathcal{X} and generated data $\hat{\mathcal{X}}$ into a latent space, enabling metric calculations within this space. This process involves two steps, as illustrated in Figure 7.2: training the model on real data and using the feature extractor (excluding the final layer) to encode both real and generated samples into latent spaces \mathbf{V} and $\hat{\mathbf{V}}$, respectively, such as:

$$\mathbf{V} = \mathcal{F}(\mathcal{X}) \text{ and } \hat{\mathbf{V}} = \mathcal{F}(\hat{\mathcal{X}}) \quad (7.1)$$

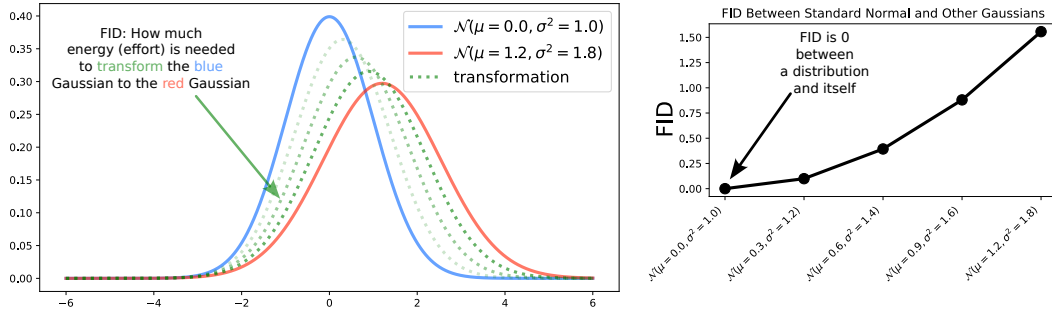
where both \mathbf{V} and $\hat{\mathbf{V}}$ are two-dimensional matrices, corresponding to the number of examples in \mathcal{X} and $\hat{\mathcal{X}}$ respectively, with each dimension representing features f .

For each metric discussed in this section, we compute two versions: one using generated samples (and real samples, as applicable) and one using only real samples. This approach provides a reference metric value for $\mathcal{P}_{\mathcal{R}}$. We achieve this by randomly splitting \mathbf{V} into two subsets, \mathbf{V}_1 and \mathbf{V}_2 . Metrics are then calculated by treating \mathbf{V}_1 as the latent space for real samples and \mathbf{V}_2 as the latent space for generated samples.

7.2.2 Fidelity Metrics

The fidelity metrics in the literature are either distribution based, neighbor based or accuracy based.

FIGURE 7.3: On the left, we illustrate the energy (FID) needed to transform a **standard Gaussian distribution** into another **Gaussian distribution with a higher mean and variance**. On the right, the plot shows that as the mean (μ) and variance (σ^2) of the target distribution increase, the required transformation energy (FID) also increases progressively.



7.2.2.1 Fréchet Inception Distance (FID)

In the previous chapter, we utilized the Fréchet Inception Distance (FID) due to its widespread use in evaluating generative models. In this section, we present the history and background of this metric. Introduced by (Heusel et al., 2017), the Fréchet Inception Distance (FID) is a popular metric for evaluating generative models. It builds on the Inception Score (IS) (Salimans et al., 2016), which assesses generated samples using a pre-trained Inception model, indirectly considering the real distribution $\mathcal{P}_{\mathcal{R}}$. Unlike IS, FID quantifies the difference between the real distribution $\mathcal{P}_{\mathcal{R}}$ and the generated distribution $\mathcal{P}_{\mathcal{G}}$. It does this by calculating the Fréchet Distance (Fréchet, 1906) between two Gaussian distributions in the Inception model's latent space of both \mathcal{X} and $\hat{\mathcal{X}}$.

The Fréchet Distance (FD) (Fréchet, 1906) measures the similarity between two continuous curves. To understand what FD measures, a famous example goes as follows: *Imagine a person and their dog, each wanting to traverse a different finite curved path. The speed of the person and the dog can vary but they are not allowed to go backward on the path. The FD between these two curves is the length of a leash, small enough so that both the person and the dog can traverse the whole finite curve.* For probability distributions, FD is calculated between their Cumulative Distribution Functions (CDFs) (Fréchet, 1957). For multidimensional Gaussian distributions (Dowson and Landau, 1982) $\mathcal{P}_1 \sim \mathcal{N}(\mu_1, \Sigma_1)$ and $\mathcal{P}_2 \sim \mathcal{N}(\mu_2, \Sigma_2)$, both of dimension f , the FD is calculated as follows:

$$FD(\mathcal{P}_1, \mathcal{P}_2)^2 = \text{trace}(\Sigma_1 + \Sigma_2 - 2(\Sigma_1 \cdot \Sigma_2)^{1/2}) + \sum_{i=1}^f (\mu_{1,i} - \mu_{2,i})^2 \quad (7.2)$$

where the values of FD (or FID) range from 0 to $+\infty$.

Setup for generative models First, we empirically estimate the mean vectors μ and $\hat{\mu}$ for both \mathbf{V} and $\hat{\mathbf{V}}$, along with their covariance matrices Σ and $\hat{\Sigma}$. Second, we compute the Fréchet Distance (FD) using Eq. 7.2. For consistency with the literature, we refer to this metric as FID throughout this work, even though the Inception network is not used for human motion.

Interpretation The FID represents the amount of energy or effort needed to transform one Gaussian distribution into another. Figure 7.3 illustrates this concept, showing the probability density functions of two Gaussian distributions. The energy required to change $\mathcal{N}(\mu = 0.0, \sigma^2 = 1.0)$ to $\mathcal{N}(\mu = 1.2, \sigma^2 = 1.8)$ increases with the mean and variance differences. Since no energy is needed to transform a distribution into itself, the starting point on the plot (right side of Figure 7.3) is 0.0. This aligns with the FID’s definition as a distance metric.

Many studies claim that a lower FID indicates higher fidelity in generated samples. However, this can be misleading. For instance, if a generative model merely replicates real samples, it would achieve a perfect FID of 0, showing no new value. Therefore, to accurately compare two generative models using the FID metric, we propose following this principle:

Theorem 3 (Fréchet Inception Distance Interpretation) *A generative model Gen_1 is considered more fidelitous than another model Gen_2 on the FID metric if $FID_{gen1} < FID_{gen2}$ while respecting the following constraint:*

$$\forall \epsilon > 0, \quad FID_{gen} = FID_{real} + \epsilon$$

7.2.2.2 Accuracy On Generated (AOG)

Generative models can incorporate relevant characteristics of each sample for better control. For labeled datasets, this might include discrete labels, continuous values, or text descriptions. This conditioning, as mentioned in Chapter 6 enhances the precision of generated outputs. For example, a model generating human motion sequences can be conditioned to produce specific actions like “running” or “jumping” ensuring alignment with the desired activity.

To evaluate the conditioning capability of a generative model, we can use the score of a classifier pre-trained on real samples \mathcal{X} , treating the generated set $\hat{\mathcal{X}}$ as unseen data. The classifier, $\mathcal{G} \circ \mathcal{F}$, helps measure this capability. We refer to this metric as Accuracy On Generated (AOG), adapted from the Accuracy metric of (Guo et al., 2020), formulated as follows:

$$AOG(\hat{\mathcal{X}}, \hat{Y}, \mathcal{G} \circ \mathcal{F}) = \frac{1}{G} \sum_{i=1}^G \mathbb{1}\{\mathcal{G} \circ \mathcal{F}(\hat{\mathcal{X}}_i) == \hat{Y}_i\} \quad (7.3)$$

where \hat{Y} represents the set of labels employed to condition the generation process, serving as ground truth labels that $\mathcal{G} \circ \mathcal{F}$ is expected to predict. Additionally, $\mathbb{1}$ denotes the indicator function defined as:

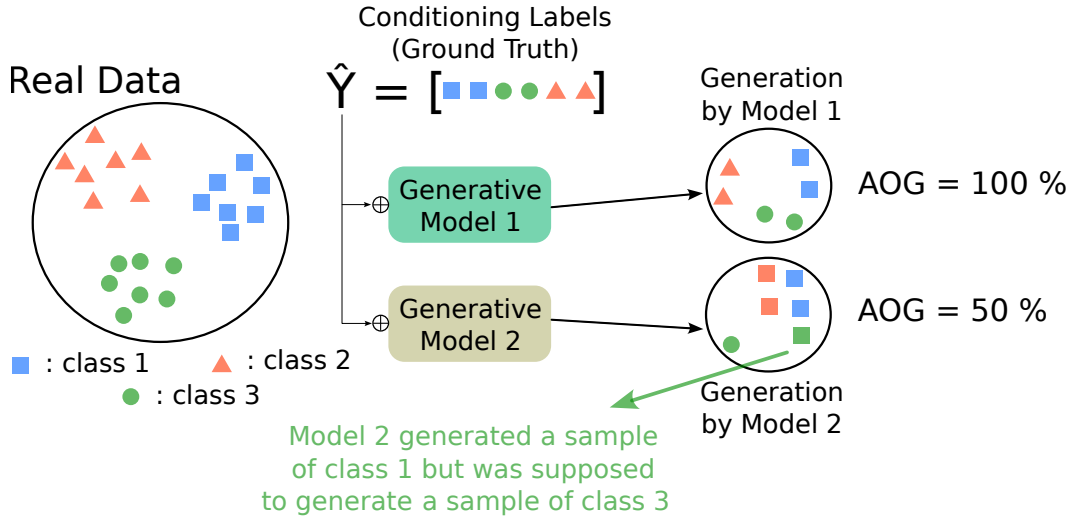
$$\mathbb{1}\{condition\} = \begin{cases} 1 & \text{if condition is True} \\ 0 & \text{if condition is False} \end{cases} \quad (7.4)$$

where the values of AOG in Eq. 7.3 range from 0 to 1.

Setup for generative models The AOG metric is calculated by comparing the ground truth labels \hat{Y} with the predictions made by $\mathcal{G} \circ \mathcal{F}$ using Eq. 7.3.

Interpretation The AOG metric is a strong indicator of a generative model’s conditioning capability, but it must be interpreted carefully. A very low AOG might suggest the model generates samples from a narrow set of labels. Conversely, a perfect AOG score doesn’t necessarily mean high fidelity to $\mathcal{P}_{\mathcal{R}}$; the generated samples

FIGURE 7.4: This example demonstrates the AOG metric for two generative models. **Model1** achieves a perfect AOG of 100% by accurately generating samples conditioned on three classes **red triangles**, **blue squares** and **green circles**. In contrast, **Model2** only achieves 50%, indicating it struggles with correct conditional generation. The AOG metric reflects the classification accuracy of generated samples compared to ground truth labels \hat{Y} .



could contain residual noise that doesn't affect the classifier's performance. Therefore, a high AOG might give a false impression of generation quality. Figure 7.4 demonstrates this nuanced behavior of the AOG metric.

7.2.2.3 Density and Precision

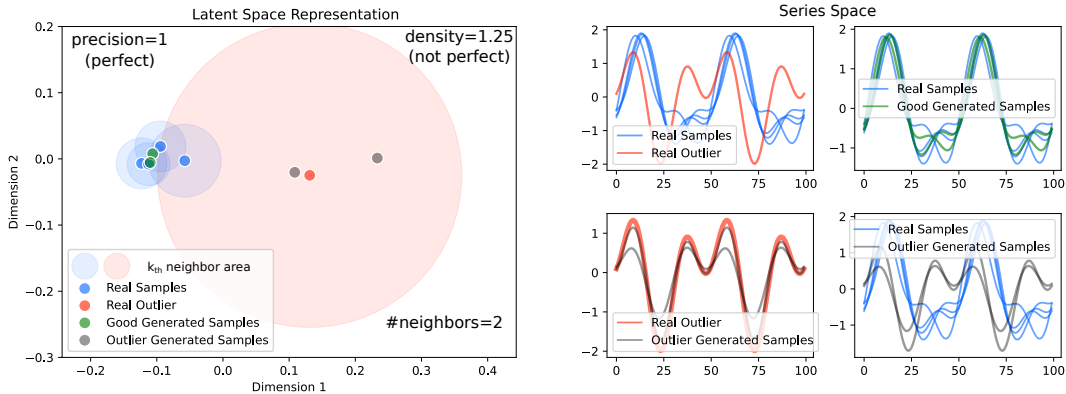
Using a single metric to evaluate generative models is often insufficient due to the complexity of assessing both fidelity and diversity. (Sajjadi et al., 2018) highlighted that two models might share the same FID score but differ in these qualities. To address this, (Sajjadi et al., 2018) introduced precision and recall metrics to evaluate fidelity and diversity separately. (Kynkäänniemi et al., 2019) refined these metrics by incorporating the k -nearest neighbor algorithm to better estimate density functions. In particular, precision represents the portion of samples generated by \mathcal{P}_G that can be sampled from \mathcal{P}_R as well., and its improved formulation (referred to as precision in the rest of this work) is as follows:

$$\text{precision}(\mathbf{V}, \hat{\mathbf{V}}, k) = \frac{1}{G} \sum_{j=1}^G \mathbf{1}(\hat{\mathbf{V}}_j \in \text{manifold}(\mathbf{V}_1, \dots, \mathbf{V}_N)) \quad (7.5)$$

where $\text{manifold}(\{a_1, a_2, \dots, a_n\}) = \bigcup_{i=1}^n B(a_i, \text{NND}_k(a_i))$, $B(c, r)$ is a sphere in $\mathbb{R}^{\text{dimension}(a_i)}$ of center c and radius r , and $\text{NND}_k(a_i)$ is the distance from a_i to its k th nearest neighbor in the set $\{a_j\}_{j=1, j \neq i}^N$. The values of precision range from 0 to 1.

(Naeem et al., 2020) identified key limitations in the precision and recall metrics for evaluating generative models. They proposed density and coverage as new metrics for fidelity and diversity, respectively. This section addresses fidelity, with diversity discussed in Section 7.2.3. The precision metric has two main issues: (1) no closed formulation for the expected precision when real and generated samples follow the

FIGURE 7.5: This example demonstrates the computation of density and precision metrics on a synthetic dataset. The left side shows the latent representation of: real data, the real outlier, generated samples near the outlier and near non-outliers. For each real sample we represent its neighborhood area. The right side depicts the original data series. The density metric, unlike precision, correctly identifies the outlier, giving a score of 1.25 instead of 1. This illustrates how density better reflects fidelity by accounting for outliers. Both metrics use 2 neighbors.



same distribution (i.e. $\mathcal{P}_{\mathcal{R}}$ and $\mathcal{P}_{\mathcal{G}}$ are identical), and (2) outliers in the real data \mathcal{X} can produce misleading precision values, suggesting good performance even when it is not accurate.

The mathematical formulation of the density metric is as follows:

$$density(\mathbf{V}, \hat{\mathbf{V}}, k) = \frac{1}{k \cdot G} \sum_{j=1}^G \sum_{i=1}^N \mathbf{1}(\hat{\mathbf{V}}_j \in B(\mathbf{V}_i, NND_k(\mathbf{V}_i))) \quad (7.6)$$

where the values of *density* range from 0 to $\frac{N}{k}$.

(Naeem et al., 2020) showed that when real and generated distributions ($\mathcal{P}_{\mathcal{R}}$ and $\mathcal{P}_{\mathcal{G}}$) are identical, the expected value of density is 1. This means that with enough samples and a high number of neighbors, the density metric converges to 1, accurately reflecting the fidelity of generated samples. Additionally, density has an advantage over precision by detecting outliers in the real distribution.

Figure 7.5 illustrates an outlier scenario with a synthetic dataset. On the left, it shows the latent space of five real samples and four generated samples, highlighting an outlier in red. The generated samples correctly cluster around the four real samples, with two near the outlier. Precision fails here, giving a misleading perfect score of 1, which suggests high fidelity. However, the density metric reveals the issue, as it identifies the two generated samples influenced by the outlier, resulting in a more accurate, non-perfect score of 1.25.

Setup for generative models First, we determine the distance from each sample in $\mathbf{V} = \mathcal{F}(\mathcal{X})$ to its k_{th} nearest neighbor within $\hat{\mathbf{V}} = \mathcal{F}(\hat{\mathcal{X}})$. Next, we compute the precision and density metrics using Eqs. 7.5 and 7.6, respectively.

Interpretation The precision metric measures the number of generated samples that fall within at least one real sample's neighboring sphere. Conversely, the density

metric counts how many neighboring spheres each generated sample occupies. While both metrics assess how well generated samples match real ones, density provides a more detailed analysis by considering each real-generated pair individually. Precision, however, overlooks potential biases from real outliers by focusing only on the union of neighboring spheres, missing the nuanced fidelity captured by density.

7.2.3 Diversity Metrics

Evaluating fidelity alone does not fully ensure the reliability of generated samples; hence, diversity measures are necessary. Next, we introduce the diversity metrics commonly used in the literature, including both distance-based and neighbor-based approaches.

7.2.3.1 Average Pair Distance (APD)

Another common metric we used in the previous chapter is the Average Pair Distance (APD). Originally proposed by (Zhang et al., 2018) for measuring distances between images, it was adapted by (Guo et al., 2020) for evaluating the diversity of human motion generative models. APD calculates the average Euclidean Distance, in the latent space of the pre-trained encoder, between randomly selected sample pairs, repeated R times over S_{apd} pairs. The final APD value is the average result of these experiments. This metric can evaluate the diversity of any dataset, not just generated samples. The APD metric calculated on the generated set of samples, for one random selection $r \in \{1, 2, \dots, R\}$ is formulated as follows:

$$APD_r(\mathcal{S}, \mathcal{S}') = \frac{1}{S_{apd}} \sum_{i=1}^{S_{apd}} \sqrt{\sum_{j=1}^f (\mathcal{S}_{i,j} - \mathcal{S}'_{i,j})^2} \quad (7.7)$$

where \mathcal{S} and \mathcal{S}' are two randomly selected subsets of $\hat{\mathbf{V}} = \mathcal{F}(\hat{\mathcal{X}})$, i.e. $\mathcal{S}, \mathcal{S}' \subset \hat{\mathbf{V}}$.

The APD metric is then calculated by averaging over the R random experiments:

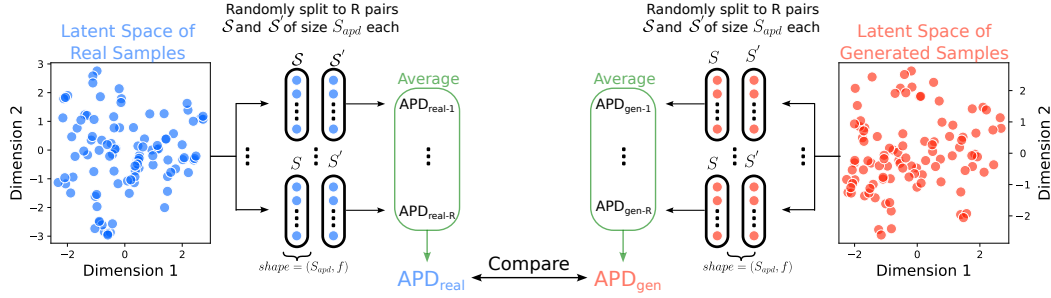
$$APD(\hat{\mathcal{X}}) = \frac{1}{R} \sum_{r=1}^R APD_r(\mathcal{S}^r, \mathcal{S}'^r) \quad (7.8)$$

where $APD_r(\hat{\mathcal{X}})$ is calculated using Eq. (7.7). An illustration of the APD metric is represented in Figure 7.6 highlighting the procedure to calculate APD on real and generated data separately.

Setup for generative models We calculate the APD metric using Eqs 7.7 and 7.8. This is done for both real and generated datasets independently of each other, with only the encoder, pre-trained on real data, used for both computations.

Interpretation The APD metric assesses whether a generative model can avoid mode collapse, where it generates the same outcome repeatedly. Ideally, the APD metric should be as high as possible to indicate diverse outputs. However, a potential issue arises if $APD_{gen} > APD_{red}$, as it suggests that the generated space is more diverse than the real one, which is an implausible outcome. To address this, (Guo et al., 2020) provided further interpretation, leading to the following theorem:

FIGURE 7.6: This example demonstrates the calculation of the APD metric for both **real samples** and **generated samples**. For each latent representation, two sets \mathcal{S} and \mathcal{S}' of randomly selected values, each of size S_{apd} , are created. The APD metric is then computed between these sets. This process is repeated RR times, and the final APD value is the **average of all computed APD values**.



Theorem 4 (Average Pair Distance Interpretation) *A generative model Gen_1 is considered more diverse than another model Gen_2 if $APD_{gen1} > APD_{gen2}$, while respecting the following constraint:*

$$\forall \epsilon > 0, |APD_{gen1} - APD_{real}| < \epsilon$$

In simpler terms, a generative model's APD diversity should not surpass that of the real distribution $\mathcal{P}_{\mathcal{R}}$. To illustrate, if real data has an APD_{real} of 5 and a generative model is randomly initialized without training, the APD_{gen} could exceed 5. However, this higher diversity would be due to random generation, not a meaningful correlation with $\mathcal{P}_{\mathcal{R}}$. This demonstrates that exceeding too much the real data's diversity doesn't necessarily reflect a well-trained model.

7.2.3.2 Average per Class Pair Distance (ACPD)

The Average per Class Pair Distance (ACPD) (Guo et al., 2020) metric, like APD, evaluates the diversity of generated samples but at a more detailed level. While APD measures diversity across the entire distribution $\mathcal{P}_{\mathcal{R}}$, ACPD focuses on individual sub-clusters within $\mathcal{P}_{\mathcal{R}}$. This allows for a more nuanced assessment of how well the model captures diversity within specific categories. ACPD computes the average APD for each sub-cluster, formed using the class labels, providing insights into class-specific diversity. The mathematical formulation of ACPD is as follows:

$$ACPD_r(\mathcal{S}, \mathcal{S}') = \frac{1}{C \cdot S_{acpd}} \sum_{i=1}^{S_{acpd}} \sqrt{\sum_{j=1}^f (\mathcal{S}_{c,i,j} - \mathcal{S}'_{c,i,j})^2} \quad (7.9)$$

where C is the total number of classes in $\mathcal{P}_{\mathcal{R}}$, $\mathcal{S}_c, \mathcal{S}'_c$ are randomly selected subsets from $\hat{\mathbf{V}}[\hat{Y} = c]$, and \hat{Y} are the labels used to generated $\hat{\mathcal{X}}$.

Similar to APD, due to the randomness involved in ACPD, the experiment is repeated R times to calculate $ACPD_r$ for $r \in \{1, 2, \dots, R\}$. The final ACPD value

is then obtained by averaging these repeated calculations:

$$ACPD(\hat{\mathcal{X}}) = \frac{1}{R} \sum_{r=1}^R ACPD_r(\mathcal{S}^r, \mathcal{S}'^r) \quad (7.10)$$

It is important to note that this metric is restricted only to labeled datasets where labels are discrete, e.g. classification.

Setup for generative models We calculate ACPD using Eqs. 7.9 and 7.10. This is done for both real and generated datasets independently of each other, with only the encoder, pre-trained on real data, used for both computations.

Interpretation The ACPD metric assesses the diversity of generated samples within each sub-cluster of $\mathcal{P}_{\mathcal{R}}$, ensuring that the model doesn't over-focus on a single cluster. This addresses the common issue of imbalanced labeled data in machine learning, where some classes may have more diversity than others. Similar to the APD metric, ACPD is calculated for both real and generated samples, resulting in $ACPD_{real}$ and $ACPD_{gen}$. A generative model is deemed class diverse when $ACPD_{gen}$ closely matches $ACPD_{real}$, indicating balanced generation across all categories.

7.2.3.3 Coverage and Recall

As mentioned in Section 7.2.2.3, (Naeem et al., 2020) proposed new metrics to replace the improved precision and recall metrics introduced by (Sajjadi et al., 2018; Kynkäänniemi et al., 2019). Their recall metric measures how well the generated distribution $\mathcal{P}_{\mathcal{G}}$ can sample real examples from $\mathcal{P}_{\mathcal{R}}$. This is achieved by counting the number of real samples that appear in at least one neighborhood of a generated sample. The recall metric is formulated as follows:

$$recall(\mathbf{V}, \hat{\mathbf{V}}, k) = \frac{1}{N} \sum_{i=1}^N \mathbf{1}(\mathbf{V}_i \in manifold(\hat{\mathbf{V}}_1, \hat{\mathbf{V}}_2, \dots, \hat{\mathbf{V}}_M)) \quad (7.11)$$

where $manifold(\cdot)$ and $\mathbf{1}(\cdot)$ follow the same definition detailed in Section 7.2.2.3. The recall metric is bounded between 0 and 1.

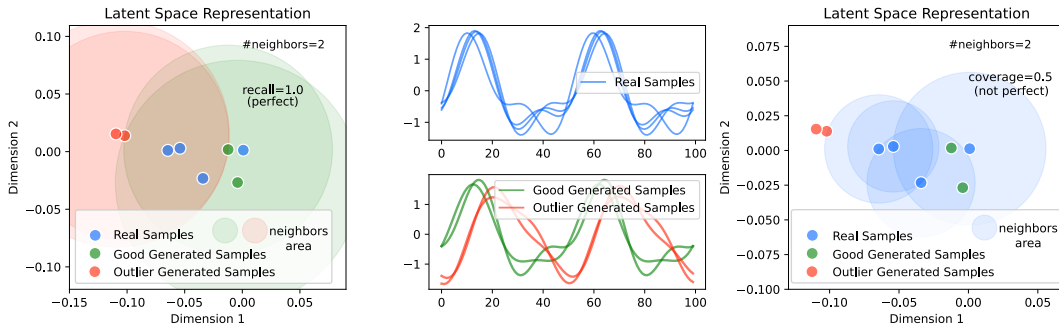
(Naeem et al., 2020) identified several limitations of the recall metric, summarized as follows:

1. Defining neighborhood areas based on generated samples can lead to misinterpretations, as outliers are more likely to be sampled by $\mathcal{P}_{\mathcal{G}}$ than by $\mathcal{P}_{\mathcal{R}}$.
2. There is no closed-form solution for the expected value of the recall metric when $\mathcal{P}_{\mathcal{R}}$ and $\mathcal{P}_{\mathcal{G}}$ are identical distributions, complicating the evaluation process.

To overcome the limitations of the recall metric, (Naeem et al., 2020) proposed the coverage metric. This metric focuses on neighborhood areas around the real samples \mathcal{X} . It counts how many real samples include at least one generated sample from $\hat{\mathcal{X}}$. The coverage metric provides a more accurate representation by measuring the presence of generated samples within the vicinity of real samples. The formulation of the coverage metric is as follows:

$$coverage(\mathbf{V}, \hat{\mathbf{V}}, k) = \frac{1}{N} \sum_{i=1}^N \mathbf{1}(\exists j \text{ s.t. } \hat{\mathbf{V}}_j \in B(\mathbf{V}_i, NND_k(\mathbf{V}_i))) \quad (7.12)$$

FIGURE 7.7: The computation of coverage and recall metrics over a synthetic dataset is shown on the left and right side of the figure. The figure's left and right sides depict the latent space with **real samples** and generated samples both **reliable**, and **outliers**. The middle shows the original series space, highlighting the differences between the three spaces. The left plot shows neighbor areas around generated samples (recall metric), while the right plot shows neighbor areas around real samples (coverage metric). The coverage metric correctly identifies outliers, resulting in a non-perfect measure, unlike the recall metric. Both metrics use 2 neighbors.



where $B(\cdot, \cdot)$ and $NND_k(\cdot)$ follow the same definitions detailed in Section 7.2.2.3. The coverage metric is bounded between 0 and 1.

The coverage metric addresses the recall metric's limitation by avoiding the use of generated sample neighborhoods. Figure 7.7 illustrates this with a synthetic example. The recall metric falsely shows perfect diversity due to over-estimated neighborhoods caused by outliers (left scatter plot). In contrast, the coverage metric accurately differentiates between valid and outlier samples by focusing on the neighborhoods of real samples. This results in a more reliable assessment of the generative model's diversity.

The coverage metric also resolves the second limitation of recall, as demonstrated by (Naeem et al., 2020). They showed that for identical distributions $\mathcal{P}_{\mathcal{R}}$ and $\mathcal{P}_{\mathcal{G}}$, the expected value of coverage has a simplified closed-form solution, as such:

$$\mathbb{E}[\text{coverage}] = 1 - \frac{(N-1) \dots (N-k)}{(G+N-1) \dots (G+N-k)} \quad (7.13)$$

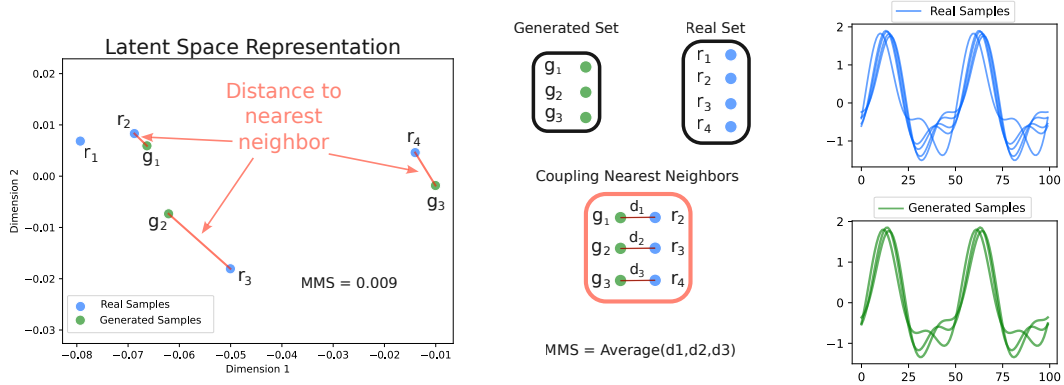
which reduces to, in the case where both N and G are high enough:

$$\mathbb{E}[\text{coverage}] = 1 - \frac{1}{2^k}. \quad (7.14)$$

Setup for generative models First, we calculate the recall metric by determining the distance of each sample in $\hat{\mathbf{V}}$ to its k_{th} nearest neighbor in $\hat{\mathbf{V}}$ and applying Eq. 7.11. Second, we compute the coverage metric by finding the distance of each sample in \mathbf{V} to its k_{th} nearest neighbor in \mathbf{V} and using Eq. 7.12.

Interpretation The recall metric calculates the proportion of real samples that fall within the neighborhood of at least one generated sample. Conversely, the coverage metric determines the proportion of real samples that have at least one generated sample in their neighborhood. While both metrics assess diversity, the coverage metric is more reliable as it is based on real sample neighborhoods. With an expected value

FIGURE 7.8: This example illustrates the MMS metric computation on a synthetic dataset. The left side shows the latent representation of real samples and generated samples. The right side displays the original series space. First, each generated point's nearest neighbor in the real set is identified using the Euclidean Distance. Second, the MMS metric is obtained by averaging all these distances.



of $1 - \frac{1}{2^k}$ for identical $\mathcal{P}_{\mathcal{R}}$ and $\mathcal{P}_{\mathcal{G}}$, the interpretation of high diversity for the coverage metric depends on the chosen number of neighbors k .

7.2.3.4 Mean Maximum Similarity (MMS)

Originally proposed in (Cervantes et al., 2022), the Mean Maximum Similarity (MMS) metric evaluates the novelty of generated data. Generative models can sometimes produce data almost identical to the training set, mimicking its diversity without solving the intended task. MMS addresses this by quantifying the novelty of generated samples, which we interpret as a measure of diversity in this context. This ensures that the generated data is not just varied but also distinct from the training set.

The MMS quantifies novelty/diversity by averaging the distances of each of the generated samples to its real nearest samples. It is given by:

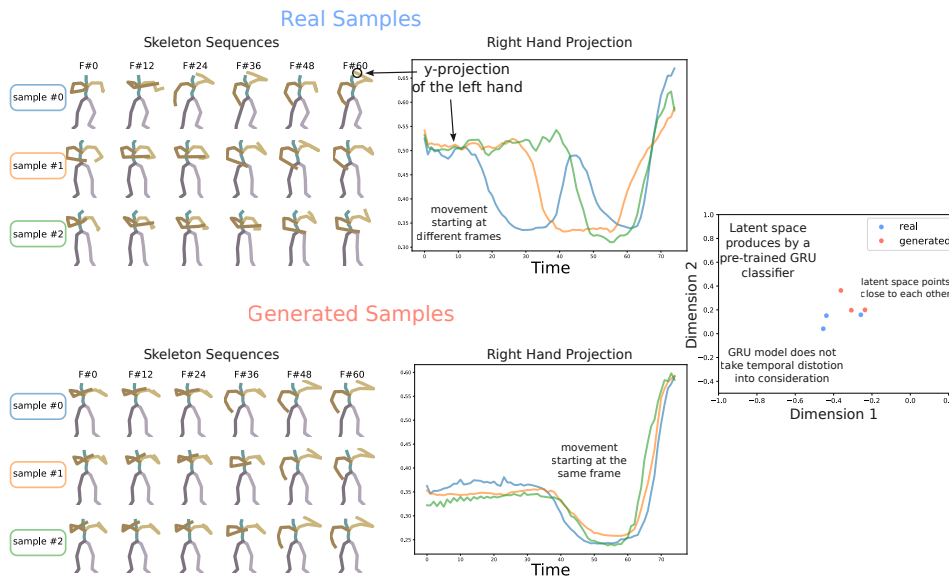
$$MMS(\mathbf{V}, \hat{\mathbf{V}}) = \frac{1}{G} \sum_{j=1}^G \sqrt{\sum_{d=1}^f (\hat{\mathbf{V}}_{j,d} - \mathbf{V}_{NN_j,d})^2} \quad (7.15)$$

where \mathbf{V}_{NN_j} (from the real set) is the nearest neighbor to $\hat{\mathbf{V}}_j$ (from the generated set). A visual representation of the MMS metric is shown in Figure 7.8.

Setup for generative models First, for each sample in $\hat{\mathbf{V}}$, calculate its distance to the nearest neighbor in \mathbf{V} and average these distances to obtain MMS_{gen} . Second, for each sample in \mathbf{V} , calculate the distance to the second nearest neighbor within \mathbf{V} and average these to determine MMS_{real} . We adhere to the method outlined in (Stefan, Athitsos, and Das, 2012a) and do not use the \mathbf{V}_1 and \mathbf{V}_2 sets for the MMS metric calculation.

Interpretation (Stefan, Athitsos, and Das, 2012a) suggested that MMS_{gen} should always be higher than MMS_{real} to signify high novelty. However, this metric has limitations, particularly when the model generates random samples far from the real set,

FIGURE 7.9: This figure demonstrates the need for a temporal distortion diversity metric. On the left side, three real (top) and three generated (bottom) human motion sequences performing the "drink-with-left-hand" action are presented. In the middle, the y -axis projection of the subject's left-hand motion is displayed for the three samples from both real and generated spaces. The real samples show variability in the starting frame, while the generated samples start consistently. On the right, the latent representation of real and generated samples using a pre-trained GRU classifier reveals that the model does not account for temporal distortion diversity.



leading to an overestimation of novelty. Thus, relying solely on MMS for evaluating a generative model's performance is insufficient. Additionally, MMS_{real} is calculated within the entire real sample set, not between two subsets, which differs from the approach used for other metrics.

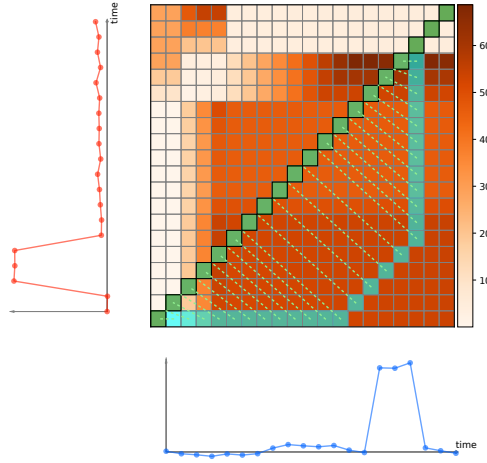
7.3 Proposed Metric: Warping Path Diversity (WPD)

Each diversity metric in Section 7.2.3 relies on a pre-trained encoder \mathcal{F} to extract latent features, assuming an input latent space. However, for temporal data like human motion sequences, some temporal distortions exist, such as shifting and frequency changes. For instance, as presented in Figure 7.9, real samples from the HumanAct12 dataset show the action of drinking starting at different frames, while generated samples lack this variability. The pre-trained encoder \mathcal{F} fails to account for these distortions, affecting metrics like APD, which measure Euclidean distances in latent space. To address this, we propose a new metric that uses Dynamic Time Warping (DTW) (Müller, 2007) (see Chapter 1) to capture and quantify temporal distortions between sequences.

To simplify, we assume both sequences xx and yy have the same length L . For the sequences in Figure 7.10, three scenarios can occur:

1. **Worst-case scenario:** The sequences are poorly aligned, with the DTW path running along the matrix edges, resulting in a path length of $L_{\pi} = 2L$.

FIGURE 7.10: The distance matrix between two time series is shown in a heat map where each point represents the squared difference between corresponding time stamps. The optimal Dynamic Time Warping (DTW) path, captures the temporal distortion between the series. The connections between the warping path and the diagonal indicate how much the two series deviate from having no temporal distortion.



2. **Best-case scenario:** The sequences are perfectly aligned along the diagonal, making DTW equivalent to Euclidean Distance.
3. **Intermediate scenario:** Temporal distortions cause the path to deviate from the diagonal but remain shorter than the maximum value; $L_\pi < 2L$.

To measure the diversity of temporal distortions (warping) between two sequences, we propose quantifying the distance of the warping path from the diagonal. This involves summing the distances from each point on the warping path to the diagonal, as illustrated in Figure 7.11. Each point on the path is considered within an integer coordinate space with axes ranging from 1 to L . For equal-length sequences, the triangle at each warping path point is a right isosceles triangle, making the hypotenuse's median half its length.

Theorem 5 (Warping Path Diversity's Distance To Diagonal Computation)

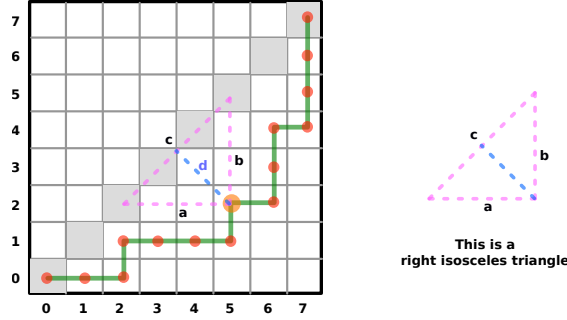
Given two sequences \mathbf{x} and \mathbf{y} both of length L , with warping path π of length $L \leq L_\pi \leq 2L$, the distance from the t_{th} point of the path π , where $t \in \{1, 2, \dots, L_\pi\}$, to the diagonal (perfect alignment) is defined as follows:

$$distance(\pi_t, diagonal) = \frac{\sqrt{2}}{2} |t_1 - t_2|$$

proof: Using the annotations of a , b , c and d in Figure 7.11 as the summit of points π_t on the warping path π , then $d = distance(\pi_t, diagonal)$ is calculated as follows:

$$\begin{aligned} d &= \frac{1}{2} \sqrt{c^2} = \frac{1}{2} \sqrt{a^2 + b^2} = \frac{1}{2} \sqrt{2 * a^2} \\ &= \frac{1}{2} \sqrt{2 * (t_1 - t_2)^2} = \frac{\sqrt{2}}{2} |t_1 - t_2| \end{aligned} \tag{7.16}$$

FIGURE 7.11: Mathematical basis of the WPD metric: For each point on the warping path, the corresponding triangle is always a right isosceles triangle, given that the series are of equal length. Hence the distance from the point to the diagonal can be easily calculated with the Pythagorean theorem (Maor, 2019).



The WPD value between \mathbf{x} and \mathbf{y} is the average distance of all points on the warping path to the diagonal, as follows:

$$WPD_d(\mathbf{x}, \mathbf{y}) = \frac{\sqrt{2}}{2L_\pi} \sum_{t=1}^{L_\pi} |t_1 - t_2| \quad (7.17)$$

Finally, the WPD metric of a generative model is calculated, like for the APD metric, between random subsets of samples from both real and generated samples:

$$WPD_r(\mathcal{S}, \mathcal{S}') = \frac{1}{S_{wpd}} \sum_{i=1}^{S_{wpd}} WPD_d(\mathcal{S}_i, \mathcal{S}'_i) \quad (7.18)$$

where \mathcal{S} and \mathcal{S}' are two randomly selected subsets, of size S_{wpd} , from $\hat{\mathbf{V}} = \mathcal{F}(\hat{\mathcal{X}})$, i.e., $\mathcal{S}, \mathcal{S}' \subset \hat{\mathbf{V}}$ and $r \in \{1, 2, \dots, R\}$ is the number of repetitions of this random experiment to avoid the bias of a random selection. The final WPD metric is calculated as:

$$WPD(\hat{\mathcal{X}}) = \frac{1}{R} \sum_{r=1}^R WPD_r(\mathcal{S}^r, \mathcal{S}'^r) \quad (7.19)$$

with WPD bounded between 0 and $\frac{\sqrt{2}}{4}(L+1)$.

The same methodology is followed to calculate WPD on the real set of samples \mathcal{X} . The characteristics of our proposed WPD metric are summarized in Table 7.1 along with all the other metrics presented in this study.

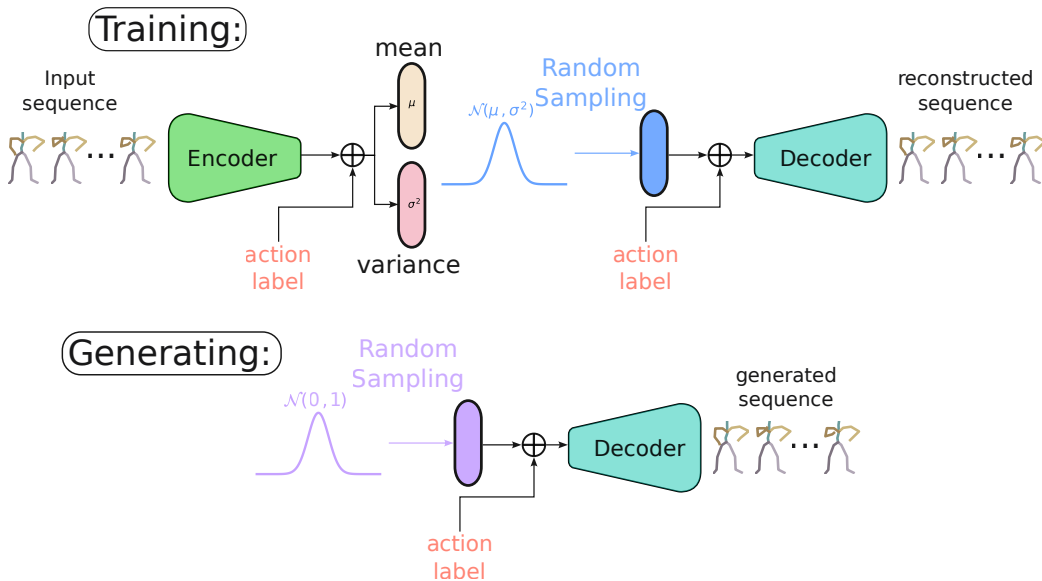
7.4 Experimental Setup

To analyze the behavior of each metric during evaluation, we conduct an experiment using Conditional Variational Auto-Encoders (CVAE) to generate human motion sequences. The conditioning feature of the CVAE allows precise control over the generated actions by specifying the action class. Figure 7.12 illustrates the training and generating phases of a CVAE with human motion sequences, providing a visual

TABLE 7.1: Summary of the Generative Models Metrics in this study.

Metric	Category	Space	Hyperparameters	Bounds	Interpretation	Better Version	Used in Study
<i>FID</i>	fidelity	latent	None	$0 \leq FID < \infty$	Higher but close to FID_{real}	None	yes
<i>AOG</i>	fidelity/accuracy	latent	None	$0 \leq AOG \leq 1$	Close to 1 (100% accuracy)	None	yes
<i>density</i>	fidelity	latent	k : number of neighbors	$0 \leq density \leq N/k$ N being the number of real samples	closer to $density_{real}$ which is close to 1	None	yes
<i>precision</i>	fidelity	latent	k : number of neighbors	$0 \leq precision \leq 1$	closer to 1	<i>density</i>	no
<i>coverage</i>	diversity	latent	k : number of neighbors	$0 \leq coverage \leq 1$	closer to $coverage_{real}$ which is close to $1 - 1/2^k$	None	yes
<i>recall</i>	diversity	latent	k : number of neighbors	$0 \leq recall \leq 1$	closer to 1	<i>coverage</i>	no
<i>APD</i>	diversity	latent	S_{apd} : size of random subset R : number of random experiments	$0 \leq APD < \infty$	Lower but close to APD_{real}	None	yes
<i>ACPD</i>	diversity	latent	S_{apd} : size of random subset R : number of random experiments	$0 \leq ACPD < \infty$	Lower but close to $ACPD_{real}$	None	yes
<i>MMS</i>	diversity/novelty	latent	None	$0 \leq MMS < \infty$	Higher but close to MMS_{real}	None	yes
<i>WPD (ours)</i>	diversity/warping	raw	S_{apd} : size of random subset R : number of random experiments	$0 \leq WPD \leq \frac{\sqrt{2}}{4}(L+1)$ L being the length of the sequence	Depends on the application	None	yes

FIGURE 7.12: In our experiments, the CVAE undergoes two phases: training and generation. **During training**, the **Encoder** and **Decoder** are trained simultaneously. The **Encoder** extracts features from input sequences and projects them into a Gaussian latent space with a learned **mean** and **variance**, conditioned on the **action label**. The **Decoder** then reconstructs the input sequence from a **sample in this space**. **In the generation phase**, a **random sample from a Normal distribution** is fed to the **Decoder** to generate a new sequence, also conditioned on the desired **action label**.



representation of our experimental setup. This approach enables a comprehensive assessment of how different metrics respond to the generated data.

7.4.1 Backbone Architectures

The CVAE model employs an encoder-decoder architecture using three well-known neural network backbones: Convolutional Neural Networks (CNNs), Recurrent Neural Networks (RNNs), and Transformer Networks. The CNN-based CVAE (CConvVAE) uses symmetrical convolution and de-convolution blocks. The RNN-based CVAE (CGRUVAE) uses stacked Gated Recurrent Units (GRUs) for both encoding and decoding, repeating the input for sequence generation. The Transformer-based CVAE (CTransVAE) features self-attention mechanisms in both encoder and decoder, with matching layers and parameters. Each architecture maintains symmetry between its encoder and decoder components.

7.4.2 Implementation Details

The three CVAE variants in this work are implemented using *tensorflow* (Abadi et al., 2015) Python package and trained for 2,000 epochs with a batch size of 32, utilizing a learning rate decay method. The CConvVAE employs three convolution and three de-convolution blocks with 128 filters and kernel sizes of 40, 20, and 10. The CGRUVAE has two GRU layers in both the encoder and decoder, with a hidden state size of 128. The CTransVAE uses convolution embedding followed by two Multi-Head Attention layers in both the encoder and decoder, with 128 filters and a head size of 32. All three variants have a latent space dimension of 16. To train the generative models, we utilize a publicly available action recognition dataset, HumanAct12 (Guo et al., 2020). Prior to training, we normalize all sequences in the dataset using a min – max scalar on each of the $x - y - z$ dimensions independently. It is important to note that for all the metrics used in this work, no prior train-test splits are required, instead all the dataset can be used.

7.4.3 Training on Different Loss Parameters

In this experimental work, we assess how slight changes in a model’s parameters may affect the interpretation of evaluation metrics by experimenting with the model’s loss parameters. We train a CVAE model to optimize a weighted sum of two losses: reconstruction loss and Kullback-Leibler (KL) divergence loss. The total loss is defined as:

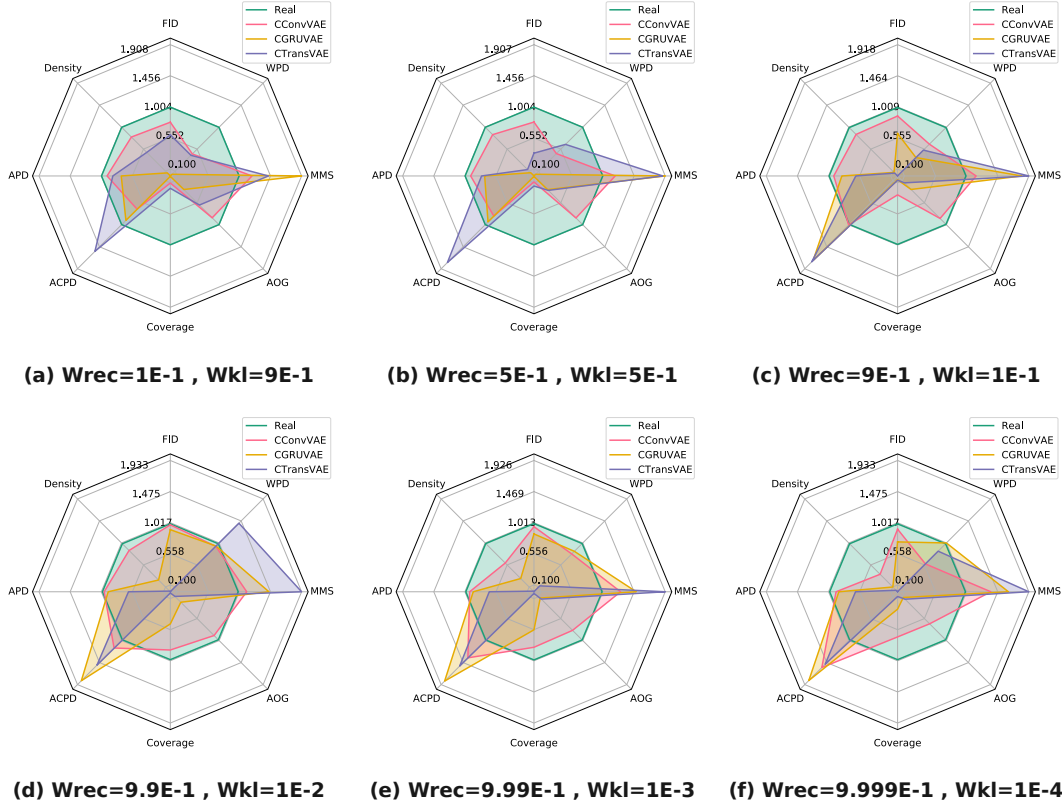
$$\mathcal{L} = \alpha \cdot \mathcal{L}_{rec} + \beta \cdot \mathcal{L}_{KL} \quad (7.20)$$

where α and β are scalar weights between 0 and 1 for each of the reconstruction and KL loss respectively. In the ideal case, it is preferable to maintain the following constraint:

$$\alpha + \beta = 1 \quad (7.21)$$

As seen in chapter 1, α is set to $1 - \beta$ to preserve convexity. Instead of selecting a specific (α, β) pair, we experiment with various values: $(1E^{-1}, 9E^{-1})$, $(5E^{-1}, 5E^{-1})$, $(9E^{-1}, 1E^{-1})$, $(9.9E^{-1}, 1E^{-2})$, $(9.99E^{-1}, 1E^{-3})$, $(9.999E^{-1}, 1E^{-4})$. This approach highlights how different weightings influence model performance and metric interpretation.

FIGURE 7.13: Radar charts compare the performance of three CVAE variants across eight metrics. Each chart, labeled from **a** to **d**, represents a different (α, β) parameter set. The charts feature four polygons: one for each CVAE variant and one for real data metrics. For all metrics except FID, a higher summit indicates better performance. For FID, a higher summit means worse performance.



7.4.4 Class Imbalanced Generation Setup

To unify the evaluation method and ensure fairness, we propose a generation setup that addresses the class imbalance problem in training datasets, relevant to any supervised generative model, including those used for human action recognition. Given that all metrics compare real and generated distributions, it's crucial to ensure fair evaluation. To do this, we match the label distribution of generated samples with that of the training set, preventing the model from over-representing majority classes. When generating more samples than available in the training set, a proportional factor is applied to maintain the original label distribution, ensuring balanced and unbiased sample generation.

7.5 Results and Analysis

To evaluate our models, we use radar charts due to the varying ranges of our metrics, which offers a clearer comparison than simply stating numerical differences. For each (α, β) pair, a radar chart displays four polygons (see Figure 7.13): one for each CVAE variant and one for real samples. Metrics are normalized between 0 and 1 and transformed for comparison, with a summit lower than the real polygon indicating $metric_{gen} < metric_{real}$, except for FID where it indicates $FID_{gen} > FID_{real}$.

Optimal performance is shown by generative model polygons closely matching the real polygon, except for the MMS metric where higher generative values are better.

Figure 7.13 illustrates the difficulty in finding a generative model that excels across all metrics simultaneously. Changes in the backbone architecture or loss parameters can significantly impact metric values. Our experiments with the HumanAct12 dataset reveal that selecting the best model, CConvVAE, is only feasible for a specific set of (α, β) values, as shown in Figure 7.13-d. However, this parameter search is not always practical, making it challenging to identify the best model across all metrics. Therefore, depending on the application, we may need to prioritize specific metrics or even a single metric.

We now present an analysis of the results by comparing three CVAE models on each metric individually. For each metric, we explain what it means for a model to perform best.

- **FID:** In certain (α, β) configurations, Figure 7.13 demonstrates that CConvVAE achieves the lowest FID value, closely approaching FID_{real} . This suggests that CConvVAE generates samples with superior fidelity compared to CGRUVAE and CTransVAE. The model efficiently learns a distribution $\mathcal{P}_{\mathcal{G}}$ that is easier to align with $\mathcal{P}_{\mathcal{R}}$ than the distributions produced by the other models. However, despite having the smallest and most accurate FID, there are cases where the gap between CConvVAE and FID_{real} is still considerable (Figures 7.13-a-b-c).
- **Density:** Just as with the FID metric, for certain (α, β) pairs, CConvVAE produces a Density value that is closer to Density_{real} than the other CVAE variants. This suggests that CConvVAE is more likely to generate samples resembling $\mathcal{P}_{\mathcal{R}}$ than CGRUVAE and CTransVAE. However, even though CConvVAE often comes closest to matching Density_{real} , a notable gap between Density_{gen} and Density_{real} can still be observed in some instances.
- **AOG:** The AOG metric is crucial for evaluating a generative model’s conditional effectiveness. Factors like data scarcity, underfitting, or poor hyperparameters can impact performance. Figure 7.13 shows CConvVAE often leads in this metric, but not always successfully; for instance, in Figure 7.13-f, CConvVAE’s AOG value diverges significantly from AOG_{real} . Meanwhile, CTransVAE and CGRUVAE consistently fail to manage sub-classes across all settings, indicating persistent issues with their conditional mechanisms.
- **APD:** Regarding the APD diversity metric, CConvVAE stands out by consistently achieving values near APD_{real} across various hyperparameter settings, particularly excelling in Figure 7.13-d. However, CGRUVAE also shows strong performance on the APD metric in some configurations. This demonstrates that while CConvVAE may significantly outperform CGRUVAE in one aspect, such as FID, CGRUVAE can still excel in other metrics, highlighting its overall competence.
- **ACPD:** The ACPD metric evaluates diversity per sub-class, while the APD metric assesses overall diversity. Figure 7.13 shows that nearly half the hyperparameter settings have all three CVAE variants outperforming the real data on ACPD, indicating greater sub-class diversity. However, this can result from overfitting, instability, and class imbalance. Excelling in one metric doesn’t imply overall superiority. For example, CGRUVAE outperforms CConvVAE

in ACPD in Figure 7.13-a but has a much higher FID, indicating unreliable results. This highlights the need for multiple evaluation metrics.

- **Coverage:** For most hyperparameter settings, CConvVAE surpasses other CVAE variants in terms of coverage, indicating it generates a greater number of samples that align with the real distribution $\mathcal{P}_{\mathcal{R}}$ compared to CGRUVAE and CTransVAE. However, in Figures 7.13-a-b, CTransVAE outperforms CConvVAE in coverage, showing that despite CConvVAE’s strong APD diversity, it can perform poorly in coverage under certain conditions.

This raises the question: What is the difference between APD and coverage if they both quantify diversity? Both metrics use a latent space and Euclidean Distance, however APD measures the distance between randomly selected pairs to measure the volume of space occupied by $\mathcal{P}_{\mathcal{R}}$ and $\mathcal{P}_{\mathcal{G}}$, independently. Conversely, coverage evaluates the nearest neighbor relationships between real and generated samples to quantify how much of $\mathcal{P}_{\mathcal{R}}$ ’s space is occupied by the generated samples.

- **MMS:** The MMS metric measures diversity by evaluating the novelty of generated samples, ideally with MMS_{gen} values higher but close to MMS_{real} . This metric can be more challenging to interpret. CConvVAE demonstrates the most stable MMS values among the three variants, maintaining a higher yet comparable level to MMS_{real} . In contrast, CTransVAE’s MMS values exceed the radar plot’s limits. This indicates that CConvVAE excels at producing novel human motion sequences.
- **WPD:** The WPD metric assesses temporal diversity by measuring warping and distortions between samples. There are three interpretations for WPD:
 1. $|WPD_{real} - WPD_{gen}| < \epsilon$ (where ϵ is very small): This signifies a perfect replication of all temporal distortions from $\mathcal{P}_{\mathcal{R}}$ to $\mathcal{P}_{\mathcal{G}}$.
 2. $WPD_{gen} \gg \gg WPD_{real}$: This indicates that the generative model has identified and created similar but new temporal distortions.
 3. $WPD_{gen} \ll \ll WPD_{real}$: This implies the model fails to replicate temporal distortions, generating consistent but limited distortions.

Figure 7.13 shows that, apart from CTransVAE in Figure 7.13-d, all WPD values are less than WPD_{real} . This means most models can re-create some temporal distortions, though not all. Notably, in Figure 7.13-d, the minimal gap between WPD_{real} and WPD for CConvVAE and CGRUVAE suggests a near perfect replication of temporal distortions in $\mathcal{P}_{\mathcal{R}}$.

7.6 Conclusion

In this chapter, we provided a comprehensive review of evaluation metrics used to assess the reliability of generative models for human motion generation. Recognizing that human motion data are temporal and represented as multivariate time series, we introduced a novel metric to evaluate diversity in terms of temporal distortion. We proposed a unified evaluation framework, with eight metrics measuring fidelity and diversity, that allows for fair comparisons between different models. Our experiments with three generative model variants on a publicly available dataset demonstrated that no single metric can universally determine model superiority. Instead, a combination of different metrics is often necessary to accurately evaluate model reliability.

Our findings indicate that the CConvVAE model outperforms others on the highest number of metrics, which can give the impression of being the best overall model. However, minor hyper-parameter adjustments can significantly impact its performance across various metrics. This underscores the difficulty of identifying the *best model*, the challenge of finding *The One Metric To Rule Them All*, and highlights the importance of tailoring model selection to specific applications. For instance, in gaming, where generating diverse actions is crucial, diversity metrics are more important than fidelity metrics like FID. Conversely, in medical research, where precise replication of movements is critical, fidelity takes precedence.

Additionally, we offer publicly available, user-friendly code for calculating all the metrics we used, applicable to any generative model with any parameterization. We hope this work serves as a valuable starting point for newcomers to the field of human motion generation and helps establish a clear framework for unified evaluation. However, we acknowledge that the metrics discussed are not exhaustive, as the field is rapidly evolving. It is also important to adapt metrics when labels in the real data are unavailable.

Chapter 8

Reproducible Research

8.1 Introduction

Reproducibility is a fundamental aspect of scientific research, as it ensures that our work can be replicated and adapted by other researchers for their own applications. In this chapter, we underscore the significance of reproducibility in research and outline the measures taken to guarantee that the work presented in this thesis aims to adhere to high standards of reproducibility.

A notable feature of this thesis is that almost all of the contributions have been integrated into an open-source Python package called *aeon* (Middlehurst et al., 2024), for which I am a core developer. This package serves as a centralized repository for the tools and methods developed during this research, ensuring their accessibility and usability for the broader scientific community. By packaging our contributions in this way, we not only promote reproducibility but also encourage the wider use and continuous improvement of our work.

A key aspect of this thesis is that all the work detailed in the previous chapters is supported by publicly available code. This transparency allows other researchers to replicate our experiments, validate our findings, and build upon our work with confidence. By making our code accessible, we contribute to a more open and collaborative scientific community.

In this chapter, we will detail the specific requirements we follow to define good reproducible work. These requirements include clear documentation and adherence to best practices in software development, to the best of our capabilities. We believe that by following these standards and taking feedback from the community, we can continually improve the reproducibility and reliability of our research.

Finally, every program used locally to produce figures or assist in analysis has been made available. While these tools may not be directly associated with any particular paper, they are crucial to the overall research process. We will present these programs in this chapter, highlighting their roles and functionalities.

In summary in this chapter we:

- introduce the *aeon* Python package, which encapsulates the contributions of this thesis.
- highlight the importance of reproducibility in research, by outlining the requirements and practices that define a reproducible work.
- present the local programs used for figure generation and analysis.

By committing to these principles of reproducibility and actively seeking feedback from the community, we aim to enhance the transparency, reliability, and impact of our research.

8.2 Time Series Analysis With *aeon*

The *aeon* Python package is a versatile open-source library developed to facilitate various time series machine learning tasks. It provides tools for classification, clustering, transformations, regression, forecasting, anomaly detection, similarity search and segmentation, making it a comprehensive solution for handling time series data.

aeon is designed with ease of use and extensibility in mind, offering clear documentation and an intuitive interface. As a core developer of this package, the contributions from this thesis have been integrated into *aeon*, ensuring that the methods and tools developed are accessible to the broader scientific community. This section will introduce *aeon*, showcasing its capabilities and demonstrating its application in diverse time series machine learning scenarios.

8.2.1 Deep Learning For Time Series With *Aeon*

My involvement in the *aeon* project began with the task of defining the deep learning framework from the ground up. This framework had to be developed with several key principles in mind: ease of contribution for new developers, clarity of code, straightforward functionality, and comprehensive documentation. Ensuring that new contributors could easily understand and extend the code was paramount. As a result of these efforts, all the models reviewed in the deep learning for TSC (Ismail Fawaz et al., 2019) are now implemented in *aeon* for both classification and regression tasks. Additionally, new models such as InceptionTime (Ismail Fawaz et al., 2020), our own H-InceptionTime (Chapter 3), and LITETime (Chapter 4) have been incorporated, further enhancing the package's capabilities and robustness.

The maintenance of this framework is ongoing and involves several critical activities:

- **Bug Fixes:** Regular updates are made to identify and resolve bugs promptly, ensuring the stability and reliability of the framework.
- **Documentation Improvement:** Continuous efforts are made to enhance the documentation, making it clearer and more comprehensive for users and contributors.
- **Feature Enhancement:** New features and capabilities are regularly added to the framework, expanding its functionality and keeping it at the forefront of time series machine learning research.
- **Unit Testing:** Rigorous unit testing is conducted to ensure the code remains robust and compatible with updates to *tensorflow* (Abadi et al., 2015) and *keras* (Chollet et al., 2015). This testing helps maintain the integrity and performance of the framework as the underlying libraries evolve.

By committing to these maintenance activities, we ensure that the *aeon* package remains a valuable and reliable tool for the scientific community.

Recently, I started working on the deep learning for time series clustering module in *aeon*, building upon the foundational work established in the original review (Lafabregue et al., 2022). This module is still under development, aiming to provide robust and efficient tools for clustering time series data using deep learning techniques. So far, I have included two original models from the review into the module, Auto-Encoder based deep learning models with FCN and ResNet backbone networks, laying the groundwork for further expansion. In addition, I have been actively involved

in mentoring a Google Summer of Code internship ¹, guiding the intern to enhance and develop more models for this module. This collaborative effort aims to accelerate the development process and ensure the inclusion of state-of-the-art deep clustering models in *aeon*.

The upcoming work in deep learning within the *aeon* package includes developing modules for time series anomaly detection (Schmidl, Wenig, and Papenbrock, 2022), averaging (Terefe et al., 2020), and domain adaptation (Fawaz et al., 2023). These enhancements will broaden *aeon*'s capabilities, enabling it to tackle a wider range of time series challenges and better serve the research community.

8.2.2 Other Tasks With *Aeon*

My involvement with the *aeon* project extends beyond deep learning. In the distances module, I contributed to and continue to maintain the ShapeDTW similarity measure (Zhao and Itti, 2018), which is integral to my development of the ShapeDBA (Chapter 6) method in the averaging module. Additionally, I significantly optimized the runtime complexity of the PAA (Keogh et al., 2001) and SAX (Lin et al., 2007) representation codes, making them much faster and more efficient. Beyond code contributions, I have also been actively involved in improving general documentation, creating example notebooks, and co-authoring the open-source software paper citeaeon with the rest of the core developers.

We believe that these efforts collectively enhance reproducibility within the research community, making tools more accessible and reliable for all users.

8.3 What Makes A Work Reproducible ?

Reproducibility is crucial in scientific research, enabling others to verify and build upon previous work. In this section, I will outline the key requirements we followed to ensure our research is reproducible. A reproducible codebase must be well-documented, extendable, easily modifiable, and well-architected. These practices cover technical aspects like code development and data management, as well as broader principles like clear documentation and transparency. By adhering to these standards, we aim to make our research both rigorous and accessible.

8.3.1 Code Documentation

While providing a GitHub repository might seem sufficient for ensuring code reproducibility, it is crucial to provide clear instructions for users who wish to re-run the experiments associated with the paper.

8.3.1.1 Dependencies

A key component of code documentation is a complete list of dependencies that the paper's code relies on is essential. Without this list, a new user would need to manually inspect all the code files to determine which dependencies are required, and in some cases, they might also need to identify the specific versions, especially if the code relies on older versions of these dependencies.

For this reason, we ensured that every project published during this thesis included a complete list of dependencies, thereby supporting better open-source reproducible research.

¹<https://summerofcode.withgoogle.com/programs/2024/projects/Hvd0DfkD>

8.3.1.2 Adapting Configuration To The User’s Side

Often, users may need to make minor adjustments to the code in order to successfully re-run it. This does not diminish the code’s reproducibility, but it does make it essential for the repository to include a detailed, step-by-step guide. Such a guide should specify which variables need to be modified, where to make these changes, and how to do so. These variables might include the root directory for datasets. Some instructions can be for downloading datasets from a provided link etc.

Providing this information in the code’s documentation is crucial; without it, users may encounter errors that prevent the code from running properly.

8.3.2 Extensibility

Ensuring that code is easily executable by others is a crucial first step towards creating a reproducible repository. However, research often involves incremental contributions, which means the original work must be designed to be extendable. For example, consider the deep learning for TSC review by (Ismail Fawaz et al., 2019), if a researcher wanted to add new models or datasets on top of this work, it should be easily achievable. If the code is not designed to allow such modifications, it cannot be considered truly extendable or modifiable.

8.3.3 Code Architecture

When the code from a research paper is intended to be studied by students, employees, or other researchers, it is essential that the code be well architected. A poorly structured codebase makes it difficult, if not impossible, for others to understand and build upon the work. Clear and thoughtful architecture is fundamental for ensuring that the techniques, algorithms, and overall project can be effectively comprehended and utilized by others.

1. **Variable naming:** One critical element of well-architected code is the use of meaningful variable names. For instance, vague or arbitrary names like “ $X = Y + Z.dot(alpha_xyz)$ ” should be avoided. Instead, variables should be named descriptively, especially when they represent parameters or concepts from the paper’s algorithm. For example, if the method includes a parameter for the number of filters, the code should use a name like “ $n_filters$ ” rather than something ambiguous like “ f ”.
2. **File management:** Proposing a repository where a single file contains over 10 000 lines of code is simply unacceptable. Code should be organized in a way that allows users to easily locate specific functionalities. For example, if the project includes multiple classifiers and normalization functions, each classifier should be placed in its own file within a dedicated sub-folder, while all normalization functions could be grouped together in a separate file, as these are typically concise. The choice of file management structure doesn’t follow a rule of thumb; it should be tailored to the specific needs of the project.
3. **Code Structure:** While there is no one-size-fits-all approach to file management, the choice of code structure often follows certain best practices. For instance, if the code does not require defining objects with multiple functionalities, using only functions is sufficient, and introducing classes would be unnecessary. Conversely, if the code benefits from encapsulating behavior within objects, then using classes is more appropriate. Furthermore, if several classes

share common code, it's not good practice to copy and paste these functionalities across different classes. Instead, defining a base class that these classes can inherit from is a better approach. This also applies when working with abstract methods, class methods, and similar concepts.

8.3.4 How To Check For All These Requirements

When serving as the main developer of a project, it's often not ideal to be the one assessing whether all the necessary requirements for reproducibility and code quality are met. This is due to inherent human bias, as developers tend to view their own projects as being in an optimal state. To mitigate this bias, a better practice is to seek feedback from a fellow researcher, student, PhD candidate or a thesis supervisor. For example, you could ask one of these peers to try adding new functions to your code and provide feedback on how easily your code can be extended.

8.4 Hardware Utilization and Accessible Code Repositories

Throughout this thesis, I utilized a diverse set of hardware to support the computational demands of deep learning models, including a GTX1080ti with 8GB of VRAM, an RTX3090 with 24GB of VRAM, an RTX4090 with 24GB of VRAM, and the Mesocentre High Performance Computing Center of the University of Strasbourg. Initially, setting up the GPUs involved manually configuring the necessary CUDA tools, which required significant time and effort to ensure compatibility and performance. However, as the work progressed, I transitioned to using Docker containers, which provided several advantages, including simplified environment management, enhanced portability, and the ability to encapsulate all dependencies within a container. This ensured that the code ran consistently across different machines and facilitated easier scaling and deployment.

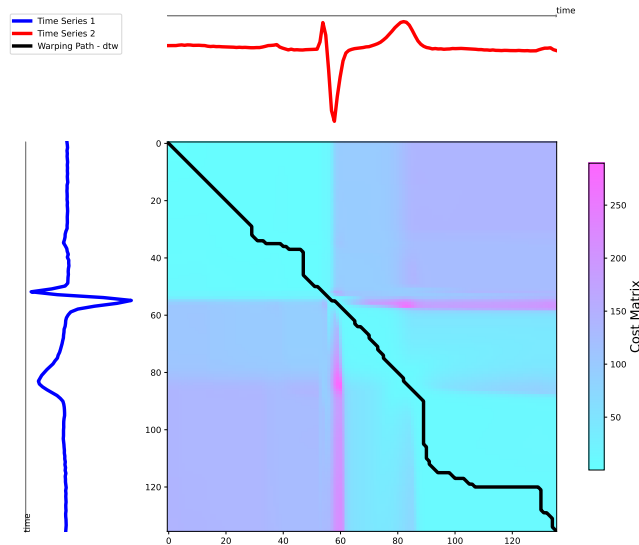
For each published article, I ensured that the community has access to all source codes and resources necessary to reproduce the work, as outlined previously in Table 1. The provided Dockerfiles encapsulate the code and configure the environment for seamless GPU integration, allowing users to execute the code efficiently with just two to three commands, leveraging GPU acceleration without the need for complex manual configurations. Additionally, all codes were developed following the guidelines outlined in the previous section, ensuring consistency, reliability, and ease of use for others in the community.

8.5 Published Work Serving For Analysis And Reproducibility

A central goal of this thesis has been to ensure that all tools used in our analysis are accessible to the broader community. By making these resources available, we enhance the community's ability to understand, replicate, and build upon our work, thereby increasing its impact and clarity for future readers.

We accomplished this through two main strategies: first, by publishing public repositories that contain the code used to generate visualizations and support our research analysis; and second, by creating web pages featuring interactive tools that go beyond what can be presented in a paper or GitHub repository. These efforts aim

FIGURE 8.1: Warping path example between two time series from the ECGFiveDays dataset.



to deepen the community’s understanding and facilitate wider engagement with our research.

8.5.1 Elastic Warping Visualization

A fundamental approach to analyzing time series data involves assessing how sensitive the samples are to temporal distortions. While there are various methods to achieve this, the most effective way is often through direct visualization. To facilitate this, we developed a public GitHub repository (Ismail-Fawaz et al., 2024b) available here: https://github.com/MSD-IRIMAS/Elastic_Warping_Vis. This repository allows users to visualize the warping path and temporal distortions between any two time series samples, with outputs available in either PDF format, as shown in Figure 8.1, or as MP4 format ².

The code leverages the *aeon* Python package for computing the warping path and distance matrix, and uses *matplotlib* for visualization (Hunter, 2007). Users can apply any of the distance functions implemented in *aeon* ³.

The repository not only meets all the requirements discussed in Section 8.3 for public availability on GitHub but is also conveniently installable via PyPi ⁴.

8.5.2 Convolutional Filter Space Visualization

Training a CNN often requires post-training analysis of the convolutional filter space. For example, in Chapter 3 this type of analysis was conducted to ensure that the model was not relearning hand-crafted filters, as illustrated in Figure 3.11. After publishing this work, we developed a GitHub repository that provides code to generate similar figures for any pre-trained model. This tool ⁵ produces visualizations in both PDF format, like Figure 3.11 and in a web-friendly format using *bokeh* (Bokeh

²https://github.com/MSD-IRIMAS/Elastic_Warping_Vis/blob/main/exps/dtw-vis/ECGFiveDays/dtw.mp4

³https://www.aeon-toolkit.org/en/stable/api_reference/distances.html

⁴<https://pypi.org/>

⁵https://github.com/MSD-IRIMAS/filter1D_visualization

Development Team, 2018), a visualization tool for web interfaces ⁶. This resource will assist researchers in better analyzing the convolutional filter space when working with CNNs.

8.5.3 Augmenting Time Series Classification Datasets With Elastic Averaging

Since the publication of (Forestier et al., 2017), research on data augmentation for time series data has seen a significant increase in both quantity and diversity. The work in (Forestier et al., 2017) focuses on using weighted elastic averaging, specifically DBA (Petitjean, Ketterlin, and Gançarski, 2011), for data augmentation to enhance the performance of TSC models. Although the original implementation was written in Java, the method continues to attract attention and further development. In response, we proposed an open-source Python implementation of this approach (Ismail-Fawaz et al., 2024h) ⁷, utilizing the *aeon* (Middlehurst et al., 2024) library as the backend for similarity and averaging computations. Our code adheres to open-source standards and offers flexibility, allowing users to parameterize the augmentation function with any similarity measure they choose.

8.5.4 KAN It Work For Time Series Classification ?

Following the publication of a new approach to neural networks using Kolmogorov-Arnold Networks (KANs) (Liu et al., 2024), which are designed to effectively model complex relationships within tabular data by leveraging the Kolmogorov-Arnold representation theorem, we were interested in testing their applicability to time series data. Given their success with tabular data, we proposed a method that involves extracting Catch22 (Lubba et al., 2019) features from time series data before feeding them into the KAN model for classification tasks. Our goal was to provide an open-source repository (Ismail-Fawaz et al., 2024d) ⁸ for this work, encouraging the time series community to engage with KAN models and fostering continued research and innovation in this area.

8.5.5 Published Webpages With Associated Papers

Developing webpages can be essential when visualizations, such as videos or interactive tools, cannot be effectively presented in a paper. For the hand-crafted convolution filters contribution, we created a webpage ⁹ featuring an interactive tool, utilizing the code discussed in Section 8.5.2. Similarly, for the ShapeDBA paper, we developed a webpage ¹⁰ showcasing video visualizations of the ShapeDTW alignment, highlighting the differences between DBA and ShapeDBA in terms of the underlying similarity measure.

8.5.6 Deep Learning For Time Series Classification: A Webpage

Since the publication of the deep learning for TSC review (Ismail Fawaz et al., 2019), the research community has shown significant interest in this domain. However, with the increasing number of models, some of which are introduced in this

⁶https://maxime-devanne.com/pages/filter1D_visualization/

⁷<https://github.com/MSD-IRIMAS/Augmenting-TSC-Elastic-Averaging>

⁸<https://github.com/MSD-IRIMAS/Simple-KAN-4-Time-Series>

⁹<https://msd-irimas.github.io/pages/HCCF-4-tsc/>

¹⁰<https://msd-irimas.github.io/pages/ShapeDBA/>

thesis, revisiting the review with another paper wasn't ideal. Instead, we developed a webpage ¹¹ that features a detailed overview of each model from the 2019 review, along with newer models. This includes information on the number of parameters, FLOPS, and links to the original papers. The webpage also features a CD diagram ¹² and an MCM from Chapter 2 to present the results across the UCR archive (Dau et al., 2019).

Additionally, we created *bokeh* (Bokeh Development Team, 2018) based 1v1 scatter plots, allowing users to compare models of their choice. Furthermore, we included an interactive *bokeh* plot to showcase the average performance of all models concerning their FLOPS and parameter counts across all UCR archive datasets. Users can also select specific datasets instead of viewing the average performance.

We believe that this webpage, with ongoing maintenance, will provide the research community with easy access to comprehensive details, results, and comparisons needed for deep learning in the TSC task.

8.6 Conclusion

In this chapter, we emphasized the critical role of reproducibility in scientific research, particularly within the context of time series analysis and deep learning. Ensuring that research is transparent and replicable allows others to confidently build upon existing work. To this end, we have meticulously documented our code and methodologies, providing clear instructions providing clear instructions that facilitate accurate reproduction of our experiments. Additionally, we have focused on creating a well-structured and organized codebase, adhering to best practices in software engineering. This approach not only ensures the code's functionality but also makes it easier for other researchers to extend and adapt our work.

Moreover, we have made significant efforts to share the tools and resources developed during this thesis with the broader research community. By publishing our work on GitHub and integrating it into the *aeon* Python package, we have made these resources widely accessible, fostering a collaborative environment for further innovation. The development of interactive web tools further enhances the accessibility and understanding of our work, allowing users to explore complex data and results dynamically. Through these efforts, we aim to contribute to a culture of reproducibility in research, ensuring that our work serves as a reliable foundation for future advancements in time series analysis.

¹¹<https://msd-irimas.github.io/pages/dl4tsc/>

¹²<https://github.com/hfawaz/cd-diagram>

Conclusion and future works

Overview Of Contributions

The work presented in this thesis brings significant progress to the field of time series analysis, particularly in areas concerning supervised and unsupervised learning, benchmarking machine learning models, foundation models for time series classification, generative models and model complexity reduction. Through comprehensive experimentation and rigorous evaluation, the thesis has developed and demonstrated several novel methodologies for addressing some of the most challenging aspects of time series data, such as high-dimensionality, multivariate dependencies, and limited labeled data.

Chapter 1 lays the groundwork for the research, providing an extensive review of the state-of-the-art techniques for time series analysis. It introduces both supervised and unsupervised learning methods, including Time Series Classification and Extrinsic Regression. In addition, the chapter discusses self-supervised learning techniques, paving the way for the novel approaches later introduced in the thesis. This chapter serves as an essential foundation, offering insight into existing challenges and the research landscape in deep learning for time series analysis.

A central contribution of this thesis is the introduction of more refined tools for model benchmarking in time series analysis especially discriminative models. Chapter 2 critiques traditional methods like the Critical Difference Diagram (CDD) (Demšar, 2006), which suffers from instabilities and overlooks the magnitude of performance differences. The Multiple Comparison Matrix (MCM) is introduced as an alternative, offering more reliable comparisons across datasets, addressing weaknesses in existing statistical tests. This new method improves the precision of model evaluation and provides clearer insights into relative model performance.

In Chapter 3, the search for foundational models that can generalize across time series data is explored. A key contribution here is the development of pre-trained models capable of adapting to various classification tasks. This includes PHIT (Pre-trained H-InceptionTime), which shows significant improvements in performance when compared to non-pre-trained models across a large number of time series datasets. By establishing a foundation for transfer learning in time series, this chapter paves the way for future applications of foundational models. These models leverages a second key contribution introduced in this chapter, the hand-crafted convolution filters that help generalization of the deep learning models by offering prior non-trainable filters to detect specific patterns in the time series. Extensive experiments on the UCR archive (Dau et al., 2019) highlights how our proposed domain foundation models outperforms classical baseline deep learning techniques with no pre-training.

Chapter 4 presents the LITE and LITEMV models, showing significant advancements in reducing the computational complexity of deep learning models for Time Series Classification. LITE offers a simplified architecture based on Inception (Ismail Fawaz et al., 2020), reducing the number of parameters while maintaining competitive performance. Additionally, LITEMV adapts this architecture for multivariate time series, incorporating DepthWise Convolutions (Howard et al., 2017) to handle

data from multiple channels more efficiently. These models represent a major step toward making deep learning more accessible in resource-constrained environments. Experiments on both the UCR archive (univariate) (Dau et al., 2019) and the UEA archive (multivariate) (Bagnall et al., 2018) demonstrate that smaller models can be just as effective as complex ones. This is achieved with only a few boosting techniques to address the trade off between model complexity and performance.

Building on the challenges of acquiring labeled data, Chapter 5 introduces TRILITE, a self-supervised model using triplet loss (Franceschi, Dieuleveut, and Jaggi, 2019) to learn representations from unlabeled time series data. This model excels in situations where labeled data is scarce, offering a solution for improving classifier performance in both supervised and semi-supervised scenarios. The use of data augmentation adapted to time series enhances its ability to learn meaningful patterns. This work opens up new possibilities for applying self-supervised learning techniques to time series tasks beyond classification. Extensive experiments on the UCR archive showcase the performance of TRILITE in two cases, where the dataset lacks a lot labeled samples, and when the datasets lacks a lot of samples even if they are labeled.

In order to highlight the practical relevance of the theoretical contributions made in this thesis, we explored their application in a real-world context, such as human motion analysis. Hence Chapter 6 focuses on the analysis of human movement using time series data captured by Kinect cameras (Asteriadis et al., 2013). The model LITEMVTime, introduced earlier, is applied to classify the quality of human movements in rehabilitation contexts. Using datasets such as Kimore (Capecci et al., 2019), the model provides accurate assessments of patient movements, outperforming other deep learning architectures. Additionally, the chapter introduces generation pipelines for generating realistic human motion sequences, including a prototyping method through a novel approach we proposed called ShapeDBA and a CNN-based deep Supervised Variational Autoencoder (SVAE). Both models, capable of generating high-fidelity and diverse human motion sequences, are particularly beneficial for applications in the medical and entertainment domains. This generation capability opens the door for further exploration in areas like real-time motion generation in gaming and rehabilitation contexts.

In Chapter 7, we revisit the topic of evaluation introduced in Chapter 2, but with a specific focus on evaluating generative models. The challenges of evaluating generative models for human motion are addressed. A new metric, Warping Path Diversity (WPD), is introduced to account for temporal distortions in generated sequences, complementing traditional metrics like Fréchet Inception Distance (FID) (Heusel et al., 2017). This unified evaluation framework helps in assessing both the fidelity and diversity of generated human movements. These metrics are essential for applications like video games and medical simulations, where realism and variability are crucial.

Chapter 8 highlights the importance of reproducibility in machine learning research. A significant contribution here is the development of the open-source *aeon* package (Middlehurst et al., 2024), which integrates the models and methodologies presented throughout the thesis. This package, available to the research community, ensures that experiments are reproducible and that tools developed can be widely used and extended. By providing detailed documentation and modular code, this thesis promotes transparency and collaboration in time series research.

While the contributions of this research have provided strong foundations for time series classification and analysis, several areas remain ripe for future exploration. In the following section we discuss some of the future perspectives for the advancements in this field.

Discussion Of Future Works

While the benchmarking contributions have provided a more comprehensive way to evaluate models, the introduction of more sophisticated statistical tools could refine these comparisons further. As models become increasingly complex, it will be essential to develop new methods for evaluating not just their performance, but also their scalability, robustness, and interpretability. Developing tools that combine the insights from MCM with other multi-objective optimization techniques might provide more holistic evaluation metrics.

While this thesis has laid the groundwork for foundation models in time series classification tasks, future work could explore extending these models to time series forecasting. Forecasting presents unique challenges, such as the need to predict future data points based on past observations, which requires models to capture long-term dependencies effectively. Future research could investigate how pre-trained foundation models, like PHIT, can be adapted to handle time series forecasting (**forecasting-foundatio**), potentially incorporating attention mechanisms to focus on relevant parts of the data (Goswami et al., 2024). Another area of interest would be transfer learning techniques for forecasting tasks (Ehrig, Cleophas, and Forestier, 2024), enabling models trained on one domain to generalize effectively to another, such as transitioning from medical time series data to financial market predictions. This extension would significantly broaden the applicability of foundation models in real-world scenarios.

An additional key area of future work is the development of lightweight and efficient models like LITE and LITEMV. These models have demonstrated great promise in low-resource environments, but more research is needed to optimize them for even larger and more complex datasets. Additionally, extending these models to other domains such as real-time streaming data or applications in Internet of Things (IoT) (Azar et al., 2020) systems could unlock further potential.

Another potential direction is the extension of TRILITE and similar self-supervised models to other types of time series tasks beyond classification. Future research could explore how these models might be adapted for tasks such as time series forecasting (Park et al., 2024), anomaly detection (Darban et al., 2025), or even generative tasks. Moreover, there is considerable room to improve the data augmentation techniques used in triplet loss frameworks to further enhance their robustness in diverse scenarios (Foumani et al., 2024b).

The generative models introduced in this thesis, particularly for human motion generation, have shown promise in generating realistic motion sequences. However, future work could focus on improving the temporal diversity of these generated motions. Current models can generate high-quality movements but may lack variability in timing and execution styles. Incorporating techniques such as adversarial training or variational approaches could enhance the diversity of generated motions, making them more useful for applications like virtual reality, gaming, and medical simulations. Furthermore, exploring multimodal data inputs, such as combining visual data with motion sensor data, could improve the robustness of generated sequences, allowing models to better mimic real-world human movements. This would broaden the scope of applications for human motion data generation, particularly in scenarios where subtle variations in motion are crucial, such as in rehabilitation exercises or fine motor skill training. Regarding the Warping Path Diversity, it takes into consideration DTW based warping distortions, however exploring the disentanglement of shape and temporal patterns (Marteau, 2019a) could improve upon traditional DTW, enabling a more detailed and nuanced analysis of time series variability.

Moreover, the *aeon* package’s continued development (Middlehurst et al., 2024) should focus on incorporating more advanced deep learning architectures, as well as improving the ease with which users can contribute and extend the framework. Incorporating more interactive visualization tools that allow researchers to explore model outputs and hyper-parameters could enhance the usability of the package.

Finally, deep learning for Time Series Extrinsic Regression (Tan et al., 2020) remains an unfinished area of research, largely because most existing models are adaptations of architectures originally designed for classification tasks. While classification tasks aim to categorize time series data into discrete classes (Bagnall et al., 2017), extrinsic regression deals with predicting continuous values, which often requires handling more nuanced relationships in the data. The current approach involves repurposing classification models (Mohammadi Foumani et al., 2024), such as convolutional or recurrent networks, to perform regression by simply changing the final layer to output continuous values. However, this overlooks the fundamental differences between the tasks, especially in terms of loss functions and evaluation metrics. No models have been specifically designed with the unique challenges of extrinsic regression in mind, such as effectively capturing long-range dependencies and handling variability in the magnitude of predictions. A dedicated architecture tailored for regression tasks, which could leverage techniques like dynamic temporal scaling or specific optimization for continuous outputs, would be a crucial step forward in making deep learning models more effective for time series extrinsic regression. This gap presents an opportunity for future research to innovate and address the complexities that are unique to regression in time series data.

These directions point to a broad set of possibilities that build upon the foundation laid by this thesis. By continuing to focus on model efficiency, self-supervised learning, benchmarking, and reproducibility, the field of time series analysis will be well-positioned to address both current and future challenges.

Financing

The DELEGATION project, "DEep LEarning for Generating humAn moTION," is focused on developing a sophisticated deep learning framework for generating expressive, skeleton-based human motions. This system addresses complex challenges in motion analysis, such as noise and variability in human movement data, and aims to create realistic, controllable motion sequences. Its applications span areas like physical rehabilitation, where accurate motion representation is essential.

This thesis is funded under the DELEGATION project, which is supported by the Agence Nationale de la Recherche (ANR) under grant number ANR-21-CE23-0014. The financial support from ANR facilitates in-depth research into cutting-edge techniques in human motion generation and analysis, allowing for significant contributions to this emerging field.

In addition to its innovative goals, the DELEGATION project involves a strong collaboration between several key partners. The project is coordinated by Dr. Maxime Devanne from the Institut de Recherche en Informatique, Mathématiques, Automatique et Signal (IRIMAS) at Université de Haute-Alsace in Mulhouse, France, alongside Prof. Germain Forestier and Dr. Jonathan Weber. Other partners include the Media Integration and Communication Center (MICC) at University of Florence in Italy, led by Dr. Stefano Berretti as the local PI, the CHRU of Brest, France, with Prof. Olivier Remy-Neris as the local PI, and the Centre de Réadaptation de Mulhouse (CRM) in Mulhouse, France, with Fabienne Ernst Kuteifan as the local PI.

A portion of the DELEGATION grant was dedicated to facilitating an academic visit to Dr. Stefano Berretti at the Media Integration and Communication Center (MICC) in Florence, Italy. I had the opportunity to spend two weeks there in June 2024, where I gained valuable expertise and discussed with other PhD students involved in similar projects. The visit was highly beneficial, fostering new ideas and approaches that enriched my research, while strengthening international collaboration within the project's framework.

Bibliography

- Abadi, Martín et al. (2015). *TensorFlow: Large-scale machine learning on heterogeneous systems* (cit. on pp. [122](#), [130](#), [154](#), [201](#), [208](#)).
- Aliakbarian, Sadegh et al. (2021). “Contextually plausible and diverse 3d human motion prediction”. In: *Proceedings of the IEEE/CVF International Conference on Computer Vision*, pp. 11333–11342 (cit. on p. [174](#)).
- Anghinoni, Leandro et al. (2019). “Time series trend detection and forecasting using complex network topology analysis”. In: *Neural Networks* 117, pp. 295–306 (cit. on p. [19](#)).
- Asteriadis, Stylianos et al. (2013). “Estimating human motion from multiple kinect sensors”. In: *Int. Conf. on Computer Vision/Computer Graphics Collaboration Techniques and Applications*, pp. 1–6 (cit. on pp. [11](#), [149](#), [152](#), [174](#), [216](#)).
- Azar, Joseph et al. (2020). “Robust IoT time series classification with data compression and deep learning”. In: *Neurocomputing* 398, pp. 222–234 (cit. on p. [217](#)).
- Bagnall, Anthony et al. (2015). “Time-series classification with COTE: the collective of transformation-based ensembles”. In: *IEEE Transactions on Knowledge and Data Engineering* 27.9, pp. 2522–2535 (cit. on p. [40](#)).
- Bagnall, Anthony et al. (2017). “The great time series classification bake off: a review and experimental evaluation of recent algorithmic advances”. In: *Data mining and knowledge discovery* 31, pp. 606–660 (cit. on pp. [22](#), [28](#), [218](#)).
- Bagnall, Anthony et al. (2018). “The UEA multivariate time series classification archive, 2018”. In: *arXiv preprint arXiv:1811.00075* (cit. on pp. [9](#), [24](#), [28](#), [35](#), [40](#), [50](#), [56](#), [120](#), [130](#), [185](#), [216](#)).
- Bagnall, Anthony et al. (2020). “On the usage and performance of the hierarchical vote collective of transformation-based ensembles version 1.0 (hive-cote v1. 0)”. In: *Advanced Analytics and Learning on Temporal Data: 5th ECML PKDD Workshop, AALTD 2020, Ghent, Belgium, September 18, 2020, Revised Selected Papers 6*. Springer, pp. 3–18 (cit. on p. [40](#)).
- Bahdanau, Dzmitry, Kyunghyun Cho, and Yoshua Bengio (2014). “Neural machine translation by jointly learning to align and translate”. In: *arXiv preprint arXiv:1409.0473* (cit. on p. [47](#)).
- Benavoli, Alessio, Giorgio Corani, and Francesca Mangili (2016). “Should we really use post-hoc tests based on mean-ranks?” In: *The Journal of Machine Learning Research* 17.1, pp. 152–161 (cit. on pp. [4](#), [77](#), [79](#), [80](#), [101](#)).
- Benavoli, Alessio et al. (2017). “Time for a change: a tutorial for comparing multiple classifiers through Bayesian analysis”. In: *Journal of Machine Learning Research* 18.77, pp. 1–36 (cit. on pp. [77](#), [84–88](#)).
- Berrar, Daniel (2022). “Using p-values for the comparison of classifiers: pitfalls and alternatives”. In: *Data Mining and Knowledge Discovery* 36.3, pp. 1102–1139 (cit. on pp. [77](#), [84](#), [85](#)).
- Bertalaníč, Blaž, Marko Meža, and Carolina Fortuna (2022). “Resource-aware time series imaging classification for wireless link layer anomalies”. In: *IEEE Transactions on Neural Networks and Learning Systems* (cit. on p. [28](#)).

- Bogdan, Victor, Cosmin Bonchiş, and Ciprian Orhei (2019). “Custom extended sobel filters”. In: *arXiv preprint arXiv:1910.00138* (cit. on pp. 6, 95).
- Bokeh Development Team (2018). *Bokeh: Python library for interactive visualization*. <https://bokeh.pydata.org/en/latest/> (cit. on pp. 212, 214).
- Breiman, Leo (2001). “Random forests”. In: *Machine learning* 45, pp. 5–32 (cit. on pp. 33, 38).
- Bromley, Jane et al. (1993). “Signature verification using a " siamese " time delay neural network”. In: *Advances in neural information processing systems* 6 (cit. on p. 72).
- Cai, Haoye et al. (2018). “Deep video generation, prediction and completion of human action sequences”. In: *Proceedings of the European conference on computer vision (ECCV)*, pp. 366–382 (cit. on p. 173).
- Cao, Zhe et al. (2020). “Long-term human motion prediction with scene context”. In: *Computer Vision—ECCV 2020: 16th European Conference, Glasgow, UK, August 23–28, 2020, Proceedings, Part I 16*. Springer, pp. 387–404 (cit. on p. 172).
- Capecchi, Marianna et al. (2018). “A Hidden Semi-Markov Model based approach for rehabilitation exercise assessment”. In: *Journal of biomedical informatics* 78, pp. 1–11 (cit. on p. 171).
- Capecchi, Marianna et al. (2019). “The kimore dataset: Kinematic assessment of movement and clinical scores for remote monitoring of physical rehabilitation”. In: *IEEE Transactions on Neural Systems and Rehabilitation Engineering* 27.7, pp. 1436–1448 (cit. on pp. 11, 12, 19, 24, 149, 151–153, 157, 164, 165, 167, 216).
- Cervantes, Pablo et al. (2022). “Implicit neural representations for variable length human motion generation”. In: *European Conference on Computer Vision*. Springer, pp. 356–372 (cit. on p. 196).
- Chen, Ting et al. (2020). “A simple framework for contrastive learning of visual representations”. In: *International conference on machine learning*. PMLR, pp. 1597–1607 (cit. on p. 72).
- Cho, Kyunghyun et al. (2014). “Learning phrase representations using RNN encoder-decoder for statistical machine translation”. In: *arXiv preprint arXiv:1406.1078* (cit. on pp. 48, 49).
- Chollet, François et al. (2015). *Keras*. <https://keras.io> (cit. on p. 208).
- Chollet, Francois (2021). *Deep learning with Python*. Simon and Schuster (cit. on p. 112).
- Christ, Maximilian, Andreas W Kempa-Liehr, and Michael Feindt (2016). “Distributed and parallel time series feature extraction for industrial big data applications”. In: *arXiv preprint arXiv:1610.07717* (cit. on p. 33).
- Christ, Maximilian et al. (2018). “Time series feature extraction on basis of scalable hypothesis tests (tsfresh—a python package)”. In: *Neurocomputing* 307, pp. 72–77 (cit. on pp. 33, 57).
- Courty, Benoit et al. (May 2024). *mlco2/codecarbon: v2.4.1*. Version v2.4.1. DOI: 10.5281/zenodo.11171501. URL: <https://doi.org/10.5281/zenodo.11171501> (cit. on pp. 122, 124).
- Cuturi, Marco and Mathieu Blondel (2017). “Soft-dtw: a differentiable loss function for time-series”. In: *International conference on machine learning*. PMLR, pp. 894–903 (cit. on pp. 31, 63, 64, 158, 161).
- Cuturi, Marco et al. (2007). “A kernel for time series based on global alignments”. In: *2007 IEEE International Conference on Acoustics, Speech and Signal Processing-ICASSP'07*. Vol. 2. IEEE, pp. II–413 (cit. on p. 28).
- Darban, Zahra Zamanzadeh et al. (2025). “CARLA: Self-supervised contrastive representation learning for time series anomaly detection”. In: *Pattern Recognition* 157, p. 110874 (cit. on p. 217).

- Dau, Hoang Anh et al. (2019). “The UCR time series archive”. In: *IEEE/CAA Journal of Automatica Sinica* 6.6, pp. 1293–1305 (cit. on pp. 4, 7, 9, 10, 24, 28, 30, 33, 35, 36, 39, 40, 50, 59, 78, 88, 90, 97, 99, 100, 106, 108, 116, 120, 122–124, 127, 129, 139, 141, 158, 159, 161, 164, 185, 214–216).
- Dempster, Angus, François Petitjean, and Geoffrey I Webb (2020). “ROCKET: exceptionally fast and accurate time series classification using random convolutional kernels”. In: *Data Mining and Knowledge Discovery* 34.5, pp. 1454–1495 (cit. on pp. 9, 22, 34–36, 57, 88).
- Dempster, Angus, Daniel F Schmidt, and Geoffrey I Webb (2021). “Minirocket: A very fast (almost) deterministic transform for time series classification”. In: *Proceedings of the 27th ACM SIGKDD conference on knowledge discovery & data mining*, pp. 248–257 (cit. on p. 35).
- (2023a). “Hydra: Competing convolutional kernels for fast and accurate time series classification”. In: *Data Mining and Knowledge Discovery* 37.5, pp. 1779–1805 (cit. on p. 36).
- (2023b). “QUANT: A Minimalist Interval Method for Time Series Classification”. In: *arXiv preprint arXiv:2308.00928* (cit. on p. 39).
- Demšar, Janez (2006). “Statistical comparisons of classifiers over multiple data sets”. In: *The Journal of Machine learning research* 7, pp. 1–30 (cit. on pp. 4, 77, 78, 85, 215).
- Deng, Houtao et al. (2013). “A time series forest for classification and feature extraction”. In: *Information Sciences* 239, pp. 142–153 (cit. on pp. 38, 39).
- Deng, Jia et al. (2009). “Imagenet: A large-scale hierarchical image database”. In: *2009 IEEE conference on computer vision and pattern recognition*. Ieee, pp. 248–255 (cit. on p. 51).
- Devanne, Maxime et al. (2014). “3-d human action recognition by shape analysis of motion trajectories on riemannian manifold”. In: *IEEE transactions on cybernetics* 45.7, pp. 1340–1352 (cit. on pp. 11, 19, 21, 28, 149).
- Dosovitskiy, Alexey et al. (2020). “An image is worth 16x16 words: Transformers for image recognition at scale”. In: *arXiv preprint arXiv:2010.11929* (cit. on p. 174).
- Dowson, DC and BV666017 Landau (1982). “The Fréchet distance between multivariate normal distributions”. In: *Journal of multivariate analysis* 12.3, pp. 450–455 (cit. on p. 188).
- Ehrig, Claudia, Catherine Cleophas, and Germain Forestier (2024). “The impact of data set similarity and diversity on transfer learning success in time series forecasting”. In: *arXiv preprint arXiv:2404.06198* (cit. on p. 217).
- Elman, Jeffrey L (1990). “Finding structure in time”. In: *Cognitive science* 14.2, pp. 179–211 (cit. on p. 48).
- Evin, Inan, Perttu Hämäläinen, and Christian Guckelsberger (2022). “Cine-AI: Generating video game cutscenes in the style of human directors”. In: *Proceedings of the ACM on Human-Computer Interaction* 6.CHI PLAY, pp. 1–23 (cit. on p. 172).
- Fawaz, Hassan Ismail et al. (2018). “Transfer learning for time series classification”. In: *2018 IEEE international conference on big data (Big Data)*. IEEE, pp. 1367–1376 (cit. on p. 107).
- (2019). “Deep neural network ensembles for time series classification”. In: *2019 International Joint Conference on Neural Networks (IJCNN)*. IEEE, pp. 1–6 (cit. on p. 53).
- Fawaz, Hassan Ismail et al. (2023). “Deep Unsupervised Domain Adaptation for Time Series Classification: a Benchmark”. In: *arXiv preprint arXiv:2312.09857* (cit. on p. 209).

- Flynn, Michael, James Large, and Tony Bagnall (2019). “The contract random interval spectral ensemble (c-RISE): The effect of contracting a classifier on accuracy”. In: *Hybrid Artificial Intelligent Systems: 14th International Conference, HAIS 2019, León, Spain, September 4–6, 2019, Proceedings 14*. Springer, pp. 381–392 (cit. on p. 40).
- Forestier, Germain et al. (2017). “Generating synthetic time series to augment sparse datasets”. In: *2017 IEEE international conference on data mining (ICDM)*. IEEE, pp. 865–870 (cit. on pp. 157, 165, 213).
- Foumani, Navid Mohammadi et al. (2024a). “Improving position encoding of transformers for multivariate time series classification”. In: *Data Mining and Knowledge Discovery* 38.1, pp. 22–48 (cit. on pp. 10, 55, 56, 130, 133).
- Foumani, Navid Mohammadi et al. (2024b). “Series2vec: similarity-based self-supervised representation learning for time series classification”. In: *Data Mining and Knowledge Discovery*, pp. 1–25 (cit. on p. 217).
- Foumani, Seyed Navid Mohammadi, Chang Wei Tan, and Mahsa Salehi (2021). “Disjoint-cnn for multivariate time series classification”. In: *2021 International Conference on Data Mining Workshops (ICDMW)*. IEEE, pp. 760–769 (cit. on pp. 10, 54, 55, 130).
- Franceschi, Jean-Yves, Aymeric Dieuleveut, and Martin Jaggi (2019). “Unsupervised scalable representation learning for multivariate time series”. In: *Advances in neural information processing systems* 32 (cit. on pp. 10, 67, 72, 73, 140, 143, 146, 216).
- Fréchet, Maurice (1906). “Sur quelques points du calcul fonctionnel”. In: (cit. on p. 188).
- (1957). “Sur la distance de deux lois de probabilité”. In: *Annales de l’ISUP*. Vol. 6. 3, pp. 183–198 (cit. on p. 188).
- Freund, Yoav, Robert E Schapire, et al. (1996). “Experiments with a new boosting algorithm”. In: *icml*. Vol. 96. Citeseer, pp. 148–156 (cit. on p. 33).
- Friedman, Milton (1940). “A comparison of alternative tests of significance for the problem of m rankings”. In: *The annals of mathematical statistics* 11.1, pp. 86–92 (cit. on pp. 4, 79).
- Fulcher, Ben D and Nick S Jones (2017). “hctsa: A computational framework for automated time-series phenotyping using massive feature extraction”. In: *Cell systems* 5.5, pp. 527–531 (cit. on p. 33).
- Gao, Wenshuo et al. (2010). “An improved Sobel edge detection”. In: *2010 3rd International conference on computer science and information technology*. Vol. 5. IEEE, pp. 67–71 (cit. on pp. 6, 95).
- Garcia, Salvador and Francisco Herrera (2008). “An Extension on " Statistical Comparisons of Classifiers over Multiple Data Sets" for all Pairwise Comparisons.” In: *Journal of machine learning research* 9.12 (cit. on p. 77).
- Gee, Alan H et al. (2019). “Explaining deep classification of time-series data with learned prototypes”. In: *CEUR workshop proceedings*. Vol. 2429. NIH Public Access, p. 15 (cit. on p. 157).
- Geurts, Pierre, Damien Ernst, and Louis Wehenkel (2006). “Extremely randomized trees”. In: *Machine learning* 63, pp. 3–42 (cit. on p. 39).
- Ghasedi Dizaji, Kamran et al. (2017). “Deep clustering via joint convolutional auto-encoder embedding and relative entropy minimization”. In: *Proceedings of the IEEE international conference on computer vision*, pp. 5736–5745 (cit. on pp. 67, 69).
- Godahewa, Rakshitha et al. (2021). “Monash time series forecasting archive”. In: *arXiv preprint arXiv:2105.06643* (cit. on p. 19).

- Golub, Gene H and Charles F Van Loan (2013). *Matrix computations*. JHU press (cit. on p. 66).
- Goodfellow, Ian et al. (2014). “Generative adversarial nets”. In: *Advances in neural information processing systems* 27 (cit. on pp. 13, 173).
- Goswami, Mononito et al. (2024). “Moment: A family of open time-series foundation models”. In: *arXiv preprint arXiv:2402.03885* (cit. on pp. 23, 217).
- Graves, Alex, Abdel-rahman Mohamed, and Geoffrey Hinton (2013). “Speech recognition with deep recurrent neural networks”. In: *2013 IEEE international conference on acoustics, speech and signal processing*. Ieee, pp. 6645–6649 (cit. on p. 48).
- Guijo-Rubio, David et al. (2024). “Unsupervised feature based algorithms for time series extrinsic regression”. In: *Data Mining and Knowledge Discovery*, pp. 1–45 (cit. on pp. 56, 57).
- Guillaume, Antoine, Christel Vrain, and Wael Elloumi (2022). “Random dilated shapelet transform: A new approach for time series shapelets”. In: *International Conference on Pattern Recognition and Artificial Intelligence*. Springer, pp. 653–664 (cit. on p. 36).
- Guo, Chuan et al. (2020). “Action2motion: Conditioned generation of 3d human motions”. In: *Proceedings of the 28th ACM International Conference on Multimedia*, pp. 2021–2029 (cit. on pp. 11, 14, 15, 23, 24, 150, 151, 172, 174, 177, 178, 182, 189, 192, 193, 201).
- He, Kaiming et al. (2016). “Deep residual learning for image recognition”. In: *Proceedings of the IEEE conference on computer vision and pattern recognition*, pp. 770–778 (cit. on pp. 44, 52, 53).
- Herrmann, Matthieu and Geoffrey I Webb (2023). “Amercing: an intuitive and effective constraint for dynamic time warping”. In: *Pattern Recognition* 137, p. 109333 (cit. on p. 33).
- Herrmann, Matthieu et al. (2023). “Proximity Forest 2.0: A new effective and scalable similarity-based classifier for time series”. In: *arXiv preprint arXiv:2304.05800* (cit. on p. 33).
- Heusel, Martin et al. (2017). “Gans trained by a two time-scale update rule converge to a local nash equilibrium”. In: *Advances in neural information processing systems* 30 (cit. on pp. 15, 188, 216).
- Higgins, Irina et al. (2017). “beta-vae: Learning basic visual concepts with a constrained variational framework.” In: *ICLR (Poster)* 3 (cit. on pp. 69, 177).
- Hills, Jon et al. (2014). “Classification of time series by shapelet transformation”. In: *Data mining and knowledge discovery* 28, pp. 851–881 (cit. on p. 36).
- Ho, Jonathan, Ajay Jain, and Pieter Abbeel (2020). “Denoising diffusion probabilistic models”. In: *Advances in neural information processing systems* 33, pp. 6840–6851 (cit. on pp. 174, 175).
- Hochreiter, Sepp and Jürgen Schmidhuber (1997). “Long short-term memory”. In: *Neural computation* 9.8, pp. 1735–1780 (cit. on pp. 48, 49).
- Hoerl, Arthur E and Robert W Kennard (1970). “Ridge regression: Biased estimation for nonorthogonal problems”. In: *Technometrics* 12.1, pp. 55–67 (cit. on pp. 33, 35–38, 146).
- Holder, Christopher, David Guijo-Rubio, and Anthony Bagnall (2023). “Barycentre averaging for the move-split-merge time series distance measure”. In: *15th International Joint Conference on Knowledge Discovery, Knowledge Engineering and Knowledge Management* (cit. on p. 61).
- Holder, Christopher, Matthew Middlehurst, and Anthony Bagnall (2024). “A review and evaluation of elastic distance functions for time series clustering”. In: *Knowledge and Information Systems* 66.2, pp. 765–809 (cit. on pp. 61, 157, 159).

- Holm, Sture (1979). “A simple sequentially rejective multiple test procedure”. In: *Scandinavian journal of statistics*, pp. 65–70 (cit. on pp. 82, 85).
- Howard, Andrew G et al. (2017). “Mobilenets: Efficient convolutional neural networks for mobile vision applications”. In: *arXiv preprint arXiv:1704.04861* (cit. on pp. 9, 43, 215).
- Hubert, Lawrence and Phipps Arabie (1985). “Comparing partitions”. In: *Journal of classification* 2, pp. 193–218 (cit. on p. 160).
- Hunter, John D (2007). “Matplotlib: A 2D graphics environment”. In: *Computing in science & engineering* 9.03, pp. 90–95 (cit. on p. 212).
- Imani, Shima et al. (2020). “Introducing time series snippets: a new primitive for summarizing long time series”. In: *Data Mining and Knowledge Discovery* 34, pp. 1713–1743 (cit. on p. 21).
- Ismail-Fawaz, Ali et al. (2022). “Deep learning for time series classification using new hand-crafted convolution filters”. In: *2022 IEEE International Conference on Big Data (Big Data)*. IEEE, pp. 972–981 (cit. on p. 24).
- Ismail-Fawaz, Ali et al. (2023a). “An approach to multiple comparison benchmark evaluations that is stable under manipulation of the compare set”. In: *arXiv preprint arXiv:2305.11921* (cit. on p. 24).
- Ismail-Fawaz, Ali et al. (2023b). “Enhancing time series classification with self-supervised learning”. In: *International Conference on Agents and Artificial Intelligence (ICAART)*. SCITEPRESS-Science and Technology Publications, pp. 40–47 (cit. on p. 24).
- Ismail-Fawaz, Ali et al. (2023c). “Lite: Light inception with boosting techniques for time series classification”. In: *2023 IEEE 10th International Conference on Data Science and Advanced Analytics (DSAA)*. IEEE, pp. 1–10 (cit. on p. 24).
- Ismail-Fawaz, Ali et al. (2023d). “ShapeDBA: Generating Effective Time Series Prototypes using ShapeDTW Barycenter Averaging”. In: *ECML/PKDD Workshop on Advanced Analytics and Learning on Temporal Data*, pp. 1–8. URL: https://doi.org/10.1007/978-3-031-49896-1_9 (cit. on p. 24).
- Ismail-Fawaz, Ali et al. (2024a). “A Supervised Variational Auto-Encoder for Human Motion Generation using Convolutional Neural Networks”. In: *4th International Conference on Pattern Recognition and Artificial Intelligence (ICPRAI)* (cit. on p. 24).
- (2024b). *Elastic Warping Visualization For Time Series*. <https://github.com/yourusername/dtw-visualization> (cit. on pp. 24, 212).
- (2024c). “Establishing a Unified Evaluation Framework for Human Motion Generation: A Comparative Analysis of Metrics”. In: *arXiv preprint arXiv:2405.07680* (cit. on p. 24).
- (2024d). *Feature-Based Time Series Classification with Kolmogorov-Arnold Networks*. <https://github.com/MSD-IRIMAS/Simple-KAN-4-Time-Series> (cit. on pp. 24, 213).
- (2024e). “Finding foundation models for time series classification with a pretext task”. In: *Pacific-Asia Conference on Knowledge Discovery and Data Mining*. Springer, pp. 123–135 (cit. on p. 24).
- (2024f). “Look Into the LITE in Deep Learning for Time Series Classification”. In: *arXiv preprint arXiv:2409.02869* (cit. on p. 24).
- (2024g). “Weighted Average of Human Motion Sequences for Improving Rehabilitation Assessment”. In: *ECML/PKDD Workshop on Advanced Analytics and Learning on Temporal Data* (cit. on p. 24).

- (2024h). *Weighted Elastic Barycenter Averaging to Augment Time Series Data*. <https://github.com/MSD-IRIMAS/Augmenting-TSC-Elastic-Averaging> (cit. on pp. 24, 213).
- Ismail Fawaz, Hassan et al. (2019). “Deep learning for time series classification: a review”. In: *Data mining and knowledge discovery* 33.4, pp. 917–963 (cit. on pp. 22, 28, 40, 50, 53, 66, 67, 90, 100, 108, 154, 208, 210, 213).
- Ismail Fawaz, Hassan et al. (2020). “Inceptiontime: Finding alexnet for time series classification”. In: *Data Mining and Knowledge Discovery* 34.6, pp. 1936–1962 (cit. on pp. 6, 8–10, 12, 23, 53, 54, 74, 88, 94, 97–99, 108, 119, 121, 126, 127, 208, 215).
- Jiang, Wenchao and Zhaozheng Yin (2015). “Human activity recognition using wearable sensors by deep convolutional neural networks”. In: *Proceedings of the 23rd ACM international conference on Multimedia*, pp. 1307–1310 (cit. on p. 152).
- Karevan, Zahra and Johan AK Suykens (2020). “Transductive LSTM for time-series prediction: An application to weather forecasting”. In: *Neural Networks* 125, pp. 1–9 (cit. on p. 19).
- Keogh, Eamonn and Chotirat Ann Ratanamahatana (2005). “Exact indexing of dynamic time warping”. In: *Knowledge and information systems* 7, pp. 358–386 (cit. on p. 30).
- Keogh, Eamonn et al. (2001). “Dimensionality reduction for fast similarity search in large time series databases”. In: *Knowledge and information Systems* 3, pp. 263–286 (cit. on pp. 37, 38, 209).
- Keogh, Eamonn J and Michael J Pazzani (1998). “An enhanced representation of time series which allows fast and accurate classification, clustering and relevance feedback.” In: *Kdd*. Vol. 98, pp. 239–243 (cit. on pp. 3, 58, 60).
- Kim, Dong Seong and Jong Sou Park (2003). “Network-based intrusion detection with support vector machines”. In: *Information Networking: International Conference, ICOIN 2003, Cheju Island, Korea, February 12-14, 2003. Revised Selected Papers*. Springer, pp. 747–756 (cit. on p. 19).
- Kingma, Diederik P and Max Welling (2013). “Auto-encoding variational bayes”. In: *arXiv preprint arXiv:1312.6114* (cit. on pp. 13, 68, 175).
- Kramer, Mark A (1991). “Nonlinear principal component analysis using autoassociative neural networks”. In: *AIChE journal* 37.2, pp. 233–243 (cit. on p. 68).
- Krizhevsky, Alex, Ilya Sutskever, and Geoffrey E Hinton (2012). “Imagenet classification with deep convolutional neural networks”. In: *Advances in neural information processing systems* 25 (cit. on pp. 22, 51).
- Kynkäänniemi, Tuomas et al. (2019). “Improved precision and recall metric for assessing generative models”. In: *Advances in Neural Information Processing Systems* 32 (cit. on pp. 190, 194).
- Lafabregue, Baptiste et al. (2022). “End-to-end deep representation learning for time series clustering: a comparative study”. In: *Data mining and knowledge discovery* 36.1, pp. 29–81 (cit. on pp. 3, 21, 22, 66, 67, 69, 70, 208).
- Large, James, Jason Lines, and Anthony Bagnall (2019). “A probabilistic classifier ensemble weighting scheme based on cross-validated accuracy estimates”. In: *Data mining and knowledge discovery* 33.6, pp. 1674–1709 (cit. on p. 40).
- Lecoutre, Bruno et al. (2014). *The significance test controversy revisited*. Springer (cit. on p. 85).
- LeCun, Yann, Yoshua Bengio, and Geoffrey Hinton (2015). “Deep learning”. In: *nature* 521.7553, pp. 436–444 (cit. on pp. 22, 34, 40, 45, 51).

- Li, Longze and Aleksandar Vakanski (2018). “Generative adversarial networks for generation and classification of physical rehabilitation movement episodes”. In: *International journal of machine learning and computing* 8.5, p. 428 (cit. on p. 172).
- Lin, Jessica et al. (2007). “Experiencing SAX: a novel symbolic representation of time series”. In: *Data Mining and knowledge discovery* 15, pp. 107–144 (cit. on pp. 2, 37, 209).
- Lines, Jason and Anthony Bagnall (2015). “Time series classification with ensembles of elastic distance measures”. In: *Data Mining and Knowledge Discovery* 29, pp. 565–592 (cit. on pp. 32, 33, 40).
- Lines, Jason, Sarah Taylor, and Anthony Bagnall (2018). “Time series classification with HIVE-COTE: The hierarchical vote collective of transformation-based ensembles”. In: *ACM Transactions on Knowledge Discovery from Data (TKDD)* 12.5, pp. 1–35 (cit. on pp. 2, 40, 53).
- Liu, Ziming et al. (2024). “Kan: Kolmogorov-arnold networks”. In: *arXiv preprint arXiv:2404.19756* (cit. on p. 213).
- Loh, Wei-Yin (2011). “Classification and regression trees”. In: *Wiley interdisciplinary reviews: data mining and knowledge discovery* 1.1, pp. 14–23 (cit. on p. 57).
- Lubba, Carl H et al. (2019). “catch22: CANonical Time-series CHaracteristics: Selected through highly comparative time-series analysis”. In: *Data Mining and Knowledge Discovery* 33.6, pp. 1821–1852 (cit. on pp. 33, 213).
- Lucas, Benjamin et al. (2019). “Proximity forest: an effective and scalable distance-based classifier for time series”. In: *Data Mining and Knowledge Discovery* 33.3, pp. 607–635 (cit. on p. 33).
- Lucas, Thomas et al. (2022). “Posegpt: Quantization-based 3d human motion generation and forecasting”. In: *European Conference on Computer Vision*. Springer, pp. 417–435 (cit. on pp. 174, 182).
- Lun, Roanna and Wenbing Zhao (2015). “A survey of applications and human motion recognition with microsoft kinect”. In: *International Journal of Pattern Recognition and Artificial Intelligence* 29.05, p. 1555008 (cit. on p. 149).
- Ma, Qianli et al. (2019). “Learning representations for time series clustering”. In: *Advances in neural information processing systems* 32 (cit. on pp. 67, 70).
- Maaten, Laurens Van der and Geoffrey Hinton (2008). “Visualizing data using t-SNE.” In: *Journal of machine learning research* 9.11 (cit. on pp. 94, 103, 116, 166).
- MacQueen, James et al. (1967). “Some methods for classification and analysis of multivariate observations”. In: *Proceedings of the fifth Berkeley symposium on mathematical statistics and probability*. Vol. 1. 14. Oakland, CA, USA, pp. 281–297 (cit. on pp. 3, 63).
- Maor, Eli (2019). *The Pythagorean theorem: a 4,000-year history*. Vol. 65. Princeton University Press (cit. on p. 199).
- Marteau, Pierre-François (2019a). “On the separation of shape and temporal patterns in time series-Application to signature authentication”. In: *arXiv preprint arXiv:1911.09360* (cit. on p. 217).
- Marteau, Pierre-Francois (2019b). “Times series averaging and denoising from a probabilistic perspective on time-elastic kernels”. In: *International Journal of Applied Mathematics and Computer Science* 29.2 (cit. on p. 63).
- Marteau, Pierre-François and Sylvie Gibet (2014). “On recursive edit distance kernels with application to time series classification”. In: *IEEE transactions on neural networks and learning systems* 26.6, pp. 1121–1133 (cit. on p. 28).

- Martinez, Julieta, Michael J Black, and Javier Romero (2017). “On human motion prediction using recurrent neural networks”. In: *Proceedings of the IEEE conference on computer vision and pattern recognition*, pp. 2891–2900 (cit. on p. 149).
- Meade, Nigel and Towhidul Islam (2015). “Forecasting in telecommunications and ICT—A review”. In: *International Journal of Forecasting* 31.4, pp. 1105–1126 (cit. on p. 19).
- Middlehurst, Matthew and Anthony Bagnall (2022). “The freshprince: A simple transformation based pipeline time series classifier”. In: *International Conference on Pattern Recognition and Artificial Intelligence*. Springer, pp. 150–161 (cit. on pp. 33, 57).
- Middlehurst, Matthew, James Large, and Anthony Bagnall (2020). “The canonical interval forest (CIF) classifier for time series classification”. In: *2020 IEEE international conference on big data (big data)*. IEEE, pp. 188–195 (cit. on p. 39).
- Middlehurst, Matthew, Patrick Schäfer, and Anthony Bagnall (2024). “Bake off redux: a review and experimental evaluation of recent time series classification algorithms”. In: *Data Mining and Knowledge Discovery*, pp. 1–74 (cit. on pp. 21, 23, 28, 33, 39, 57, 154).
- Middlehurst, Matthew et al. (2021). “HIVE-COTE 2.0: a new meta ensemble for time series classification”. In: *Machine Learning* 110.11, pp. 3211–3243 (cit. on pp. 39, 40, 53, 54, 57).
- Middlehurst, Matthew et al. (2024). “aeon: a Python toolkit for learning from time series”. In: *arXiv preprint arXiv:2406.14231* (cit. on pp. 16, 24, 207, 213, 216, 218).
- Miller, Lynn et al. (2022). “Multi-modal temporal CNNs for live fuel moisture content estimation”. In: *Environmental Modelling & Software* 156, p. 105467 (cit. on p. 19).
- Minsky, Marvin and Seymour Papert (1969). “An introduction to computational geometry”. In: *Cambridge tiass., HIT* 479.480, p. 104 (cit. on p. 50).
- Mohammadi Foumani, Navid et al. (2024). “Deep learning for time series classification and extrinsic regression: A current survey”. In: *ACM Computing Surveys* 56.9, pp. 1–45 (cit. on pp. 23, 218).
- Müller, Meinard (2007). “Dynamic time warping”. In: *Information retrieval for music and motion*, pp. 69–84 (cit. on pp. 15, 197).
- Muro-De-La-Herran, Alvaro, Begonya Garcia-Zapirain, and Amaia Mendez-Zorrilla (2014). “Gait analysis methods: An overview of wearable and non-wearable systems, highlighting clinical applications”. In: *Sensors* 14.2, pp. 3362–3394 (cit. on p. 152).
- Naeem, Muhammad Ferjad et al. (2020). “Reliable fidelity and diversity metrics for generative models”. In: *International Conference on Machine Learning*. PMLR, pp. 7176–7185 (cit. on pp. 14, 15, 167, 185, 190, 191, 194, 195).
- Nemenyi, Peter Bjorn (1963). *Distribution-free multiple comparisons*. Princeton University (cit. on pp. 4, 77, 79, 80).
- Nweke, Henry Friday et al. (2018). “Deep learning algorithms for human activity recognition using mobile and wearable sensor networks: State of the art and research challenges”. In: *Expert Systems with Applications* 105, pp. 233–261 (cit. on p. 152).
- Paparrizos, John and Luis Gravano (2015). “k-shape: Efficient and accurate clustering of time series”. In: *Proceedings of the 2015 ACM SIGMOD international conference on management of data*, pp. 1855–1870 (cit. on pp. 22, 65, 66).

- Park, Junwoo et al. (2024). “Self-Supervised Contrastive Learning for Long-term Forecasting”. In: *The Twelfth International Conference on Learning Representations* (cit. on p. 217).
- Pereira, Joao and Margarida Silveira (2019). “Learning representations from health-care time series data for unsupervised anomaly detection”. In: *2019 IEEE international conference on big data and smart computing (BigComp)*. IEEE, pp. 1–7 (cit. on p. 19).
- Petitjean, François, Alain Ketterlin, and Pierre Gançarski (2011). “A global averaging method for dynamic time warping, with applications to clustering”. In: *Pattern recognition* 44.3, pp. 678–693 (cit. on pp. 21, 61, 63, 64, 156–158, 161, 213).
- Petitjean, François et al. (2014). “Dynamic time warping averaging of time series allows faster and more accurate classification”. In: *2014 IEEE international conference on data mining*. IEEE, pp. 470–479 (cit. on pp. 61, 157).
- Petrovich, Mathis, Michael J Black, and Gül Varol (2021). “Action-conditioned 3d human motion synthesis with transformer vae”. In: *Proceedings of the IEEE/CVF International Conference on Computer Vision*, pp. 10985–10995 (cit. on pp. 23, 149, 164, 172, 174, 182).
- Pimentel, Marco AF et al. (2016). “Toward a robust estimation of respiratory rate from pulse oximeters”. In: *IEEE Transactions on Biomedical Engineering* 64.8, pp. 1914–1923 (cit. on p. 56).
- Pravilovic, Sonja et al. (2014). “Wind power forecasting using time series cluster analysis”. In: *Discovery Science: 17th International Conference, DS 2014, Bled, Slovenia, October 8-10, 2014. Proceedings 17*. Springer, pp. 276–287 (cit. on p. 21).
- Radford, Alec et al. (2018). “Improving language understanding by generative pre-training”. In: (cit. on p. 174).
- Rajan, Deepta and Jayaraman J Thiagarajan (2018). “A generative modeling approach to limited channel ECG classification”. In: *2018 40th Annual International Conference of the IEEE Engineering in Medicine and Biology Society (EMBC)*. IEEE, pp. 2571–2574 (cit. on pp. 19, 21).
- Ribeiro, Marco Tulio, Sameer Singh, and Carlos Guestrin (2016). ““ Why should i trust you?” Explaining the predictions of any classifier”. In: *Proceedings of the 22nd ACM SIGKDD international conference on knowledge discovery and data mining*, pp. 1135–1144 (cit. on p. 152).
- Rodriguez, Juan José, Ludmila I Kuncheva, and Carlos J Alonso (2006). “Rotation forest: A new classifier ensemble method”. In: *IEEE transactions on pattern analysis and machine intelligence* 28.10, pp. 1619–1630 (cit. on pp. 33, 57).
- Ronneberger, Olaf, Philipp Fischer, and Thomas Brox (2015). “U-net: Convolutional networks for biomedical image segmentation”. In: *Medical image computing and computer-assisted intervention—MICCAI 2015: 18th international conference, Munich, Germany, October 5-9, 2015, proceedings, part III 18*. Springer, pp. 234–241 (cit. on p. 175).
- Rumelhart, David E, Geoffrey E Hinton, and Ronald J Williams (1986a). “Learning representations by back-propagating errors”. In: *nature* 323.6088, pp. 533–536 (cit. on p. 41).
- (1986b). “Learning representations by back-propagating errors”. In: *nature* 323.6088, pp. 533–536 (cit. on p. 42).
- Sajjadi, Mehdi SM et al. (2018). “Assessing generative models via precision and recall”. In: *Advances in neural information processing systems* 31 (cit. on pp. 190, 194).
- Salimans, Tim et al. (2016). “Improved techniques for training gans”. In: *Advances in neural information processing systems* 29 (cit. on p. 188).

- Sanwlan, Monica and M Vijayalakshmi (2013). “Forecasting sales through time series clustering”. In: *International Journal of Data Mining & Knowledge Management Process* 3.1, p. 39 (cit. on p. 21).
- Schäfer, Patrick (2015). “The BOSS is concerned with time series classification in the presence of noise”. In: *Data Mining and Knowledge Discovery* 29, pp. 1505–1530 (cit. on pp. 1, 2, 38, 40).
- Schäfer, Patrick and Mikael Höggqvist (2012). “SFA: a symbolic fourier approximation and index for similarity search in high dimensional datasets”. In: *Proceedings of the 15th international conference on extending database technology*, pp. 516–527 (cit. on p. 38).
- Schäfer, Patrick and Ulf Leser (2017). “Fast and accurate time series classification with weasel”. In: *Proceedings of the 2017 ACM on Conference on Information and Knowledge Management*, pp. 637–646 (cit. on p. 38).
- (2023). “WEASEL 2.0: a random dilated dictionary transform for fast, accurate and memory constrained time series classification”. In: *Machine Learning* 112.12, pp. 4763–4788 (cit. on pp. 22, 38).
- Schmidl, Sebastian, Phillip Wenig, and Thorsten Papenbrock (2022). “Anomaly detection in time series: a comprehensive evaluation”. In: *Proceedings of the VLDB Endowment* 15.9, pp. 1779–1797 (cit. on pp. 19, 209).
- Schroff, Florian, Dmitry Kalenichenko, and James Philbin (2015). “Facenet: A unified embedding for face recognition and clustering”. In: *Proceedings of the IEEE conference on computer vision and pattern recognition*, pp. 815–823 (cit. on pp. 10, 73, 138).
- Senin, Pavel and Sergey Malinchik (2013). “Sax-vsm: Interpretable time series classification using sax and vector space model”. In: *2013 IEEE 13th international conference on data mining*. IEEE, pp. 1175–1180 (cit. on p. 37).
- Serra, Joan, Santiago Pascual, and Alexandros Karatzoglou (2018). “Towards a Universal Neural Network Encoder for Time Series.” In: *CCIA*, pp. 120–129 (cit. on pp. 52, 53).
- Shaw, Peter, Jakob Uszkoreit, and Ashish Vaswani (2018). “Self-attention with relative position representations”. In: *arXiv preprint arXiv:1803.02155* (cit. on p. 55).
- Shifaz, Ahmed et al. (2020). “TS-CHIEF: a scalable and accurate forest algorithm for time series classification”. In: *Data Mining and Knowledge Discovery* 34.3, pp. 742–775 (cit. on p. 40).
- Stefan, Alexandra, Vassilis Athitsos, and Gautam Das (2012a). “The move-split-merge metric for time series”. In: *IEEE transactions on Knowledge and Data Engineering* 25.6, pp. 1425–1438 (cit. on pp. 15, 196).
- (2012b). “The move-split-merge metric for time series”. In: *IEEE transactions on Knowledge and Data Engineering* 25.6, pp. 1425–1438 (cit. on pp. 29, 61, 62).
- Streijl, Robert C., Stefan Winkler, and David S. Hands (2014). “Mean opinion score (MOS) revisited: methods and applications, limitations and alternatives”. In: *Multimedia Systems* 22.2, pp. 213–227. ISSN: 1432-1882. DOI: [10.1007/s00530-014-0446-1](https://doi.org/10.1007/s00530-014-0446-1). URL: <http://dx.doi.org/10.1007/s00530-014-0446-1> (cit. on pp. 14, 185).
- Sutskever, Ilya, Oriol Vinyals, and Quoc V Le (2014). “Sequence to sequence learning with neural networks”. In: *Advances in neural information processing systems* 27 (cit. on p. 48).
- Szegedy, Christian et al. (2017). “Inception-v4, inception-resnet and the impact of residual connections on learning”. In: *Proceedings of the AAAI conference on artificial intelligence*. Vol. 31. 1 (cit. on p. 53).

- Tan, Chang Wei et al. (2020). “Monash University, UEA, UCR time series extrinsic regression archive”. In: *arXiv preprint arXiv:2006.10996* (cit. on pp. 19, 56, 57, 218).
- Tan, Chang Wei et al. (2022). “MultiRocket: multiple pooling operators and transformations for fast and effective time series classification”. In: *Data Mining and Knowledge Discovery* 36.5, pp. 1623–1646 (cit. on pp. 35, 57).
- Terefe, Tsegamlak et al. (2020). “Time series averaging using multi-tasking autoencoder”. In: *2020 IEEE 32nd International Conference on Tools with Artificial Intelligence (ICTAI)*. IEEE, pp. 1065–1072 (cit. on pp. 23, 209).
- Theissler, Andreas et al. (2022). “Explainable AI for time series classification: a review, taxonomy and research directions”. In: *Ieee Access* 10, pp. 100700–100724 (cit. on p. 155).
- Tripathy, RK and U Rajendra Acharya (2018). “Use of features from RR-time series and EEG signals for automated classification of sleep stages in deep neural network framework”. In: *Biocybernetics and Biomedical Engineering* 38.4, pp. 890–902 (cit. on p. 19).
- Tulyakov, Sergey et al. (2018). “Mocogan: Decomposing motion and content for video generation”. In: *Proceedings of the IEEE conference on computer vision and pattern recognition*, pp. 1526–1535 (cit. on p. 173).
- Van Den Oord, Aaron, Oriol Vinyals, et al. (2017). “Neural discrete representation learning”. In: *Advances in neural information processing systems* 30 (cit. on p. 174).
- Vapnik, Vladimir (2013). *The nature of statistical learning theory*. Springer science & business media (cit. on pp. 28, 143).
- Vaswani, Ashish et al. (2017). “Attention is all you need”. In: *Advances in neural information processing systems* 30 (cit. on pp. 47, 55, 174).
- Virtanen, Pauli et al. (2020). “SciPy 1.0: fundamental algorithms for scientific computing in Python”. In: *Nature methods* 17.3, pp. 261–272 (cit. on pp. 153, 177).
- Vlasic, Daniel et al. (2007). “Practical motion capture in everyday surroundings”. In: *ACM transactions on graphics (TOG)* 26.3, 35–es (cit. on pp. 11, 149).
- Wang, Zhiguang, Weizhong Yan, and Tim Oates (2017). “Time series classification from scratch with deep neural networks: A strong baseline”. In: *2017 International joint conference on neural networks (IJCNN)*. IEEE, pp. 1578–1585 (cit. on pp. 6, 9, 10, 12, 50–53, 67, 69, 74, 97, 98, 134, 138, 155, 175, 177).
- Webb, Geoffrey I and François Petitjean (2021). “Tight lower bounds for dynamic time warping”. In: *Pattern Recognition* 115, p. 107895 (cit. on p. 30).
- Wickstrøm, Kristoffer et al. (2022). “Mixing up contrastive learning: Self-supervised representation learning for time series”. In: *Pattern Recognition Letters* 155, pp. 54–61 (cit. on pp. 73, 74, 140, 143, 146).
- Wilcoxon, Frank (1992). “Individual comparisons by ranking methods”. In: *Breakthroughs in statistics: Methodology and distribution*. Springer, pp. 196–202 (cit. on pp. 4, 8, 77, 80, 100).
- Xie, Junyuan, Ross Girshick, and Ali Farhadi (2016). “Unsupervised deep embedding for clustering analysis”. In: *International conference on machine learning*. PMLR, pp. 478–487 (cit. on p. 67).
- Xin, Chu et al. (2024). “Enhancing Human Action Recognition with 3D Skeleton Data: A Comprehensive Study of Deep Learning and Data Augmentation”. In: *Electronics* 13.4, p. 747 (cit. on p. 164).
- Yang, Qiang and Xindong Wu (2006). “10 challenging problems in data mining research”. In: *International Journal of Information Technology & Decision Making* 5.04, pp. 597–604 (cit. on p. 19).

- Yang, Xinyu, Zhenguo Zhang, and Rongyi Cui (2022). “Timeclr: A self-supervised contrastive learning framework for univariate time series representation”. In: *Knowledge-Based Systems* 245, p. 108606 (cit. on p. 74).
- Ye, Lexiang and Eamonn Keogh (2009). “Time series shapelets: a new primitive for data mining”. In: *Proceedings of the 15th ACM SIGKDD international conference on Knowledge discovery and data mining*, pp. 947–956 (cit. on pp. 19, 36).
- (2011). “Time series shapelets: a novel technique that allows accurate, interpretable and fast classification”. In: *Data mining and knowledge discovery* 22, pp. 149–182 (cit. on pp. 1, 36).
- Zhang, Mingyuan et al. (2024a). “Motiondiffuse: Text-driven human motion generation with diffusion model”. In: *IEEE Transactions on Pattern Analysis and Machine Intelligence* (cit. on pp. 175, 182).
- Zhang, Richard et al. (2018). “The unreasonable effectiveness of deep features as a perceptual metric”. In: *Proceedings of the IEEE conference on computer vision and pattern recognition*, pp. 586–595 (cit. on p. 192).
- Zhang, Yaqi et al. (2024b). “Motiongpt: Finetuned llms are general-purpose motion generators”. In: *Proceedings of the AAAI Conference on Artificial Intelligence*. Vol. 38. 7, pp. 7368–7376 (cit. on p. 172).
- Zhao, Bendong et al. (2017). “Convolutional neural networks for time series classification”. In: *Journal of Systems Engineering and Electronics* 28.1, pp. 162–169 (cit. on p. 51).
- Zhao, Jiaping and Laurent Itti (2018). “shapedtw: Shape dynamic time warping”. In: *Pattern Recognition* 74, pp. 171–184 (cit. on pp. 31, 32, 158–160, 209).
- Zhong, Chongyang et al. (2022). “Learning uncoupled-modulation cvae for 3d action-conditioned human motion synthesis”. In: *European Conference on Computer Vision*. Springer, pp. 716–732 (cit. on pp. 174, 182).
- Zhou, Bolei et al. (2016). “Learning deep features for discriminative localization”. In: *Proceedings of the IEEE conference on computer vision and pattern recognition*, pp. 2921–2929 (cit. on pp. 152, 155).
- Zhu, LiuJun et al. (2021). “Live fuel moisture content estimation from MODIS: A deep learning approach”. In: *ISPRS Journal of Photogrammetry and Remote Sensing* 179, pp. 81–91 (cit. on pp. 19, 56).
- Zou, Shihao et al. (2020). “3D human shape reconstruction from a polarization image”. In: *Computer Vision—ECCV 2020: 16th European Conference, Glasgow, UK, August 23–28, 2020, Proceedings, Part XIV 16*. Springer, pp. 351–368 (cit. on p. 174).